UNIVERSITY OF SOUTHAMPTON

SCHOOL OF ENGINEERING SCIENCES

MATERIALS RESEARCH GROUP

FATIGUE ANALYSIS OF AUSTEMPERED DUCTILE IRON SUITABLE FOR AUTOMOTIVE CAMSHAFT APPLICATIONS

By Ben Stokes

Thesis submitted for the degree of Doctor of Philosophy

April 2003

UNIVERSITY OF SOUTHAMPTON

ABSTRACT

FACULTY OF ENGINEERING AND APPLIED SCIENCES
MATERIALS RESEARCH GROUP

Doctor of Philosophy

FATIGUE ANALYSIS OF AUSTEMPERED DUCTILE IRON SUITABLE FOR AUTOMOTIVE CAMSHAFT APPLICATIONS

By Ben Stokes

Fretting fatigue damage is of major concern during camshaft service, and a fundamental microstructurally based assessment of the mechanisms of simple fatigue failure is required to complement the empirical studies currently being carried out by Federal Mogul Camshafts. In investigating the effects of various Austempered Ductile Iron (ADI) microstructures on fatigue initiation and early crack growth, a micro-mechanistically based understanding is being developed that can be used in defining appropriate alloy development. Three ADI microstructures have been investigated: one produced by austenitising at 800^0C and austempering at 260^0C, one by austenitising at 800^0C and austempering at 390^0C, and the other by austenitising at 900^0C and austempering at 390^0C. The duration for austenitisation and austempering was two hours. The present results have been compared with previous work carried out at Southampton, and the Loughborough University microstructure evolution model has been used to estimate the proportions of the various phases. Crack initiation and early growth behaviour was assessed under three point bend short fatigue crack conditions. Averaged crack propagation behaviour has been assessed by long fatigue crack tests. Under all tested stress levels the '900/390' heat treatment outperformed both the '800/290' and '800/390' conditions. Crack initiation and propagation has been studied and two regimes of failure mechanism were identified. The softer, more damage tolerant '900/390' condition exhibited a generally propagation-dominated failure, whilst the harder, less damage tolerant '800/260' condition failed by varying degrees of crack linking by coalescence. The brittle '800/390' condition exhibited completely coalescence dominated failure. Primary initiation events for the '900/390' condition occurred exclusively at pores. Further micro-crack initiation occurred at decohered graphite nodules in the monotonic plastic zone ahead of the advancing dominant macro-crack tip. Initiation sites for the '800/260' and '800/390' condition have been identified as carbides remaining from the as cast ductile iron. The number of carbides cracking on loading to stresses greater than 275 MPa is critical in determining the failure mechanism. When the number is high the extent of surface propagation is minimal and crack growth is almost completely controlled by crack coalescence and growth in the depth direction. When the number of initiation events is significantly lower, the extent of crack linking by coalescence is reduced. Under these conditions the '800/260' heat treatment exhibits fatigue performance approaching that of the '900/390' specimens but at a higher hardness. Individual carbides and carbide populations have been characterised using finite body tessellation and SUPANOVA techniques in an attempt to quantify the factors promoting carbide fracture.

Table of Contents

Acknowledgements

Firstly I would like to express my gratitude to Dr. P.A.S. Reed for her dedicated supervision, support and encouragement throughout the course of this work. I am also grateful to K.K. Lee and D. Putman for running the *SUPANOVA* and *Microstructural Prediction* models on my behalf. Furthermore, I would like to thank the financial and technical support of Federal Mogul Camshafts, particularly Dr. A. Lapish.

I cannot forget to acknowledge the support of the clerical and technical staff; D. Beckett, 'Big' and 'Little' Erik, G. Skiller, G. Rood and S. Walker. I must thank E. Bonner especially, who had to machine my numerous samples (with the assistance of Betty), often at short notice. I also wish to thank my colleagues and friends in my office and the Engineering Materials Research Group in general.

Last, but not least, I am deeply grateful for the unconditional support and understanding of Marisa and my parents.

1 Introduction

Austempered Ductile Iron (ADI) is seen by many industrialists to be the material that offers a good combination of low cost, design flexibility, high strength-to-weight ratio and good toughness, wear resistance and fatigue strength. The mechanical properties of ADI may be tailored to suit particular applications by adjusting heat treatment parameters or material compositions. This has the effect of altering the proportions of the major phases present in the microstructure: bainitic ferrite, high carbon austenite and graphite (in the form of nodules). Generally ADI alloys possess mechanical properties superior to conventional ductile iron, cast iron and comparable to heat treated forged steels. Compared to conventional grades of ductile iron, ADI offers twice the tensile strength at comparable elongation.

It is these properties that are currently placing ADI as a candidate material for camshaft manufacture. The high strength, good wear properties, castability and low cost of ADI make it particularly attractive. However, due to a demand for improved engine performance, the service conditions for a camshaft have changed. The camshaft is a critical component in a combustion engine and advanced engine designs have changed the nature of camshaft contact from sliding contact (Figure 1.1) to rolling contact (Figure 1.2). This reduces friction in the contact area and hence improves efficiency. However, this improvement has also changed the nature of the stresses suffered by the camshaft and hence the requirement of the material from which it is forged. The traditional camshaft design (Figure 1.1) requires the camshaft material to withstand considerable amounts of wear. Grey cast iron, chilled at the cam nose to create a hard white cast iron layer was well suited to this application. The new developments (Figure 1.2) have changed what is required from the camshaft material. Contact fatigue is now a major concern of camshaft manufacturers. Rather than abrasion resistance, strength, ductility, fretting and rolling fatigue resistance are the properties now required from the camshaft material [1]. Grey cast iron is no longer wholly suited to this application and the alternative of ADI is becoming more attractive. However, the optimum ADI heat treatments to create the best micro-mechanical properties for this application are still not fully developed.

In considering the camshaft application it is clear both wear and fretting fatigue play an important role. Fretting fatigue is a very situation-specific service phenomenon. The construction of appropriate test conditions is extremely complicated. A study of the initiation and propagation of short fatigue cracks provides an insight into the resistance of a microstructure to fretting fatigue damage. A particular emphasis has been placed in understanding the fatigue failure mechanisms in order to define the requirements for optimisation of a fatigue resistant microstructure.

This project builds on the previous work performed at Southampton University [2,3,4,5,6] and assesses the effect of altering heat treatment parameters on the mechanical properties of ADI, focusing on those that are relevant for quantifying its suitability for camshaft applications. The properties of interest include fatigue resistance and hardness. In assessment of these properties long and short fatigue crack testing, hardness testing, and extensive image analysis and fractography have been used to study microstructures and the related failure mechanisms.

1.1 Project Objectives

The primary objective of this project is to explicitly quantify the local microstructural effects of fatigue failure on a range of alloy variants based on a ductile iron suitable for automotive camshaft applications. Four ADI alloys (from previous projects) will be compared with three new heat treatments and two chilled variants (one chilled ADI and one chilled ductile iron) Particular attention will be paid to fatigue initiation, early propagation and general fatigue crack growth behaviour. It is critical that a micro-mechanical understanding of the underlying fatigue processes is developed to allow the founding of quantitative performance optimisation criteria. This will enable feed back to the microstructural optimisation work being performed at Loughborough University [7,8,9].

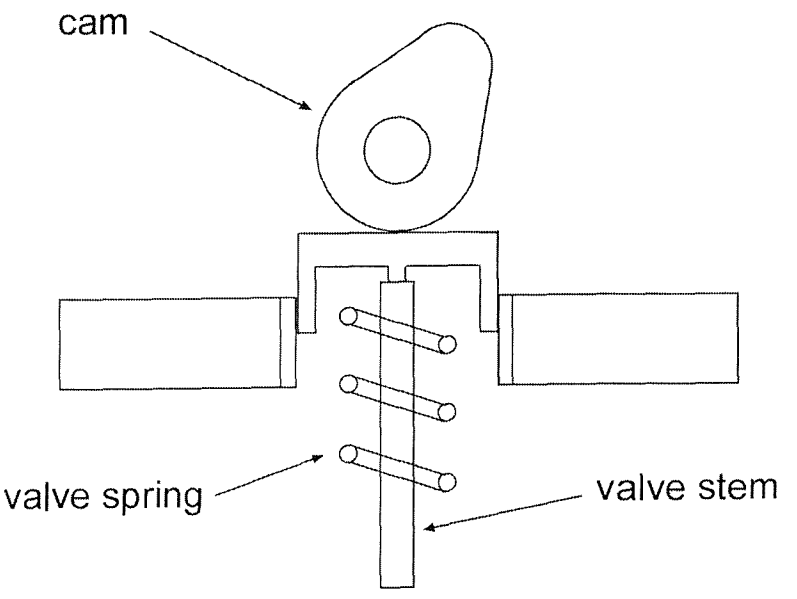

Figure 1.1: Traditional overhead camshaft

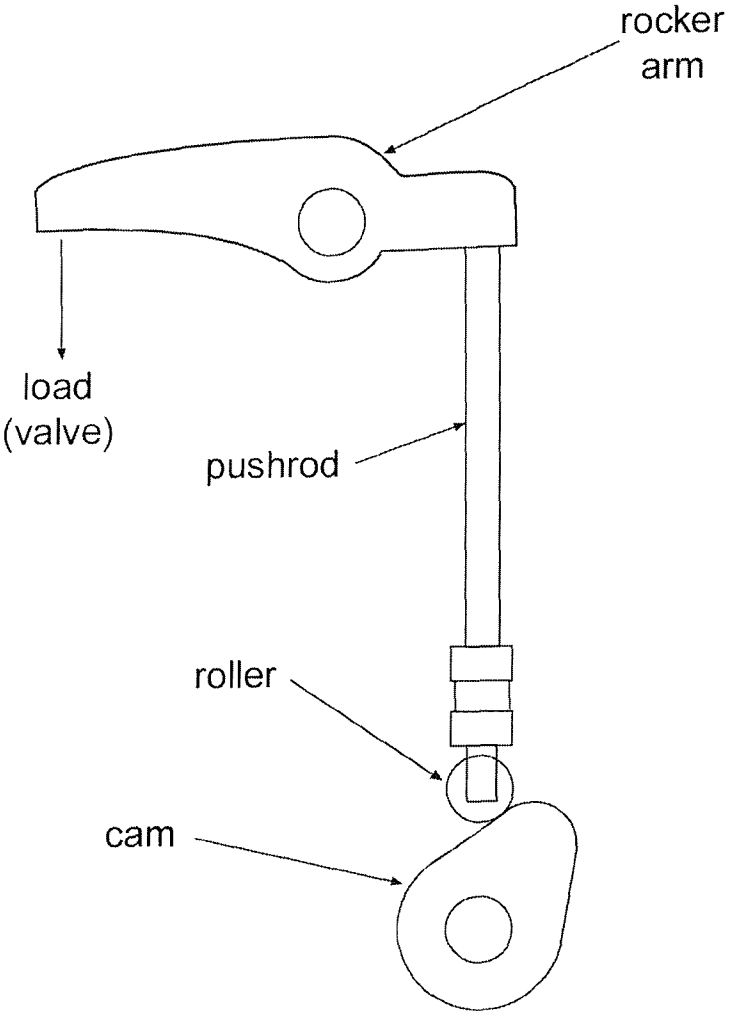

Figure 1.2: Modern camshaft with roller follower

2 Fatigue in Metals

The subject matter of the literature review for this project has been divided into three distinct sections. The first deals with the principles of fatigue in metals. The second section considers the microstructural features of ADI and is reviewed in chapter 3. The final section concerns the mechanical properties of ADI. This is reviewed in chapter 4.

Fatigue is defined as failure of a component or structure due to application of cyclic stresses. Loading that causes fatigue may be quantified in a number of ways.

Mean stress;

$$\sigma_m = \frac{(\sigma_{\max} + \sigma_{\min})}{2} \qquad \textit{Equation 2.1}$$

Cyclic stress;

$$\Delta\sigma = \sigma_{\max} - \sigma_{\min} \qquad \textit{Equation 2.2}$$

Load ratio;

$$R = \frac{\sigma_{\min}}{\sigma_{\max}} \qquad \textit{Equation 2.3}$$

Where σ_{max} *= maximum applied stress*

σ_{min} *= minimum applied stress*

Under such loads, it is possible for the failure to occur at loads much lower than static tensile or yield strengths. Fatigue failures are estimated to be responsible for approximately 90% of all metallic failures and final failure may be sudden and catastrophic. Failure occurs in a brittle-like manner with little gross plastic deformation even in ductile metals. The process commences with the initiation of fatigue cracks, followed by the propagation and possible subsequent coalescence of *short* cracks, to form a dominant crack or cracks, the propagation of the dominant crack or cracks and ultimately final failure. In most metallic materials, a significant amount of stable crack propagation may occur before catastrophic failure [10].

2.1 The Fatigue Limit and the S-N Curve

It is often convenient to represent the fatigue behaviour of a specimen or component in the form of a S-N curve, an example of which is shown in Figure 2.1. This plots the number of cycles to final failure (N_f) of a component or specimen at a given stress amplitude (σ_a). Rotating bend specimens or even the whole component may be tested to collect S-N data. Some materials exhibit a critical stress level below which the specimen may be cycled indefinitely without failure. This stress amplitude is referred to as the fatigue limit or endurance limit σ_e. For materials that do not exhibit a fatigue limit, the safe-life fatigue limit, or endurance limit is defined as the stress for a life of 10^7 cycles. The S-N curve shown in Figure 2.1 represents the total fatigue life of a smooth-surface, defect-free material. Total fatigue life describes both the number of cycles to initiate fatigue cracks in a defect-free specimen, and the number of cycles to propagate a dominant crack to catastrophic failure. It is suggested in literature however, that crack nucleation, not crack initiation is the critical event since crack initiation is instantaneous in most materials [11,12,13]. A crack nucleus is defined as the largest non-propagating flaw below the fatigue limit. Generally, a crack nucleus grows rapidly after initiation before decelerating with the interaction of microstructural barriers. If the stress levels experienced are below the fatigue limit, crack propagation will diminish until eventual crack arrest. At higher stress levels, the crack will continue to propagate accelerating as the crack length increases. This behaviour is indicative of short fatigue cracks and is discussed further in section 2.13.

2.2 Fracture Mechanics

The S-N approach assesses a component's total life, and does not give detailed understanding of the fundamental fatigue crack behaviour. To gain such information we may employ fracture mechanics approaches.

2.2.1 Griffith Fracture Theory

The work of Griffith, [14] who formulated criteria for unstable crack propagation in brittle materials, provides the basis for modern fracture mechanics. Griffith considered brittle continuum behaviour in terms of the balance between stored

strain energy at the crack tip and the increase of surface energy as the crack advances.

By considering an elliptical hole in an infinite elastic plate (Figure 2.2) Griffith postulated that the critical stress for fracture initiation is:

$$\sigma_{fracture} = \sqrt{\left(\frac{2E\gamma_e}{\pi a}\right)} \qquad \text{Equation 2.4}$$

$E = Young's\ Modulus$
$\gamma_e = surface\ energy\ per\ unit\ area$
$2a = crack\ length$

However the Griffith concept cannot be directly applied to most engineering solids, since the crack tip stresses experienced by all but the most brittle materials are higher than not only the global stresses but also the yield stress. This causes plastic deformation near the crack tip and there is no allowance for this plastic zone in Griffith's theory. The brittle fracture concept was advanced by Orowan [15] to include plastic deformation by considering the work needed to advance the crack tip plastic deformation by crack growth. Supplementing the surface energy term in equation 4 with a plastic energy dissipation term

$$\sigma_{fracture} = \sqrt{\left(\frac{2E(\gamma_e + \gamma_p)}{\pi a}\right)} \qquad \text{Equation 2.5}$$

$\gamma_p = plastic\ work\ per\ unit\ area$

If $\gamma_p >> \gamma_e$ the equation is reduced to

$$\sigma_{fracture} = \sqrt{\left(\frac{2E(\gamma_p)}{\pi a}\right)} \qquad \text{Equation 2.6}$$

2.2.2 Crack Driving Force and Energy Release Rate

An approach to characterise the driving force for fracture in cracked elastic bodies was also suggested by Irwin [16]. This work was conceptually equivalent to the Griffith Energy model and was based on a cracked elastic plate of uniform

thickness as in Figure 2.3. The term G, the strain energy release rate, was introduced by Irwin for this purpose, where

$$G = -\frac{dW_p}{da}$$ Equation 2.7

dW = change in potential energy of a cracked plate
da = change in crack length

By considering load-controlled displacement and displacement-controlled loading of the cracked elastic plate Irwin showed the Griffith Criterion for fracture initiation in a brittle solid may be expressed in terms of G such that:

$$G = \frac{\pi a \sigma^2}{E} = 2(\gamma_e + \gamma_p)$$ Equation 2.8

Comparison of this work and Linear Elastic Fracture Mechanics follows in section 2.3.4.

2.3 Linear Elastic Fracture Mechanics

The following section describes how the critical conditions for the growth of cracks may be characterised by means of linear elastic stress analysis. This approach provides a more explicit description of crack tip stress states than the previously mentioned global energy balance theories.

2.3.1 Macroscopic Modes of Fracture

The three basic modes of fracture are shown in Figure 2.4. Mode I is the tensile opening load. Mode II is the in-plane sliding mode, and mode III is the tearing anti-plane shear mode [10]. The quantification of the near-tip stress fields for the elastic crack in terms of a stress intensity factor, K, was first proposed by Irwin [17] who considered a semi-infinite crack in an infinite plate as shown in figure 2.1. Since the characterisation of fatigue cracks in a wide range of conditions is largely based on linear elastic fracture mechanics, a discussion of near-tip stress fields for a mode I crack in this section is appropriate. Consider the semi-infinite crack in an infinite plate as in Figure 2.5.

For the 2D plane stress problem (modes I and II), the equilibrium equations in the absence of body forces are, in polar co-ordinates centred at the crack tip as follows:

$$\frac{\partial \sigma_{rr}}{\partial r} + \frac{1}{r}\frac{\partial \sigma_{r\theta}}{\partial \theta} + \frac{\sigma_{rr} - \sigma_{\theta\theta}}{r} = 0 \qquad \textit{Equation 2.9}$$

$$\frac{\partial \sigma_{r\theta}}{\partial r} + \frac{1}{r}\frac{\partial \sigma_{\theta\theta}}{\partial \theta} + \frac{2\sigma_{r\theta}}{r} = 0 \qquad \textit{Equation 2.10}$$

It can be shown that for the plane stress problem the crack tip stresses are described by:

$$\sigma_{ij} = \frac{K_I}{\sqrt{2\pi r}}\tilde{\sigma}_{ij}^{I}(\theta) + T\delta_{ix}\delta_{jx} \qquad \textit{Equation 2.11}$$

Where K_I is the stress intensity factor for mode I loading, δ_{ij} is the Krondecker delta and $\tilde{\sigma}_{ij}^{I}$ describes the far field mode I stress. This can be written in terms of the in-plane stress components thus:

$$\begin{pmatrix} \sigma_{xx} & \sigma_{xy} \\ \sigma_{yx} & \sigma_{yy} \end{pmatrix} = \frac{K_I}{\sqrt{2\pi r}} \begin{pmatrix} \tilde{\sigma}_{xx}^{I}(\theta) & \tilde{\sigma}_{xy}^{I}(\theta) \\ \tilde{\sigma}_{yx}^{I}(\theta) & \tilde{\sigma}_{yy}^{I}(\theta) \end{pmatrix} + \begin{pmatrix} T & 0 \\ 0 & 0 \end{pmatrix} \textit{(terms that vanish at the crack tip)}$$

Equation 2.12

The first term is the leading singular term for linear elastic mode I problems, whilst the second or 'T term' contains the non-singular stress. The leading singular term is generally adequate for characterising most linear elastic fatigue crack growth problems. The omission of the 'T stress' can however give large errors in certain fatigue situations. Such situations include: (i) short fatigue cracks, (ii) cracks subjected to high mode mixity, and (iii) small cracks inclined at a small angle to the applied tensile axis.

The leading terms for mode I stress fields in Cartesian co-ordinates omitting the 'T-term' are

$$\begin{Bmatrix}\sigma_{xx}\\ \sigma_{yy}\\ \sigma_{zz}\end{Bmatrix} = \frac{K_I}{\sqrt{2\pi r}}\cos\frac{\theta}{2}\begin{Bmatrix}1-\sin\frac{\theta}{2}\sin\frac{3\theta}{2}\\ 1+\sin\frac{\theta}{2}\sin\frac{3\theta}{2}\\ \sin\frac{\theta}{2}\cos\frac{3\theta}{2}\end{Bmatrix} \qquad \textit{Equation 2.13}$$

Similar expressions may be derived for modes II and III.

2.3.2 Conditions of K-dominance

The stress intensity factors in Equation 2.13 are a measure of the intensity of the near crack tip stress fields under purely linear elastic conditions. However they are only valid in an annular region ahead of the crack tip, known as the region of K-dominance [10]. Within this region the parameter K provides a unique measure of the stress and strain intensity and deformation. The outer radius of this region determined by the singular K term may deviate from the full elastic solutions including the 'T' and non-singular terms.

K is often used to characterise the near crack tip stress state conditions for fatigue crack initiation and propagation. However, fatigue is a locally plastic phenomenon, and the formulation of K is based on purely linear elastic assumptions as detailed in previous sections. K therefore cannot be used to explicitly characterise the elasto-plastic conditions occurring in the plastic zone at the crack tip. Thus the size of this plastic deformation zone (generally referred to as the 'process zone') dictates the inner radius of the region of K-dominance. K is however valid for the area surrounding this zone within the region of K-dominance. This condition, known as small scale yielding requires that the crack tip plastic zone be confined well within the region of K-dominance.

2.3.3 Fracture Toughness

The initiation of a crack under quasi-static loading conditions may be characterised using linear elastic fracture mechanics with the critical value of stress intensity factor, K_C. The value of this parameter is dependent on the mode of loading, the chemical environment, the material microstructure, the test

temperature, the strain rate, and the state of stress. The critical value of mode I stress intensity factor under plane strain conditions is referred to as the fracture toughness, K_{IC}, of the material. The corresponding fracture toughness values in the sliding and tearing modes are referred to as K_{IIC} and K_{IIIC} respectively. For F_C to be a constant material parameter defining fracture toughness for a given material, small scale yielding conditions must be obeyed. This requires that

$$a, W-a, B \leq \left(\frac{K}{\sigma_y}\right)^2 \qquad \textit{Equation 2.14}$$

$a = crack\ length$
$B = specimen\ breadth$
$W = specimen\ width$

are all satisfied [18].

2.3.4 Equivalence of G and K

The stress intensity factor approach to fracture has a direct equivalence to the energy approach. Using a virtual work argument, the work done by surface forces acting along a crack increment 'δa' as a crack closes from 'a + δa' to 'a' will equal the change in energy of a body as a whole as a crack grows by this increment. For the plane stress condition:

$$G = \frac{K^2}{E} \qquad \textit{Equation 2.15}$$

The parameter K can be calculated from the applied stress and crack geometry but gives a magnitude of the crack tip stress field. This allows analysis of the crack tip characteristics from parameters that are experimentally easy to quantify.

2.4 Crack Tip Plasticity

Whilst LEFM analysis of sharp cracks predicts infinite stress at the crack tip, real materials suffer finite stresses at the crack tip since the crack tip radius must be finite [19]. Inelastic material deformation (plasticity in metals) leads to further relaxation of crack tip stresses. LEFM becomes increasingly less accurate as the

plastic region at the crack tip grows. Simple corrections allow LEFM to be applied to cracks where moderate yielding occurs.

2.5 Plastic Zone Size in Monotonic Loading

2.5.1 The Irwin Approach [10,19]

The Irwin approach estimates of the crack tip plastic zone by considering the elastic-plastic boundary. On the crack plane where θ=0, Equation 2.13 simplifies to

$$\sigma_{xx} = \sigma_{yy} = \frac{K_I}{\sqrt{2\pi r}} \qquad \textit{Equation 2.16}$$

It is assumed that the boundary between elastic and plastic behaviour occurs when the stresses given Equation 2.16 satisfy a yield criterion. For plane stress conditions

$$\sigma_{yy} = \sigma_{YS} \qquad \textit{Equation 2.17}$$

$$where \sigma_{YS} = uniaxial\ material\ yield\ strength$$

Substituting into Equation 2.16 and solving for *r* gives a first order approximation of crack tip plastic zone size.

$$r_y = \frac{1}{2\pi}\left(\frac{K_I}{\sigma_{YS}}\right)^2 \qquad \textit{Equation 2.18}$$

If strain hardening is neglected, the stress distribution for $r \le r_y$ is shown in Figure 2.6. The horizontal line at $\sigma_{yy} = \sigma_{YS}$ represents the truncation of the stress singularity by yielding at the crack tip. This estimation is not strictly correct, since the solution is based on an elastic crack tip. When yielding occurs, stresses must redistribute to satisfy equilibrium. The plastic zone size increases as it accommodates the forces present in an elastic material, which cannot be

sustained in an elastic-plastic material since the stresses cannot exceed yield. This is represented by the hatched area in Figure 2.6.

Solving a simple force balance gives:

$$r_p = \frac{1}{\pi}\left(\frac{K_I}{\sigma_{YS}}\right)^2 \qquad \textit{Equation 2.19}$$

$$r_p = \frac{1}{3\pi}\left(\frac{K_I}{\sigma_{YS}}\right)^2 \qquad \textit{Equation 2.20}$$

for plane stress and plane strain conditions respectively.

2.5.2 The Dugdale Model [10,19]

The estimation of the plastic crack tip zone ahead of a mode I crack in a non-hardening material subject to plane stress was first proposed by Dugdale and Barenblatt in 1960. In this model, the plastic crack tip zone is envisaged as a long slender (of near zero height) strip that extends a distance r_p, such that the total crack length is equivalent to $2a + 2r_p$ (Figure 2.7). A closure stress equal to σ_{YS} is applied at each crack tip, as shown in Figure 2.8.

The stress intensity due to the closure stress may be estimated by considering an external load *P* applied to the crack a distance *x* from the centre line. Hence, the stress intensities for the two crack tips are given by:

$$K_{I(+a)} = \frac{P}{\sqrt{\pi a}}\sqrt{\frac{a+x}{a-x}} \qquad \textit{Equation 2.21}$$

$$K_{I(-a)} = \frac{P}{\sqrt{\pi a}}\sqrt{\frac{a-x}{a+x}} \qquad \textit{Equation 2.22}$$

By replacing *a* with $a + r_p$ the total stress intensity at each crack tip resulting from closure stresses is given by:

$$K_{closure} = -2\sigma_{YS}\sqrt{\frac{a+r_p}{\pi}\cos^{-1}\left(\frac{a}{a+r_p}\right)}$$ Equation 2.23

Balancing the stress intensity from the remote tensile stress and that from closure gives:

$$\frac{a}{a+r_p} = \cos\left(\frac{\pi\sigma}{2\sigma_{YS}}\right)$$ Equati1 2won

2.24

Therefore, since r_p approaches infinity as $\sigma > \sigma_{YS}$ the plastic zone size when $\sigma << \sigma_{YS}$ is given by:

$$r_p = \frac{\pi}{8}\left(\frac{K_I}{\sigma_{YS}}\right)^2$$ Equation 2.25

This compares well with the result determined by the Irwin method (Equation 2.19) since $^1/_\pi = 0.318$ and $^\pi/_8 = 0.392$. These two models therefore, predict similar plastic zone sizes.

2.6 Plastic Zone Size in Cyclic Loading [10,19]

The calculation of the crack tip plastic zone during cyclic loading is complicated by the phenomenon of reversed plasticity during unloading. A plastic zone forms when a material is loaded to K_{max}. Upon unloading, material in proximity to the crack tip suffers reverse plasticity, resulting in a compressive plastic zone. The compressive stress field ahead of the crack influences subsequent crack growth.

The stresses within the reversed plastic zone may be calculated from the work of Rice. As the far-field tensile load P of a cracked plate is reduced by an amount ΔP (as with cyclic loading) to a tensile load P-ΔP, reverse plastic flow occurs. Providing the extent of crack blunting is assumed to be negligible, the infinitely large stress concentration factor at the crack tip leads to the formation of a reversed plastic zone within the monotonic plastic zone as shown schematically in Figure 2.9.

For the case of proportional loading, the changes in the crack tip fields due to the reduction of load are derived from the solutions for monotonic loading. The loading parameter is replaced by the load range ΔP. Since the material in the compressive plastic zone is stressed from $+\sigma_y$ to $-\sigma_y$ the effective stress for reverse yielding is $2\sigma_y$. Therefore, the size of r_c is calculated by the following equation

$$r_c = \frac{1}{\pi}\left(\frac{\Delta K_I}{2\sigma_{YS}}\right)^2 \qquad \textit{Equation 2.26}$$

2.7 Plastic Zone Shape

The estimations of plastic zone size so far presented have only considered the crack plane θ=0. It is possible to estimate the extent of plasticity at all angles by applying an appropriate yield criterion to Equation 2.13. By considering the von Mises equation (where yielding occurs when $\sigma_e = \sigma_{YS}$) and the two dimensional Mohr's circle relationship, solving for r obtains estimates of the plane stress mode I plastic zone radius in terms of θ:

Monotonic: $$r_y = \frac{1}{4\pi}\left(\frac{K_{\max}}{\sigma_y}\right)^2\left[1+\cos\alpha+\frac{3}{2}\sin^2\alpha\right] \qquad \textit{Equation 2.27}$$

Cyclic: $$r_y = \frac{1}{4\pi}\left(\frac{\Delta K}{2\sigma_y}\right)^2\left[1+\cos\alpha+\frac{3}{2}\sin^2\alpha\right] \qquad \textit{Equation 2.28}$$

2.8 Characterisation of Fatigue Crack Growth

The propagation of a fatigue crack subjected to constant amplitude stress reversals is quantified as the crack length increment per cycle, $^{da}/_{dN}$. Values of $^{da}/_{dN}$ are determined experimentally by recording changes in crack length over an elapsed number of cycles. Generally, when the applied stress range is held

constant, the rate of crack growth increases with increasing number of cycles [10]. A typical fatigue crack growth curve is shown in Figure 2.10.

2.9 Characterisation of fatigue crack growth by K

Under fatigue conditions a crack may initiate or propagate at (maximum) stress intensity factors that are considerably lower than the fracture toughness, K_{IC}. Under small scale plastic yielding conditions, Paris et al [20,21] proposed that the growth rate of a fatigue crack should be related to the stress intensity factor range

$$\Delta K = K_{max} - K_{min} \qquad \textit{Equation 2.29}$$

K_{max} and K_{min} are the maximum and minimum values of stress intensity factor during a fatigue stress cycle. For an edge-cracked fatigue test specimen

$$K_{max} = Y\sigma_{max}\sqrt{\pi a} \qquad \textit{Equation 2.30}$$

$$K_{min} = Y\sigma_{min}\sqrt{\pi a} \qquad \textit{Equation 2.31}$$

$$\Delta K = Y\Delta\sigma\sqrt{\pi a} \qquad \textit{Equation 2.32}$$

where Y is a geometrical factor which depends on the ratio of crack length to the specimen width ($^a/_W$), and σ_{max} and σ_{min} are the maximum and minimum values of cyclic stress. Paris et al [20,21] showed that the relationship between crack growth rate and stress intensity factor is governed by the law

$$\frac{da}{dN} = C(\Delta K)^m \qquad \textit{Equation 2.33}$$

where C and m are constants influenced by material, material microstructure, environment, temperature and load ratio, R.

$$R = \frac{\sigma_{min}}{\sigma_{max}} = \frac{K_{min}}{K_{max}} \qquad \textit{Equation 2.34}$$

2.10 Microscopic stages of fatigue crack growth

It is generally accepted that fatigue crack growth may be divided into three regimes. The first of these (Stage I) occurs when the crack and the zone of plastic deformation ahead of the crack tip have dimensions confined to a few grain diameters (Initial crack growth after initiation for example). Within this regime crack growth is highly microstructurally dependent, with propagation occurring via a single slip mechanism in the direction of the primary slip system [10]. Stage I crack growth is generally relatively slow and leads to a zigzag crack path and a rough, facetted fracture surface. Typically the extent of this regime is only a few grains, although this depends on microstructure and loading. Initiation itself in the absence of pre-existing defects was shown by Forsyth [22] to occur along slip planes with the highest shear stress (those at 45^0 to the applied stress). The rapid and repeated movement of dislocations along this slip band will eventually cause a small crack to form, which can then propagate into other grains.

At higher stress intensity range values, the plastic zone ahead of the crack tip is large enough to encompass several grains. The resulting duplex slip system (simultaneous or alternating flow along two slip-systems) results in a crack path perpendicular to the remote tensile axis and is referred to as stage II growth [10]. The fracture surfaces of stage II crack growth may exhibit striations or 'beach marks' as first reported by Zappfe and Worden [23]. Furthermore, as shown by Forsyth and Ryder [24] it is possible to relate crack growth rate to striation spacing. A micro-mechanical model rationalizing the formation of fatigue striations in stage II crack growth was proposed by Laird and Smith [25]. They proposed that the increment of crack extension per fatigue cycle occurs due to plastic blunting and re-sharpening of the crack tip as shown in Figure 2.11.

The third and final regime of crack growth is the accelerated growth to failure where K_{max} is 70-80% of K_{IC} and monotonic failure modes contribute to the failure process. In most engineering components this regime is very short lived and may be ignored in fatigue life calculations.

2.11 Different Regimes of Fatigue Crack Propagation

The Paris law, showing a linear variation of $log\ {}^{da}/_{dN}$ with $log\ \Delta K$ only applies to a region of stable fatigue fracture that is only a portion of the total crack resistance curve for an alloy as shown in Figure 2.12. This plot shows three distinct regimes of crack growth. Regime A depicts *average* crack growth rate increments from below the atomic lattice spacing down to rates where no crack propagation is discernible. The stress intensity factor range below which no crack propagation is observed is known as the component's fatigue threshold (K_{th}). Crack propagation rates may be as low as fractions of atomic lattice spacing. This is possible since the crack may propagate discontinuously: through out of plane crack growth, the crack failing to advance during every cycle, or discontinuous crack growth along the crack front. Crack growth in this regime is associated with stage I failure and is largely microstructurally dependent. With discontinuous crack growth, it is necessary to identify the determination of fatigue threshold. This is generally accepted to be at crack growth rates of less than $10^{-8}\ {}^{mm}/_{cycle}$. Regime B, referred to as the Paris regime exhibits a linear variation of $log\ {}^{da}/_{dN}$ with $log\ \Delta K$ (Equation 2.33). Crack growth in this regime is associated with stage II failure and is generally microstructurally independent. Regime C is associated with the range of high ΔK values where accelerated crack propagation rates related to bursts of monotonic fracture cause rapid catastrophic fracture.

2.12 Crack Closure

Elber [26,27] showed that for a crack to propagate at the highest rates it must be able to open and close fully under cyclic loading. He introduced the term 'closure' to describe the condition when a fatigue crack is prevented from fully closing under minimum load. Elbers work and further work by Ritchie and Suresh [28,29,30,31] show that closure may arise from several sources. Those documented include: plasticity, surface roughness, oxide, viscous fluid and phase change induced closure. A detailed analysis of these closure mechanisms can be found in Suresh [10]; however brief summaries follow in this review.

Not withstanding the mechanism of how it is induced, the degree of closure can be effectively described using the parameters K_{cl}, and K_{op}, which represent the

stress intensity factors when the crack is closed and opened respectively. Elber proposed that fatigue cracks can only propagate during the period of loading when the crack faces are separated. Therefore, with the presence of closure, the crack grows under an effective stress range $\Delta\sigma_{eff}$ and the corresponding stress intensity factor range ΔK_{eff}.

$$\Delta\sigma_{eff} = \Delta\sigma_{max} - \Delta\sigma_{op} \text{ if } \sigma_{op} > \sigma_{min} \qquad \text{Equation 2.35}$$

$$\Delta K_{eff} = \Delta K_{max} - \Delta K_{op} \text{ if } K_{op} > K_{min} \qquad \text{Equation 2.36}$$

Hence at high R-ratios where K_{min} is greater than K_{op} closure free behaviour will be observed. The corresponding characterization of fatigue crack growth rates based on LEFM becomes:

$$\frac{da}{dN} = C\left(\Delta K_{eff}\right)^m \qquad \text{Equation 2.37}$$

2.12.1 Oxide-Induced Crack Closure

The presence of a moist atmosphere during the propagation of a fatigue crack will lead to the oxidation of the freshly formed fracture surface. At low ΔK levels a constant breaking and reforming of the oxide scale behind the crack tip caused by small crack tip opening displacements and mixed mode loading conditions increases the possibility of crack face contact leading to the build up of oxide layers via a fretting mechanism that are of similar dimensions to the crack opening displacement. This build up may therefore completely wedge open the crack. The effect of the fretting oxidation mechanism is less significant at high R-ratios due to larger crack tip opening displacements reducing the possibility of repeated crack face contact and hence this mechanism plays less of a role in influencing closure.

2.12.2 Roughness-Induced Closure

Stage I crack growth typically associated with regime A crack propagation and short cracks (see later section) leads to a highly serrated fracture morphology (i.e. faceted fracture surfaces). Any permanent plastic deformation (i.e. irreversible mode II displacements) ahead of the crack tip under these conditions will cause mismatch between the fracture surface asperities. The resulting tortuous crack

paths combined with the presence of crack face asperity mismatch provide a mechanism for enhanced crack closure.

2.12.3 Phase Transformation-Induced Crack Closure

Phase transformations at the crack tip can lead to retardation in crack growth rates. This process is referred to as TRIP (TRansformation-Induced Plasticity). The TRIP effect is characterized by phase transformation at the crack tip leading to a net increase in the volume of the transforming region. The enlarged material causes a reduction in the crack tip opening displacement once the crack has advanced further into the material. In addition the residual displacements in the crack wake enhance crack closure. This is particularly relevant to Iron based alloys and Austenitic Steels where strain induced martensitic transformation may occur at the crack tip [32,33].

2.12.4 Viscous Fluid-Induced Closure

If oil penetrates a fatigue crack, considerable internal oil pressure will be generated during the unloading phase. This has been shown to develop a hydrodynamic wedging of the crack causing closure [34]. The level of closure is dependent on the fluid's properties, since both the degree of crack penetration and subsequent internal oil pressure are dependent upon viscosity.

2.13 Short Fatigue Cracks

The analysis of fatigue crack behaviour on the basis of fracture mechanics is generally based on fatigue testing of specimens containing 'long' flaws typically a number of millimetres in length. There are a number of engineering components which require understanding of the fatigue behaviour of cracks of significantly smaller dimensions. Typically these small flaws range from a number of microns to a few millimetres. When continuum approaches have been applied to characterise these small cracks it has been shown that the growth of short cracks exhibits significant differences in behaviour when compared with long cracks. For a similar range of stress intensity factor, a short crack may show higher rates of propagation than long cracks under nominally similar conditions. Furthermore, crack growth may be seen at stress intensity factors that are lower than the threshold value for long cracks. The direct application of the expected fatigue behaviour derived from the analysis of long flaws to a component containing short

cracks leads therefore, to dangerous overestimations in fatigue life. A comparison of the fatigue behaviour of long and short cracks can be seen in Figure 2.13.

Pearson [35] first observed the accelerated propagation of short fatigue cracks. In the study of precipitation hardened aluminium alloy he found that the growth of short surface flaws was up to 100 times faster than longer flaws at the same nominal ΔK. The same studies also observed the growth of short cracks at nominal stress intensity levels below the threshold for long cracks. Further works [36, 37, 38, 39, 40] on a number of alloy systems documented several transient acceleration and deceleration characteristics associated with short crack propagation. In these works the periodic retardation of a short crack occurs as a crack tip encounters a grain boundary in the material. Suresh also observed the deflection of short cracks associated with the crystallographic reorientation of the crack tip as it traverses through the grain boundary to the adjacent grain. Suresh gives useful definitions for what constitutes a small crack:[10]

2.13.1 Microstructurally short cracks:

Where crack length is similar to a characteristic microstructural dimension. This may be grain size in monolithic materials, or particle spacing in discontinuously reinforced composites. Crack arrest in the microstructure short crack regime controls the *material* fatigue limit.

2.13.2 Mechanically short cracks:

Where length is similar to the crack tip plastic zone in smooth specimens, or where the plastic strain field of a notch engulfs the crack. Such situations cast doubts on the validity of K to characterise crack growth since calculations of K are based on linear elastic approximations.

2.13.3 Physically short cracks:

Cracks that are relatively small in comparison to the component in which they occur yet larger than any microstructural dimensions or plastic zones. Crack propagation rates in the physical short crack regime determine the fatigue life at stresses above the fatigue limit.

2.13.4 Chemically short cracks:

Cracks that show anomalous behaviour below a certain size as a result of an environmental factor such as stress corrosion.

2.13.5 Microstructural Aspects of Small Crack Growth

Local microstructural discontinuities, such as grain boundaries, inclusions, precipitates and reinforcements may affect the path and growth rate of short cracks since their size scale is comparable to the depth of a microstructurally small flaw. These features, as well as the crystallographic orientation of the grains have a significantly diminished effect on long crack growth. The transition from physical short cracks to long cracks is considered to occur when the crack tip plastic zone exceeds the strongest microstructural barrier spacing [41]. The crack tip of a long fatigue crack is therefore large enough to sample many grains and the fracture behaviour observed is representative of the materials bulk properties. Generally, fatigue resistance in short fatigue cracks can be improved by refining the microstructure. In contrast, the coarsening of the microstructure may decrease long crack propagation rates by utilizing roughness-induced crack closure.

Microscopic growth mechanisms of small fatigue cracks may be different from those of long cracks at nominally identical values of ΔK because of the differences in the constraint imposed by the surrounding elastic material. The crystallographic stage I growth of a small near surface flaw promotes severe local mixed mode loading at the crack tip.

Even when the loading conditions and the crack size satisfy the requirements for LEFM characterization, the physical smallness of the fatigue flaw generates faster propagation rates. This is because a short crack with its resulting short plastic wake benefits less from premature contact due to a variety of crack closure mechanisms. Tanaka [42] showed the influence of the lower crack closure levels by characterizing long and short cracks by both nominal ΔK and the closure-corrected ΔK_{eff}. The large difference in crack growth rate between the small and large cracks disappeared when ΔK_{eff} was considered.

2.14 Fretting Fatigue Mechanisms

Cyclic loading of components can arise in a number of ways and the complex applied stress states arising will clearly affect subsequent fatigue behaviour. The phenomena of fretting fatigue occurs as two pieces of material are pressed *together* by an external cyclic load, and are subsequently subject to a small amplitude oscillatory motion such that the relative parallel displacement is less than 0.1mm causing wear of the mating faces [43,44]. Fretting damage can take two forms; these being wear induced fretting (WIF) and cracking induced by fretting (CIF). It is the second case that leads to fretting fatigue damage. CIF occurs via the removal of protective oxide layers on the surfaces of the contacting faces. This allows metal-to-metal contact. If the two contacting metals offer a very strong metallic adhesion micro-welds may form between the two surfaces after around 100 fretting cycles. If the cyclic tangential slip is not enough to break these welds, the welded junction will grow to a relatively large size. The edge of this welded region is subjected to very high cyclic shear stresses, which have been shown to initiate fatigue cracking. Fretting is deleterious to the fatigue resistance of the material due to the high stress concentration experienced at the edges of the welded areas. The micro-cracks caused by fretting fatigue may form at stress levels below the threshold for long fatigue crack growth. They however, may not necessarily prove problematic unless they penetrate the material enough to become macro-cracks and propagate under normal cycling loads. Once the crack has grown to a length comparable to the dimensions of the contact, the influence of the contact itself diminishes, and the crack behaves similarly to one caused by plain fatigue [45]. In considering the fretting fatigue problem, it is clear that it is the initiation and early stage of crack growth (i.e. small defects) that predominate. Fretting fatigue is a significant concern of camshaft manufacturers and an understanding of the fretting processes in ADI and hence short crack behaviour is particularly desirable.

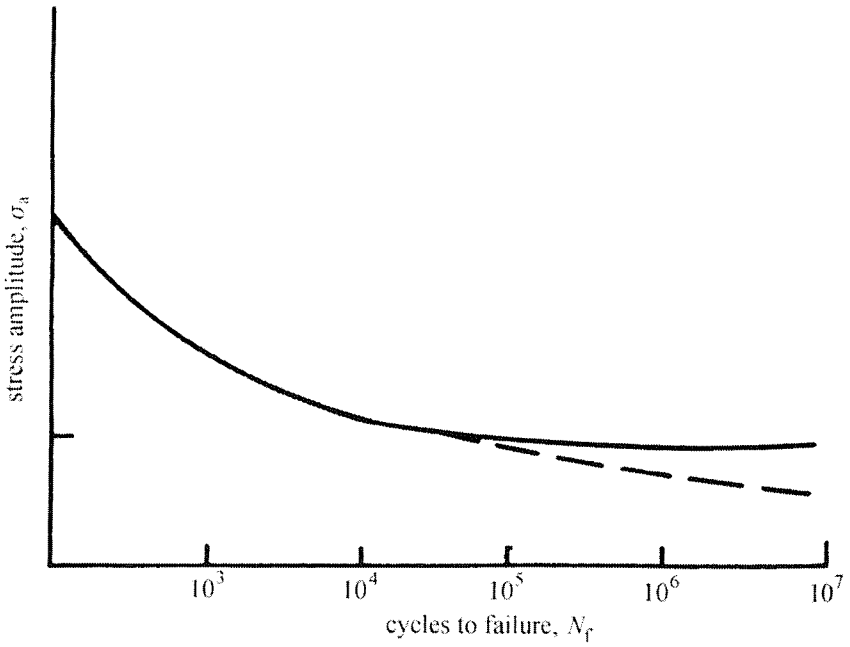

Figure 2.1: Typical S-N diagram showing the variation of stress amplitude as a function of the number of cycles to failure. [10]

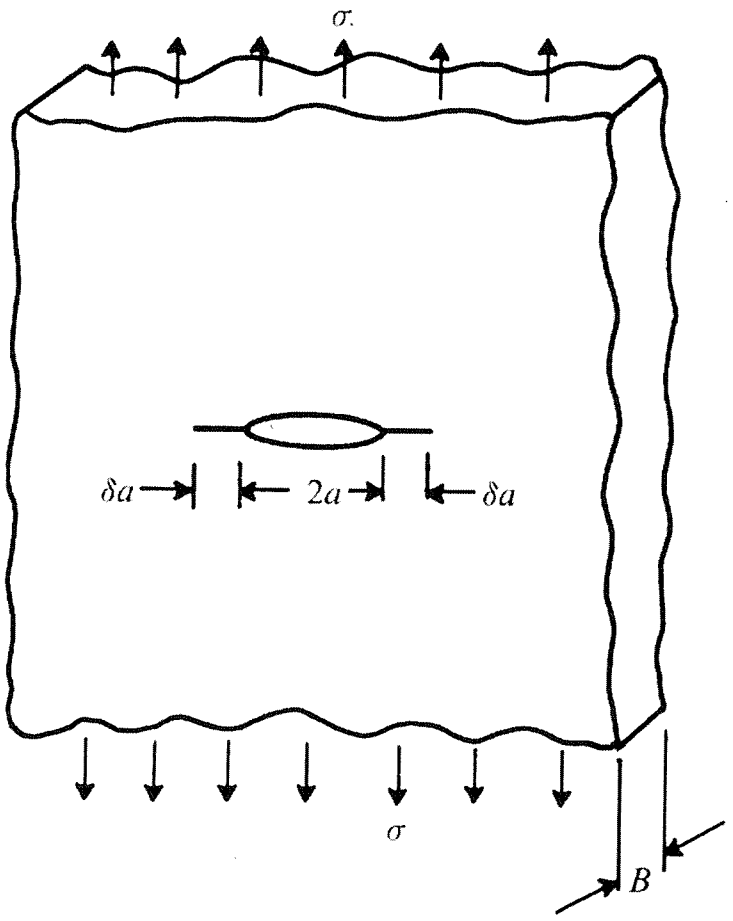

Figure 2.2: A large plate of elastic material containing a crack of 2a. [10]

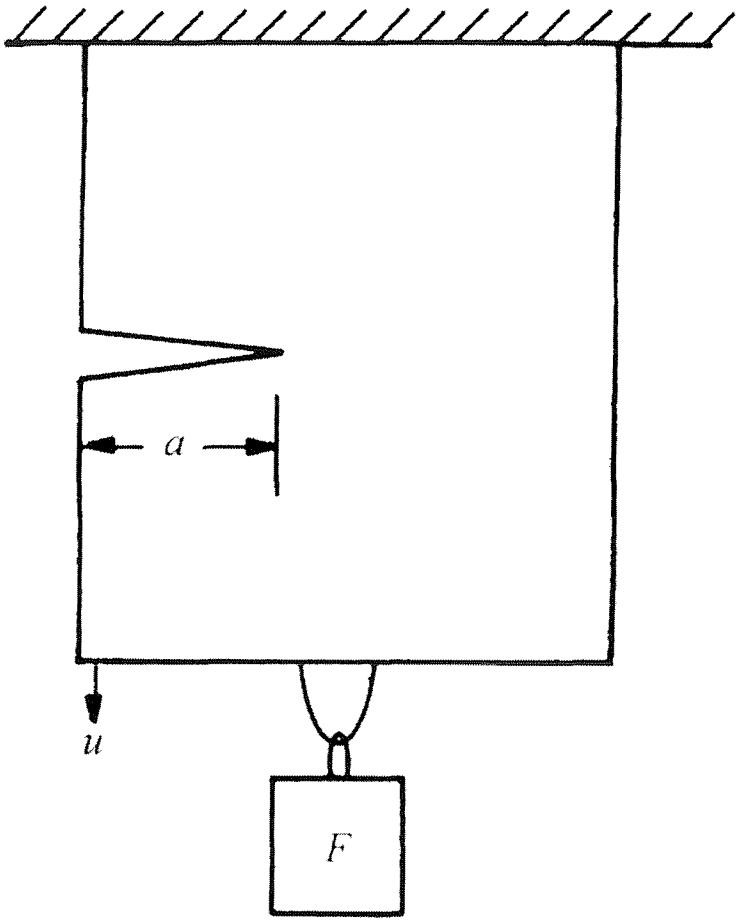

Figure 2.3: An elastic plate containing an edge crack subjected to dead weight loading. [10]

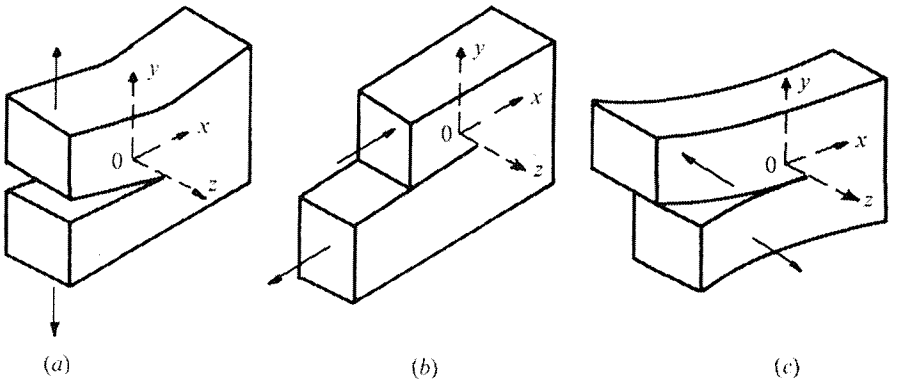

Figure 2.4: The three basic modes of fracture. (a) mode I. (b) mode II. (c) mode III. [10]

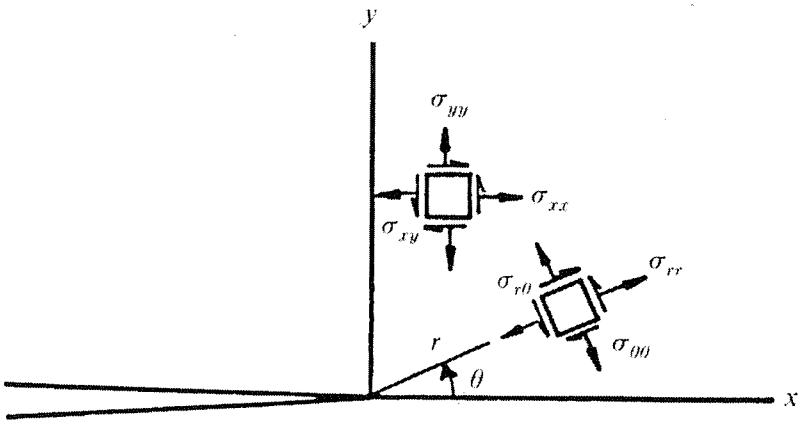

Figure 2.5: Co-ordinate system and stresses in the near tip region of a crack in a plate. [10]

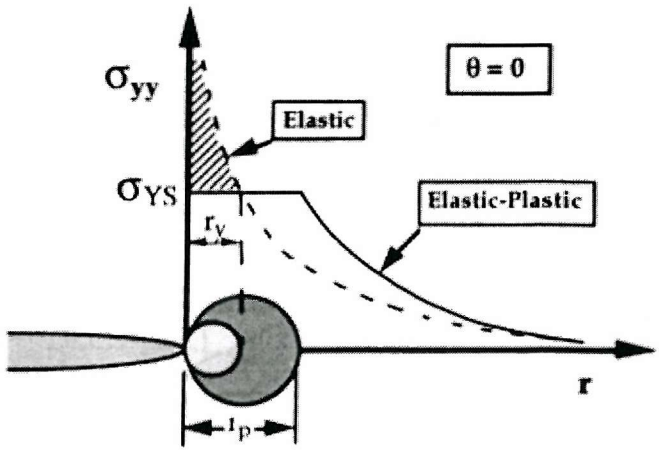

Figure 2.6: First and second order estimations of crack tip plastic zone size. [10]

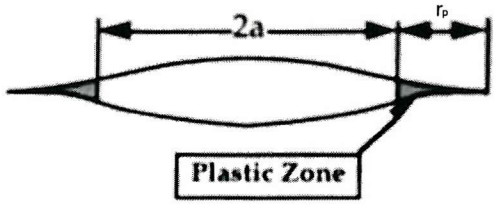

Figure 2.7: The Dugdale model. [10]

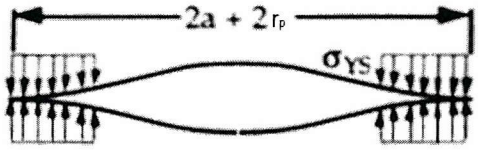

Figure 2.8: The Dugdale model. The plastic zone is modelled by compressive stress equivalent to yield at each crack tip. [10]

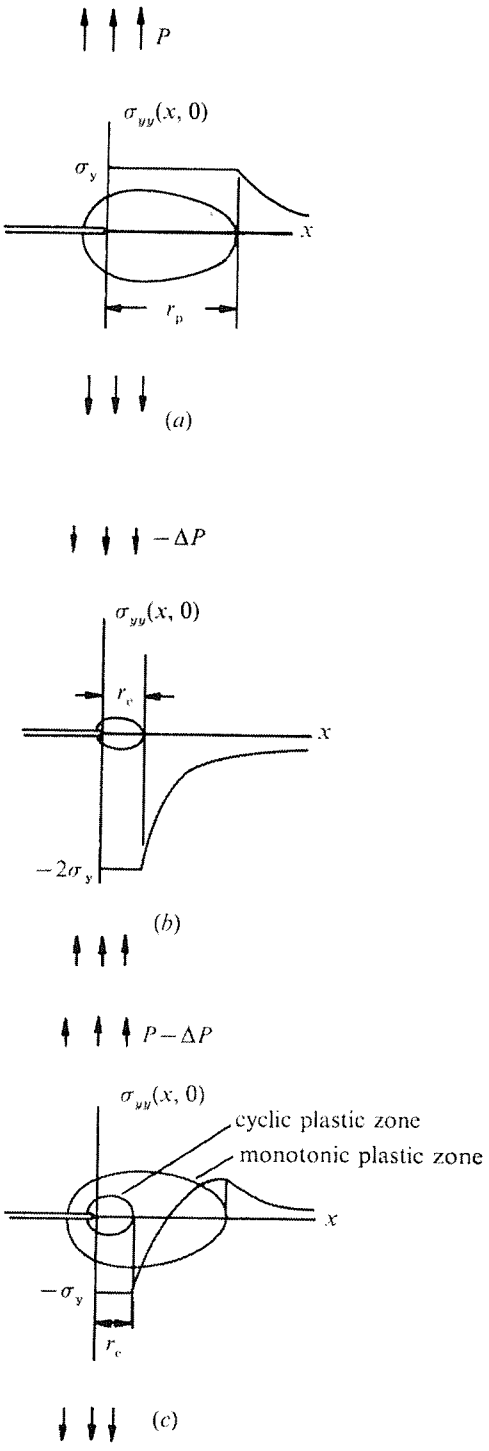

Figure 2.9: Schematic representation of the development of a cyclic plastic zone during unloading. (a) Monotonic plastic zone created by far-field tensile load; (b) Stress distribution due to reduction of the load by ΔP; (c) The superposition of (a) and (b) . [10]

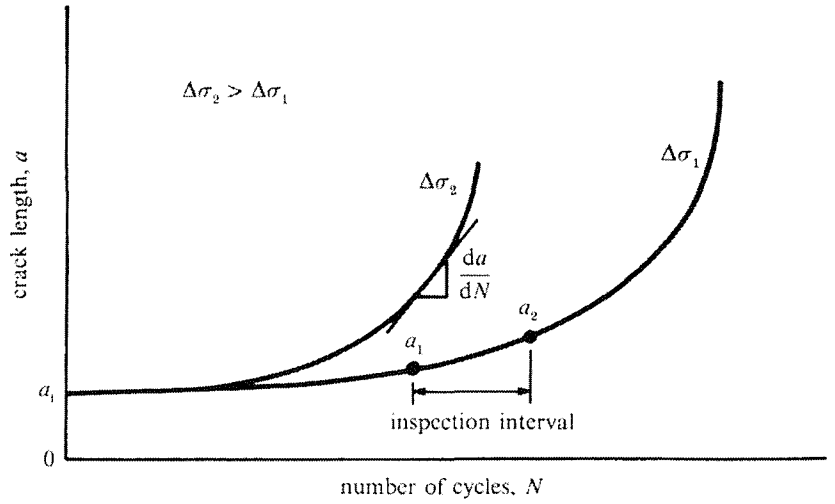

Figure 2.10: Typical crack growth behaviour in constant amplitude fatigue loading. [10]

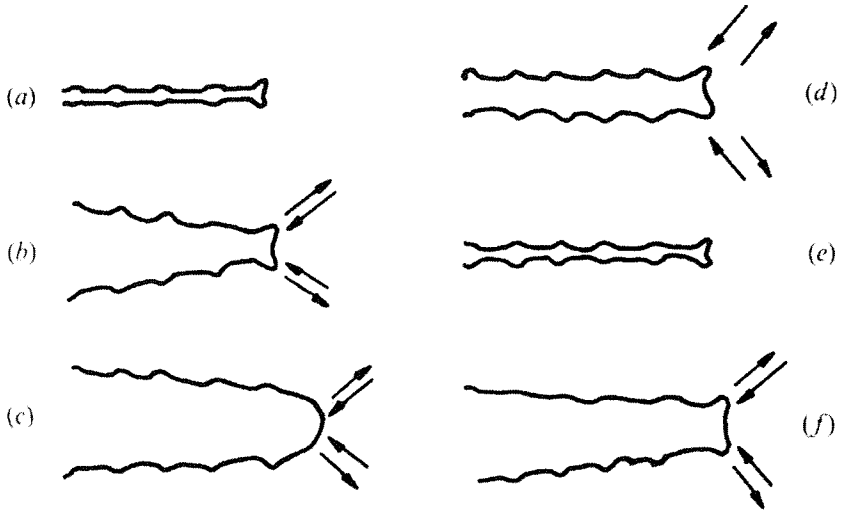

Figure 2.11: An idealization of plastic blunting and sharpening which leads to stage II fatigue growth. (a) Zero load, (b) small tensile load, (c) peak tensile load, (d) peak tensile load, (e) peak compressive load, (f) small tensile load in subsequent cycle. Arrows indicate slip direction. [10]

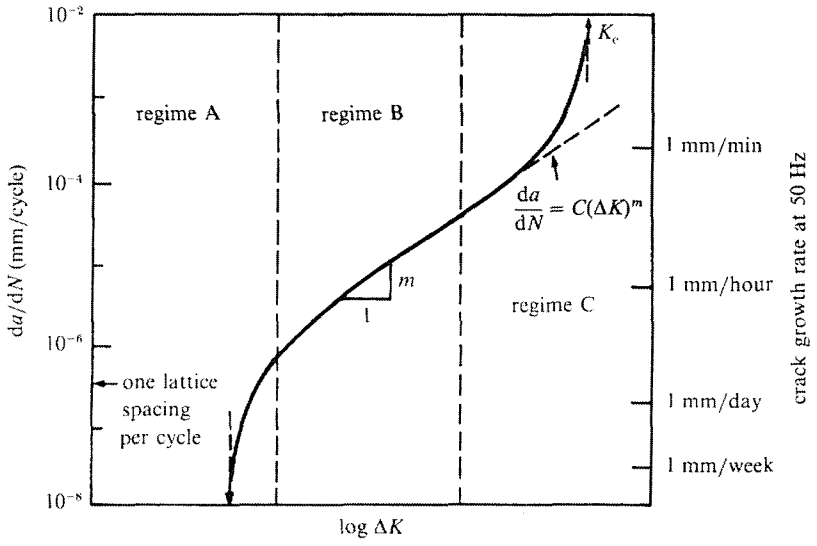

Figure 2.12: Schematic illustration of the different regimes of stable fatigue crack growth. [10]

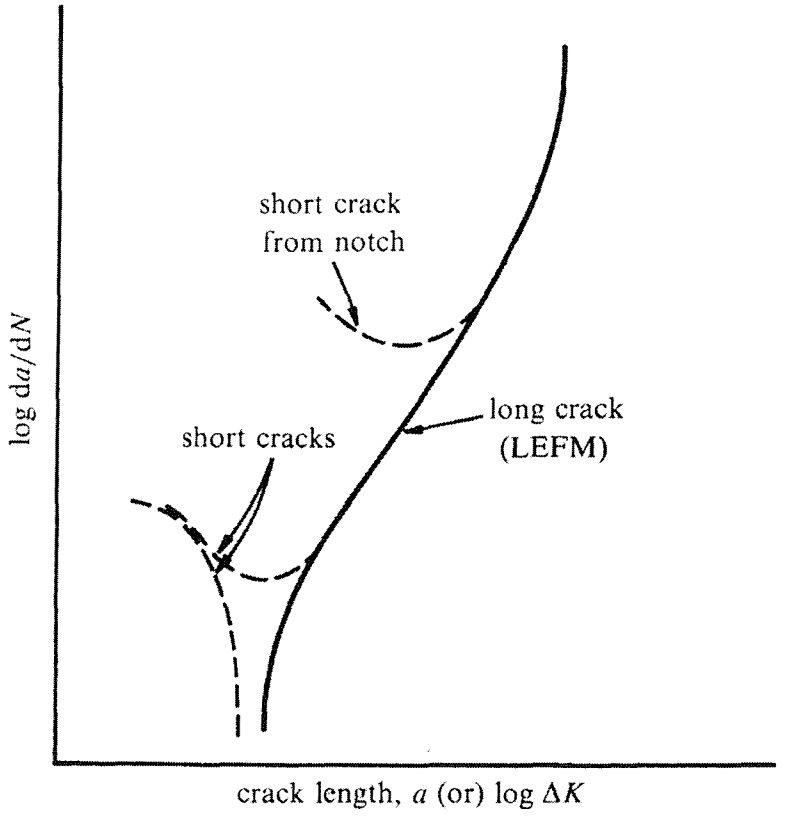

Figure 2.13: Schematic illustration of the differences between long and short crack growth. [10]

3 Microstructural Properties of ADI

ADI is formed from Ductile Iron via specific heat treatments. Whilst Ductile Iron itself has a ferritic or ferrite/pearlite matrix surrounding graphite nodules, the ADI heat treatment permits a multi-constituent matrix whilst retaining the spheroidal nature of the graphite. Bainitic ferrite and austenite form by far the largest portion of the ADI matrix. The mixture of ferrite and austenite is sometimes referred to as 'ausferrite' but are considered individually in this research. Pearlite, martensite and carbides may also be found in small amounts. The unique microstructure produces a range of cast irons that exhibit better ductility than grey irons and higher tensile strengths than ductile irons. Once austempered the mechanical properties of these alloys compare favourably with, and indeed in certain cases out perform cast steels. Heat treatments and alloying additions can dramatically alter the micro-structural features and hence the mechanical properties allowing ADI alloys to be tailored to suit specific applications.

3.1 The ADI Process

In general, ADI alloys undergo a four-stage heat treatment [9].

Austenitising: The as-cast ductile iron is raised to a temperature of 800 to 950 ^{0}C and subsequently held for between one and four hours. The matrix of the as cast Ductile Iron transforms to austenite. The as-cast structure and the austenitising temperature determine the rate of this transformation.

Quenching: Following austenitising the alloy is rapidly quenched to the austempering temperature.

Austempering: The final bainitic matrix is formed whilst the alloy is held for one to four hours at a temperature of 250 to 450 ^{0}C.

Cooling: The alloy is finally left to cool following the austempering stage. If the austenite carbon content is too low, the cooling may bring about the transformation of austenite to martensite.

A schematic of this process can be seen in Figure 3.1. By adjusting the heat treatment parameters the mechanical properties of ADI alloys may therefore be significantly altered.

3.2 The Matrix Microstructure of ADI

As with most cast irons, the majority of mechanical properties are dependent on the matrix microstructure. The properties and characteristics of each constituent are briefly detailed below.

3.2.1 Bainite

A product of the austenitic transformation, bainite forms between 550^0C and 250^0C, temperatures that are intermediate for pearlite and martensite formation. The microstructure of bainite consists of both ferrite and cementite; hence, diffusion is involved in its formation. The exact composition of the bainite microstructure is very temperature dependent, with two distinctly different microstructures possible. The pearlite and bainite formations are competitive to the extent that once one has formed, in some part of the alloy, the formation of the other micro-constituent is not possible without re-heating to form austenite.

Upper Bainite - is formed during austempering above 400^0C. Upper bainite forms at ferrite laths nucleated at austenite grain boundaries. Upper bainite has coarse feathery laths of ferrite surrounded in cementite and significant amounts of austenite. This structure gives good ductility and fracture toughness. However, in general it also reduces strength and hardness. Any carbides that are formed do not exist in the bainite itself but rather in the retained austenite.

Lower Bainite - is formed with austempering between 235^0C and 350^0C. The microstructure contains laths of ferrite finer than those found in Upper Bainite. The laths have a plate like structure with needle-like inter-lath cementite. The product has high hardness and strength but lower ductility and toughness compared to Upper Bainite. Unlike upper bainite, carbides can grow within the ferritic platelets as well as in the surrounding austenite.

It is possible to achieve a mixed microstructure by austempering at mid range temperatures giving more intermediate properties.

3.2.2 Retained Austenite (RA)

The austenite in ADI is formed during the austenitising stage of the heat treatment. The carbon content of the austenite depends on the austenitising parameters and the alloy content. On cooling to the austempering temperature the austenite does not immediately transform and is termed metastable austenite. Ideally all of the austenite remains; however, in large castings pearlite can be produced. During subsequent austempering, the metastable austenite undergoes a transformation to produce bainitic ferrite and retained austenite. As the transformation to bainite occurs, carbon is rejected by the austenite. Some of this carbon forms carbides whilst the remainder dissolves into the remaining austenite thus increasing the austenite carbon content. The retained austenite therefore contains high carbon content. It is from this high carbon austenite that martensite can form upon final cooling. The tendency of martensite formation is dependent upon the carbon content of the retained austenite. The higher the carbon content, the lower the tendency for martensite transformation. Any remaining austenite is known as un-transformed or retained austenite.

3.2.3 Pearlite

Pearlite is usually regarded as an undesirable phase in ADI. It is a relatively hard constituent, which has good machinability and moderate toughness with reduced thermal conductivity. It generally forms due to unsuitable heat treatment. However, in certain conditions, such as large castings, the formation of pearlite may be unavoidable.

3.2.4 Martensite

Like pearlite, martensite is considered as an undesirable product of the austenitic transformation. Martensite may be formed upon cooling as a result of too short an austempering time leaving a relatively low carbon austenite.

3.2.5 Carbides

The majority of carbides in ADI are iron or iron containing and may form within or between ferrite sheaves depending on the bainitic ferrite structure [9]. It is possible

for carbides to form in both locations in lower bainite, whilst upper bainite only exhibits carbides between ferrite sheaves. The austempering process is responsible for the formation of most of these carbides. During austempering, carbides may form in lower bainite throughout stage one and two. However, upper bainite is generally impervious to carbide formation until stage-two of austempering is reached. For an explanation of stages one and two see section 3.3.2.

3.3 The Effect of Heat Treatment Parameters on ADI Microstructure

The final microstructural balance of an ADI alloy is a complex function of alloying composition, austenitising temperature and time and austempering temperature and time. The following section briefly describes the effect of these heat treatment parameters on the matrix microstructure. The majority of work investigating the effects of heat treatment parameters on ADI microstructure has concentrated on the austempering process. There is significantly less information on the effects of austenitising parameters.

3.3.1 Austenitising Parameters

Darwish and Elliott observed that increasing the austenitising temperature increases the degree to which the matrix transforms to austenite, the rate of the transformation and the carbon solubility in austenite which in turn affects the structure and properties of the austempered casting [46,47]. High austenitising temperatures give high carbon content in austenite and hence increase the austemperability of the alloy and decrease the probability of martensite formation during final cooling [47,48]. However, the thermodynamic driving force for the transformation of austenite to bainitic ferrite during austempering is also decreased (the significance of this will be explained later). Furthermore, the austenitising time also affects the carbon content of the austenite by determining how close the austenite gets to the equilibrium carbon content. High austenitising temperatures lead to the formation of blocky pools of retained austenite, whereas low temperatures tend to produce a finer retained austenite region. Darwish and Elliot [48,49] also noted that increasing the austenitising temperature coarsened the bainitic ferrite structure, leading to the formation of two types of retained austenite

(blocky interconnecting pools and inter-lath), and enhanced the formation of martensite in intercellular regions within the blocky austenite pools.

3.3.2 Austempering Parameters

The austempering treatment can be visualised as a two-stage process [9]. During stage-one, the metastable austenite transforms to bainitic ferrite. During stage-two, the retained austenite begins to decompose into ferrite and (particularly at high temperatures) coarse carbides, which form between the ferrite platelets. Excessive austempering temperatures and duration take the treatment into stage-two [50]. Prasad Rao et al [51] noted that as the austempering temperature increases so does the retained austenite content. It was also observed that the carbon content in austenite increased with austempering temperature, reached a maximum value at 300^0C and then decreased thereafter. Furthermore it was noted that the carbon content in austenite also increased with increasing austempering duration before saturating at certain temperatures. The carbon content in austenite controls the formation of martensite upon cooling to the effect that reducing the carbon content promotes the transformation to martensite [50]. Therefore, avoiding low austempering temperatures and too short austempering times reduces the possibility of martensite formation. It can be shown that a 'processing window' exists during a range of austempering times when the formation of martensite and carbides is reduced [52]. The location of this window is affected by the driving force for stage I of the transformation [47]. The effects of austenitising on the driving force for stage I of the transformation can influence the location of this window and hence the appropriate austempering parameters. Excessive austempering durations that take the treatment beyond this window are deleterious to the material's mechanical properties. This will be discussed in more detail in the next section.

As previously mentioned, bainite morphology differs with austempering temperature. At lower austempering temperatures, the Bainite has an acicular structure, commonly referred to as Lower Bainite. Upper Bainite is formed at higher austempering temperatures and is typified by a 'feathery' morphology. A high austempering temperature leads to relatively low bainite volume fractions with retained austenite distributed in large interconnecting pools throughout the matrix.

3.4 Modelling of ADI Microstructural Evolution

A generic model has been developed by Loughborough University to predict the amount of bainite, austenite, graphite and martensite in ADI as a function of composition and heat treatment parameters [7,8]. Kinetic and thermodynamic theory, MTDATA and a modification of the theory to describe bainite formation in steels [53,54] were used to this end. Thermodynamic modelling techniques were employed to investigate the high temperature equilibrium between graphite and austenite and to predict the proportion of graphite. The model commences with the estimation of carbon concentration in austenite at the start of austempering. This was validated using Gibbs free energy minimisation and critical analysis of existing databases and previously published data. The next step considers the bainite transformation within the microstructure as a function of temperature and time. This is achieved by predicting the limiting carbon content for diffusionless transformation. The kinetics of this transformation are determined by a modification of a model designed for steels. The inherent segregation present in the microstructure is considered using a Schiel approach [9]. This enables the prediction of microstructural constituents as a function of their distance from a graphite nodule. This model is being used by Loughborough University to predict the proportion of microstructural constituents in both new and old heat treatments considered for fatigue analysis at Southampton University.

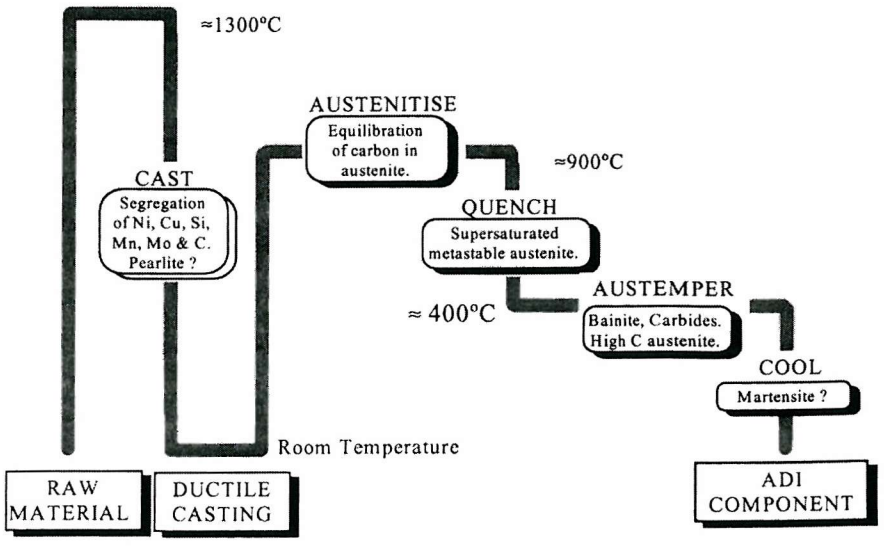

Figure 3.1: Schematic of ADI heat treatment process [9]

4 Mechanical Properties of ADI

Finding the exact effect of each matrix micro-constituent on the mechanical properties of ADI has proved difficult since the literature generally considers the effect of heat treatments in a given study rather than in terms of a detailed assessment of microstructures. This may be misleading since it is the microstructures that ultimately define the mechanical properties. Even when detailed analysis of the effects of microstructure has been undertaken, there is a tendency to consider bainitic ferrite and retained austenite as discrete features. To consider these two micro-constituents in this fashion seems somewhat inappropriate since it is difficult to separate their effects [55] in such a complex microstructure. What follows in this section is a critical review of data in the literature with the aim of identifying the effects of microstructure on each mechanical property in turn.

4.1.1 Modelling of the Mechanical Properties of ADI

The microstructural evolution model developed by Loughborough University described in section 3.4 has been expanded to predict a number of basic mechanical properties [56]. The model is based on the assumption that each phase contributes proportionally to the overall value of the mechanical property with the application of a law of mixtures approach.

4.1.2 Proof Stress

It was observed by Aranzabal et al [55] that the 0.2% proof stress of ADI was influenced by the distribution and carbon content of retained austenite within the matrix. When the austempering temperature (370^0C and 410^0C) gave large blocky interconnecting pools of austenite in addition to inter-lath films, the proof stress is controlled by the mechanical (in)stability of the retained austenite. At lower austempering temperatures, the austenite is mechanically stable. This is due to the high carbon content in retained austenite and to the fine distribution of this phase throughout the matrix microstructure. In this case, the proof stress of the material is controlled by both the retained austenite and the bainite.

4.1.3 Toughness

Prasad Rao and Putatunda [57] observed a dependence of toughness with microstructure. A high austenite content within an upper bainitic structure leads to improved toughness over a low austenite content and a lower bainitic structure.

4.1.4 Ductility

It has been noted [55,58,59] the dependence of ductility (%el.) on the presence of retained austenite, the presence of which significantly enhances this property. It was also observed by these authors and others [48,60] that austempering parameters that take the treatment out of the processing window (i.e. into stage II) are deleterious to the ductility. The presence of martensite and carbides has been identified as responsible for this. Furthermore, Prasad Rao and Putatunda [57] noted a high austenite content within an upper bainitic structure leads to improved ductility over a low austenite content and a lower bainitic structure.

4.1.5 Fracture Toughness

Until recently there had been little investigation in the area of fracture toughness of ADI [60]. There was a particular dearth of information on the relationship between heat treatment parameters and fracture toughness. Zum Gahr and Wagner performed one of the earliest works on the fracture toughness of ADI [61]. Their work showed that ADI has better ductility and fracture toughness than quenched and tempered ductile iron. A decrease in fracture toughness was also observed with increasing austempering temperature over a range of 310^{0}C to 550^{0}C. Doong *et al.* [62] investigated fracture toughness for four ADI microstructures austempered for five hours at 300^{0}C, 350^{0}C, 400^{0}C, and 450^{0}C. They observed higher values of fracture toughness for the 300^{0}C and 350^{0}C austempers than the 400^{0}C and 450^{0}C austempers, concluding that lower bainite therefore has superior fracture toughness to that of upper bainite. It should be considered that these results were obtained from microstructures that were austempered for 5 hours. As explained previously these microstructures would have entered stage II of the austempering process and hence were not representative of the optimum austempering treatment, nor indeed industrial practice. Furthermore, Prasad Rao *et al.* [60] have suggested that the cause of fracture for the 400^{0}C and 450^{0}C austempers is more attributable to the

embrittling effect of carbide precipitation rather than the upper bainite microstructure.

Doong and Chen [63] went on to investigate the effect of various heat treatment parameters on the fracture toughness of ADI. Austempering temperatures in the range of 250^{0}C to 450^{0}C were investigated. It was observed that maximum fracture toughness was obtained for austempers in the range of 300^{0}C to 350^{0}C.

More recently Prasad Rao *et al.* [60,64] investigated the relation of heat treatment parameters, microstructure and fracture toughness. It was observed that fracture toughness increases with austempering temperature to a maximum at ~300^{0}C and decreases with austempering temperature beyond 300^{0}C, although generally, lower bainite shows better fracture toughness than upper bainite. Furthermore it was noted that the carbon content in retained austenite followed a similar trend; increasing content with increasing austempering temperature up to a maximum value ~300^{0}C and decreasing thereafter. They therefore concluded that fracture toughness increased with increasing carbon content in retained austenite. Hence, fracture toughness is a function of microstructure which is in turn a function of heat treatment. Also reported was the effect of retained austenite volume fraction on fracture toughness. A volume fraction of 25%-30% was suggested to give the best fracture toughness.

The volume fraction of RA in the final microstructure will determine the fracture mode of the alloy. When the volume fraction of RA is in the range of 28% to 46%, the alloy will fracture in a ductile manner, where as a volume fraction in the range of 5% to 28%, the alloy will exhibit mixed fracture modes (ductile and cleavage). Finally, below a 5% volume fraction cleavage failure occurs.

4.2 Fatigue in ADI

4.2.1 Fatigue Threshold

It has been observed by Bartosiewicz et al [65], that the fatigue threshold of ADI increased with an increase in the volume fraction of RA. This has also been noted by previous work at Southampton [5,6]. The high levels of RA associated with higher temperature austempers gave greater values for threshold. It has been suggested that the higher threshold values associated with higher volume fractions of RA are due to the transformation of austenite to martensite at the crack tip. The resultant volume change caused by this transformation is proposed to invoke greater closure effects. The transformation of austenite to martensite under strain at crack tips produces three distinct regions radiating from the crack tip. In closest proximity to the fracture surface the RA undergoes a complete transformation to martensite. Moving away from the fracture surface partial transformations occur until, furthest away, there is only a small amount of transformation.

4.2.2 Fatigue Limit

C. –K. Lin et al. [59] observed that under high cycle fatigue (low stress) conditions, ADI alloys with large amounts of retained austenite exhibited an increased fatigue limit. However, C. –K. Lin et al. also observed [66,67] that under low cycle fatigue (high stress) conditions ADI with larger volume fractions of retained austenite displayed inferior fatigue limits. This effect was attributed to the higher maximum stress levels applied to low cycle fatigue tests leading to a greater amount of stress-induced martensitic transformation. The proposed result is an embrittlement of the matrix and premature nucleation of micro-cracks from graphite nodules.

Shanmugam et al [68] and Bahmani et al [69] observed that austenitising at lower temperatures increased the fatigue limit. Additionally, for an ADI alloy austenitised at 900^{0}C, Bahmani et al [69] noted a maximum value of fatigue limit when austempered at 370^{0}C. A decrease in fatigue limit was observed when austempered at temperatures above and below this value. Shanmugam et al. also noted moderate austempering temperatures and lengthy austempering durations

increase fatigue limit. Bahmani et al. suggested the formation of coarser, blocky austenite (hence longer bainite needles) and treatment of the material outside of the processing window was deleterious to fatigue limit. A fine bainitic structure and high carbon content in austenite was proposed to improve fatigue limit. Shanmugam et al. attributed an increase in fatigue limit to increased retained austenite and matrix carbon contents, smaller prior austenite grain size and the presence of small bainite sheaves. Carbide precipitation and low carbon prior austenite was observed to be deleterious to fatigue limit. However, the volume fractions of bainite and retained austenite claimed by Shanmugam et al. do not seem to correspond to images of the microstructures. Application of the Loughborough microstructure evolution model to the microstructural composition and heat treatment parameters from the work of Shanmugam et al. produce significantly different volume fractions of bainite and retained austenite (Appendix 11.1). It was suggested by D. Putman [70] that the processing window was closed for the higher temperature austempers which may effect the model predictions. Nether-the-less, the relationship between fatigue strength and retained austenite volume fraction suggested by Shanmugam et al. should be considered carefully even when only considering the lower temperature austempers. Indeed, the microstructure evolution model suggests fatigue limit is in fact inversely proportional to retained austenite volume fraction for these alloys.

4.2.3 Fatigue Crack Initiation

Fatigue crack initiation has been observed in ADI at graphite nodules, inclusions and micro shrinkage pores. However, it is widely accepted that fatigue cracks initiate at the interface between the matrix and graphite nodules [5,6,69,59,71,72] in the absence of larger defects, e.g. porosity. Greno et al [72] suggested that since the graphite-matrix interfaces are irregular, with sharp corners they act as stress raisers causing the initiation of micro cracks. Marrow and Cetinel suggested that graphite nodules therefore act as micro-notches. Cracks tend to subsequently propagate from these decohered nodules perpendicularly to the applied tensile stress. Work has been done by several authors to quantitatively identify which (if any) nodules decohere. Palin Luc et al [73] concluded that with Spheroidal Graphite Iron, nodules that were either less than one diameter from another nodule, or were very irregular in shape preferentially initiated. Hockley et al [5] used finite body tessellation approaches to determine the effect of graphite nodule

distribution on crack initiation in ADI. They observed that larger than average graphite nodules of individually high volume fraction within a macroscopic region of low volume fraction act as preferential initiation sites. It was suggested that large nodules whilst not actually increasing the local stress concentration due to their spherical nature give a larger sampling volume for potential initiation points. It was also proposed that macroscopically low volume fraction regions are effectively stiffer than their surroundings and therefore, may be subject to load transfer effects. Graphite nodules within these regions would then experience a greater proportion of the applied stress.

4.2.4 High Cycle Fatigue (HCF)

C. –K. Lin et al's [59] work on HCF using rotary bend specimens noted the fatigue limit of ADI was not proportional to its tensile strength, but to its toughness and retained austenite content. ADI alloys with large amounts of retained austenite exhibited greater toughness and an increased fatigue limit. The greater fatigue crack resistance was attributed to the transformation of low-carbon austenite to martensite under plastic conditions encouraging crack closure mechanisms. The mechanism of crack growth under HCF conditions was identified as the decohesion of graphite nodules; subsequent micro-cracking originating from nodules; the link up of selected micro-cracks with dominant cracks; and crack propagation by connecting of graphite nodules.

4.2.5 Low Cycle Fatigue (LCF)

Contrary to observations made for HCF it has been shown [66,67] that under LCF conditions ADI with larger volume fractions of retained austenite displayed inferior fatigue resistance. This was attributed to the higher maximum stress levels applied to LCF tests leading to a greater amount of stress-induced martensitic transformation as discussed in section 4.2.2. The mechanism of crack growth under LCF conditions was identified as the decohesion of graphite nodules; subsequent initiation of micro-cracks from nodules; the coalescence of selected micro-cracks with dominant cracks; and crack propagation by connecting of graphite nodules. The crack path was suggested to be strongly influenced by the location of the next graphite nodule ahead of the crack-tip, but is in general perpendicular to the tensile axis. The crack propagation path between two nodules was not observed to be the shortest distance as with typical brittle

cleavage. Instead, the crack was suggested to favour the localised least-energy path, namely the interface between bainite sheaves and austenite. However, sensitivity to the orientation of the interface with respect to the tensile axis and the presence of precipitated carbides (that facilitate a micro-crack to propagate through bainite laths) was observed. Additionally, an increase in LCF strength was observed in for an ADI of a given composition with an increase in nodularity and nodule count.

4.2.6 Mechanisms of Fatigue Crack Propagation

In addition to the observations of crack propagation during LCF and HCF tests made by Lin et al. there has been research that has the primary aim of identifying mechanisms of fatigue crack growth [72,74].

It was suggested by Greno et al. [72] that the main propagation mechanism in ADI is as follows: As a fatigue crack propagates through the microstructure micro-crack initiation takes place ahead of the advancing macro-crack tip. Initiation occurs at surface irregularities on graphite nodules and grows towards the principal crack. Similar mechanisms were observed by Lin et al. [59,66,67] (see sections 4.2.4 and 4.2.5). The initiation of these micro-cracks is activated by the stress rise produced when the crack-tip is sufficiently proximate to the nodule. These cracks subsequently coalesce with the principal crack, which continues to grow in a conventional manner until another nodule is approached. Unlike the observations of Lin et al. the effect of matrix microstructure was suggested to be minor. Since the analysis was based on through thickness cracks it was suggested by these authors that several nodules can be involved in the growth process at different positions along the crack front. Therefore, the average crack growth rate is affected by the size, shape and distribution of graphite nodules. Furthermore it was postulated that if the micro-cracks propagate to a sufficient length the system has the required geometry to produce a load shedding effect on the main crack, reducing the applied stress intensity factor. Numerical and fracture mechanics modelling [74] has corroborated the failure mechanism detailed above. Additionally, Ortiz et al. concluded that some micro-cracks propagate towards the macro-crack tip but do not coalesce and take part in the main propagation path. Due to load shielding effects, these cracks become dormant. They went on to conclude that the shielding effects generated by crack initiation

ahead of the crack tip explain the relatively low propagation rates and high effective propagation thresholds of ADI when compared to steels.

4.2.7 Short Crack Fatigue

It is short crack fatigue behaviour that is most applicable to camshaft failure. Typically failure is due to the initiation and growth of very small cracks under Hertzian contact fatigue (see chapter 1). Surface pitting of the microstructure follows, resulting in further wear-induced failure. Therefore the study of initiation and early growth of short cracks and the effect of various microstructural features in ADI on such growth is particularly relevant.

Hwang and Chung [75] have conducted short crack fatigue studies on ADI alloys of similar composition to the materials tested at Southampton University. These experiments considered the effect of austenitising and austempering parameters on short through crack resistance. Austempers of 275^{0}C, 300^{0}C, 350^{0}C, 400^{0}C, 475^{0}C, were tested. It was found that the 350^{0}C austemper gave the best fatigue crack growth resistance. Austempers of 400^{0}C, 475^{0}C, 300^{0}C, and 275^{0}C, exhibited progressively poorer fatigue crack growth resistance. Austenitising temperatures of 850^{0}C, 900^{0}C, and 950^{0}C, (all with the same austemper) were also considered. It was found that the 900^{0}C condition gave the best fatigue performance with both the 850^{0}C and 950^{0}C conditions exhibiting slightly less fatigue crack resistance. No convincing mechanistic explanations in terms of the microstructure were put forward for these observations.

Previous work at Southampton University found ADI alloys austempered at 400^{0}C gave better fatigue crack initiation and growth resistance those austempered at 250^{0}C at similar stress ranges. Initial micro-mechanical arguments for this behaviour have been put forward. The coarser lath size and large amounts of retained austenite of the 400^{0}C austemper promote a more tortuous crack path, and intrinsic crack shielding. Current work will build upon these findings.

Marrow et al. [71,76] have assessed the fatigue endurance limit in ADI alloys by considering the short crack behaviour of stable crack nuclei. It was observed that fatigue endurance limit in ADI alloys is controlled by crack arrest and retardation mechanisms. Fatigue crack nuclei were seen to be retarded by microstructural

barriers (such as ausferrite packet boundaries and prior austenite grain boundaries) when the crack tip strain amplitude is low. Although no evidence for plasticity induced martensite transformation was seen (indicating martensite plays no significant role in short crack arrest), it was proposed that phase transformation may occur in long fatigue cracks where the plastic zone is larger than the austenite grain size. It was concluded that the fatigue endurance limit is determined by the largest crack nucleus which was observed to be controlled by the largest defect and the prior austenite grain size. Decreasing the prior austenite grain size decreases the maximum sub-critical crack nucleus size and hence increases the measured fatigue limit. It was also suggested that an increase in the volume fraction of retained austenite increases the role of stage I crack growth in austenite which encourages crack arrest at microstructural barriers. Furthermore an increase in the carbon content in austenite is likely to increase the strength of austenite and reduce the crack-tip plastic strain for a given stress amplitude. Both these effects would have the result of increasing the fatigue limit.

4.2.8 Rolling Contact Fatigue (RCF)

Time to failure under RCF is dominated by crack nucleation. For the case of nodular cast irons graphite nodules act as natural defects where cracks initiate easily [77]. This characteristic significantly reduces the RCF life for ADI. Dommarco et al. concluded the satisfactory fatigue crack propagation resistance of ADI is not sufficient to overcome the poor crack nucleation performance. It was suggested the use of surface treatments to increase the surface hardness (such as chilling) may improve the RCF performance. It was also shown by Rebasa et al. [78] that ADI samples with high nodules counts (980/mm^2) have a RCF five times higher than a ADI subject to the same heat treatment but with a low nodule count (160/mm^2). It was proposed that a consequence of a high nodule count is a low nodule size. Nodules act as geometric discontinuities on the wear track. The smaller the nodule size the smaller the discontinuity. Smaller discontinuities lead to smaller pressure spikes at the edge of the discontinuity and lead to an improved RCF life.

In more recent studies Dommarco [79] evaluated partly chilled ductile irons (PCDI). The PCDI showed a marked improvement in resistance to RCF when compared to ADI. This was attributed to the precipitation of iron carbides, an increased

nodule count and a reduction in the average nodule size. The application of PCDI was suggested to limited due to low ductility and toughness. It was also concluded from this study that ADI alloys austempered at lower temperatures have improved hardness and RCF resistance, but are still inferior to that of steels. Unfortunately, no estimations of the proportions of matrix constituents were made and hence their effect on RCF remains undetermined.

5 Experimental

The current work considered three ADI heat treatments in addition to the parent as-cast ductile iron. Furthermore a chilled variant of the as-cast ductile iron was investigated. Previous work at Southampton focused on four ADI heat treatments, from a parent ductile iron of a differing composition (see Table 5.1). Results from the previous work will be compared to the current work where appropriate. Table 5.2 summaries the heat treatments applied to the ductile iron castings in the current and previous works. The table also gives the associated material classifications used in this report. It should be noted that the previously tested heat treatments were austenitised for 60 minutes, compared with 120 minutes for the current batch.

5.1 Material Production

The four ADI heat treatments studied in the previous work were delivered as sand cast cylinders. For the current work all material was received from Federal Mogul Camshafts as sand castings, with each heat treatment taken from a single batch. However, the exception is the parent ductile iron which was received in the form of a camshaft end. The dimensions of all castings are shown in Table 5.3. A chill was applied to the narrowest face of the castings by the use of large metal chill blocks.

5.2 Metallographic Preparation

Specimen preparation involved following a well established polishing route for steels to a finish of 1 micron, as identified in Table 5.4. All grinding and polishing was performed by hand. Between grinding and polishing stages, specimens were cleaned with soap and water, and rinsed with methanol. An 8 second 2% Nital submersion etch was applied to examine the matrix microstructure. A thorough and satisfactory etch was ensured for all specimens by means of prior cleaning by immersion in an ultrasonic methanol bath.

It was noted in the ASTM Specialty Handbook for Cast Irons [80] that an excessive use of water during polishing caused graphite to be removed from the surface of

the material. This process is referred to as graphite pullout. All effort was made to avoid graphite pullout during grinding by sparing use of water.

5.3 Image Analysis

A significant amount of this thesis required the extensive use of image analysis techniques. Prior to mechanical testing each specimen underwent various microstructure classification procedures.

5.3.1 Image Capture

A DVC 1310 digital camera attached using a RS-232 digital link to a PC was used to capture images of replicas and samples examined under an Olympus BH2 optical microscope. The acquisition software used was X-cap for WinNT by Epic. It is particularly essential for tessellation analysis that the specimens were mounted such that the surface being observed was perpendicular to the lens. Failure to do so creates a brightness gradient across the image which reflects the change in distance from the light source. This gives difficulties when subsequently selecting a greyscale threshold for the image.

5.3.2 Assessing Second Phase Distribution

Several statistics methods to analyse object distribution have been formulated, with cell tessellation being perhaps the most powerful at describing distribution at an object-by-object level. Dirichlet tessellation methods utilise the centroids of objects to construct a network of cells such that any point within a cell is closer to the centroid of that cell than to any other centroid. Examples of Dirichlet tessellation can be seen in Figure 5.1 and Figure 5.2. When objects within a microstructure exhibit large variances in size object/cell overlap may occur if Dirichlet tessellation approaches are used (Figure 5.3). To provide a more meaningful description of the special distribution of objects with varying shape and size, the concept of Dirichlet tessellation had been extended to finite bodies [81]. As with Dirichlet tessellation, finite body tessellation represents the sample microstructure by generating a network of cells around objects. However, where Dirichlet tessellation uses the centroid of an object as a reference point, finite body tessellation, in contrast, uses the interfaces of each individual object as seen in Figure 5.4. Utilising this method, every point within a cell is closer to the corresponding object than to any other. This approach not only gives

quantitatively superior representations of microstructures, but is also more sensitive to heterogeneity within object populations.

5.3.3 Finite Body Tessellation (FBT) Methodology

What follows is a brief outline of the FBT procedure. The complete procedure can be seen in Appendix 11.2. *Foster Findley Associates Tessellation Analysis* software requires a binary image of the microstructure such that the phase of interest is black and the background microstructure is white or vice-versa. An image of the microstructure (Figure 5.5) is captured using the techniques described in 5.3.1 and converted to black and white using a greyscale threshold (Figure 5.6). After the binary image has been 'cleaned' the FBT may be applied. A watershed function is used to generate a network of cells around the objects of interest (Figure 5.7). The objects and cells are 'gathered' to generate the final tessellation image (Figure 5.8).

The parameters derived from the finite body tessellation approach are as follows:

Object Area (O_a):

In this case, eutectic carbide or graphite nodule area.

Object Aspect Ratio (O_{ar}):

The ratio of the minimum and maximum linear dimensions.

Object Angle (O_{ang}):

The angle from the horizontal of the primary axis (longest dimension) of an object. This corresponds to the tensile axis for all the specimens.

Cell Area (C_a):

Defines the area of the cell surrounding an object.

Cell Aspect Ratio (C_{ar}):

The aspect ratio of the cell surrounding the object.

Cell Angle (C_{ang}):

The angle of cell surrounding the object.

Local Area Fraction (LAF):

The ratio of object and cell area.

Number of Near Neighbours:

For an object defined by the number of cells sharing boundaries with this object.

Mean Near Neighbour Distance (D_{mean}):

The average of the near neighbour edge to edge distances, where the near neighbour distance is defined as the minimum edge-to-edge distance from an object to a neighbour.

Nearest Neighbour Distance (D_{min}):

The minimum edge-to-edge distance from an object to its nearest neighbour.

Nearest Neighbour Angle (NN_{ang}):

The angle from the horizontal of a straight line bisecting the centriod of an object and that of its nearest neighbour.

Schematic representations of these parameters can be seen in Figure 5.9.

5.3.4 Assessing Graphite Nodule Distribution

In order to quantify graphite nodule distributions in all test specimens five images of the top surface in the region of the maximum stress were captured before each test. A magnification of 100 times was used for every captured image for consistency. Calculations of graphite nodule distribution were performed using Foster Findlay Associates' Tessellation Analysis Program.

5.3.5 Assessing Eutectic Carbide Distribution

As is shown later in the thesis, carbide distributions were highly variable. To assess both the carbide distribution and degree of variability the following procedure was developed. Ten to twelve overlapping images of the specimen top surface were digitally captured (see Figure 5.10). A montage of these images was created such that the generated image spanned the specimen cross-section. The area covered by the montage represented the region of maximum applied stress on short fatigue crack specimens as explained in section 5.6. It was within this region that the majority of fatigue damage was expected to occur. FBT was performed on the montage, allowing the entire cross-section to be analysed at the same time with the obvious benefits of increased consistency, the unit area and reduced operating time. This procedure allowed the quantification of carbide distribution over a reasonably large area for each specimen. Additionally, this method provided a consistent means of comparison carbide distribution between

specimens in regions where the microstructure is most likely to effect fatigue behaviour.

5.4 Sample Machining

Standard bend bars with dimensions outlined in Table 5.5 were machined by spark-erosion from the castings. For the chilled specimens 2 mm were removed from the chilled surface to give a more comparable material to that of a chilled cam lobe. For long fatigue crack testing single-edge notched-bend (SENB) bars with the same overall specimen dimensions as the short fatigue crack specimens were used. A pre-existing slot of an $^{a}/_{W} = 0.25$ machined using a hot-wire-eroder.

5.5 Hardness Testing

Multiple hardness indents were carried out on all heat treatments, new and old using a Vickers Pyramid Hardness Testing. Figure 5.11 to Figure 5.14 show the effects of varying the indenter load on hardness values for all the current microstructures. It is apparent that the hardness values generated by a 5 kg load exhibit large degrees of scatter for all alloy variants. The degree of scatter decreases as the indenter load was increased. It was decided that the 20 kg load provided the most representative sampling area. The approximate tensile strength of each condition was estimated from the values of hardness.

5.5.1 Hardness Mapping

Variation in hardness along the length and breadth of specimens was investigated by the generation of a hardness map. Hardness indents were placed every two mm along the entire length and breadth of the specimen surface(s) as shown in Figure 5.15. One surface of a standard short fatigue crack bend bar would receive approximately 170 indents with this procedure. Again, a Vickers Pyramid Hardness Testing Machine was used with a load of 20 kg and an objective of $^{2}/_{3}$".

5.5.1.1 Hardness Map – Eutectic Carbide Distribution

Finite body tessellation analysis was performed on the hardness map specimens in order to quantify the relationship between eutectic carbide distribution and hardness. Images were taken from regions equidistant from four hardness indents as shown in Figure 5.16. A magnification of 100 times was used which gave an image size of 1222 x 968 μm (1300 pixels x 0.9405 μm/pixel by 1030 pixels x

0.9405 μm/pixel). This area represented a population of between 24 and 397 eutectic carbides. The data generated was correlated against the average of the four hardness values.

5.5.2 Micro-hardness Testing

A micro-hardness machine was used to identify the hardness values of particular microstructure constituents. A load of 300g was used for a dwell time of 10 seconds.

5.6 Short Fatigue Crack Experimental Method and Test Matrix

Short crack tests were performed on either 10 mm x 10 mm or 12 mm x 12 mm (depending on casting) cross-section standard bend-bar specimens varying in length from 70 mm to 100 mm, in air, at room temperature on a digitally controlled Instron 8501 servo hydraulic at 5 Hz.

A three-point bend set up (Figure 5.17) with a roller separation of 30 mm was used for all current tests. The top surface of each bend bar was ground and polished (using the approach detailed previously in 5.1) before testing. Etching of the top surface was used on some of the specimens to reveal the matrix microstructure. In addition the edges of the bars were bevelled to remove stress concentrations. A peak opening stress is produced above the centre roller in three-point bend, decreasing to zero above the outer rollers. The test conditions used for the short crack testing are summarised in Table 5.6.

Complete replica records of the specimen top surface were taken at suitable intervals (between 200-1000 cycles) under mean load. This was achieved by softening blocks of acetate in acetone and pressing them onto the top surface of the bend bar. These were then left to harden for about five minutes and were removed for subsequent analysis. This gave an impression of the top surface on the specimen. The replicas were of sufficient quality to be observed under both an optical and a scanning electron microscope and thus provided a record of crack initiation and growth through microstructure throughout the test. From study of the replica record, the number of cracks, their positions and relative lengths, as a

function of the number of cycles were determined. The objectives of the short crack testing were principally to characterise crack initiation and early growth.

5.6.1 Interrupted Short Crack Testing

In order to obtain a more detailed assessment of the interactions between the propagating crack and the matrix microstructure, analysis of a crack growing through an etched sample at high magnifications was required, and direct study of the specimen surface using an Optical Microscope and a SEM was necessary. Whilst the observation of secondary cracks on failed specimens was possible, analysis of the major crack system was felt to be more representative of crack-microstructure interactions. A number of short fatigue crack tests were therefore performed where the tests were interrupted after a chosen number of cycles. The specimens were then removed from the testing apparatus and subsequently analysed in detail using a FEG SEM.

5.6.2 Crack Length Measurement for Natural Initiating Cracks

Special care was taken to ensure the positions of the rollers were recorded accurately on every replica. Meticulous positioning of the replicas on the microscope stage using the roller positions as a reference allowed the subsequent determination of *projected* crack lengths with respect to the varying applied stress levels on the specimen top surface (see Figure 5.20 for schematic of short crack measurement). Images of cracks visible on the replicas were captured using the techniques described in 5.3.1.

Measurements of crack length from the digital images of the acetate replica record were performed using KS 300 on a PC running WinNT. Measurements were of projected crack lengths normal to the tensile axis. A calibration file automatically transforms pixel values to lengths in microns. Calculation of d2c/dN was achieved using a three point secant method. The calculation of ΔK was performed using equations as proposed by Scott and Thorpe [82] based on assumptions made for a semi-elliptical short crack (Figure 5.21).

Values of the specimen surface crack tip intensity factor (K) are given by the following equation:

$$K_I = \left[\left[M_{f0}\left(1-0.3\frac{a}{t}\right)\left(1-\left(\frac{a}{t}\right)^{12}\right)\right]+\left[0.394E(k)\left(\frac{a}{t}\right)^{12}\sqrt{\frac{a}{c}}\right]\right]\frac{\sigma}{E(k)}\sqrt{\pi a} \qquad \textit{Equation 5.1}$$

Where the surface correction factor is:

$$M_{f0} = \left[1.21-0.1\left(\frac{a}{c}\right)+0.1\left(\frac{a}{c}\right)^4\right]\sqrt{\frac{a}{c}} \qquad \textit{Equation 5.2}$$

and the elliptical integral is:

$$E(k) = \left[1+1.47\left(\frac{a}{c}\right)^{1.64}\right]^{0.5} \qquad \textit{Equation 5.3}$$

From fracture surface observations the ratio of a to c was assumed to equal 1.

5.7 Long Crack Experimental Method and Test Matrix

In order to investigate the effect of specimen microstructure on crack propagation under well defined stress states, a number of long fatigue crack tests were performed on single-edge notched-bend (SENB) bars with a pre-existing slot of an $^{a}/_{W}$ = 0.25. The notch was sharpened with a razor blade to promote crack initiation. Standard p.d. monitoring techniques were used to measure fatigue crack propagation. A constant current is passed through the specimen necessitating the use of ceramic non-conductive rollers. The potential difference across the notch mouth was monitored. Figure 5.22 shows the long crack testing set up. The long fatigue crack test matrix can be seen in Table 5.7 and Table 5.8. As the crack grows the conductive area decreased, leading to an increase in p.d. with crack growth such that:

$$\frac{a}{w} = f\left(\frac{v}{v_0}\right) \qquad \textit{Equation 5.4}$$

5.7.1 P.d Calibration and Measurement of Crack Growth

It was thought that the conductive graphite nodules in ADI might render the standard p.d. calibration invalid so the first test carried out was a beach-marking test. This was designed to establish the appropriate p.d. calibration. P.d. was monitored and a constant maximum load was applied throughout testing, alternating R-ratios of 0.1 and 0.5 were applied for p.d increments of 250mV. After failure the fracture surface was examined. Normally altering R-ratios will give differing fracture surfaces such that the crack advance can be tracked. The brittle and rather faceted nature of the fracture surface in this material is such that the beach marking was unsuccessful.

It was decided that an experimentally derived p.d calibration was required. The next test made use of a standard p.d calibration to estimate crack length. To double check this p.d. calibration, acetate replicas were taken of the sides of the specimen to monitor crack growth. These replicas were taken at suitable intervals. The $^{a}/_{W}$ values obtained from direct acetate replica observation were plotted as a function of the measured values of $^{V}/_{V0}$. The side cracks are assumed to be 95% of the mid-thickness crack length as required for ASTM 399-90 and the averaged estimated crack length used. Crack growth data from the initial 0.5 mm of growth was ignored. This was done to avoid any effects of residual stress and prior notch geometry on subsequent crack growth. The subsequent calibration was used for the next test. The process was repeated for every subsequent long fatigue crack test with the objective that the experimentally derived p.d calibration generates less error each time. Figure 5.23 shows the relationship between $^{V}/_{V0}$ and $^{a}/_{W}$ derived from the replica analysis and the initial p.d. readings for '900/390:L2'. It can be clearly observed that the p.d. calibration overestimates the values of $^{a}/_{W}$. However, the error between the two data sets appears quite constant. The experimental confirmation of side crack length to p.d. measurement for each test also allowed individual crack calibration for each test to be verified and corrected.

5.7.2 Determining da/dN vs. ΔK Curve

Load shedding to threshold and constant load amplitude growth out tests were performed to establish a da/dN vs. ΔK curves for the various material conditions. In order to establish to a materials fatigue threshold the following procedure is

used. Constant ΔK levels are applied at an R-ratio of 0.1 and a frequency of 20 Hz until crack growth equivalent to four plastic monotonic zones (MPZ) has occurred. The ΔK level is decreased by 10% every time the crack grows through four MPZ sizes. This is to ensure that characteristic crack growth rates obtained for a given ΔK value are not influenced by prior higher ΔK levels. These adjustments are referred to as major turndowns. To maintain constant ΔK levels the loads were continually adjusted downwards (minor turndowns) to maintain a value of ΔK to $^{+}$/- 2%. This load-shedding schedule (see Figure 5.24) was maintained until threshold (non-propagation of the crack) was achieved. This is defined as crack growth below $10^{\wedge 8}$ mm/cycle. Once fatigue threshold was satisfactorily achieved the specimen was cycled under constant load conditions. Hence, ΔK increases as crack length increases. This establishes crack growth behaviour under higher ΔK conditions.

5.7.3 Assessing the Effect of Microstructure on Crack Propagation

With suitable values of high, medium and low ΔK established by constant amplitude testing, constant ΔK tests were performed to identify the effect of microstructure on crack propagation. Again to maintain constant ΔK levels the loads were continually adjusted downwards to maintain a value of ΔK to $^{+}$/- 2%. Side crack replicas were taken at each minor turndown.

5.7.4 Fractography

Failed specimens were examined using an Olympus optical microscope and a JEOL 6500F FEG-SEM at an accelerating voltage of 10kV. Images were taken of specimen fracture surfaces, overall crack profiles, and primary initiation sites for all samples. In addition, images of secondary cracks on polished and etched samples were also captured.

	C	Si	Mn	P	S	Cu	Mo	Mg	Cr
Current Work	3.6-3.8	1.45-1.65	0.2-0.4	<0.05	0.01	1.0	0.5	0.035-0.055	
Previous Work	3.66	2.52	0.16	0.04	0.01	0.51		0.04	0.03

Table 5.1: Composition of as-cast ductile iron for current and previously tested ADI variants.

Classification	800/260	850/250*	800/390	850/400*	900/390	950/250*	950/400*
Austenitising Conditions	800^0C-120 mins	850^0C-60 mins	800^0C-120 mins	850^0C-60 mins	900^0C-120 mins	950^0C-60 mins	950^0C-60 mins
Austempering Conditions	260^0C-120 mins	250^0C-120 mins	390^0C-120 mins	400^0C-120 mins	390^0C-120 mins	250^0C-120 mins	400^0C-120 mins

Table 5.2: Heat treatments and material classification (*indicates previously tested heat treatments).

Classification	850/250*, 850/400*, 950/250*, 950/400*	As-cast Ductile Iron	800/260, 900/390	800/390, Chilled 800/390, Chilled DI
Cross section of Casting (mm)	Cylinder of unknown dimensions. Assumed to be camshaft cylinder dimensions	50 mm diameter	25 mm diameter	14 x 60
Length of castings (mm)		70	150	100

Table 5.3: Dimensions of castings as they were received from Federal Mogul Camshafts.

Stage	Plain Grinding	Plain Grinding	Plain Grinding	Plain Grinding	1st Polish	2nd Polish
Cloth	SiC	SiC	SiC	SiC	DP-Dur	DP-Mol
Abrasive	120 grit	600 grit	1200 grit	4000 grit	6μm diamond	1μm diamond
Lubricant	Water	Minimal amounts of water	Minimal amounts of water	Minimal amounts of water		
Time	Until Plane	1 min	2 mins	2 mins	1 mins	1 mins

Table 5.4: Polishing route used for all specimens.

Alloy Variant	As-cast ductile iron	900/390, 800/290	800/390 Chilled 800/390, Chilled Ductile Iron
Breadth (mm)	10	12	10
Width (mm)	10	12	10
Length (mm)	70	80	100

Table 5.5: Dimensions of short fatigue crack specimens.

Material Classification	Maximum applied stress (MPa) R=0.1									R=0.5	
	800	700	600	500	450	400	300	250	200	1100	800
'DI'			X	X		X					
'800/290'	x	X	X	X		X					
'800/390'			X	X		X					
'900/390'	X	X	X	X						x	x
'CDI'					X	X	X		X		

Table 5.6: Short fatigue crack test matrix.

Test	Conditions	Load	ΔK	Calibration
900/390:L1	Beach marking	Alternating R=0.1, R=0.5		n/a
900/390:L2	Fatigue threshold	Adjusted for load shedding schedule and to maintain ΔK to $^{+}$/- 2%.	Initially ~10	
	Constant load amplitude growth out	Constant for growth out region		
900/390:L3	Constant load amplitude growth out	Constant	Initially ~10	Derived experimentally from '900/390:L2'
900/390:L4	Constant ΔK	Adjusted to maintain ΔK to $^{+}$/- 2%.	~15	Derived experimentally from '900/390:L2&L3
	Constant amplitude growth out	Constant for growth out region	Initially ~15	
900/390:L5	Constant ΔK	Adjusted to maintain ΔK to $^{+}$/- 2%.	~10	Derived experimentally
	constant amplitude growth out	Constant for growth out region	Initially ~10	
900/390:L6	Fatigue threshold	Adjusted for load shedding schedule and to maintain ΔK to $^{+}$/- 2%.	Initially ~15	Derived experimentally
	Constant ΔK	Adjusted to maintain ΔK to $^{+}$/- 2%.	~10	
	Constant ΔK	Adjusted to maintain ΔK to $^{+}$/- 2%.	~20	

Table 5.7: Long fatigue crack test matrix – '900/390' specimens.

800/260:L1	Constant amplitude growth out	Constant	Initially ~10	Derived experimentally
800/260:L2	Constant ΔK	Adjusted to maintain ΔK to +/- 2%.	~10	Derived experimentally
	Constant amplitude growth out	Constant for growth out region	Initially ~10	
800/260:L3	Constant ΔK	Adjusted to maintain ΔK to +/- 2%.	~15	Derived experimentally
	Constant amplitude growth out	Constant for growth out region	Initially ~15	
800/260:L4	Fatigue threshold	Adjusted for load shedding schedule and to maintain ΔK to +/- 2%.	~15	Derived experimentally
	Constant load amplitude growth out	Constant for growth out region	Initially ~15	
DI:L1	Fatigue threshold	Adjusted for load shedding schedule and to maintain ΔK to +/- 2%.	Initially ~15	Derived experimentally
	Constant load amplitude growth out	Constant for growth out region		

Table 5.8: Long fatigue crack test matrix – '800/260' and 'DI' specimens.

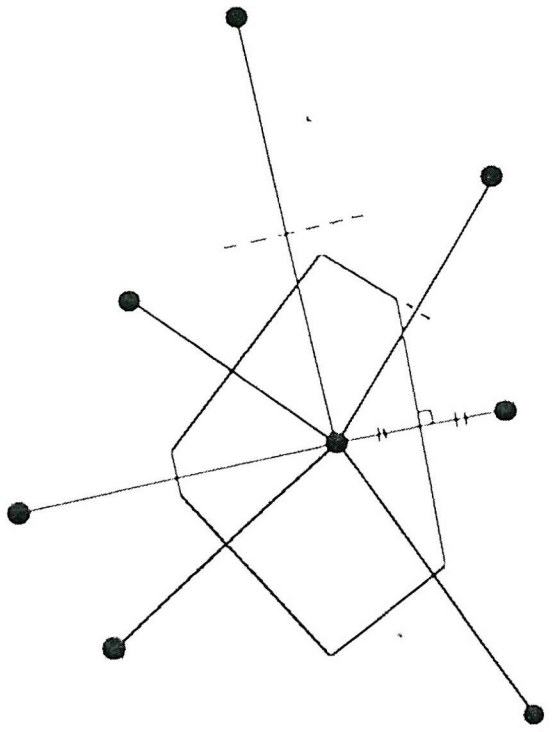

Figure 5.1: Dirichlet tessellation: The construction of a cell around an object centroid.

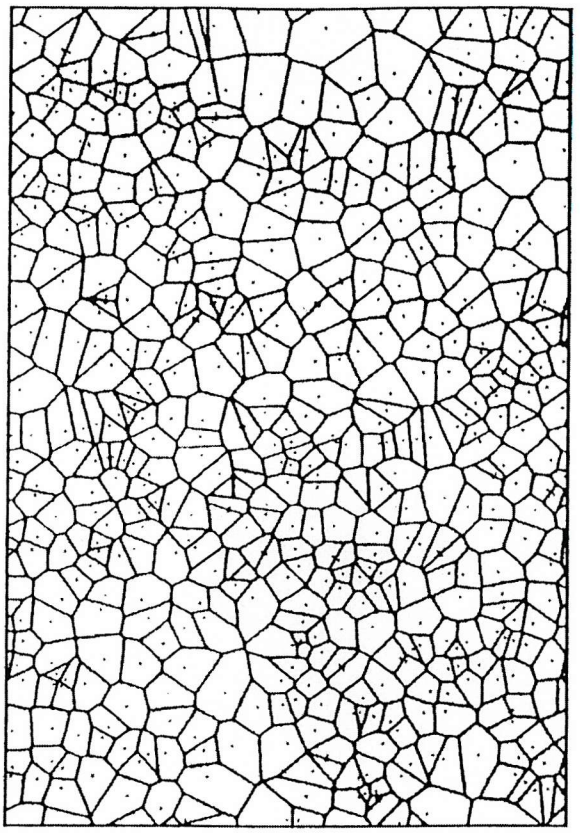

Figure 5.2: An example of Dirichlet tessellation.

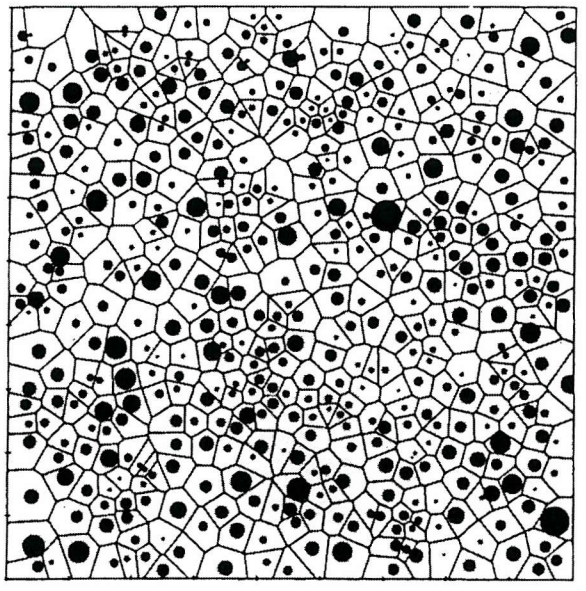

Figure 5.3: Example of object/cell overlaps [83]

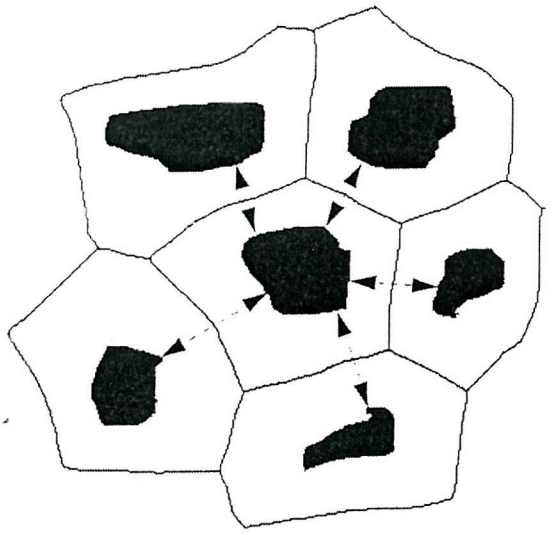

Figure 5.4: Finite body tessellation.

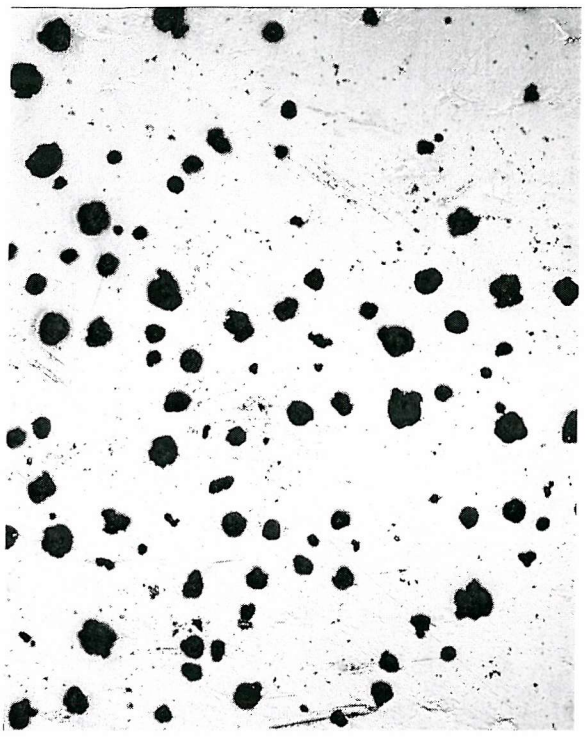

Figure 5.5: Image of a '900/390' specimen for use in graphite nodule distribution analysis.

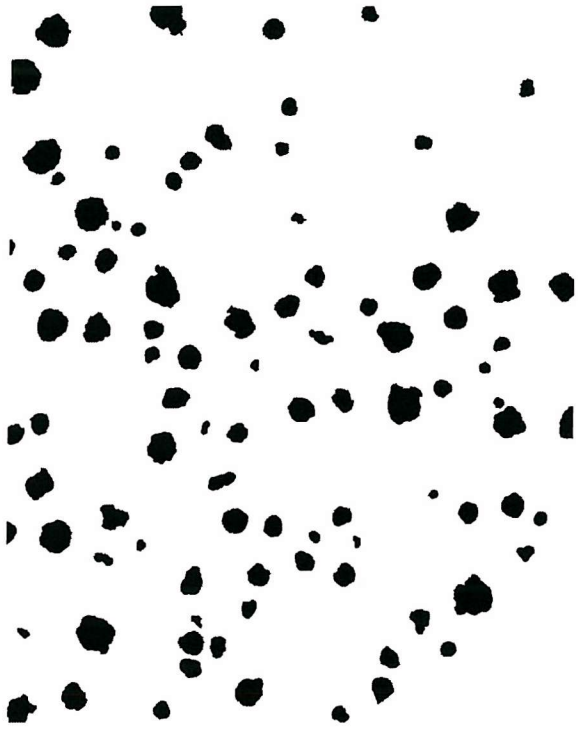

Figure 5.6: Binary of the previous image ready for tessellation analysis.

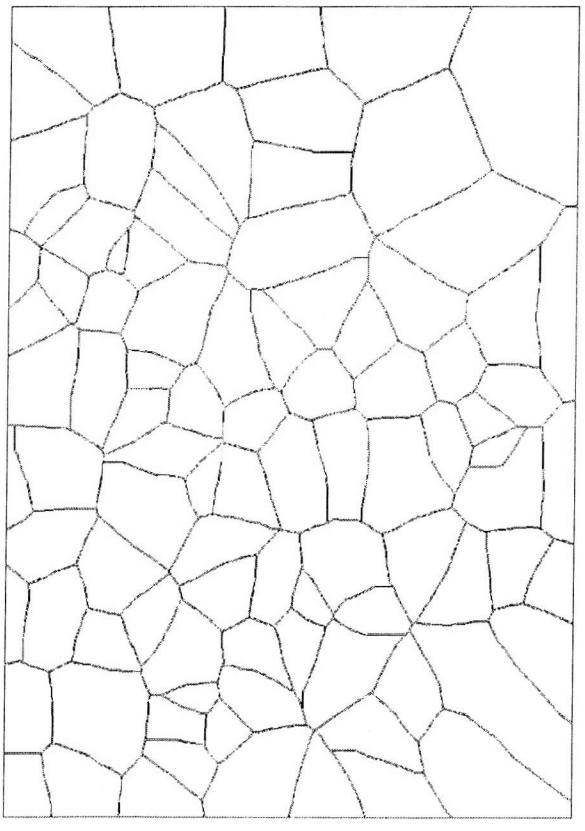

Figure 5.7: Network of cells.

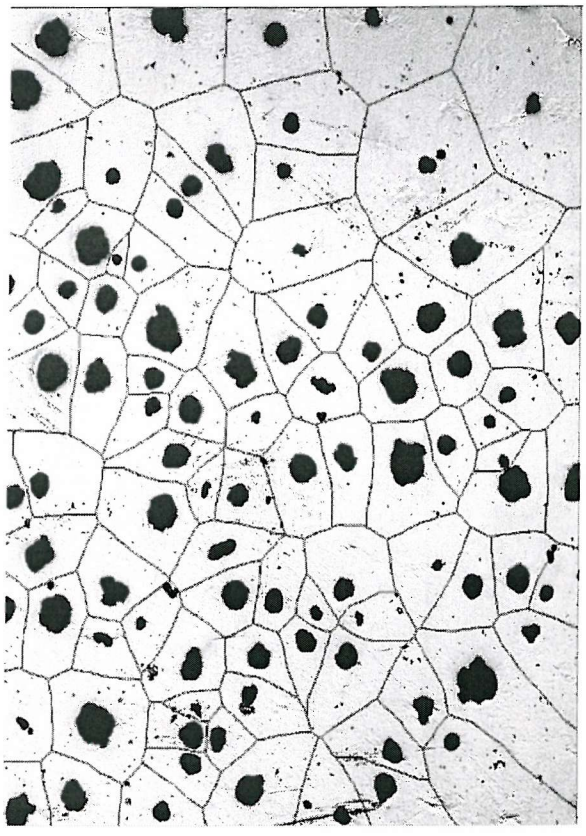

Figure 5.8: Final tessellated image.

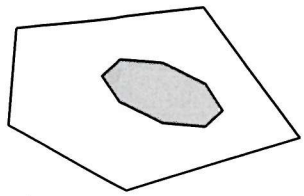

Object Area (O_a)

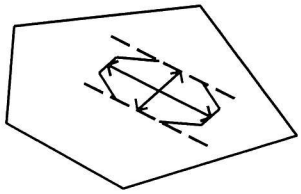

Object Aspect Ratio (O_{ar})

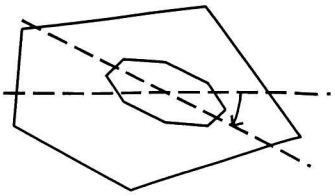

Object Angle (O_{ang})

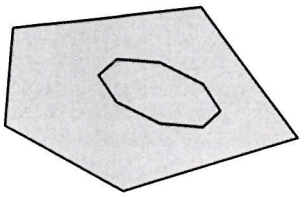

Cell Area (C_a)

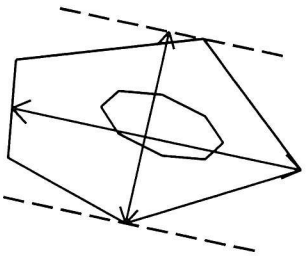

Cell Aspect Ratio (C_{ar})

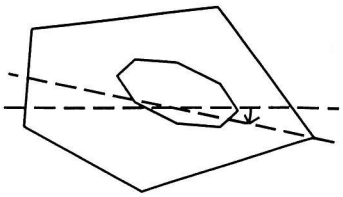

Cell Angle (C_{ang})

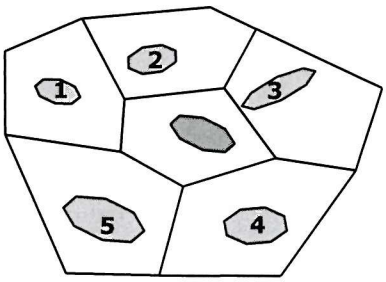

Number of Near Neighbours

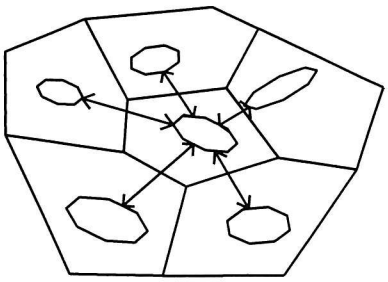

Mean Near Neighbour Distance (D_{mean})

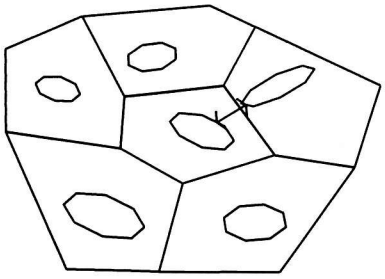

Nearest Neighbour Distance (D_{min})

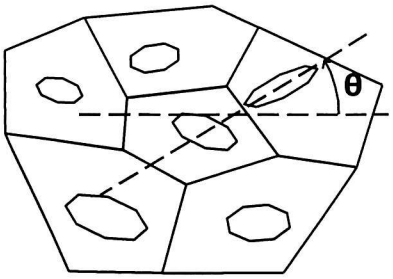

Nearest Neighbour Angle (NN_{ang})

Figure 5.9: Schematic representation of FBT measurements.

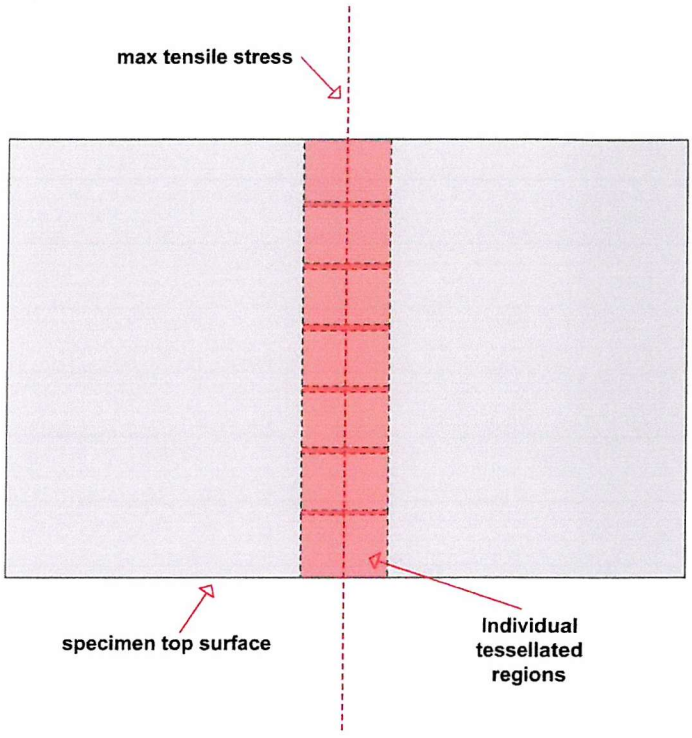

Figure 5.10: Schematic of eutectic carbide analysis of short fatigue crack specimens. Plan view of specimen top surface.

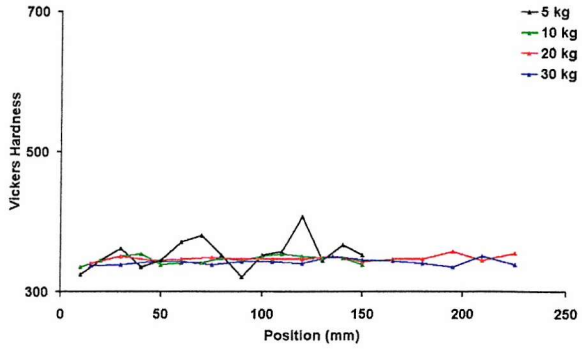

Figure 5.11: Variation of hardness with load for 900/390 specimens

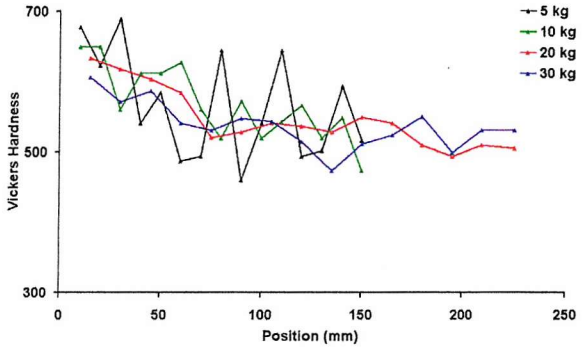

Figure 5.12: Variation of hardness with load for 800/260 specimens

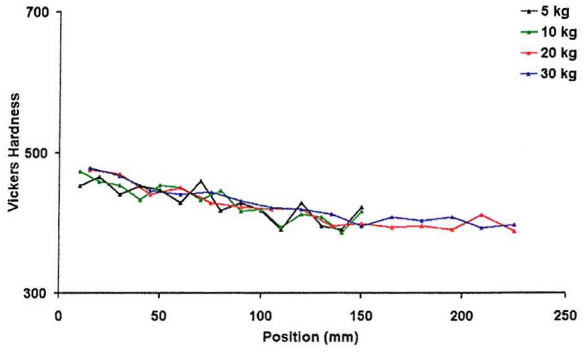

Figure 5.13: Variation of hardness with load for 800/390 specimens

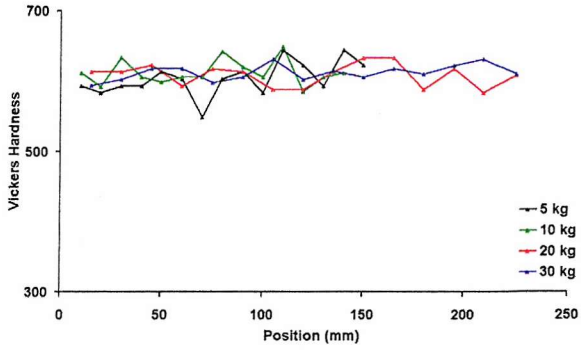

Figure 5.14: Variation of hardness with load for Chilled DI specimens

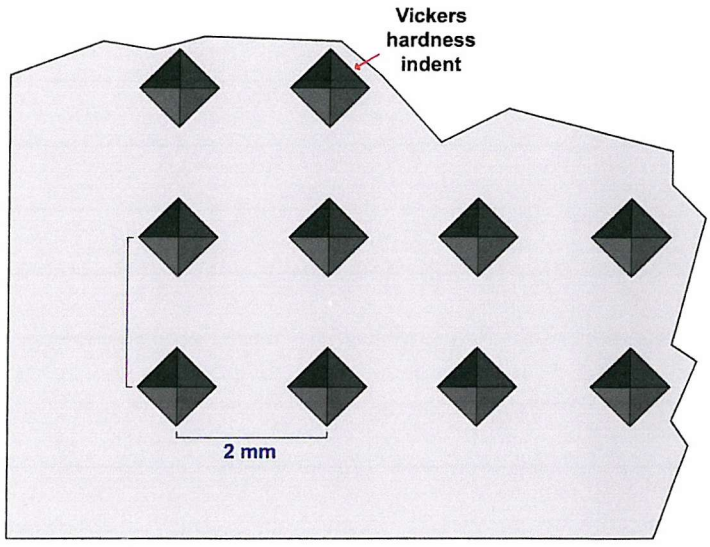

Figure 5.15: Schematic of hardness map.

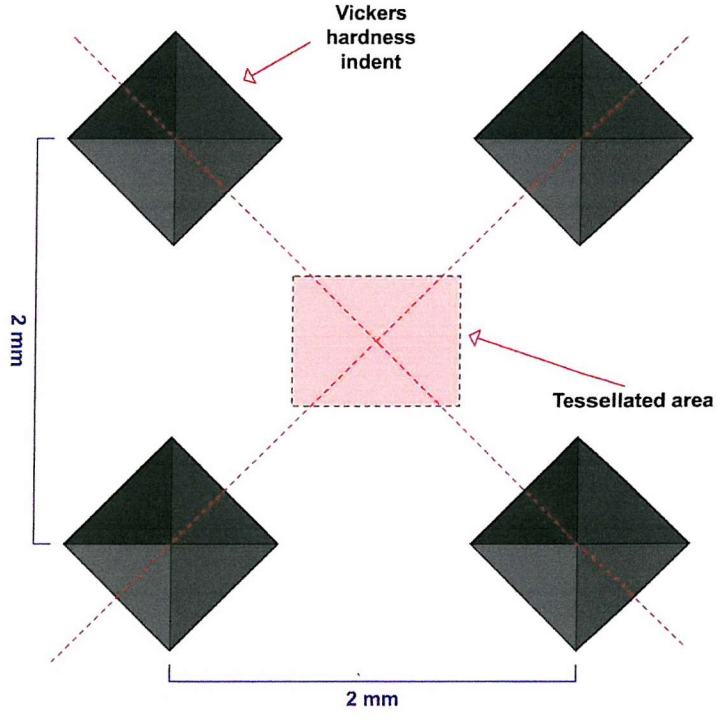

Figure 5.16: Schematic of eutectic carbide analysis of hardness map.

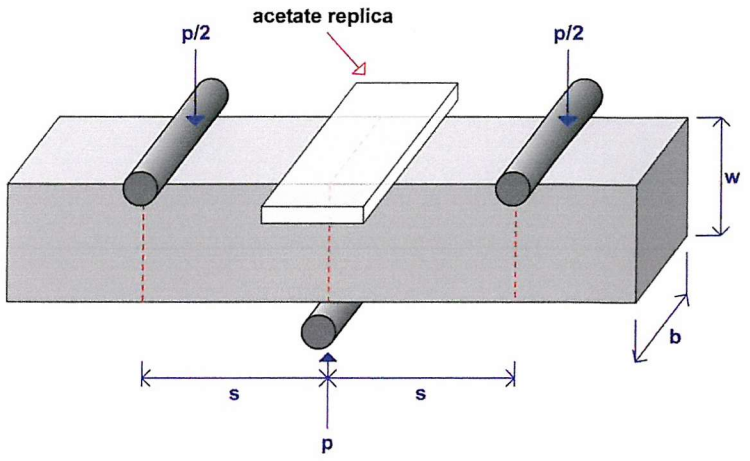

Figure 5.17: Three-point bend short crack fatigue test set-up. P = applied load; s = separation

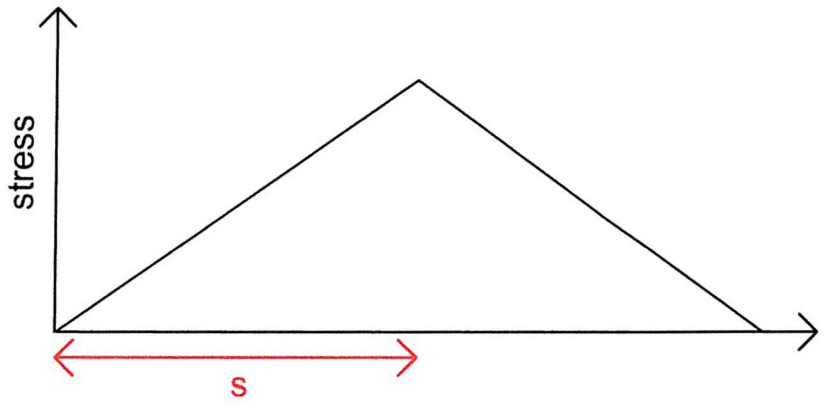

Figure 5.18: Stress distribution for three-point bend.

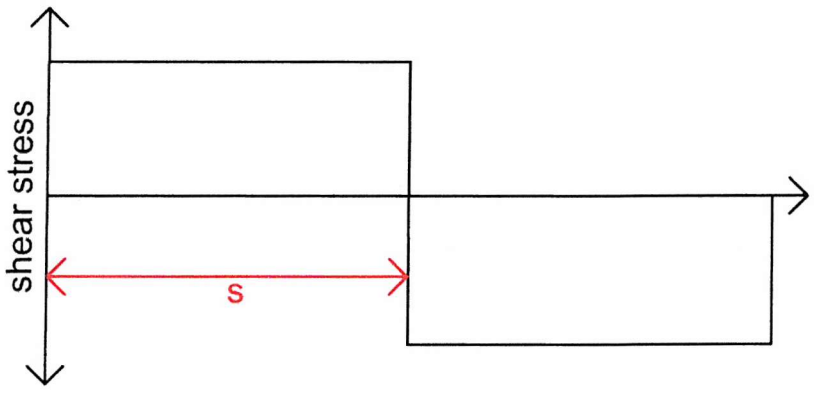

Figure 5.19: Corresponding shear stress distribution for three-point bend

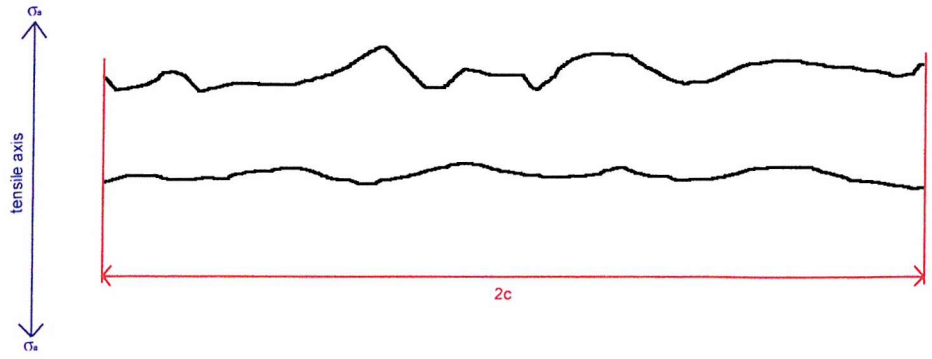

Figure 5.20: Schematic of projected crack length. It is clear that the distance travelled by the upper crack is farther than the lower crack. However, the projected crack length for the two cracks is identical.

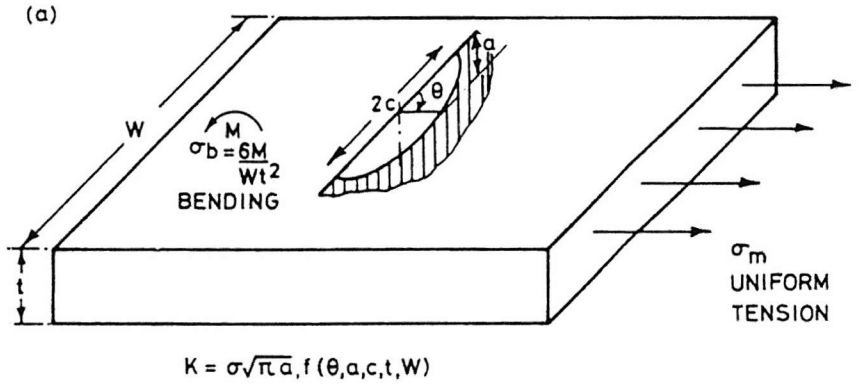

Figure 5.21: Schematic of a semi-elliptical crack in a plate. (Scott & Thorpe)

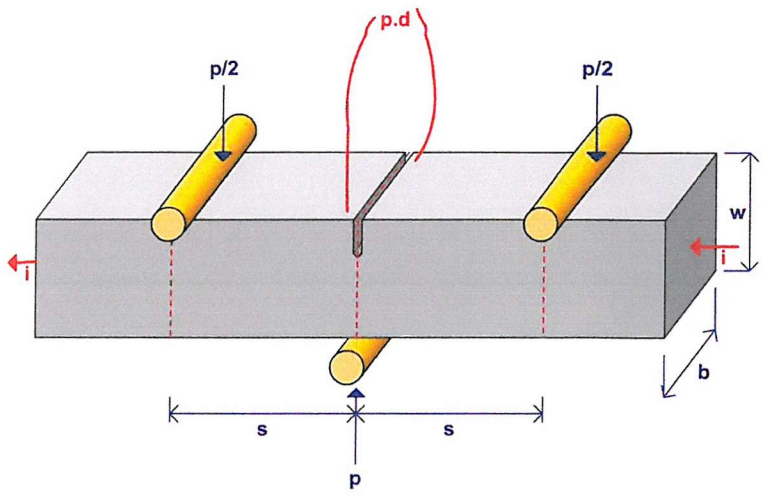

Figure 5.22: Three-point bend long crack fatigue test (with p.d. calibration) set-up. P = applied load; s = separation.

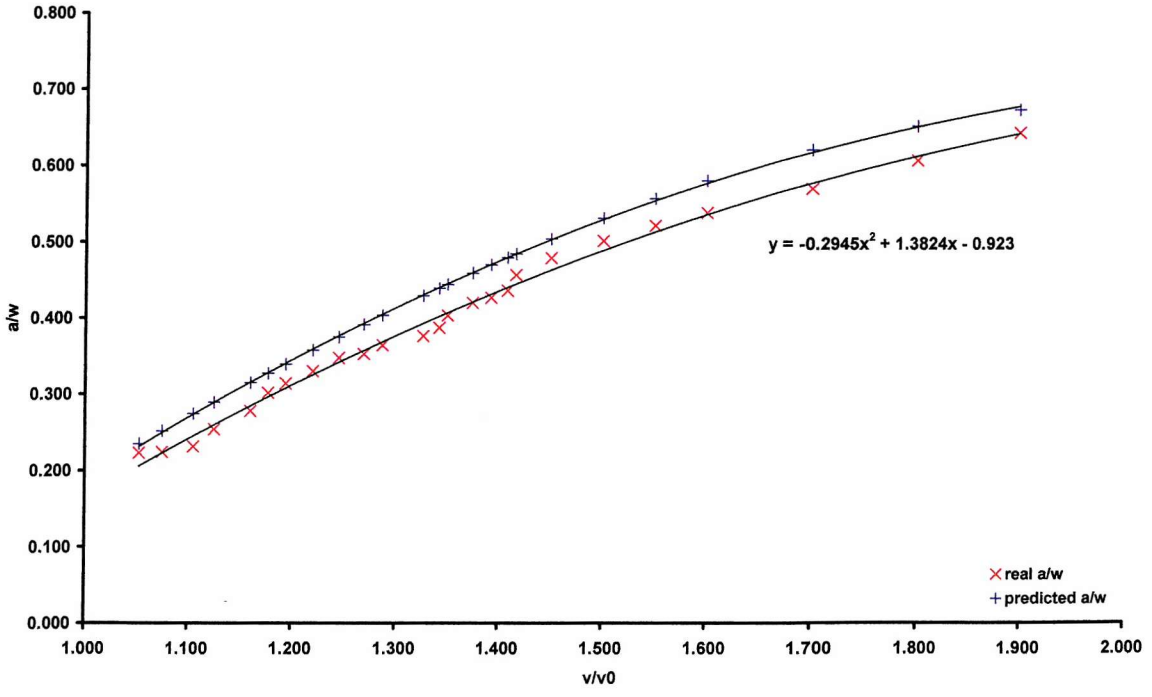

Figure 5.23: p.d. calibration graph for long-crack test '900/390:L2'

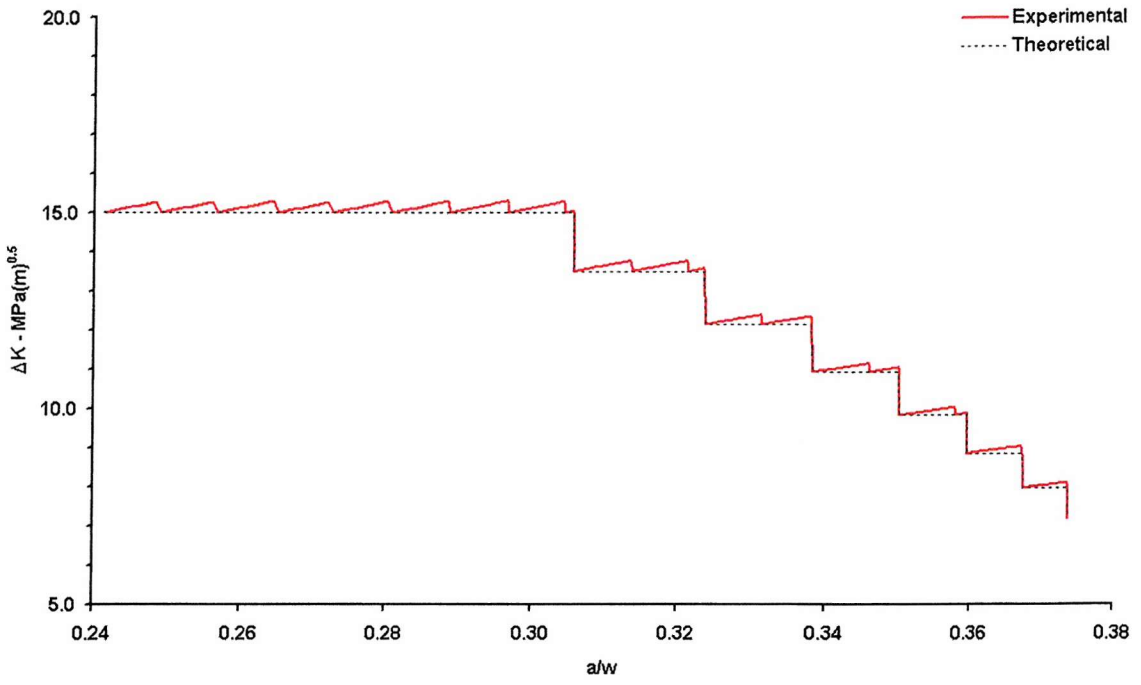

Figure 5.24: Graph to show major and minor turndowns during load shedding to fatigue threshold.

6 Microstructural Analysis

6.1 Predicted Microstructures

The volume fractions of the major matrix constituents of the alloys studied in this work and the previous comparative study [2,3,4] as predicted by Loughborough University are shown in Figure 6.1. The model of microstructural evolution employed by Loughborough is detailed in section 3.4. The volume fractions of bainite and retained austenite are a complex function of austenitising temperature and time and austempering temperature and time for any given ADI alloy. However, for these heat treatments the predicted volume fractions of the major matrix constituents appear, as a first approximation, to be principally controlled by austempering temperature, with austenitising temperature a secondary factor. The higher austempering temperatures are predicted to produce microstructures with greater proportions of retained austenite. The microstructures predicted at low austempering temperatures have large amounts of bainite and relatively small proportions of retained austenite.

However it should be noted that the distribution of retained austenite and bainite is considered by a number of authors [59, 69] to be significant in determining the fatigue life of ADI alloys, and is not predicted by the model which calculates overall volume fractions. Furthermore, the model does not distinguish between the formation of upper and lower bainite. The differences in bainite lath morphology may be significant in affecting fatigue crack propagation. For example, the coarser laths of upper bainite may conceivably increase the probability of crack deflection (as observed by previous authors [2,3,84]). Simple characterisation of any ADI alloy by the volume fractions of its major matrix micro-constituents is not likely to fully determine the fatigue resistance behaviour.

6.2 Optical Analysis of Microstructure

Figure 6.2 to Figure 6.5 are micrographs of the four etched microstructures of the previous comparative study. The volume fractions of bainite and austenite as predicted by Loughborough University are indicated under each micrograph. The study of the micrographs of the previously tested heat treatments allows

observation of the differing microstructures formed by varying heat treatment parameters. The first apparent feature is the differing bainite structure between the microstructures austempered at 250^{0}C and those austempered at 400^{0}C. The higher temperature austempers show much coarser bainite when compared with the alloys austempered at 250^{0}C. This is consistent with literature regarding the formation of upper and lower bainite. Upper bainite will be present in the 400^{0}C austempers, and lower bainite is present in the 250^{0}C austempers. The second feature is the apparent effect of austempering temperature on the location and relative areas of retained austenite. It can be seen that higher austempering temperatures give an apparent increase in the amount and relative size of blocky austenite fields. This is consistent with the microstructural predictions by Loughborough University. When considering the microstructures austenitised at 850^{0}C the Loughborough model predicts retained austenite volume fractions of 18% and 32% for the 250^{0}C and 400^{0}C austempers respectively. For the microstructures austenitised at 950^{0}C retained austenite volume fractions of 25% and 45% are predicted for the 250^{0}C and 400^{0}C austempers respectively. Furthermore, it is possible to see the effect of austenitising temperature on the relative amount of retained austenite in these four microstructures. Comparison of Figure 6.2 and Figure 6.4 suggest a higher austenitising temperature gives a larger amount of retained austenite. This is reflected by the microstructures in Figure 6.3 and Figure 6.5 and is consistent with the Loughborough model predictions. Generally, the graphite nodules are surrounded by bainite rich regions with the retained austenite seen in regions midway between. This is to be expected, since bainite forms around the graphite nodules and grows out until halted by the increased carbon content in the remaining austenite.

What is not revealed in the graph of predicted microstructures is the formation of Widmanstatten ferrite within the matrix microstructure of the '850/250' heat treatment. The presence of which can be clearly seen in micrographs of this heat treatment. Thomson et al [84] have considered the TTT curves for this composition and heat treatment, it is apparent that the cooling rate from austenitising to austempering and the start temperature for displacive transformation is sufficiently high to allow formation of Widmanstatten ferrite, particularly when cooling to the

lower austemper (250^0C) condition. The current Loughborough microstructure model does not predict this.

The composition of the as-cast ductile iron of the current heat treatments is sufficiently different to the previous heat treatments to cause significant changes in austempered matrix morphology. Federal Mogul Camshafts increased the chill tendency of the as-cast ductile iron by specifying a relatively low silicon concentration. The chill tendency of a ductile iron refers to the likelihood of eutectic carbide formation on solidification. As can be seen in Figure 6.6 the amounts of carbon and silicon in the as-cast ductile iron place it in the high chill tendency region of the graph. Large carbidic structures can be observed in the as-cast microstructure Figure 6.7. EDX suggests these carbide structures are eutectic in nature. The microstructure is not that of a white iron since carbon is still present in the form of graphite nodules. The surrounding matrix is pearlitic in nature. In Figure 6.7c and d the amount of carbide is significantly lower and the structure appears markedly different resembling that of intercellular carbides caused by constituent segregation. Constituent segregation occurs during solidification of the original ductile iron casting as the elements separate into different regions within the matrix [9]. Negative segregants such as Si, Ni, and Cu tend to segregate into areas adjacent to the graphite nodules, which are the first to cool. Later, the intercellular regions between graphite nodules solidify. Positive segregants such as Mn, and Mo migrate to these regions and promote carbide formation.

The dissolution of the eutectic carbides may occur if the subsequent austenitisation conditions are sufficient. For the three heat treatments presently being studied the austenitising temperature has a significant effect on the dissolution of these carbides. The eutectic carbide structures present in the as-cast microstructure remain after heat treating in the '800/260' and '800/390' conditions. The near total absence of these carbide structures in the '900/390' heat treatment indicates that the austenitising temperature of 900^0C is sufficient to cause their dissolution. This process is not predicted by the Loughborough model and is likely to have a considerable effect on the bainite and retained austenite volume fractions, and also the retained austenite carbon content. The matrix

microstructure of the '800/260' heat treatment exhibits fine lower bainite sheathes and inter-lath austenite (see Figure 6.8). In Figure 6.8 there is also evidence of constituent segregation. Coarser upper bainite laths are representative of the '800/390' microstructure as shown in Figure 6.9. Furthermore, pools of retained austenite are smaller than those in the '900/390' heat treatment. This agrees with observations of the previously tested heat treatments regarding the effect of austenitising temperature. The lack of the large carbidic structures gives the '900/390' heat treatment a more conventional ADI appearance (Figure 6.10). The matrix microstructure generally consists of coarse bainite laths and large blocky pools of retained austenite. The bainite structure is far from homogeneous however. During the austempering, the nucleation of bainite occurs at the graphite/austenite interface [9] and grows by sympathetic nucleation of further plates into the austenite. As this transformation occurs the growing bainite rejects carbon into the austenite. Therefore during the bainite transformation, as the distance from graphite nodules progressively increases so does the carbon content in austenite such that it reaches a point where no further transformation to bainite can occur. Due to the growth of bainite sheaves away from the graphite, these regions of supersaturated austenite exist in areas remote from nodules. Hence, for a conventional ADI alloy, as the distance from the graphite nodules increases, the proportion of austenite increases. However, in this case, there are large regions free of blocky austenite pools, the location of which unconventionally appears unrelated to that of graphite nodules. The dissolution of eutectic carbide that remains from the as-cast ductile iron during the austenitisation process is likely to have a significant effect on the relative carbon content of the austenite prior to austempering. This is likely to have an effect on the bainite transformation kinetics and subsequent matrix morphology.

The presence of intercellular constituent segregation in the as-cast ductile iron will also have an effect on the final austempered microstructure. The presence of an enrichment of Mn in the intercellular regions may cause a significant delay in austempering response when compared to other areas [46,47,48,49]. The effect of this is visible in the microstructure of the '800/260' heat treatment (Figure 6.8). Generally speaking, the microstructural characterisation of the previously and

currently tested heat treatments suggest that both austenitising and austempering parameters have significant effects on the matrix microstructures of ADI alloys.

Figure 6.11 to Figure 6.12 show the microstructure of the chilled ductile iron. The micrographs were taken from a specimen where the top surface is approximately 2 mm from the chilled face of the cast block. The chilled surface is clearly carbidic. The absence of graphite is conspicuous and suggests the chill successfully produced a white iron surface. The structure of the carbides is clearly dendritic and orientated perpendicularly to the chilled surface. The carbidic structure has been formed by the rapid cooling through the eutectic temperature that was brought on by the chill. Additionally, the low silicon composition increased the chilling tendency. Quench cracks have been observed on one of the prepared specimens, although the others appear uncompromised. Additionally, one of the specimens suffered from extensive surface porosity.

When the carbide structure of the chilled '800/390' ADI is compared to the carbide structure of the chilled DI it is apparent that the dendrite structure is finer, smaller and more randomly distributed. Figure 6.13 shows the microstructure of the chilled '800/390' ADI. The surface in the micrograph was again 2 mm from the chilled face. Quench-cracks were quite extensive and easily visible on the prepared chilled ADI specimens (see Figure 6.14). The presence of these quench-cracks prevented meaningful fatigue testing of this material.

6.2.1 Graphite Nodule Distribution

Finite body tessellation data for graphite nodule distribution in each of the ADI heat treatments is presented in Table 6.1. It is apparent that the mean nodule area for the '900/390' and '800/260' are comparable. The mean nodule area for the '800/390' is significantly smaller. This has a consequential effect on local area fraction where the same trend is observed. The values of nodule aspect ratio for the three heat treatments are the same. Object angle has therefore been omitted since the nodules are approximately spherical. Mean and nearest neighbour distances for the two ADI variants austenitised at 800^0C are similar with the '900/390' heat treatment slightly lower but within one standard deviation. All other FBT terms are comparable for all three alloy variants.

6.2.2 Eutectic Carbide Distribution

Quantification of the eutectic carbide distribution in the vicinity of peak applied stress was important for the as-cast ductile iron, '800/260' and '800/390' alloy variants. Overlapping digital images covering the full breadth of the short crack specimen in the region experiencing maximum stress (see Figure 5.10) were taken. A montage of these images was subsequently generated in Paint Shop Pro 7, a Jasc Software product. The entire montage could then be tessellated in one run. The advantage of this procedure is the reduction in the number of 'edge cells' and hence the optimisation of the amount of data gained per unit area.

A summary of the data generated from the application of tessellation analysis to the carbide distributions in 'ductile iron', '800/260', and '800/390' specimens is presented in Table 6.2. Numerous specimens were analysed for each microstructure. Seven, twenty eight and eleven specimens were assessed for the ductile iron, '800/260' and '800/390' respectively. The means, standard deviations and coefficients of variance for each of the tessellation parameters were calculated for each individual specimen. These values were then averaged to generate the data for each of the alloy variants.

The '800/260' and ductile iron microstructures appear to have statistically comparable eutectic carbide populations. However, it is clear that the eutectic carbide population of the '800/390' heat treatment differs significantly. The carbide area fraction for the '800/390' microstructure is three times that of the other two. The mean carbide area, cell area and mean near neighbour distance suggest a highly concentrated population of relatively small carbides. The carbide populations of the as-cast ductile iron and the '800/260' condition exhibit, as a whole, larger less densely packed carbides. It should be remembered that the '800/390' samples were prepared from castings of quite a differing nature to the other two (see section 5.1). The differing casting dimensions are likely to have affected the cooling rates experienced by the material ultimately used in the test specimens. The amount of eutectic carbide found in all of these heat treatments is affected by rate of cooling. It is likely that the thinner section cast blocks of the '800/390' heat treatment will have suffered a faster cooling rate. Subsequently the

conditions for carbide formation in these castings is more favourable than the '800/260' and ductile iron with their larger, slower to cool castings.

It is apparent there is a variation in carbide area fraction between specimens subjected to the same heat treatment. Figure 6.15 and Figure 6.24 shows significant variation in carbide area fraction for the as-cast ductile iron and '800/260' specimens respectively. Variations between ductile iron specimens can be seen in Figure 6.16 to Figure 6.23 whilst Figure 6.25 to Figure 6.32 show simplistic comparisons between '800/260' specimens.

Ductile Iron Specimens (Figure 6.16 to Figure 6.23)

Only the graphs for mean carbide area, carbide aspect ratio and mean cell area show any significant variation between specimens. The unusually low mean carbide area shown by specimen 01 is particularly noteworthy. The other tessellation parameters show little variation.

'800/260' Specimens (Figure 6.25 to Figure 6.32)

It is apparent that the '800/260' microstructure is more variable than the as-cast ductile iron. The graphs for mean carbide area, mean carbide aspect ratio, mean cell area, mean nearest neighbour distance, and mean near neighbour distance show significant variation between specimens. The other tessellation generated parameters show less variation. It was also observed during this analysis that the eutectic carbide distribution varied along the length of individual specimens. It is suspected that the variances originate from the specimens position in the original casting. Areas nearer the centre of the casting appear to show fewer eutectic carbides. As discussed in the previous sub-section this is likely to be related to the variation in cooling rate within the casting. This was investigated further and is discussed in section 5.5.1.1.

Work by Yang et al. [85,86] have identified the coefficient of variation of mean near-neighbour distance (COV(d_{mean})) as a powerful parameter to identify homogeneity in metal matrix composites (MMCs). Homogenous particle distributions were characterised by a COV(d_{mean}) of 0.36 (+/-0.02). Distribution homogeneity may be assessed against this value, with increasingly clustered particle distributions exhibiting COV(d_{mean}) values greater than 0.36. Values of COV(d_{mean}) for

'800/260' specimens ranged from 0.52 to 0.66. This would suggest that all the specimens exhibit a clustered carbide distribution.

Comparison of the mean specimen FBT terms and carbide area fraction for all the '800/260' fatigue specimens can be seen in Figure 6.33. It is clear there is correlation between the mean specimen values of some of these terms and carbide area fraction. An increase in mean carbide area is related to an increase in carbide area fraction. A similar relationship is seen for the number of individual carbides and area fraction. This indicates that an increase in carbide area fraction is not simply a result of a greater number of carbides or a higher mean carbide area, but rather a combination of the two terms.

6.2.3 Notes on the Limitations of FBT

Finite body tessellation was developed at Southampton University to solve the problems encountered by the application of Dirichlet tessellation on irregular shaped, heterogeneously distributed second phase particles. As can be seen in Figure 6.7 the morphology of the carbide structures is far from regular. The process of only partial dissolution in the ADI heat treatments austenitised at 800^0C exaggerates the unusual carbide geometries, examples of which can be seen in Figure 6.34. Irregularities include re-entrant notches and 'islands' of matrix material inside carbide structures. Features such as these are not described by the FBT parameters and may have significant bearing on the mechanical properties of the individual carbide. As the irregularity of carbide geometry increases parameters such as object angle and object aspect ratio becomes progressively more ambiguous. Additionally, the data gathered from FBT pertains to two dimensional sections of the microstructure. It is hoped that with a large enough sampling area the data from these two dimensional sections will be sufficiently representative of the material volume.

6.2.4 Summary

It is clear that the alloy microstructures of the current work are significantly different from those previously studied at Southampton University. The current ADI heat treatments do not show the appearance of a standard ADI microstructure, there are numerous large eutectic carbide structures in the 800^0C austempers. These carbides are reasonably homogeneously distributed in the

'800/390' condition. This is not the case of the '800/260' heat treatment, where a large degree of variability is shown. This variability is thought to be caused by differing cooling rates throughout the castings. The higher austenitising temperature of the '900/390' condition is sufficient to dissolve most of the eutectic carbides giving it a more conventional ADI microstructure. Eutectic carbides aside, the nature of the ADI matrix microstructure is a function of both austempering and austenitising. These differences can be attributed to the differing compositions of the two as-cast ductile irons.

Property	Heat Treatment	Mean	St dev	Coeff Var
Nodule Area (μm^2)	'900/390'	1334	825	0.62
	'800/260'	1462	779	0.53
	'800/390'	451	204	0.45
Nodule Aspect Ratio	'900/390'	1.2	0.2	0.1
	'800/260'	1.2	0.2	0.1
	'800/390'	1.2	0.2	0.1
Cell Area (μm^2)	'900/390'	13909	6689	0.5
	'800/260'	16437	7510	0.5
	'800/390'	12694	6585	0.5
Local Area Fraction	'900/390'	9.8	5.5	0.6
	'800/260'	10.1	5.4	0.6
	'800/390'	4.6	4.6	0.7
Number Near Neighbours	'900/390'	5.7	1.3	0.2
	'800/260'	5.7	1.3	0.2
	'800/390'	5.7	1.3	0.2
Mean Near Neighbour Distance (μm)	'900/390'	84.2	29.1	0.3
	'800/260'	95.1	32.3	0.3
	'800/390'	96.1	33.5	0.3
Mean Nearest Neighbour Distance (μm)	'900/390'	30.9	20.6	0.6
	'800/260'	35.6	22.0	0.7
	'800/390'	36.3	26.1	0.7
Mean Nearest Neighbour Angle (rads)	'900/390'	0.8	0.5	0.6
	'800/260'	0.8	0.5	0.6
	'800/390'	0.8	0.4	0.5

Table 6.1: Summary of FBT data for graphite nodule characterisation.

Property	Heat Treatment	Mean	St dev	Coeff Var
Global Carbide Area Fraction (%)	Ductile Iron	6.9	2.1	0.3
	'800/260'	7.2	3.7	0.5
	'800/390'	23.0	2.8	0.1
No. Carbides	Ductile Iron	1048	220	0.2
	'800/260'	1392	435	0.3
	'800/390'	4724	186	0.04
Carbide Area (μm^2)	Ductile Iron	559.6	1276.6	2.3
	'800/260'	495.8	840.2	1.7
	'800/390'	127.1	245.7	1.9
Carbide Aspect Ratio	Ductile Iron	2.1	0.9	0.4
	'800/260'	2.1	0.9	0.4
	'800/390'	2.3	1.2	0.5
Cell Area (μm^2)	Ductile Iron	8244.8	7897.2	66.4
	'800/260'	7663.8	6778.4	17.2
	'800/390'	595.9	734.2	1.2
Number Near Neighbours	Ductile Iron	5.7	2.3	0.4
	'800/260'	5.7	2.1	0.4
	'800/390'	5.6	2.6	0.5
Mean Near Neighbour Distance	Ductile Iron	60.6	40.4	0.7
	'800/260'	59.0	34.8	0.6
	'800/390'	9.8	5.3	0.5
Mean Nearest Neighbour Distance	Ductile Iron	12.6	17.5	1.4
	'800/260'	10.8	14.8	1.4
	'800/390'	3.1	1.9	0.6
Mean Nearest Neighbour Angle	Ductile Iron	0.8	0.4	0.6
	'800/260'	0.8	0.5	0.6
	'800/390'	0.9	0.4	0.5
Class sizes	Ductile Iron	7 specimens (7884 carbides)		
	'800/260'	28 specimens (38980 carbides)		
	'800/390'	7 specimens (carbides)		

Table 6.2: Summary of tessellation generated carbide distribution data

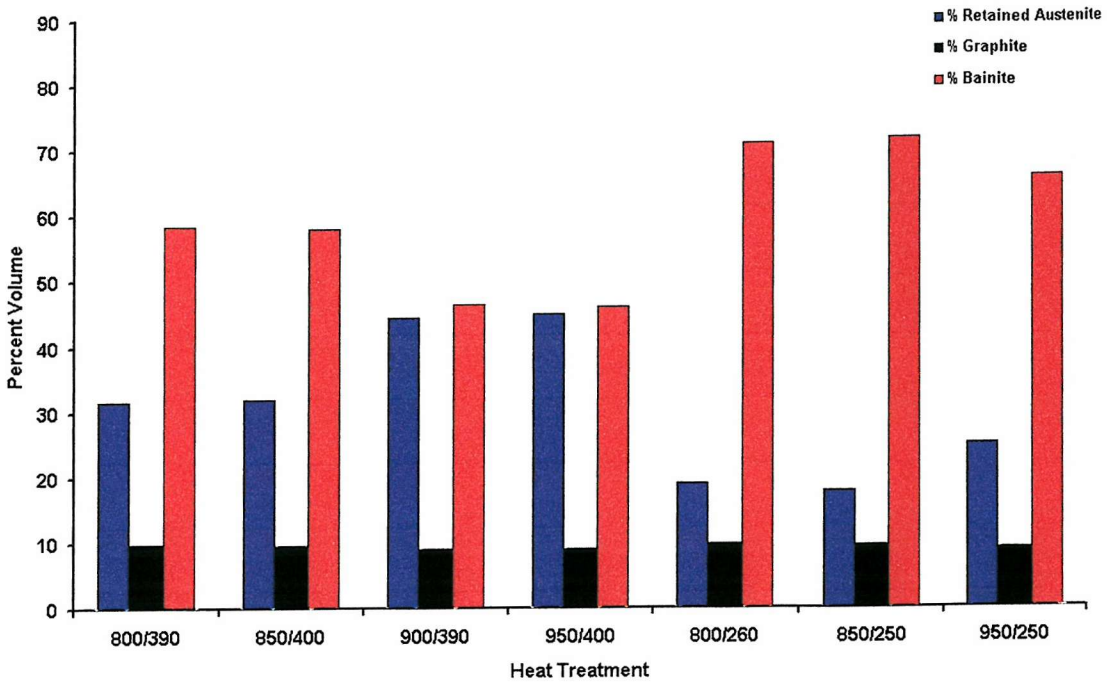

Figure 6.1: Predicted volume fractions of retained austenite, bainite and graphite for all ADI heat treatments.

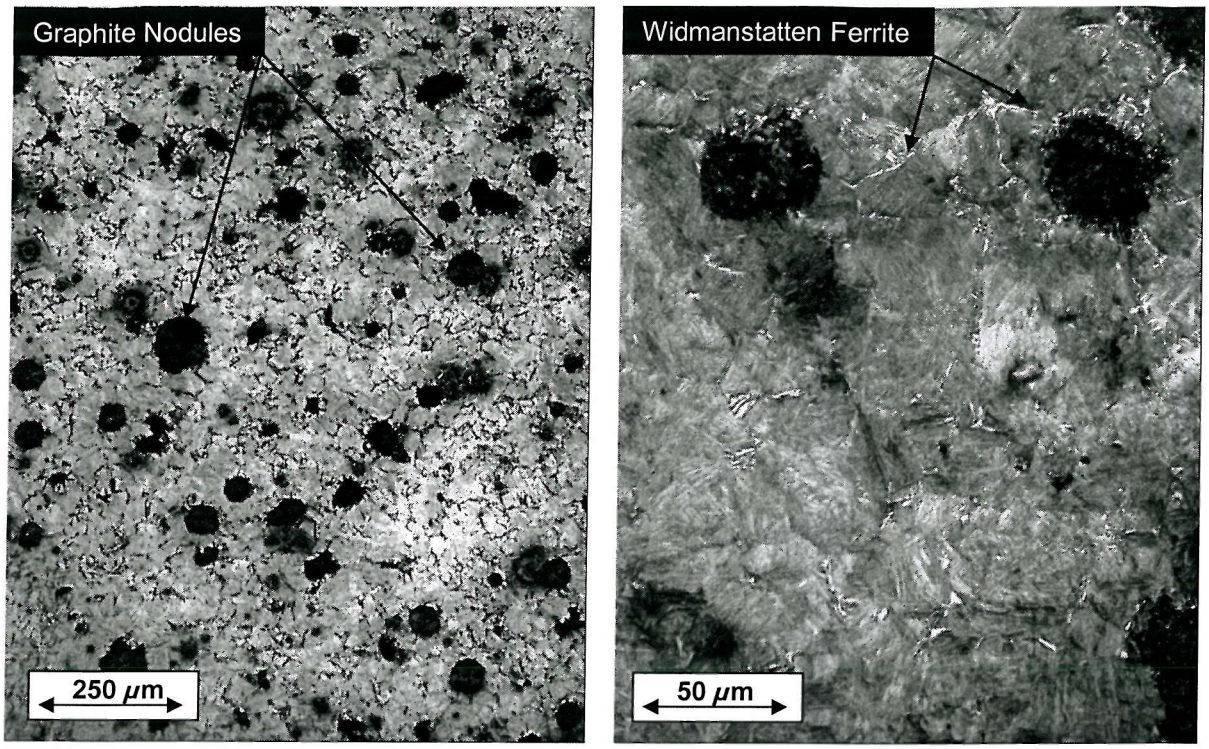

Figure 6.2a & b: '850/250' microstructure at 100x and 500x magnification respectively. Etched in 2% Nital. Predicted microstructure: 18% Retained Austenite & 72% Bainite

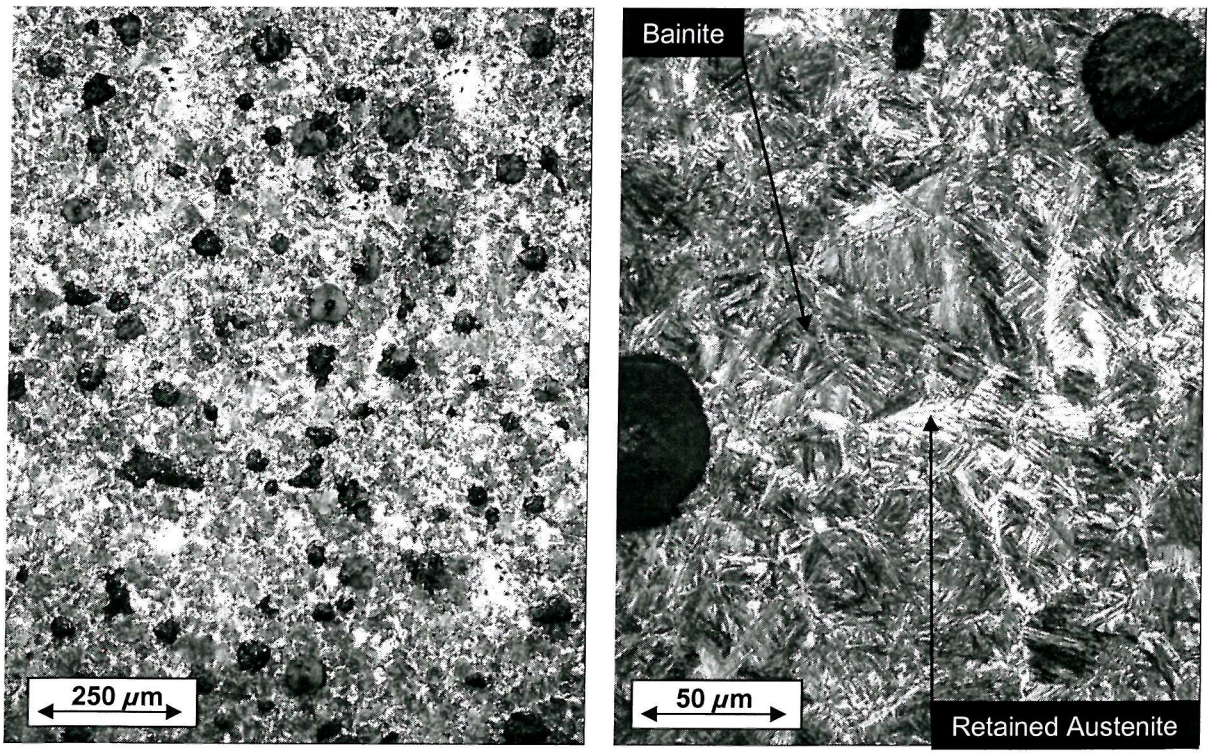

Figure 6.3a & b: '850/400' microstructure at 100x and 500x magnification respectively. Etched in 2% Nital. Predicted microstructure: 32% Retained Austenite & 58% Bainite

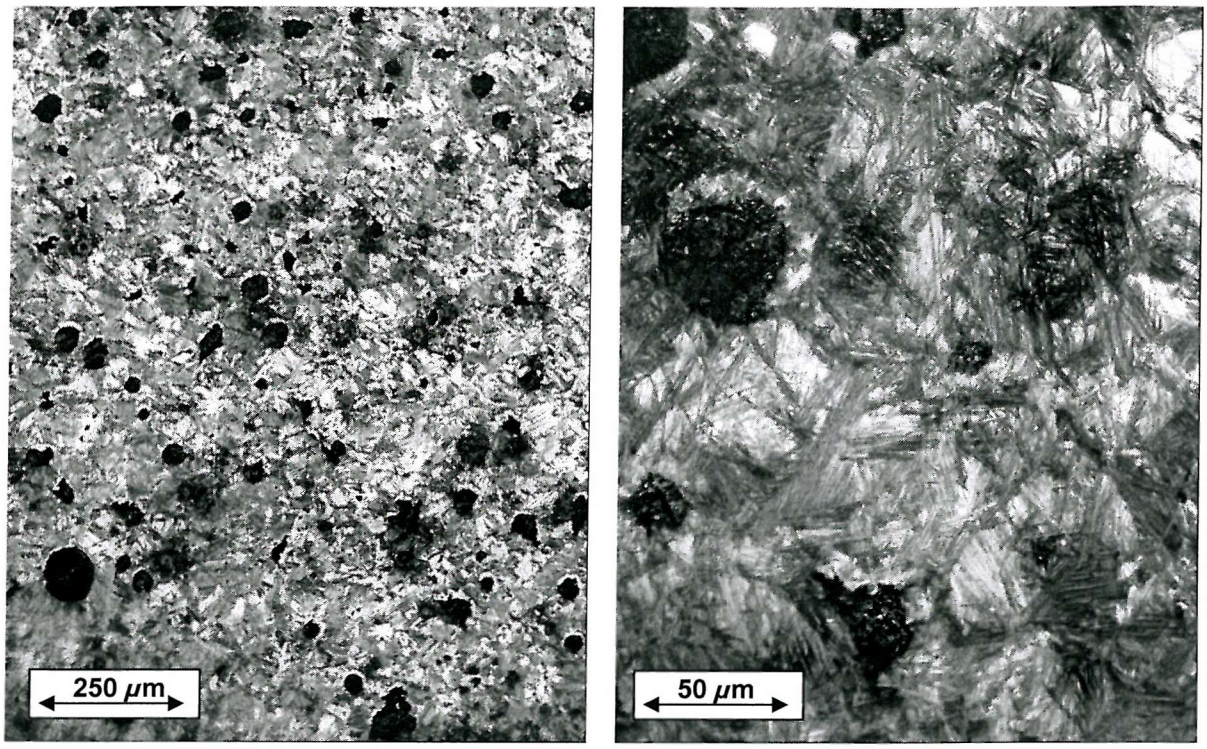

Figure 6.4a & b: '950/250' microstructure at 100x and 500x magnification respectively. Etched in 2% Nital. Predicted microstructure: 25% Retained Austenite & 66% Bainite

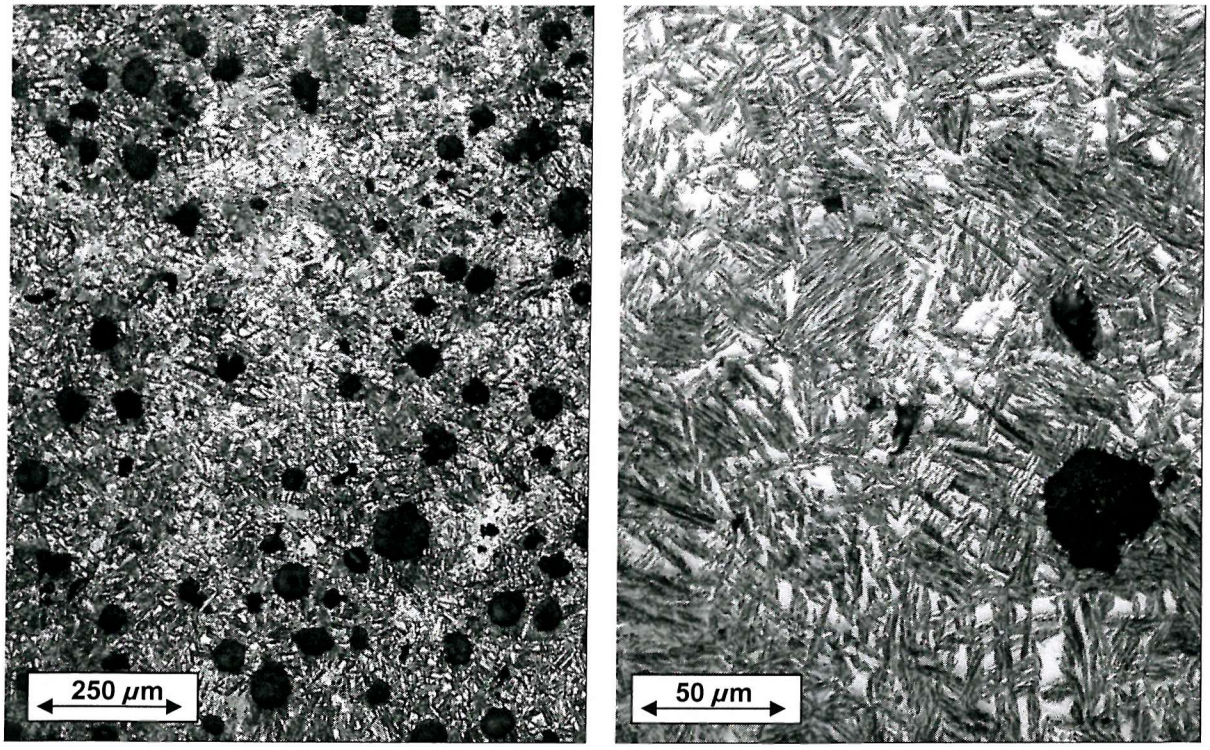

Figure 6.5a & b: '950/400' microstructure at 100x and 500x magnification respectively. Etched in 2% Nital. Predicted microstructure: 45% Retained Austenite & 46% Bainite

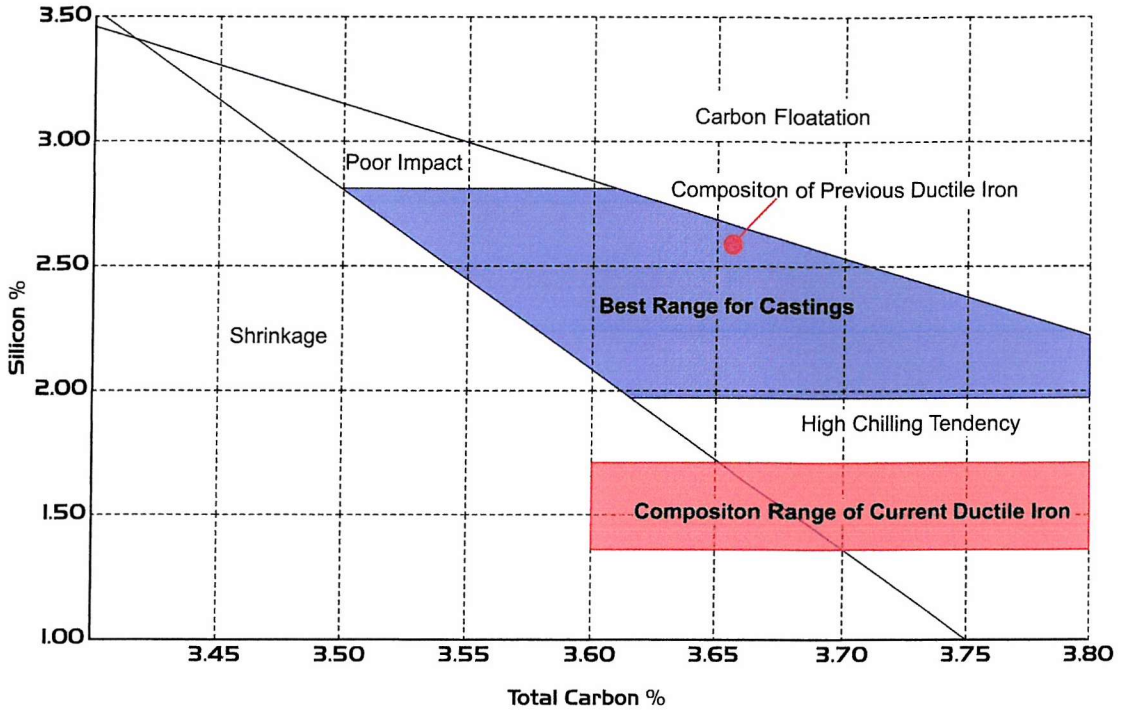

Figure 6.6: Typical carbon and silicon ranges for ductile iron castings [87].

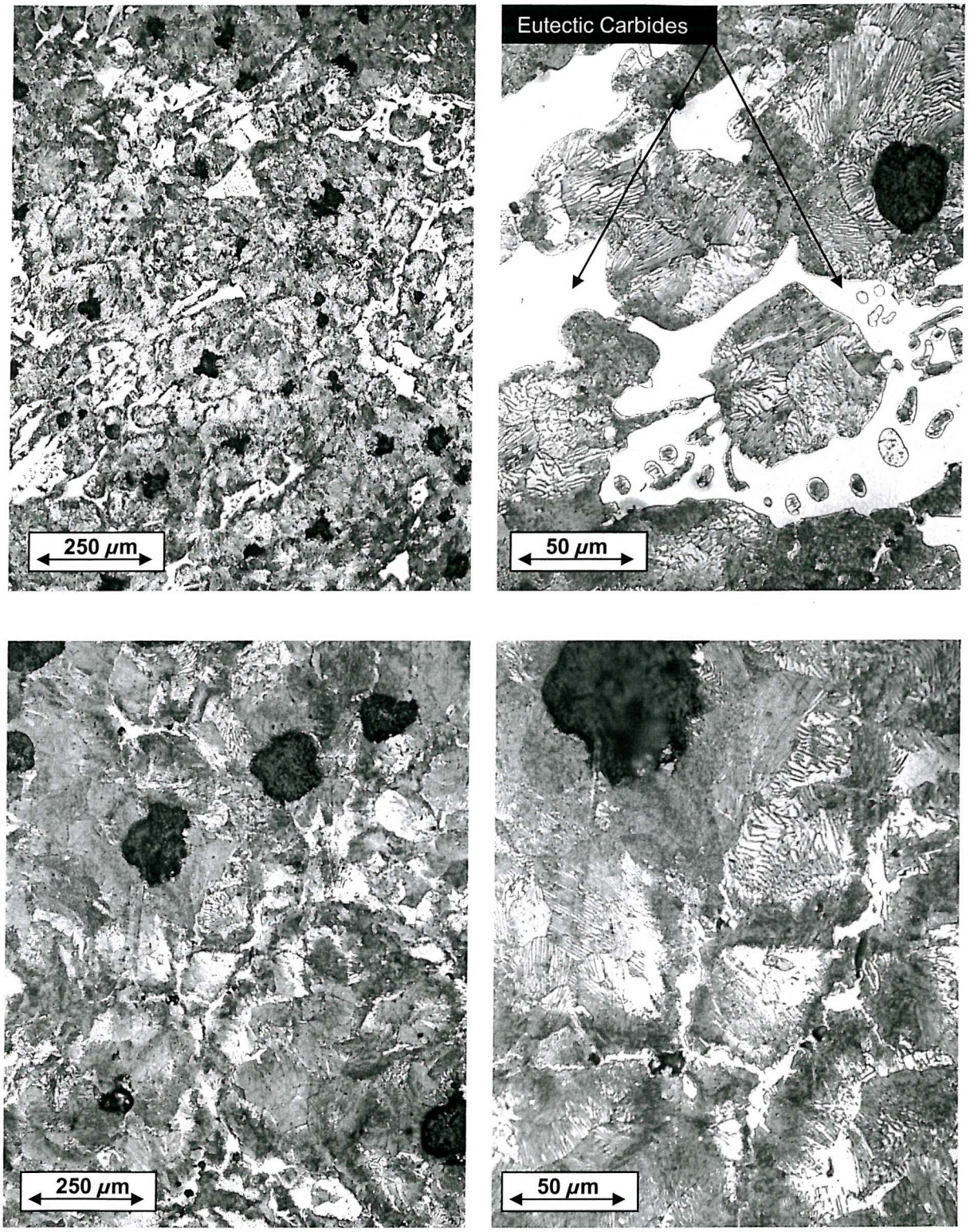

Figure 6.7a, b, c & d: As-cast ductile iron microstructure at 200x and 500x magnification respectively. Etched in 2% Nital. Primary eutectic carbides are clearly visible in 6.7a and b as large white features. 6.7c and d show areas suffering constituent segregation. Also seen is the possible evidence of intercellular carbides mid-distance between graphite nodules.

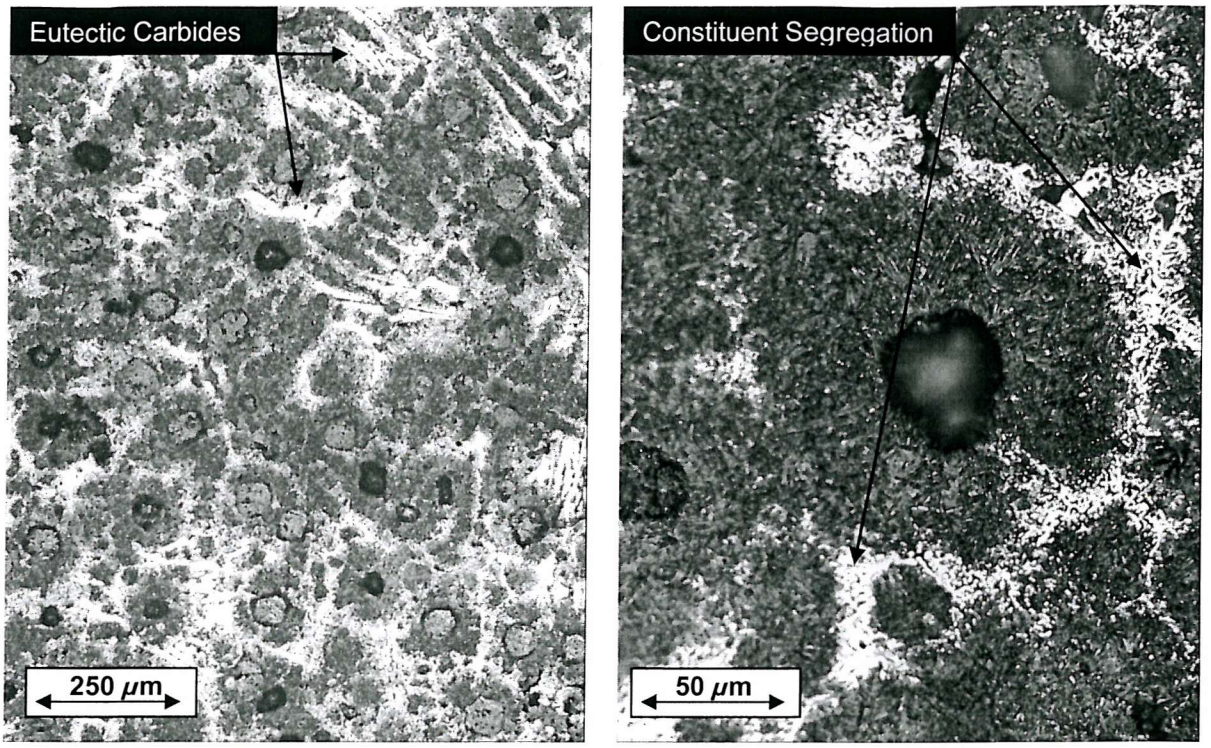

Figure 6.8a & b: '800/260' microstructure at 100x and 500x magnification respectively. Etched in 2% Nital. Predicted microstructure: 19% Retained Austenite & 71% Bainite

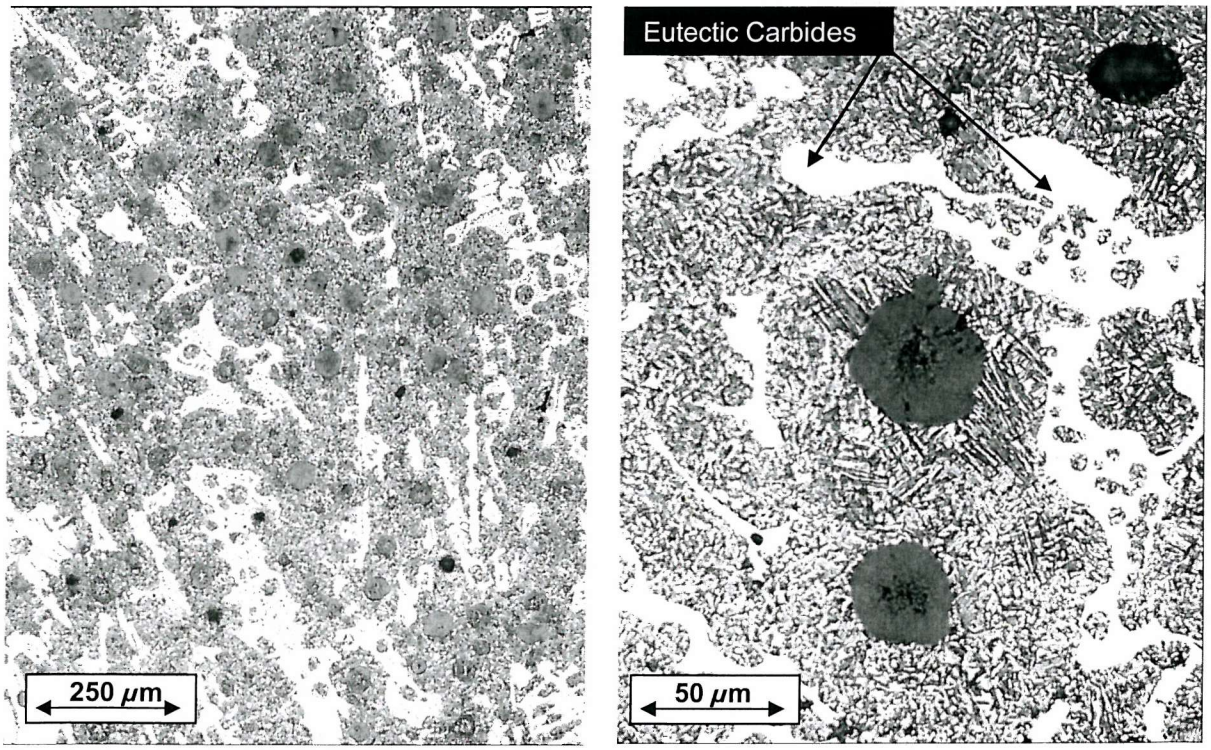

Figure 6.9a & b: '800/390' microstructure at 100x and 500x magnification respectively. Etched in 2% Nital. Predicted microstructure: 31.6% Retained Austenite & 58.5% Bainite

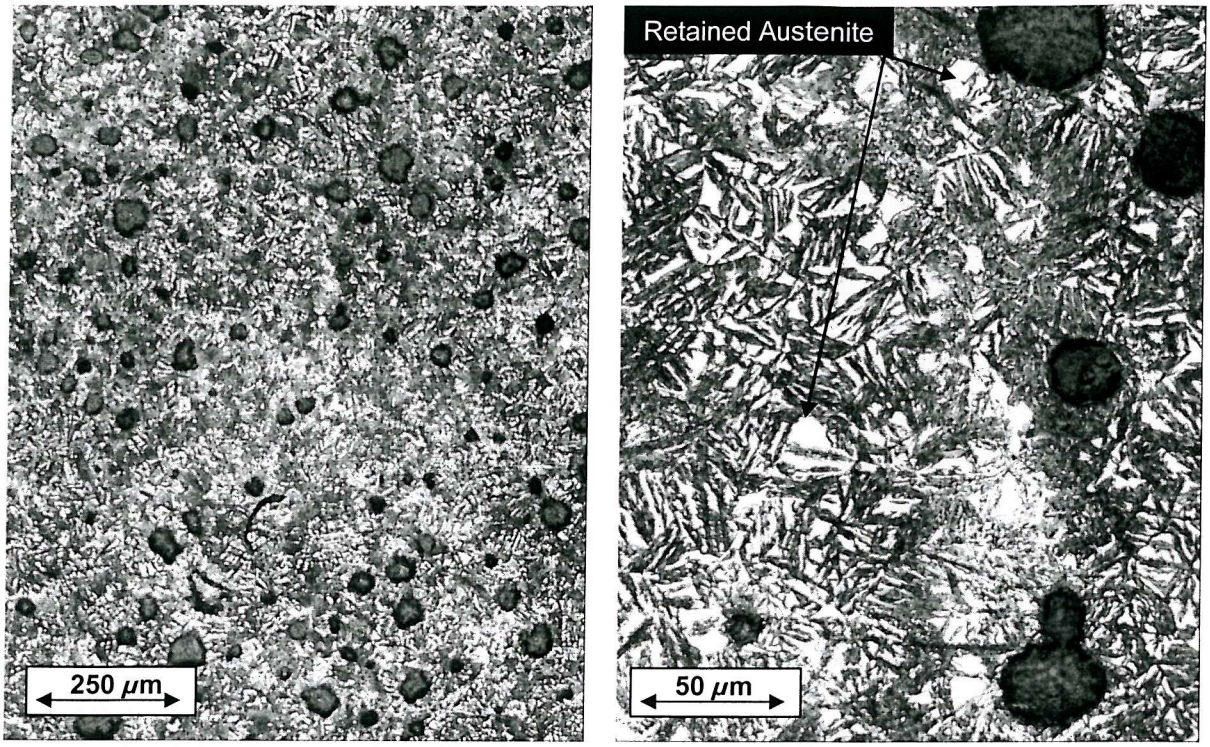

Figure 6.10a & b: '900/390' microstructure at 100x and 500x magnification respectively. Etched in 2% Nital. Predicted microstructure: 44.5% Retained Austenite & 46.4% Bainite

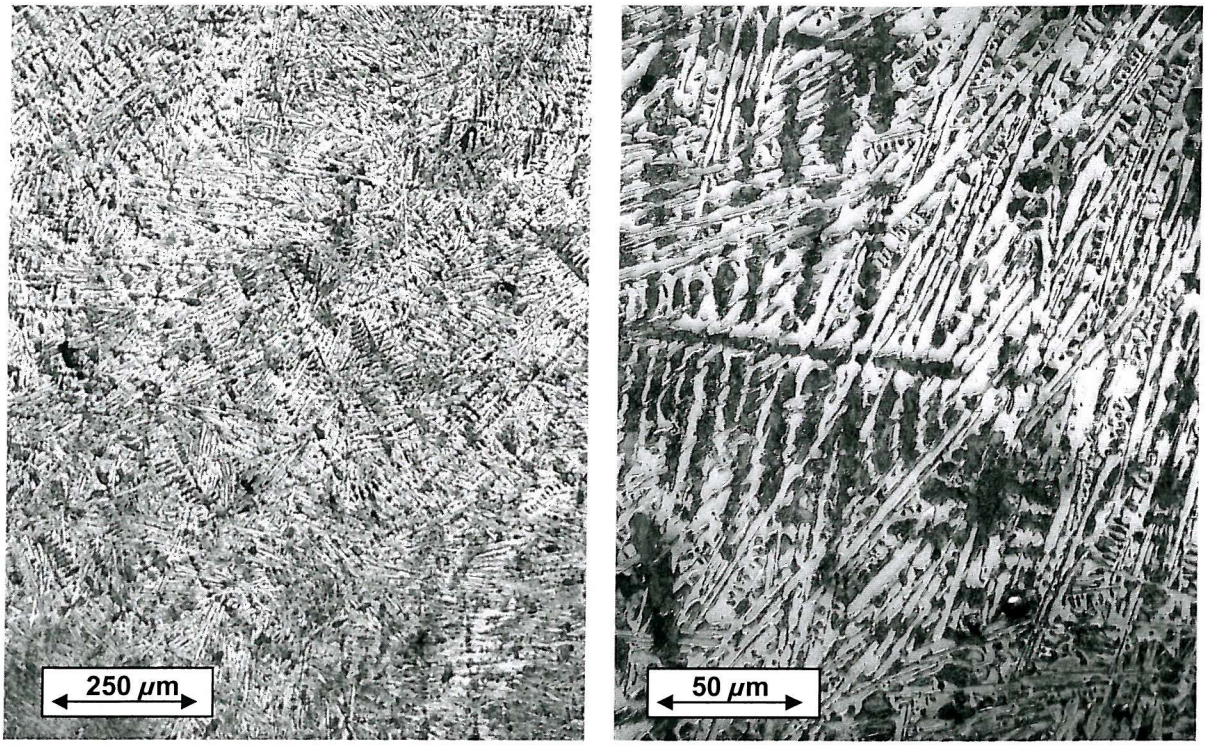

Figure 6.11a & b: Chilled Ductile Iron microstructure at 100x and 500x magnification respectively. Etched in 2% Nital.

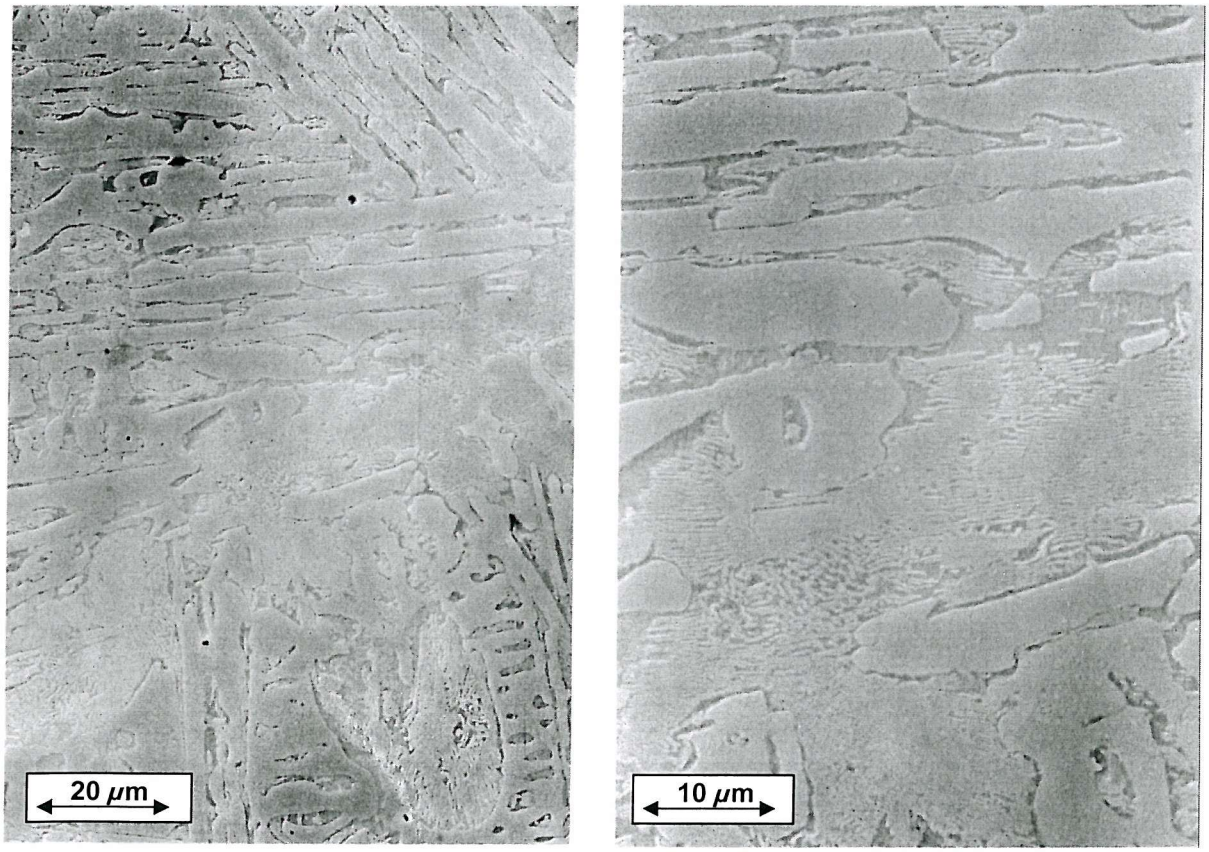

Figure 6.12a & b: Higher magnification images of chilled Ductile Iron microstructure.

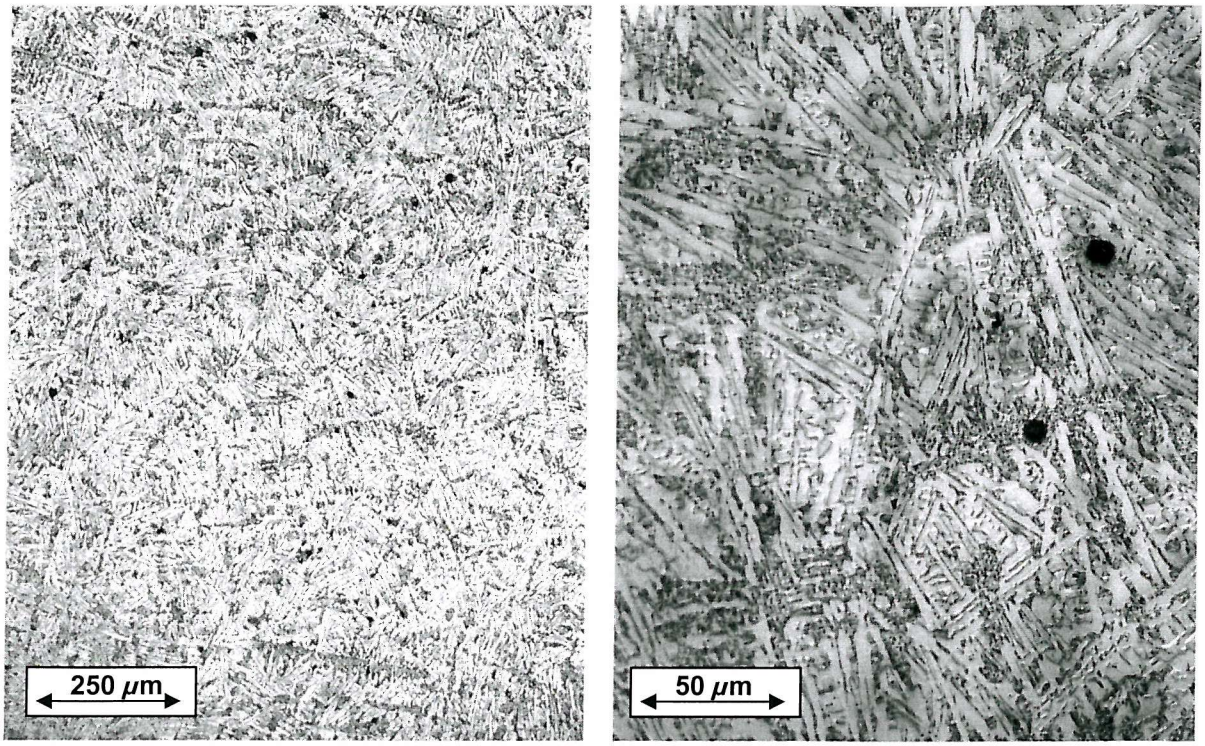

Figure 6.13a & b: Chilled '800/390' ADI microstructure at 100x and 500x magnification respectively. Etched in 2% Nital.

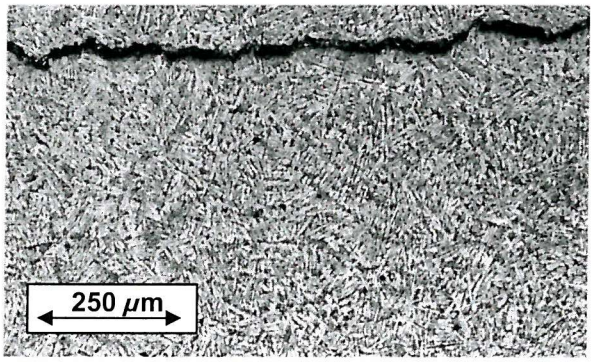

Figure 6.14: Quench crack in chilled '800/390' ADI

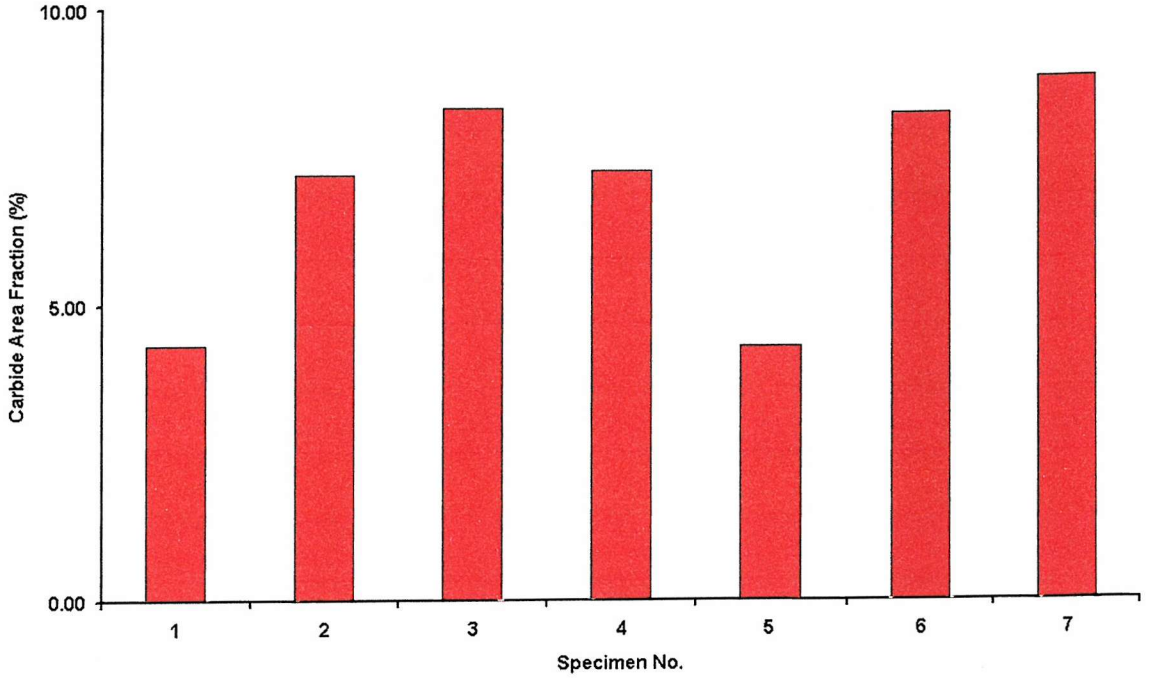

Figure 6.15: As-cast Ductile Iron; Carbide Area Fraction

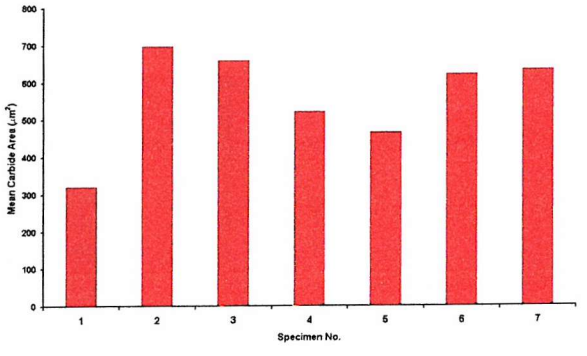

Figure 6.16: As-cast Ductile Iron; Mean O_a

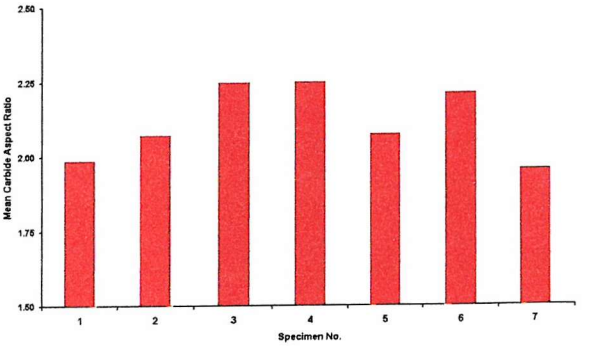

Figure 6.17: As-cast Ductile Iron; Mean O_{ar}

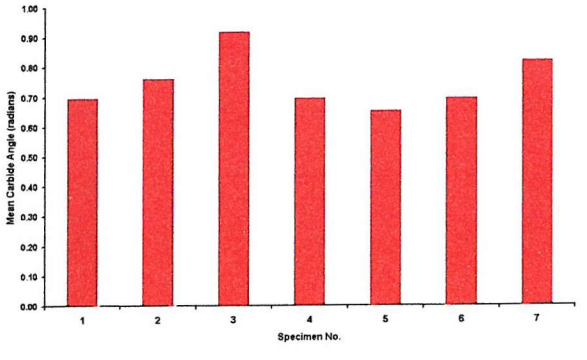

Figure 6.18: As-cast Ductile Iron; Mean O_{ang}

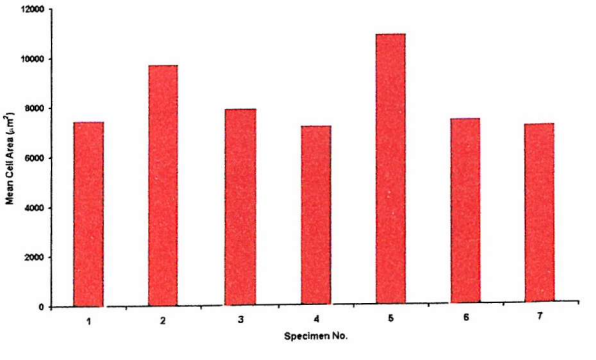

Figure 6.19: As-cast Ductile Iron; Mean C_a

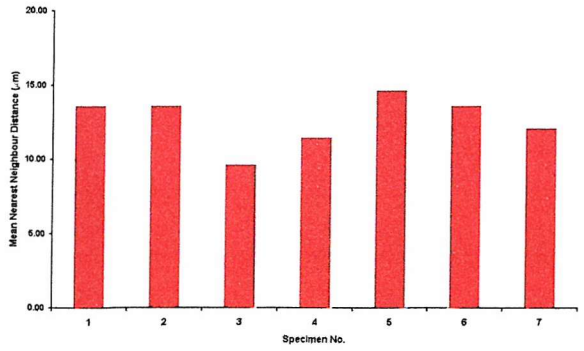

Figure 6.20: As-cast Ductile Iron; Mean D_{min}

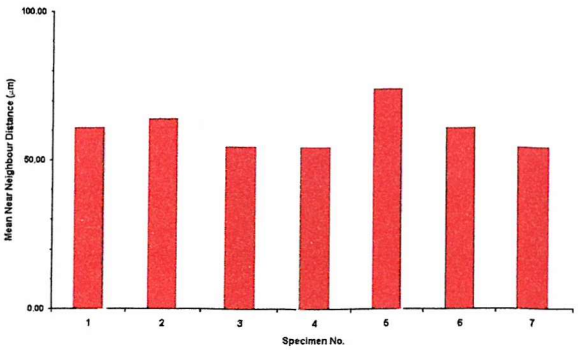

Figure 6.21: As-cast Ductile Iron; Mean D_{mean}

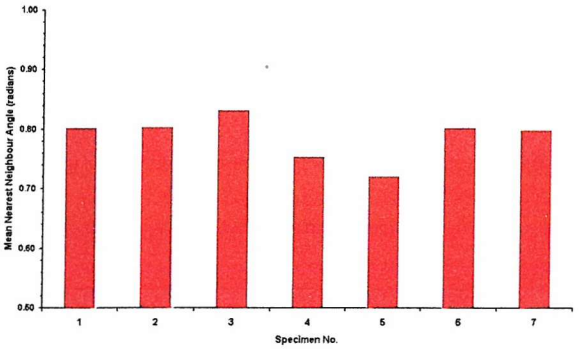

Figure 6.22: As-cast Ductile Iron; Mean NN_{ang}

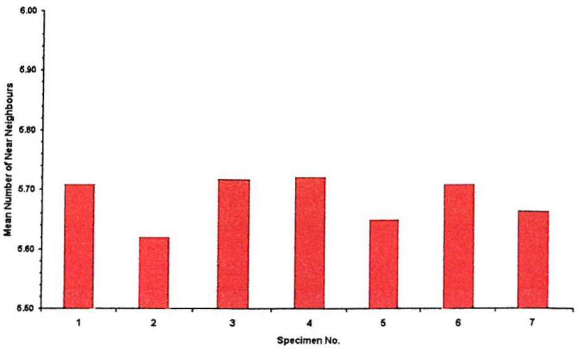

Figure 6.23: As-cast Ductile Iron; Mean Number of Nearest Neighbours

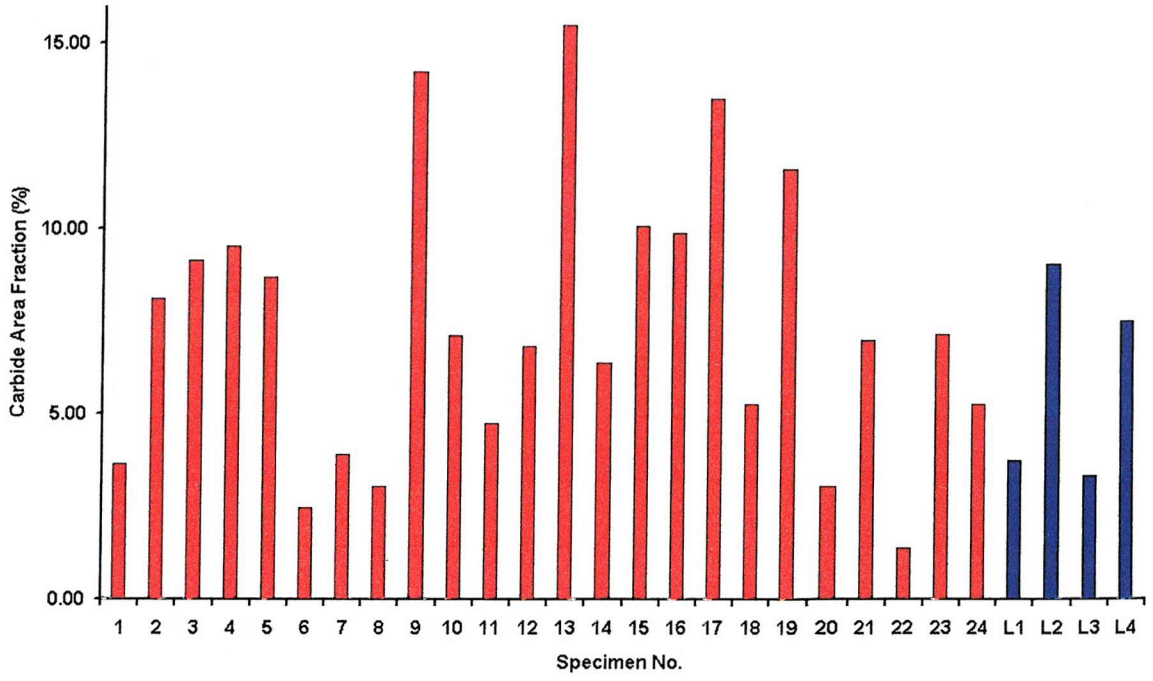

Figure 6.24: '800/260'; Carbide Area Fraction

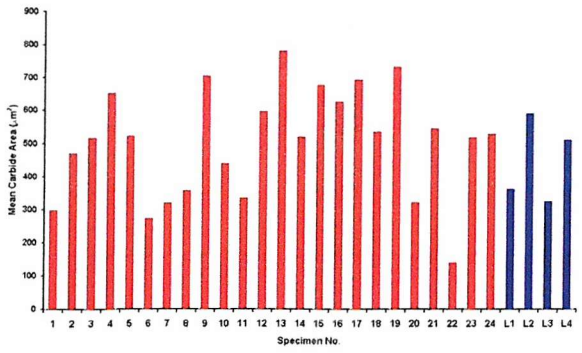

Figure 6.25: '800/260'; Mean O_a

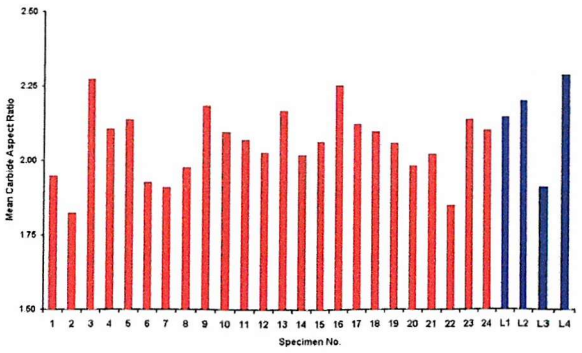

Figure 6.26: '800/260'; Mean O_{ar}

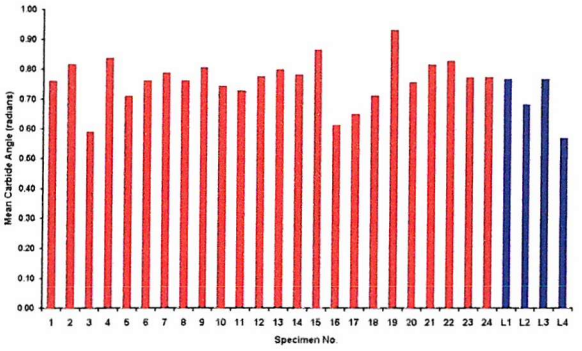

Figure 6.27: '800/260'; Mean O_{ang}

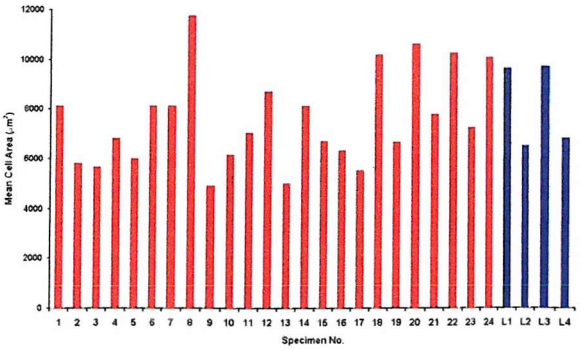

Figure 6.28: '800/260'; Mean C_a

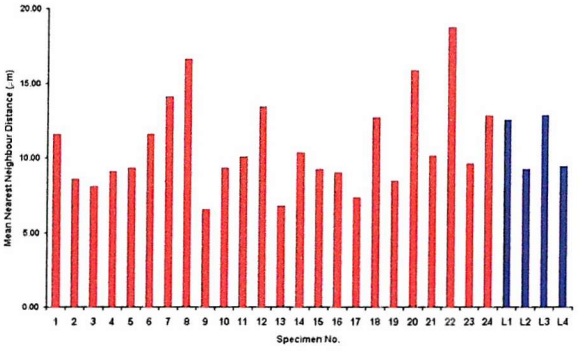

Figure 6.29: '800/260'; Mean D_{min}

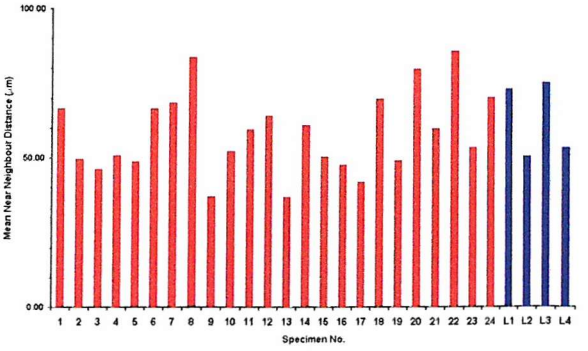

Figure 6.30: '800/260'; Mean D_{mean}

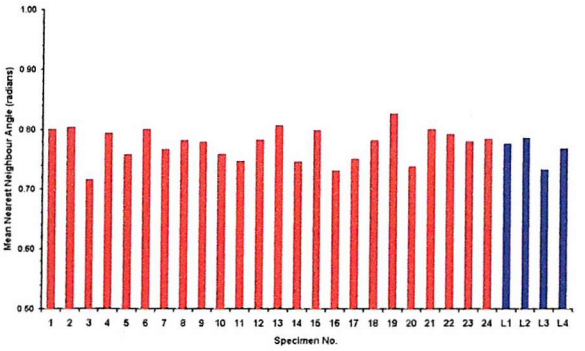

Figure 6.31: '800/260'; Mean NN_{ang}

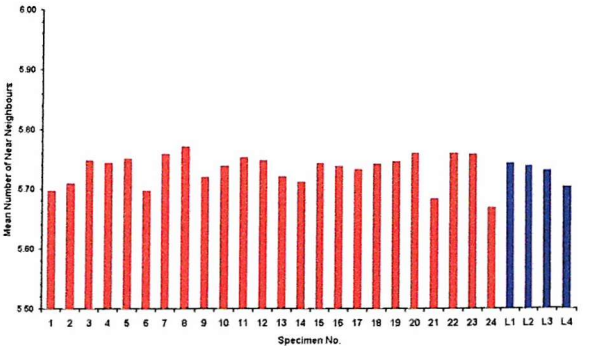

Figure 6.32: '800/260'; Mean Number of Nearest Neighbours

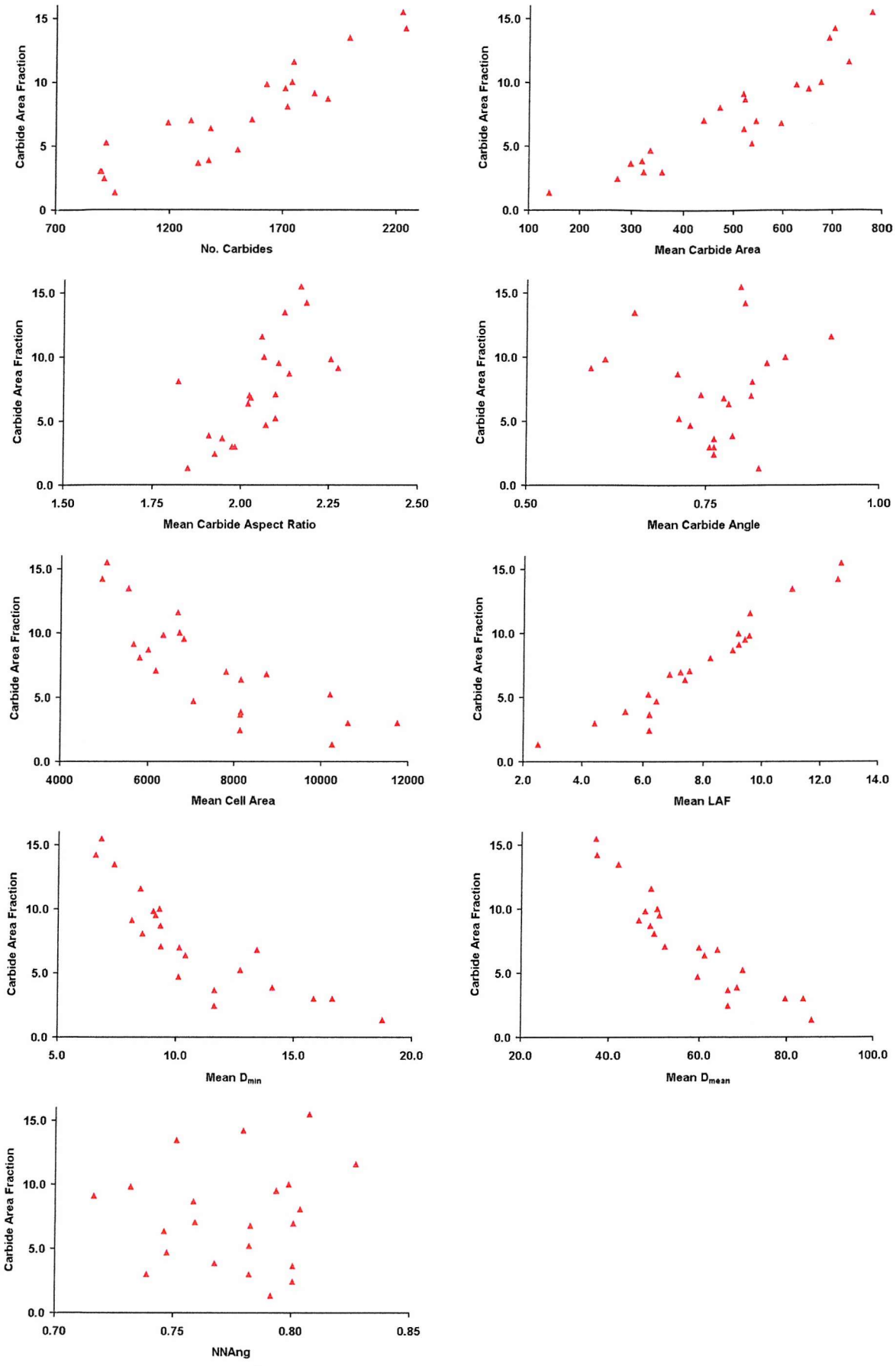

Figure 6.33: Comparison of mean FBT terms with carbide area fraction for '800/260' specimens.

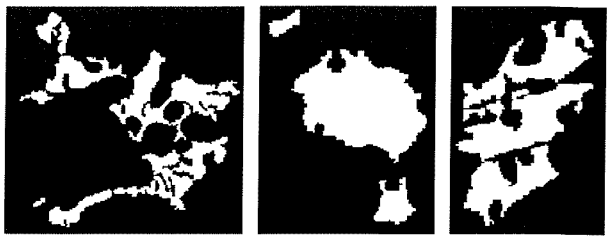

Figure 6.34: Examples of eutectic carbide geometry from binaries images. Note the presence of re-entrant notches.

7 Results

The Loughborough microstructure evolution model has recently been expanded to predict mechanical properties [88]. Predicted values of yield strength and hardness for the currently tested ADI heat treatments are presented in Table 7.1. The '800/260' heat treatment is predicted show the highest hardest whilst the '900/390' variant is the softest. Similarly the heat treatment with the highest predicted yield strength is the '800/260', whilst the lowest yield strength is predicted for the '900/390'.

7.1 Hardness Testing

Figure 7.1 summarises the hardness values of all alloy conditions. For the various ADI heat treatments it can be seen that the lower temperature austempers exhibit the higher hardness values. It is also noticeable that the as-cast ductile iron, lower temperature austempers, and the chilled variants exhibit larger standard deviations in the hardness values. When the coefficient of variation is considered it can be seen that the as-cast ductile iron and the '800/260' ADI heat treatment have conspicuously larger values. It is likely that this is a reflection of the highly variable carbide distribution within these materials. For the case of the '800/260' microstructure, this was analysed in more detail (see section 7.1.3).

The hardness ranking order for the current heat treatments is as follows:

Chilled ductile iron
Chilled 800/390
800/260
800/390
900/390
As-cast ductile iron

It should be noted that hardness tests for the chilled DI were performed on the chilled surface, which will be harder than the base material.

7.1.1 Hardness as a function of ADI microstructure

It is proposed in the literature that the amount of retained austenite present in an ADI microstructure defines the hardness of the alloy. This has been investigated for the previously tested and current ADI microstructures. The volume fractions of retained austenite as predicted by the Loughborough microstructural model have been compared to the hardness of the heat treatment in Figure 7.2. An inversely proportional relationship is seen between hardness and retained austenite volume fraction.

7.1.2 Micro-hardness Testing

Micro-hardness tests were performed on the eutectic carbides present in the as-cast ductile iron, '800/260' and '800/390' heat treatments. The carbides were consistently found to have hardness values in excess of 750 H_V. This relates to an increase in hardness of at least 50% when compared to the surrounding matrix. On a number of occasions it was observed that the indenter cracked the eutectic carbides during testing, as is shown in Figure 7.3. This illustrates the extremely brittle nature of the eutectic carbide.

7.1.3 '800/260' Hardness Mapping

Results from the hardness mapping show a variation in hardness along the length of '800/260' specimens. There is a thirty percent increase in hardness along the length of the specimen. This increase is not linear with respect to distance along the specimen; significant variation is not observed until 50 mm from the origin of the map. The minima peaks indicate where the indenter struck a pore.

The eutectic carbide distribution analysis on the area covered by the hardness map reveals a variation in carbide area fraction similar to that shown by the hardness values. Furthermore, by comparing Figure 7.4 and Figure 7.5 it is clear that regions with proportionally greater carbide area fractions exhibit higher hardness. When related to the position of the specimen in the casting, it was evident that the regions with increased carbide area fraction were at the end of the cast cylinder. The increase in the amount of eutectic carbide is likely to be a result of a faster cooling rate after casting.

The results of the hardness mapping have been used to calibrate a simple prediction of the hardness value of the region above the centre roller (peak applied stress) from carbide area fractions (Figure 7.6). The predicted hardness values of this region for each '800/260' short fatigue crack specimens may be seen in Figure 7.7. It is predicted for example that specimens 9, 13 and 17 are significantly harder than the mean.

7.2 Summary of Short Fatigue Crack Testing

A summary of all short fatigue crack tests can be seen in Table 7.2 and Table 7.3. Observations of the short fatigue crack test replica records have discovered a wide range of damage processes occurring within the various alloy conditions. Multiple cracks were observed on nearly all specimens. Furthermore, many specimens showed extensive crack interaction and coalescence events. The extent, number and density of coalescence events appeared critical in determining the fatigue lifetime of a specimen at any applied stress level. When the number or density of individual micro-cracks was low, the failure mechanism was dominated by crack propagation with a minimal influence of coalescence events. Conversely, when the number or density of micro-cracks was high, the growth of the dominant crack was strongly influenced by coalescence events and interactions with neighbouring cracks.

The '800/260' heat treatment showed the greatest range of crack coalescence events, both in number and density. The as-cast ductile iron also showed a similar variability in behaviour though not to the same extent. Failure mechanisms in the '900/390' condition were almost entirely propagation dominated. However, at the highest applied stress level, crack coalescence due to initiation ahead of the dominant crack tip was observed.

It was felt an understanding of the mechanisms behind these failure processes was critical in determining the fatigue behaviour of the group of alloy conditions under current investigation. The '800/260' and '900/360' microstructures were chosen for the most rigorous testing and analysis since it was felt that these two microstructures describe the range in failure mechanisms sufficiently to be applicable for all alloy conditions. As an improvement over the existing camshaft

material is sought, the as-cast ductile iron will be used as a baseline for the other alloy variants to allow critical comparison.

7.2.1 Short Crack Lifetime Comparison

A classic method for simple, first stage analysis of short fatigue crack testing is to plot a graph of the test specimen lifetime (in term of the number of cycles to failure) as a function of the maximum applied stress. Figure 7.8 summarises the results from short crack testing at an R-ratio of 0.1 for the five current microstructures.

For tests performed at common stress levels the ranking order for alloy variants is as follows:

900/390

800/260

Ductile iron

800/390

Chilled ductile iron

Chilled 800/390

Specimen preparation revealed extensive quench cracking on the surface of all chilled '800/390' specimens. The existence of these quench cracks provided very large pre-existing defects that rendered short fatigue crack testing non-comparable with the other materials that contained no such gross defects. Whilst large quench cracks were present on one ductile iron specimen, the remaining specimens appeared free from such defects.

The best fatigue performance in terms of number of cycles to failure at a given applied stress level was shown by the '900/390' heat treatment. Typical fatigue behaviour is observed where increasing lifetime is a product of a decrease in applied stress. It is particularly noteworthy that no failure occurred when a '900/390' specimen was tested at a maximum stress of 500 MPa with an R-ratio of 0.1. No other alloy variant could match this fatigue limit.

High R-ratio tests (R=0.5) were performed on '900/390' specimens. No failure was observed after 10 million cycles for a specimen tested at a maximum stress of 800

MPa. Further R=0.5 tests were therefore carried out at higher maximum stress levels. Failure occurred at approximately 32000 - 43000 cycles for R=0.5 tests with a maximum applied stress of 1100 MPa. When this is considered in terms of applied stress range it becomes apparent that these R=0.5 tests with a stress range of 550 MPa exhibited shorter lifetimes than R=0.1 tests with a stress range of 630 MPa. This implies that lifetime is dependent on absolute stresses as well as applied stress range, with shorter lifetimes being shown for higher overall stresses and higher applied stress range in the '900/390' microstructure. No further R=0.5 tests were performed since it was identified that R=0.1 was more representative of the service condition.

The next ranked alloy condition, in terms of fatigue lifetime is the '800/260' treatment. A large degree of scatter is apparent in the lifetime data for the '800/260' short fatigue crack specimens. Furthermore, overlapping performance between applied stress levels can be observed, such that some specimens exhibit longer lifetimes than those tested at a maximum stress of 100 MPa lower. The greatest amount of scatter is observed for tests performed at a maximum stress of 600 MPa. Specimen '800/260:22' showed the longest lifetime (N_f ~ 84000 cycles) and was comparable to '900/390' specimens tested at the same applied stress levels. The shortest lifetime was exhibited by specimen '800/260:17 (N_f ~ 9900 cycles) and was no better than the as-cast ductile iron. At no other applied stress level did the '800/260' compare to the '900/390' condition. The causes of the considerable range of scatter in the lifetimes of '800/260' short fatigue crack specimens has been subject to lengthy analysis which is detailed in latter sections of this chapter. Preliminary investigations revealed an approximate relationship between carbide area fraction, applied stress level and lifetime. The results of this simple quantification may be seen in Figure 7.10. It can be observed, that at all stress levels a high area fraction of eutectic carbide is deleterious to the lifetime of a specimen. The relationship is at its most apparent for specimens tested at 600 MPa. No failure occurred for this alloy condition when tested at a stress level of 300 MPa.

The short fatigue crack performance in terms of number of cycles to failure of the '800/390' specimens was relatively poor when compared to the other ADI heat

treatments. Tests executed with maximum applied stresses of 700 MPa and 600 MPa both failed before the completion of a single cycle. Additionally, the fatigue lifetime at a maximum stress of 400 MPa was approximately 3000 cycles. This compares to 300,000 cycles for the '800/260' condition and below the fatigue limit for the '900/390' condition.

Short crack fatigue testing of the chilled ductile iron revealed a large range of performance. No crack initiation after 10,000,000 was observed at a maximum applied stress of 250 MPa on two occasions. However, failure at 450,000 cycles was observed at a test with a maximum stress of 200 MPa. Observation of this failed specimen revealed the possible presence of very small quench cracks. This seems reasonable as many large quench cracks were also observed on an untested specimen.

7.3 Fatigue Crack Initiation Mechanisms

Essentially two mechanisms of short fatigue crack initiation were observed for the materials subject to the current investigation. Firstly, in materials where they were present (as-cast ductile iron, '800/260', '800/390') eutectic carbides were observed to fracture, often on the first fatigue cycle. These cracked carbides would subsequently nucleate micro-cracks. Secondly, in the '900/390' heat treatment, which was predominately free of eutectic carbides, initiation of the fatigue crack ultimately causing failure was seen at micro-shrinkage pores.

7.3.1 Eutectic Carbide Based Short Fatigue Crack Initiation

Short fatigue crack initiation sites for the as-cast ductile iron were unambiguously identified from etched specimens and occurred predominantly at eutectic carbides. In the case of the '800/260' and '800/390' ADI heat treatments, eutectic carbides remain from the as-cast material and proved to be responsible for the initiation of the majority of micro-cracks, except in some rare circumstances where porosity was responsible for crack initiation. The eutectic carbides, being very brittle, cracked easily, and as seen in Figure 7.12 the cracking was not always in perpendicular to the applied tensile axis. Subsequent nucleation of micro-cracks into the matrix was rapid.

For '800/260' short fatigue crack tests performed above a maximum applied stress of 500 MPa, the first initiation events were seen on application of mean load prior the cyclic loading. The number of eutectic carbides that cracked on initial loading is variable, ranging from 1 to 400, and appears to control the regime of fatigue failure. Consequently, this characteristic of the '800/260' heat treatment has been the focus of a large amount of investigation. Further initiation occurred throughout the lifetime of a specimen (see section 7.4.1). Initiation sites were always eutectic carbides.

7.3.1.1 Extent of Crack Initiation in '800/260' Short Fatigue Crack Specimens

Figure 7.14 shows the extent of carbide cracking on initial loading to mean stress in '800/260' short fatigue crack specimens and is correlated to final fatigue life. Crack density was determined from replica records by counting the number of cracks in 50 MPa regions either side of the axis of peak applied stress (see Figure 7.15). Tests performed at a maximum stress of 500 MPa or less failed to crack carbides on initial loading to mean stress. Cracked carbides were however observed on the replicas taken at the first interval (approximately 10000 fatigue cycles) for all of the 500 MPa tests. It can be seen there is significant variability between specimens particularly for specimens tested with a maximum stress of 700 MPa. Furthermore, it appears in general, that the number of cracked carbides on initial loading has a significant effect in determining the lifetime of a short fatigue crack specimen; the higher the number of cracks on initial loading, the shorter the fatigue lifetime.

7.3.1.2 Crack Initiating Eutectic Carbide Characterisation

The characterisation of crack initiating eutectic carbides was undertaken in the '800/260' specimens showing the largest number of micro-cracks. Individual crack initiating eutectic carbides were assessed and compared to the background population using the finite body tessellation (FBT) approach described in section 5.3.3. The analysis was performed after specimen fracture. Therefore the measurement of which eutectic carbides cracked along the dominant crack that caused failure was not possible although separation of which carbides cracked on initial loading and which cracked later in the fatigue lifetime was determined from comparison with the replica record.

Simple comparisons between cracked carbides and the background population in terms of means and standard deviations of the FBT parameters are summarised in Table 7.4. It is apparent that there is significant difference in means between the two classes when regarding carbide area, carbide aspect ratio, cell area, local area fraction, number of near neighbours, and mean near neighbour distance although significant scatter is observed. Therefore, as a first approximation, large carbides that tend towards a long and thin profile with a high local area fraction show a greater probability of fracture. The remaining tessellation parameters show little apparent difference between the cracked and non-cracked classes.

The tessellation parameters showing the most significant variation have been plotted as histograms in Figure 7.16 to Figure 7.21 to compare population differences in more detail. Figure 7.16 shows the variation in distribution of carbide area between cracked eutectic carbides and the background population. In general, carbides that cracked are larger than the background population. Figure 7.17 shows little obvious variation in carbide aspect ratio populations, whilst Figure 7.18 suggests that cracked carbides tend to exhibit larger cell areas. Figure 7.19 shows cracked carbides tending towards larger local area fractions. Furthermore, Figure 7.20 shows the cracked carbide population distribution is skewed to a larger number of near neighbours than the background population. This suggests that clustering of carbides is deleterious to the initiation resistance of the '800/260' heat treatment. Figure 7.21 however, counters this statement by suggesting that cracked carbides have, perhaps in general slightly larger mean near neighbour distances.

It is obvious that cracked carbides show differences from the general population. Furthermore, it is probable that the factors contributing to the failure of these carbides are a complex function of multiple parameters. An adaptive numerical modelling approach has been used to investigate this further and is detailed in section 7.3.1.3.

7.3.1.3 Classification of Carbide Based Crack Initiation Using the SUPANOVA Approach

It is clear that the mechanism of crack initiation via eutectic carbide fracture is likely to be dependent on a factor of more than one of the parameters gathered

from tessellation analysis. The simple first stage analysis of the previous section does not give a wholly satisfactorily explanation of the micro-crack initiation process. Therefore, an adaptive numerical modelling approach was used to further interpret the large amount of tessellation generated data and to assess all possible combinations of these tessellation parameters. The classification approaches developed by Southampton University for considering fatigue initiating features in conventional ADI [84] and Al Sn [89] alloys were adopted for the particular requirements of this thesis. This classification approach uses a modified adaptive numerical modelling (ANM) technique, based on support vector machines with a parsimonious ANOVA representation (SUPANOVA) [90].

Many modern approaches to classification and regression problems have employed support vector machines. The predictive models produced by this approach may accurately classify behaviour (e.g. 100% successful classification of those carbides associated with crack initiation) but the complex relationships produced are hard to use when assessing the physical mechanisms (e.g. why do these carbides cause initiation?). These complex models sacrifice the interpretability of a model in order to obtain a high classification rate and are referred to as having a lack of transparency. A method of introducing transparency to model is to use the SUPANOVA approach. The result is a predictive model that retains a high degree of interpretability and should provide a mechanistic insight to allow physically based optimisation of the process in question.

In order to quantify the process of crack initiation in '800/260' short fatigue crack specimens a comparison was made between cracked carbides and the background population in the specimen exhibiting the greatest amount of crack initiation. Tessellation data for 1236 carbides was gathered. This data was divided into two classes; cracked carbides and the background population. With 78 carbides in the cracked class and the remaining 1158 carbides making up the background population, this represents a rather imbalanced data set. In order to prevent a bias operating for the heavily represented class differing misclassification costs and a Geometric mean (G_{mean}) where used. A Geometric

mean favours a balanced classification by measuring the square root of the product of the class classification rates. This is described in detail in Lee et al [91].

7.3.1.4 Application of the SUPANOVA Classification

The following approach was applied to both methods of quantifying crack initiating carbides detailed in the previous section. The normalisation of the eleven tessellation parameters between 0 and 1 avoided bias for any particular feature. The data was partitioned into training and testing sets. For the comparison of individual carbides approach 45% of data was used for training, with the remainder used for testing. A good classification performance was obtained by tuning the misclassification costs (based on G_{mean} of the unseen data) using the pure support vector machine approach. This partitioning of data was performed ten times with a random selection of the training and testing data on each occasion. This provided ten models.

The model was run using nine of the eleven tessellation parameters since it was felt that cell aspect ratio and cell angle do little to describe the distribution of a carbide population. The full ANOVA decomposition of the nine tessellation parameters has 512 (2^9) possible terms. It was possible however, to reduce this number of terms without greatly compromising overall performance by using the sparse representation approach of the ANOVA decomposition within the SUPANOVA process.

7.3.1.5 Selected Features in the Comparison of Individual Carbides

For the comparison of individual carbide approach, the 512 terms were reduced to just five. These can be seen in Table 7.6. The sparse representation model gave a successful cracked carbide classification rate of 78%, a successful 'non-crack' classification of 86% and an overall classification performance based on the mean and variance values of G_{mean} for each of the ten data set runs of 82% and 0.009% respectively. A low variance indicates similar values of G_{mean} for each of the ten models.

Figure 7.22 and Figure 7.23 represent the relationships suggested by the SUPANOVA model and are shown with the corresponding data spread for the term(s) selected. The spread of data has been considered when interpreting the

SUPANOVA model and is discussed further in section 8.4.3. As shown in Figure 7.22:A, the first term selected by the SUPANOVA model is the univariate relating increasing cell area with the increasing probability of an individual carbide cracking. The second univariate relationship to be picked out by the classifier was the increasing probability of crack initiation with an increase in local area fraction and is shown in Figure 7.22:B. These two relationships were picked out by all of the ten data-set sampling runs. The only other univariate selected was the decreasing likelihood of crack initiation with increasing nearest neighbour distance (Figure 7.22:C). This term was selected by nine out of the ten data-set sampling runs.

The following bivariates were selected by the classifier; carbide angle vs. local area fraction (Figure 7.23:A); and carbide angle vs. nearest neighbour angle (Figure 7.23:B). Only the first of the above bivariate terms was selected by all of the data-set sampling runs. The relationship described by this term sees an increase in the probability of crack initiation with an increase in carbide angle and local area fraction. The second bivariate (selected on six out of ten occasions) describes a decrease in crack initiating probability with an increase in carbide angle and nearest neighbour angle.

7.3.2 Porosity Based Short Fatigue Crack Initiation

Without the presence of eutectic carbides, initiation of the dominant fatigue crack for '900/390' short crack tests occurred exclusively at pores, present either on the surface (Figure 7.24) or immediately below (Figure 7.25). Generally speaking these pores are angular in morphology and hence act as significant stress raisers. Evidence of initiation was present on the first replica for all tests performed at a R-ratio of 0.1 suggesting a rather easy initiation stage seemingly not affected by magnitude of applied stress particular to the range of short fatigue crack tests performed on these alloy conditions.

Further initiation events occurred ahead of the propagating dominant crack tip throughout the lifetime of the specimen. Initiation occurred at decohering graphite nodules (see Figure 7.26 and Figure 7.27 regions B to F). The extent of initiation ahead of the crack tip appears to be controlled by the applied stress level, length of the crack, and ultimately ΔK. This is discussed further in section 7.4.3.1.

7.4 Short Fatigue Crack Propagation Mechanisms

The presence or lack of eutectic carbides and the associated crack initiation mechanisms lead to differing fatigue damage mechanisms between the various alloy conditions. The wide variation in number and location of crack initiation events in the as-cast ductile iron and '800/260' heat treatments gave an equally wide range in resistance to fatigue. The '900/390' heat treatment exhibits more conventional short fatigue crack propagation from far fewer, more separated initiation sites.

7.4.1 Propagation of Eutectic Carbide Initiated Short Fatigue Cracks

The '800/260' (and to a lesser extent the as-cast ductile iron) short crack specimens exhibited a wide range of fatigue performance at all stress levels. The wide degree of scatter in the number of primary initiation sites (i.e. initiation events caused by the application of an external load and not attributable to the influence of neighbouring cracks) resulted in a large variability in the number and distribution of individual micro-cracks which in turn has a direct effect on the number of coalescence events and crack interactions suffered by each specimen. At the extremes of behaviour two distinct mechanisms have been observed. Firstly when the primary initiation sites were low in number or widely distributed, fatigue crack propagation of a dominant crack leading to failure could occur with little interference from neighbouring cracks. There have not however, been any incidents where crack propagation has occurred without coalescence events in these specimens. This mechanism will be referred to as propagation dominated. When the number of initiation sites was high or the distribution of initiation sites was such that there was a clustering of micro-cracks, a more coalescence affected regime was observed. In this regime the growth of the dominant crack/s was strongly affected by multiple coalescence events. It is believed that in this coalescence affected regime, crack shielding and crack interactions are significant in determining local crack growth rates and overall lifetime. This mechanism will be referred to as coalescence dominated. Generally speaking, in the majority of specimens both regimes co-exist.

Short crack initiation and subsequent coalescence behaviour was investigated by generating detailed maps of the '800/260' short fatigue crack specimen showing

the largest number of micro-cracks and hence greatest extent of the coalescence dominated regime. Images of replicas were captured at 0 cycles, 250 cycles, 1000 cycles, 2000 cycles, and 3250 cycles. Since these tests were performed using a three-point bend set up (giving a stress gradient along the top surface), the relationship between stress and initiation and early growth could be analysed. Regions that represent finite stress ranges were calculated and identified using a travelling microscope stage. These stress regions can be seen in Figure 7.28. Figure 7.29 shows the results of crack counting within these defined stress regions. It can be observed that the number of cracks per stress region increases by approximately 10% with each 25 MPa range of increasing stress with the exception of the 675 MPa to 700 MPa region. Also visible is the increase in crack population for all stress regions from 0 to 250 cycles. After this point in the specimen lifetime, there is a gradual decrease in the number of individual micro-cracks until final failure. This decrease in crack population is an indication of the extent of crack coalescence.

On occasions, crack propagation was sufficient to allow reasonable measurements of crack length between coalescence events. The data from short crack specimens 'DI:03' and 'DI:05' can be seen in Figure 7.30 and Figure 7.31. The cracking of a carbide results in a large initial crack length (e.g. 115 μm for test 03 and 240 μm for test 05). Crack growth data has been plotted for '800/260' short fatigue crack specimens and can be seen in Figure 7.32. Crack growth is generally faster for tests performed at higher values of applied stress at comparable crack lengths. However, there is a wide range of scatter and a certain amount of overlap between stress levels can be observed. Tests 06 and 16 were performed at maximum applied stresses of 600 MPa and 500 MPa respectively. From Figure 7.32 it can be seen that crack growth for these two tests is reasonably comparable. The crack growth curves for these short fatigue crack tests, are not smooth and tend to exhibit 'jumps' and periods of rapid acceleration. This may be directly attributable to multiple crack initiation sites, which lead to greatly increased crack growth rates when cracks coalesce. When crack length is plotted against normalised lifetime (Figure 7.33) the fatigue behaviour exhibited by the specimens at all stress levels for a given fraction of lifetime is similar with the exception of test 05. The crack growth for this test is quite erratic, a feature

reinforced in Figure 7.34. In Figure 7.35 we can see crack growth rates plotted as a function of ΔK for all '800/260' short fatigue crack replica tests. All tests exhibit classical short crack behaviour. There is a wide scatter band of crack growth rates for a given ΔK with numerous crack retardation events visible. As ΔK increases it is possible to observe the data approaching the more consistent crack growth behaviour indicative of the long crack regime. This is particularly obvious for tests 05 and 11. Furthermore, it can be observed that crack growth rates are lower at comparable values of ΔK for '800/260' specimens than for the as-cast ductile iron.

7.4.2 Comparison of '800/260' Carbide Populations

It is clear from the previous section there is a range of fatigue failure in the '800/260' microstructure. The specimens with the poorest fatigue performance exhibited the greatest magnitude of coalescence dominated failure for that stress level. Conversely, the specimens with the longest fatigue lifetimes exhibited the greatest magnitude of propagation dominated failure for that stress level. The data presented in 7.3.1.1 suggests the number of primary initiation sites determines the mechanism of failure for the '800/260' specimens. A large number of crack initiation sites promote coalescence dominated failure with the associated poor fatigue performance. A small number of initiation sites generally promote longer fatigue lifetimes associated with propagation dominated failure. However, the process of identifying individual crack initiating carbides in any specimen is extremely time consuming. This coupled with the large number of short fatigue crack specimens renders this task beyond the scope and time scale of this study. Comparison of carbide populations promoting these two failure mechanisms is more easily achieved. The data presented in Figure 7.36 to Figure 7.46 represent the comparison of global carbide distributions between specimens exhibiting the highest magnitudes of coalescence and propagation dominated failure at three applied stress levels. A summary of the specimens used for this comparison can be seen in Table 7.5.

Carbide Area, Aspect Ratio and Angle:

It is apparent from Figure 7.36 that at all stress levels, specimens showing coalescence dominated failure have a greater number of larger eutectic carbides. This feature is most noticeable for the specimens tested at applied maximum stress levels of 700 MPa and 600 MPa. Figure 7.37 shows that specimens

showing coalescence dominated failure tend have larger populations of long thin carbides. It can be seen from Figure 7.38 that carbide angle appears to have little obvious influence on the mechanism of fatigue failure.

Cell Area, Aspect Ratio and Angle:

Figure 7.39 shows that carbides with large cell areas are more common in specimens showing propagation dominated failure. The data gathered appeared to show little relationship between cell aspect ratio and cell area with the mechanism of fatigue failure (Figure 7.40 and Figure 7.41).

Local Area Fraction:

The local area fraction for carbides in specimens that show coalescence dominated failure tend to be significantly larger than those that show propagation dominated failure.

Near Neighbour Measurements:

Again no obvious trend was observed for the number of nearest neighbours (Figure 7.43). It can be seen in Figure 7.44 that the mean near neighbour distance for specimens coalescence dominated failure tend to be significantly lower. This trend is not reflected however in the data gathered for the nearest neighbour distances (Figure 7.45). Finally by observing Figure 7.46, there appears to be no obvious trends for nearest neighbour angle.

7.4.2.1 Application of SUPANOVA for Comparison of Carbide Populations

The SUPANOVA approach was applied to the comparison of eutectic carbide populations in specimens showing the highest magnitude of propagation and coalescence dominated failure. This represented a more balanced data set than the classification of crack initiating carbides. Class sizes of 1837 and 1501 represent the coalescence dominated and propagation dominated failures respectively. The SUPANOVA model was run with 43% of data from the coalescence dominated population and 53% of data from the propagation dominated population was used for model training. This represents 800 individual carbides in from each population. The remainder data from both populations was used for testing of the model.

7.4.2.2 Selected Features for Comparison of Carbide Populations

The comparison of carbide populations promoting coalescence and propagation dominated failure mechanisms reduced the 512 possible terms to seven. These can be seen in Table 7.7. The sparse representation model gave a successful coalescence dominated failure classification rate of 64%, a successful propagation dominated failure of 65% and an overall classification performance based on the mean and variance values of G_{mean} of 63% and 0.001% respectively.

Figure 7.47 and Figure 7.48 are graphs representing the univariate terms picked by the SUPANOVA classification. The first (Figure 7.47:A) describes the increased susceptibility of coalescence dominated failure for an eutectic carbide population with increasing carbide aspect ratio. This susceptibility of coalescence dominated failure appears to decrease with increasing carbide angle (Figure 7.47:B) and also with increasing cell area (Figure 7.47:C). A more complex relationship can be seen in Figure 7.48:A increasing local area fraction at first considerably heightens the susceptibility of coalescence dominated failure. The relationship reaches a maximum value of susceptibility before increased local area fraction generates a increase in the likelihood of propagation dominated failure. The next term (Figure 7.48:B) describes the increased probability of a carbide population suffering propagation dominated failure with increasing mean near neighbour distance.

Two bivariate terms were selected by the classifier. A decrease in the susceptibility of a carbide population to coalescence dominated failure was suggested by the following conditions:

- Increasing local area fraction and carbide angle (as seen in Figure 7.48:A). This relationship appears to be more dependent on local area fraction than carbide angle however.
- Increasing nearest neighbour and carbide angle (Figure 7.48:B).

7.4.3 Propagation of Porosity Initiated Short Fatigue Cracks

Crack growth in the '900/390' heat treatment was, with the comparative absence of eutectic carbides, almost entirely propagation dominated. Typically a dominant crack grew from either a single initiation site or a pair of micro-cracks from proximate initiation sites that coalesced in early-life. Generally speaking, crack interactions were limited to events following initiation events ahead of the advancing dominant crack tips which will be discussed in section 7.4.3.1. Typically there was the formation of one or two large fatigue cracks that ultimately coalesced at final specimen fracture.

The projected length of the largest crack as a function of number of fatigue cycles has been plotted for polished '900/390' specimens tested at an R-ratio of 0.1 and can be seen in Figure 7.50. Crack growth rate is faster for tests performed at higher values of applied stress at comparable crack lengths. When crack length is plotted against normalised lifetime (Figure 7.51) the fatigue behaviour exhibited by the specimens at all stress levels for a given fraction of lifetime is similar. Figure 7.52 shows crack growth rate as a function of crack length. Crack growth rate as a function of crack length is faster at longer crack lengths in the case of all stress levels. The rather erratic crack growth shown by the specimen tested at 800 MPa is a direct result of the coalescence events suffered by the dominant macro-crack. This macro-crack was formed by the coalescence of approximately 16 micro-cracks. The number of micro-cracks coalescing to form the dominant macro-crack for the 700 MPa test was far fewer; 6, and the 600 MPa test suffered no coalescence events before final fracture at all. From Figure 7.53 it can be observed that at comparable values of ΔK the '900/390' specimen show slower crack growth rates with less scatter than the as-cast ductile iron.

7.4.3.1 The Influence of Graphite Nodules on Crack Propagation

Much has been written in the literature on the influence of graphite nodules on ADI fatigue crack propagation. One method observed in the literature for analysing the extent of graphite nodule/crack interaction is to count the number of nodules present along the crack path. This has been undertaken for all '900/390' short fatigue crack specimens. The results can be seen in Table 7.8. Counts were taken at approximately 90% of the total lifetime using replica records. To assess

whether the advancing fatigue cracks were 'seeking out' graphite nodules these figures were compared to the number of nodules intercepted by simulated 'straight cracks' of equivalent length. Thirty random lines of equal length to the fatigue crack at 90% life were placed on images of each specimen to simulate non-deflected crack growth.

There is a significant increase in the frequency of graphite nodules along the crack path as the applied stress levels are increased. It is also clear for the tests performed at 800 MPa and 700 MPa that the crack path intercepts significantly more graphite nodules than the equivalent non-deflected crack. An increase of at least two hundred percent was observed for both tests. The dominant crack for the test performed at 600 MPa intercepted no more nodules than the simulated non-deflected cracks.

The number of graphite nodules as a function of dominant crack length was also investigated. The data is presented in Figure 7.54. The 'simulated non-deflected' cracks are shown for comparison. It is apparent that the data for both the 800 MPa and the 700 MPa specimens deviates from the respective 'simulated non-deflected' cracks. At corresponding crack lengths greater than 0.5 mm, significantly more graphite nodules had been intercepted by the dominant crack than the 'non-deflected' crack. Furthermore, the 800 MPa test exhibited more graphite nodules on the dominant crack than the 700 MPa test. However, the 'non-deflected' cracks for these two specimens showed a similar trend. The data from the dominant and 'non-deflected' cracks in the 600 MPa specimen is comparable, suggesting minimal influence of graphite nodules on crack propagation. This analysis was continued to determine the effect of ΔK on the number of graphite nodules on the dominant crack path. Figure 7.55 shows the data from the three polished replica tests. These are again compared to the 'simulated non-deflected' cracks for the corresponding specimen. It is clear that above a ΔK of 20 MPa$\sqrt{m}$ the number of nodules on the dominant crack path exceeds that on the 'simulated non-deflected' cracks for both the 800 MPa and 700 MPa specimens. At lower values of ΔK, the dominant cracks intersect fewer graphite nodules than the 'non-deflected' crack. It is probable that this reflects the initiation of the dominant cracks from porosity, which for these tests was not

proximate to graphite nodules. No such restriction exists for the 'simulated non-deflected' cracks. In addition, there is a marked increase in the rate in graphite nodules are intercepted by the dominant fatigue crack above 14 MPa$\sqrt{m}$.

On inspection of the replica records of the polished specimens it became apparent that micro-cracks initiate from decohered graphite nodules ahead of the crack tip. An example of this is shown in Figure 7.26. The extent of micro-crack initiation ahead of the crack tip appeared greatest in the specimen tested with a maximum stress of 800 MPa. Table 7.8 quantifies this observation. The number of decohering nodules ahead of the dominant crack was 25 for the 800 MPa test (900/390:01). This relates to 9.6 nodules per millimetre. Noticeably less nodules (4.9 per millimetre) decohered in the 700 MPa test and virtually none (0.8 per millimetre) for the 600 MPa test.

Some, but not all of these micro-cracks coalesced with the advancing dominant crack. Decohesion of graphite nodules and subsequent initiation and growth of micro-cracks may lead to deflection of the dominant crack system as they approach coalescence. Region A in Figure 7.27 is a particularly good example. The greatest extent of coalescence and subsequent crack deflection was again observed in the specimen tested with a maximum stress of 800 MPa. Table 7.8 shows that 47% of the graphite nodules along the dominant crack path initiated ahead of the crack. This compares to 25% and 14% for the tests performed at 700 MPa and 600 MPa respectively.

Therefore, to summarise, the effect of graphite nodules on the dominant crack path is as follows. Graphite nodules may decohere ahead of the advancing dominant crack. The initiation and nucleation of micro-cracks occur at the decohered interface between nodule and matrix. The subsequent propagation of these micro-cracks and the dominant crack may lead to deflection and coalescence events. Figure 7.56 to Figure 7.58 show the dominant crack paths for the polished short fatigue crack tests at 800 MPa, 700 MPa and 600 MPa respectively. Greater deflection is shown by the dominant crack as applied stress is increased. This reflects the higher number of near tip crack initiation events and subsequent crack deflection by the mechanisms outlined above.

7.4.3.2 Relationship Between Near Tip Crack Initiation and Plastic Zone Size

The location of micro crack initiation events with respect to the advancing dominant crack tip has been investigated for the '900/390' short fatigue crack tests performed at an applied stress of 800 MPa and 700 MPa. Both the distance of the initiation event from the crack tip and angle of inclination were considered. A schematic of the analysis is shown in Figure 7.59. Estimations of monotonic and cyclic plastic zone sizes were made using the following equations [19]:

Monotonic: $$r_y = \frac{1}{4\pi}\left(\frac{K_{max}}{\sigma_y}\right)^2\left[1+\cos\alpha+\frac{3}{2}\sin^2\alpha\right] \quad \textit{equation 7.1}$$

Cyclic: $$r_y = \frac{1}{4\pi}\left(\frac{\Delta K}{2\sigma_y}\right)^2\left[1+\cos\alpha+\frac{3}{2}\sin^2\alpha\right] \quad \textit{equation 7.2}$$

Values of σ_y were taken from predictions based on the relative properties and amounts of the major matrix constituents made by Loughborough University (see section 4.1.1). Equation 7.1 and Equation 7.2 consider the size and shape of the plastic zone with regards to the angle of inclination from the crack tip. The redistribution of stress due to plasticity however, is not taken into account in estimating the extent of plastic zone size. Examples of monotonic and cyclic plastic zone shape and extent for this material at various levels of ΔK can be seen Figure 7.60. Figure 7.61 compares the size of monotonic and cyclic plastic zones at the tip of the advancing dominant macro-crack and the proximity of near tip micro-crack initiation events. All data points below the x=y line indicate where micro-crack initiation occurred within the crack-tip plastic zone. It can be seen that 83% of initiation events occurred within the monotonic plastic zone. However, only 17% of all near-tip initiation events occurred within the cyclic plastic zone.

7.4.3.3 Short Crack Propagation between Graphite Nodules

The mechanisms of propagation within the matrix microstructure between graphite nodules in porosity initiated short cracks were investigated using replica records of interval tests and SEM investigation of secondary cracks and cracks formed during interrupted tests. Both deflected and non-deflected short fatigue crack growth has been observed. Microstructural features that have been observed to

cause crack deflection are; graphite nodules, the interface between retained austenite and bainite, and 'ausferrite' packets. These features do not cause crack deflection on every occasion however. Figure 7.62 shows high magnification images of an interrupted short crack test. Propagation along the interface between bainite and retained austenite causing significant crack deflection can be seen in the top of region A. Beneath this, in the centre of region A, the crack appears to have propagated around the perimeter of an 'ausferrite' packet. In region B the crack can be seen to deviate in order to impinge on a graphite nodule. Several examples of crack propagation through pools of retained austenite are visible in region C.

High magnification images of a '900/390' secondary crack profile can be seen in Figure 7.63. Region A shows crack propagation through a series of retained austenite pools. Crack deflection along the interface between bainite and retained austenite can be seen in region B. Finally, significant crack deflection along the interface between bainite and retained austenite as the short fatigue crack propagates towards a graphite nodule can be seen in region C.

7.4.4 Short Fatigue Crack Fractography

Analysis of the fractured short fatigue crack specimens commenced with simple observations of the fracture profile and fracture surface. The fracture profiles of the as-cast DI short fatigue crack specimens are shown in Figure 7.64. The approximate location of the central roller, indicating peak applied stress has been superimposed as a red line on the top surface. Images of the fracture surface have been placed adjacent to the crack profiles. Sheared ligaments and large scale crack deflection are clear, and are present on all samples. This reflects the number and distribution of individual micro-cracks. In the majority of cases the large scale crack deflection can be attributed to the coalescence of these micro-cracks usually on final failure. The fracture surfaces of each of these specimens lie some distance (up to 4.5 mm for specimen 'DI:07') from the position of peak applied stress. This distance is 15 percent of the span between centre and outer roller. Consequently, the stress suffered in this region would be 85 percent of the peak applied stress. The sheared ligaments are large enough to be clearly visible on the low magnification images of the respective fracture surfaces.

The fracture profiles and surfaces of the '900/390' short crack specimens are shown in Figure 7.65. Generally, these specimens show straighter fracture profiles than those of the as-cast condition. Sheared ligaments are visible on specimens '900/390:04', '900/390:08', '900/390:09' and '900/390:11' and are the result of the coalescence on final failure of two or three large dominant cracks that usually had initiated some distance apart, both transversally and longitudinally. Propagation of the cracks would occur in parallel directions and the transverse separation between them would, as a result, decrease. The cracks would often propagate past each other before coalescing on final failure. The longitudinal separation between the cracks would cause the sheared ligaments during the sudden fast fracture of final failure. The fracture profile between sheared ligaments is usually relatively straight and parallel to the axis of peak applied stress. The deflection caused by graphite nodule decohesion, crack initiation and coalescence ahead the dominant crack tip is not of the magnitude to be observed at this scale. Images of the fracture surfaces reveal significant quantities of porosity in approximately fifty percent of these specimens. Furthermore, several specimen fracture surfaces were not located in the region of peak applied stress. Specimens '900/390:05' and '900/390:08' were, at approximately 3.5 mm the most distant which is equivalent to 89% of the maximum applied stress.

Figure 7.66 and Figure 7.67 shows the fracture profiles of all '800/260' short fatigue crack specimens. It is apparent that the location of the final fracture surface does not always relate to position of the peak applied stress. In some ('800/260:09') cases the distance of the fracture surface from the position of the central roller is approximately 5 mm which approximates to 80% of the maximum applied stress. The influence of multiple crack initiation and coalescence may be observed on some of the specimen fracture profiles. It is usual to expect a crack profile to exhibit deflection on a small scale only. However, in some of the '800/260' specimens large deflections are visible with specimens '800/260:02' and '800/260:09' being particularly good examples. Furthermore, on specimens '800/260:16' and '800/260:21' large sheared ligaments are visible indicating the propagation of multiple well spaced large fatigue cracks. Low magnification images of the fracture surface have been placed alongside the images of fracture profile (see Figure 7.66) for each short fatigue crack specimen. It can be observed

that regions of porosity are evident in the centre of many of the specimens. Furthermore, it is apparent the degree of porosity varies significantly. For example specimen '800/260:22' appears, at this magnification to have little porosity, whilst '800/260:21' has a massive pore covering almost half the cross-sectional area.

Large scale crack deflection and sheared ligaments are present on all but one of the '800/390' short fatigue crack specimens. This is again indicative of the large number of individual micro-cracks and their distribution. In this heat treatment, porosity is largely absent from the fracture surfaces.

The fracture profiles of the chilled ductile iron short fatigue crack specimens can be seen in Figure 7.69. For all six specimens it appears there are no large scale crack deflections or sheared ligaments, as observed for some of the specimens from other heat treatments. Also seen in this figure are the corresponding fracture surfaces for these specimens. It is clear that the fracture surfaces for this alloy condition are significantly different than those previously discussed. Long linear features dominate the fracture surfaces and probably represent carbide dendrites.

Further investigation of short fatigue crack fracture surfaces at higher magnifications has also been undertaken. Common features include decohered graphite nodules (Figure 7.70 and Figure 7.71) and brittle facets that represent fractured eutectic carbides (Figure 7.72). Higher magnification images of short fatigue crack specimen '800/260:02' are shown in Figure 7.73 and Figure 7.74. This specimen showed the greatest amount of eutectic carbide cracking and crack coalescence. It is particularly noticeable that the fracture surface appears relatively devoid of graphite nodules. Specimen '800/260:09' also showed a high number of crack coalescence events. In this case however, the amount of propagation needed between coalescence events was larger. Evidence of this may be seen on the fracture surface of this specimen (Figure 7.75) where brittle facets are fewer in number and separated by regions of ductile tearing. Furthermore, graphite nodules appear to be more numerous on the fracture surface. The fracture surface surrounding nodules shows ductile tearing (Figure 7.76) and is free from brittle facets. A fewer number of brittle facets are observed on '800/260' specimens showing a greater degree of crack propagation (Figure

7.77 to Figure 7.80). On some occasions as shown in Figure 7.80, regions of the microstructure with few brittle facets show a lath-like relief similar in nature and scale to the structure of bainite found in this heat treatment.

7.5 Long Fatigue Crack Propagation

Long fatigue crack testing has identified values of ΔK_{th} and K_Q for the as-cast ductile iron, '900/390' and '800/260' ADI heat treatments and these are summarised in Table 7.10. Fatigue threshold for the as cast ductile iron composition of this study was identified as 6.0 MPa$\sqrt{m}$. A value of 19 MPa$\sqrt{m}$ was identified for K_Q. The value for fatigue threshold for the '800/260' heat treatment is comparable to that of the as-cast ductile iron whilst values of K_Q seem highly variable. Comparison of the carbide area fraction of the side crack region for each of the long crack specimens suggests this may be a feature in determining toughness. It can be seen in Table 7.10 that specimens with higher carbide area fractions exhibited lower values of K_Q. The '900/390' microstructure also shows variability in values of K_Q. There is however, an improvement in the fatigue threshold for this heat treatment.

Graphs showing da/dN vs. ΔK data for as-cast ductile iron, '900/390' and '800/260' ADI heat treatments can be seen in Figure 7.81 to Figure 7.83 respectively. Values for the constant ΔK regions have been averaged. Slight variation between the load shedding and growth out curves can be observed for the as-cast ductile iron data. Quite a noticeable scatter band can be seen for the '900/390' constant load amplitude growth out long fatigue crack tests. The varying values of K_Q can also be observed from the point at which the curves end. Constant load amplitude growth out data (downward pointing triangle plots) is quite erratic showing significant jumps in crack growth rate as ΔK increases. The '800/260' long fatigue crack data has been plotted against the '900/390' scatter band for comparison. It is apparent that the '800/260' data lies in the upper region of the '900/390' scatter band suggesting at comparable levels of ΔK crack growth rates in the '800/260' microstructure are somewhat faster. It is also noteworthy that the '800/260' data appears to show less scatter.

Images of the fracture surfaces of all long fatigue cracks tests can be seen in Figure 7.84 and Figure 7.91. From these images it is possible to see the extent of porosity for each of test specimens. It is clear that specimens '900/390:03' and '900/390:06' show considerable amounts of porosity. A significant region of porosity is also visible on specimen '800/260:01'. However, this region is not as extensive as those seen in specimens '900/390:03' and '900/390:06'. Areas of fatigue crack propagation have been superimposed on the fracture surfaces. This allows identification of which test conditions may have been affected by porosity. It is likely that the constant load amplitude growth out regions of '900/390:03' and '800/260:L1' and the constant ΔK regions of '900/390:L6' are affected by porosity. It appears that the threshold region of '900/390:L6' may be relatively clear of porosity.

7.5.1 Fatigue Threshold and Constant Load Amplitude Growth Out Tests

Fatigue threshold and constant load amplitude growth out tests allow the observation and comparison of fracture surfaces corresponding to varying values of ΔK. Micrographs from the fracture surface at low and high magnification of the as-cast ductile iron fatigue threshold and constant load amplitude growth out test at increasing values of ΔK can be seen in Figure 7.92 to Figure 7.94. In Figure 7.92:A both decohered graphite nodules, and the craters left by decohered graphite nodules are clearly visible. The conspicuously flat and featureless areas are brittle facets, perhaps representing fractured eutectic carbides and are present in all micrographs at all values of ΔK. As ΔK increases, the number of these brittle facets appears to increase. A high magnification image of brittle facets (Figure 7.93:B) shows the presence of a through thickness micro-crack.

High magnification images of the '900/390' fatigue threshold and constant load amplitude growth test can be seen in Figure 7.95 to Figure 7.97. Decohered graphite nodules are highly visible and are present at all values of ΔK. Brittle facets, perhaps representing occasional cracked eutectic carbides are visible on the higher ΔK micrographs. The number of these brittle facets is far fewer when compared to the as-cast ductile iron. The fracture surface at lower values of ΔK and those approaching threshold show quite differing features to the higher ΔK images. The number of brittle facets is notably lower. Figure 7.100 is at a higher

magnification and clearly reveals a 'feathery' fracture surface. This fracture surface is similar in morphology and scale to the bainite lath structure of this heat treatment. Furthermore, as ΔK increases the fracture surface images suggest an increase of surface roughness.

The fracture surface of long fatigue crack specimen '800/260:L4' can be observed in Figure 7.101 to Figure 7.104. Figure 7.101 represents the fracture surface at fatigue threshold. The next three figures show the crack at progressively higher values of ΔK. The conspicuous flat regions in the micrographs are brittle facets perhaps representing cracked eutectic carbides. By observing Figure 7.101 to Figure 7.104 it is apparent, that as the value of ΔK experienced by the crack increases, the number of brittle facets on the fracture surface appears to increase. Additionally, at high values of ΔK ductile tearing is visible in regions between brittle facets. This can be related to a probable increase in static monotonic failure modes as K_{max} approaches K_Q.

7.5.2 Constant ΔK Tests

The effect of ADI microstructure on crack propagation has been investigated using constant ΔK long fatigue crack tests on '900/390' and '800/260' specimens. Suitable values of ΔK were selected following the constant amplitude growth-out tests. Figure 7.105 and Figure 7.106 show the variation of ΔK and da/dN with a/w throughout the constant ΔK region of tests '900/390:04' and '900/390:06'. Constant ΔK values were achieved for the first region (ΔK~12 MPa$\sqrt{m}$) of test '900/390:L6'. This is slightly higher than the intended 10 MPa$\sqrt{m}$. This is not the case for the second constant ΔK region (ΔK~20 MPa$\sqrt{m}$) of this test and for test '900/390:L4' where in both cases a gradual decrease in ΔK can be observed. As can be observed in Figure 7.107 and Figure 7.108 constant ΔK values have been satisfactorily achieved for both '800/260' tests although for '800/260:L3' slightly lower than the predicted 15 MPa$\sqrt{m}$.

Figure 7.107 and Figure 7.108 show the variation of crack growth rate as a function of ΔK for '900/390' and '800/260' long fatigue crack testing under attempted constant ΔK conditions. The variation of crack growth rates within these attempted constant ΔK regions is noteworthy. The data from '900/390:L4' shows

significant variation in crack growth rate below a ΔK of approximately 13 $MPa\sqrt{m}$. At values of ΔK above 13 $MPa\sqrt{m}$ the crack growth rates are more consistent. The data from '900/390:L6' shows little variation in the lower constant ΔK region (ΔK~12 $MPa\sqrt{m}$). Constant ΔK conditions were not achieved for the higher region (20 $MPa\sqrt{m}$) and consequently the graph shows and increase in da/dN as a function of increasing ΔK. The data for both '800/260:L2' and '800/260:L3' show a small degree of variation (when compared to the '900/390' data) in crack growth rate within attempted constant ΔK regions. Analyses of the acetate replica records suggest that the occasionally erratic crack growth is related to acceleration events due to monotonic brittle failure modes associated with carbide cracking. Furthermore, it appears that the microstructure is more susceptible to acceleration and deceleration effects at a lower ΔK.

Fractography from the constant ΔK region of test '900/390:L6' can be seen in Figure 7.111 to Figure 7.113. As crack growth rate increases so do the number of brittle facets. There appears to be little variation in surface roughness or the number of graphite nodules. Shrinkage porosity can be seen in Figure 7.111:A. Micrographs showing increasing values of crack growth rate within the constant ΔK region of test '800/260:L3' can be seen in Figure 7.114 to Figure 7.116. It is reasonable to suggest that an increase in the quantity of brittle facets can be observed with increasing crack growth rate.

7.6 Comparison of Long and Short Fatigue Crack Growth

The long fatigue crack data have been plotted with the data from the '900/390' short crack test which showed the least number of coalescence events and can been seen in Figure 7.117. It is apparent from this graph that the short crack test data merges with the long crack regime at values of ΔK above 14 $MPa\sqrt{m}$. This represents short cracks with lengths in the order of 620 μm. The monotonic plastic zone size directly ahead of the crack tip for a short crack in this region would be 80 μm. It is also noticeable that we see short crack growth at values of ΔK below the long crack threshold and faster crack growth rates at comparable values of ΔK. This can be interpreted as 'classic' short fatigue crack behaviour as discussed in the literature review (see section 2.13).

The comparison of '800/260' long fatigue crack test specimens and the short fatigue crack test showing the greatest extent of propagation Figure 7.118 reveals classic fatigue behaviour. The short crack data exhibits a far greater degree of scatter than the long crack data. At comparable levels of ΔK the short crack data shows increased crack growth rates. At higher values of ΔK, the short crack data shows less scatter and approaches the long crack regime. However, no distinct merging of long and short crack data can be seen.

Heat treatment	Yield Strength (MPa)	Hardness (Hv)
'900/390'	647	278
'800/260'	1170	461
'800/390'	739	311

Table 7.1: Predicted values of yield strength and hardness.

Specimen	s_{Max}	R-ratio	Test Conditions	Carbide A_f	Nf	Notes
DI:01	400	0.1	Interval	4.31	143299	
DI:03	400	0.1	Interval	8.31	86191	
DI:05	500	0.1	Interval	4.28	37876	
DI:06	500	0.1	Interval	8.23	23666	
DI:07	600	0.1	Interval	8.83	6592	
CDI:01	450	0.1			0	Failed before completion of first fatigue cycle
CDI:02	300	0.1			6282	
CDI:03	200	0.1			445953	Quench cracks found on top surface
CDI:04	400	0.1			2534	
CDI:05	250	0.1			No failure	
CDI:06	250	0.1			No failure	
CDI:07	300	0.1			86136	
CDI:08	400	0.1			770	
900/390:01	800	0.1	Interval		26578	
900/390:02	800	0.1	Interval		29403	
900/390:03	800	0.5			No failure	
900/390:04	700	0.1	Interval		52143	
900/390:05	1100	0.5			43151	
900/390:06	1100	0.5	interval		32009	
900/390:07	700	0.1	Interval		40419	
900/390:08	600	0.1			54346	
900/390:09	600	0.1	Interval		71232	
900/390:10	500	0.1			No failure	
900/390:11	600	0.1	Interval		85008	
900/390:12	600	0.1	Interrupted		Stopped	
900/390:13	700	0.1	Interrupted		Stopped	

Table 7.2: Short crack test details (ductile iron, chilled ductile iron and 900/390 specimens).

Specimen	s_{Max}	R-ratio	Test Conditions	Carbide A_f	Predicted Hardness (Hv_{20})	Nf	Notes
800/260:01	800	0.1		3.66	512	1000	
800/260:02	700	0.1	Interval	8.13	515	3695	Largest no. of micro cracks
800/260:03	600	0.1		9.15	517	24304	
800/260:04	700	0.1		9.54	518	7594	
800/260:05	600	0.1	Interval	8.71	516	26283	
800/260:06	600	0.1	Interval	2.47	513	56435	
800/260:07	700	0.1		3.92	512	18071	
800/260:08	700	0.1		3.66	512	18800	
800/260:09	500	0.1		14.24	537	40673	
800/260:10	400	0.1		7.1	514	276304	
800/260:11	600	0.1	Interval	4.74	512	42897	
800/260:12	700	0.1	Interval	6.83	513	6087	
800/260:16	500	0.1	Interval	9.87	519	62680	
800/260:17	600	0.1		13.49	533	9909	
800/260:18	500	0.1	Interval	5.26	512	102306	
800/260:19	700	0.1		11.6	525	4841	
800/260:20	500	0.1	Interval	3.03	513	69096	
800/260:21	600	0.1				N/A	Huge pore
800/260:22	600	0.1		1.37	515	84119	
800/260:23	300	0.1		7.16	514	No failure	
800/390:01	700	0.1	Run-out			0	Failed before completion of first fatigue cycle
800/390:02	600	0.1	Run-out			0	Failed before completion of first fatigue cycle
800/390:03	400	0.1	Interval	26.26		3183	
800/390:04	350	0.1	Interval	21.67		10988	
800/390:05	300	0.1	Interval	21.19		18338	
800/390:06	250	0.1	Interval			45922	

Table 7.3: Short crack test details (800/260 and 800/390 specimens).

Property	Class	Mean	St dev	Coeff Var
Carbide Area (μm^2)	Cracked	2533.7	2110.6	0.8
	Background	471.2	955.0	2.0
Carbide Aspect Ratio	Cracked	2.2	1.1	0.5
	Background	1.8	0.6	0.3
Carbide Angle (radians)	Cracked	0.9	0.4	0.5
	Background	0.8	0.4	0.5
Cell Area (μm^2)	Cracked	15932.6	10455.0	0.7
	Background	5797.5	5328.0	0.9
Cell Aspect Ratio	Cracked	1.6	0.4	0.2
	Background	1.8	0.6	0.3
Local Area Fraction	Cracked	15.8	7.3	0.5
	Background	8.2	7.8	0.9
Number Near Neighbours	Cracked	8.1	3.0	0.4
	Background	5.7	2.3	0.4
Mean Near Neighbour Distance (μm)	Cracked	56.7	27.8	0.5
	Background	49.7	29.7	0.6
Nearest Neighbour Distance (μm)	Cracked	7.1	8.4	1.2
	Background	8.5	12.1	1.4
Nearest Neighbour Angle (rads)	Cracked	0.8	0.5	0.6
	Background	0.8	0.5	0.6
No. Carbides (Class size)	Cracked	78		
	Background	1718		

Table 7.4: Summary of individual crack initiating carbide classification in '800/260' short fatigue crack specimens.

Specimen	Maximum Applied Stress	Number of Cycles to Failure	Carbide Area Fraction	No. Carbides	No. Cracks on First Replica
800/260:02	700	3695	8.13	1718	212
800/260:07	700	18071	3.92	1371	7
800/260:03	600	24304	9.15	1877	44
800/260:11	600	42897	4.74	1503	0
800/260:09	500	40673	14.24	2237	90
800/260:18	500	102306	5.26	917	0

Table 7.5: Summary of specimens used for comparison of carbide populations with high and low magnitude of cracking.

Term	Occurrence	Component 1 -univariate		Component 2 -bivariate		Probability of initiation
1	100%	Cell Area	increasing			Increasing
2	100%	Local Area Fraction	increasing			Increasing
3	90%	Nearest Neighbour Distance	increasing			Decreasing
4	100%	Object Angle	increasing	Local Area Fraction	increasing	Increasing
5	60%	Object Angle	increasing	Nearest Neighbour Angle	increasing	Decreasing

Table 7.6: '800/260' SUPANOVA terms selected (and the components thereof) and their percentage occurrence over 10 modelling runs on random partitions of training and test data. Trends for each component and their effect on the probability of crack initiation are also given.

Term	Occurrence	Component 1 -univariate		Component 2 -bivariate		Probability of initiation
1	100%	Object Aspect Ratio	increasing			increasing
2	70%	Object Angle	increasing			decreasing
3	80%	Cell Area	increasing			decreasing
4	100%	Local Area Fraction	increasing			Increasing then decreasing
5	90%	Mean Near Neighbour Distance	increasing			decreasing
6	60%	Local Area Fraction	increasing	Object Angle	increasing	decreasing
7	70%	Nearest Neighbour Angle	increasing	Object Angle	increasing	decreasing

Table 7.7: '800/260' SUPANOVA terms selected (and the components thereof) and their percentage occurrence over 10 modelling runs on random partitions of training and test data. Trends for each component and their effect on the probability of crack initiation are

Specimen	900/390:01	900/390:04	900/390:11
σ_{max} (MPa)	800	700	600
Number of nodules on crack path at 90% life	17	16	9
No. nodules on crack path at 90% life as a function of crack length (nodules/mm)	6.5	5.2	2.7
No. nodules on simulated non-deflected crack as a function of unit length (nodules/mm)	2.9	2.4	2.8
No. nodules decohering ahead of crack tip as a function of crack length (nodules/mm)	9.6	4.9	0.8
Percentage of nodules on crack profile at 90% life that were seen to decohere ahead of the crack tip	47%	25%	14%

Table 7.8: Summary of the influence of graphite nodules on crack propagation in '900/390' polished short fatigue crack specimens.

No. Cycles	Micro Crack			Graphite Nodule		K_{max}	Monotonic plastic zone size
	c_m	d_m	a_m	d_n	a_n		
8000	1.0	37	0.7	30	1.0	8.9	42
10000	4.0	117	0.7	115	0.7	8.9	40
10000	1.0	102	0.8	115	0.7	8.9	40
15500	4.0	48	0.1	67	0.4	16.7	109
15500	3.0	87	0.2	67	0.4	16.7	111
16500	1.0	180	0.8	178	0.9	19.4	203
16500	2.0	169	1.0	178	0.9	19.4	211
19000	1.0	156	1.0	178	0.6	20.2	210
19000	3.0	111	0.5	93	0.6	20.2	187
19500	2.0	208	0.7	224	0.7	20.7	211
19500	4.0	221	0.6	224	0.7	20.7	202
19500	3.0	217	0.4	247	0.4	20.7	180
20000	1.0	102	0.7	128	0.6	21.5	221
23500	4.0	137	1.0	152	1.0	27.6	437
23500	6.0	169	0.9	152	1.0	27.6	419
23500	4.0	184	0.9	200	0.8	27.6	403
24000	10.0	35	0.3	48	0.1	29.7	343
24500	3.0	200	0.6	204	0.5	30.0	407
24500	4.0	213	0.5	204	0.5	30.0	397

Table 7.9: Summary of crack initiation events ahead of the advancing dominant macro-crack-tip

N = No. Cycles

c_m = Length of micro-crack (μm)

d_m = Distance of micro-crack from dominant crack (μm)

d_n = Distance of graphite nodule from dominant crack (μm)

a_m = Angle of micro-crack from dominant crack (degrees)

a_n = Angle of graphite nodule from dominant crack (degrees)

ΔK = ΔK of dominant crack ($MPa\sqrt{m}$)

pz = Estimated plastic zone size ahead of crack tip

Alloy Condition	Specimen designation	Test Conditions	K_Q (MPa$\sqrt{m}$)	ΔK_{th} (MPa$\sqrt{m}$)	Carbide area fraction
As-cast ductile iron	DI:L1	Fatigue threshold Constant load amplitude growth out	19	6	7.25
'900/390'	900/390:L3	Constant load amplitude growth out	32	-	-
	900/390:L4	Constant ΔK~15 Constant amplitude growth out	24	-	-
	900/390:L6	Fatigue threshold Constant ΔK~10 Constant ΔK~20	-	8	-
'800/260'	800/260:L1	Constant amplitude growth out	27	-	3.76
	800/260:L2	Constant ΔK~10 Constant amplitude growth out	18	-	9.06
	800/260:L3	Constant ΔK~15 Constant amplitude growth out	27	-	3.33
	800/260:L4	Fatigue threshold Constant load amplitude growth out	20	5.8	7.49

Table 7.10: Summary of data from long fatigue crack testing.

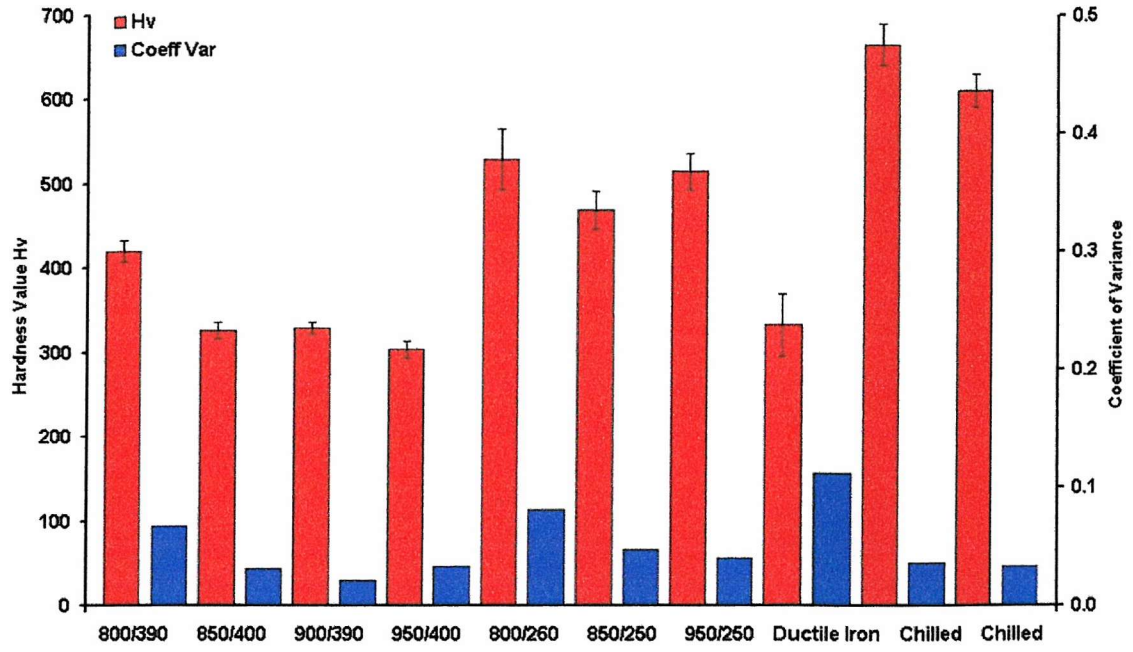

Figure 7.1 Hardness test results for all microstructures. Error bars show standard deviation for hardness values.

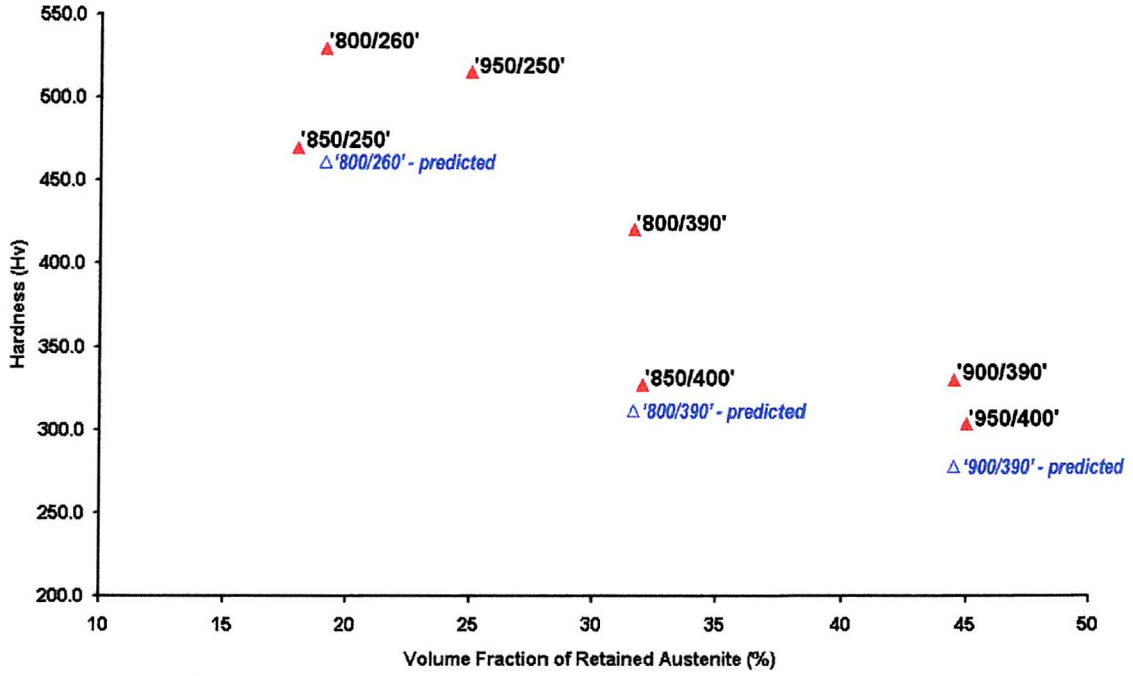

Figure 7.2: Hardness values of ADI heat treatments as a function of predicted retained austenite volume fraction. Predicted hardness values shown for comparison.

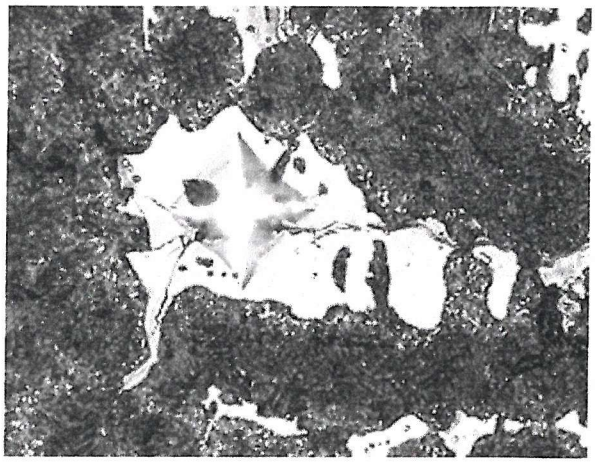

Figure 7.3: Eutectic carbide present in the '800/260' microstructure, fractured by micro-hardness indenter.

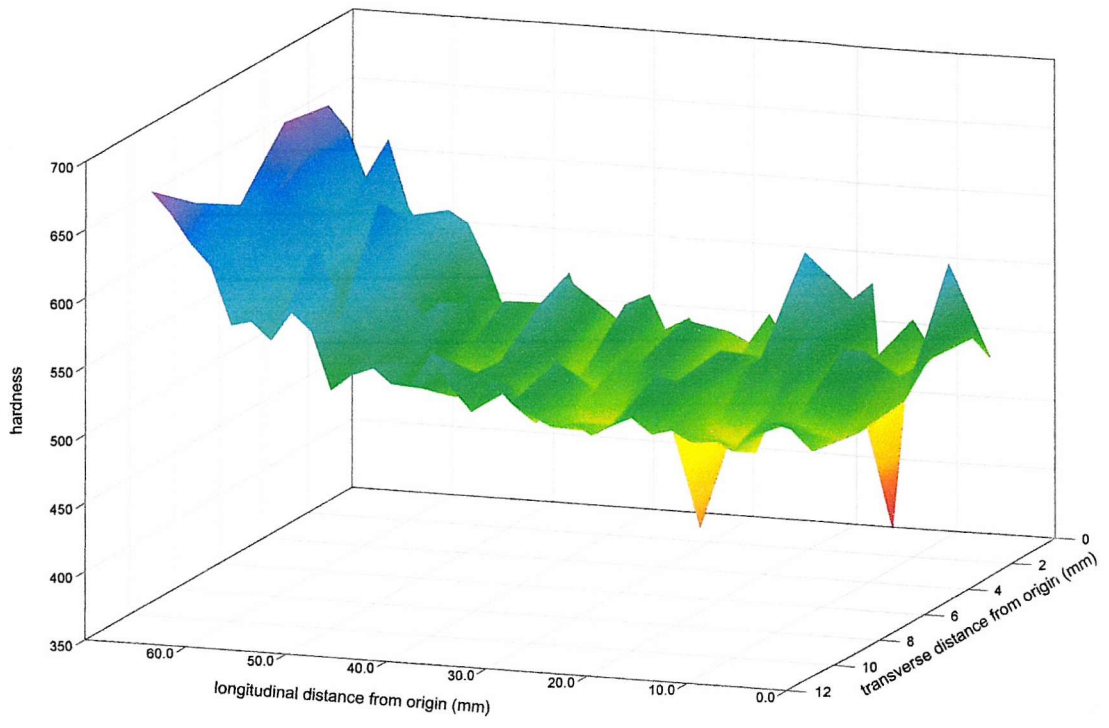

Figure 7.4: '800/260' specimen hardness map. Minima peaks represent porosity.

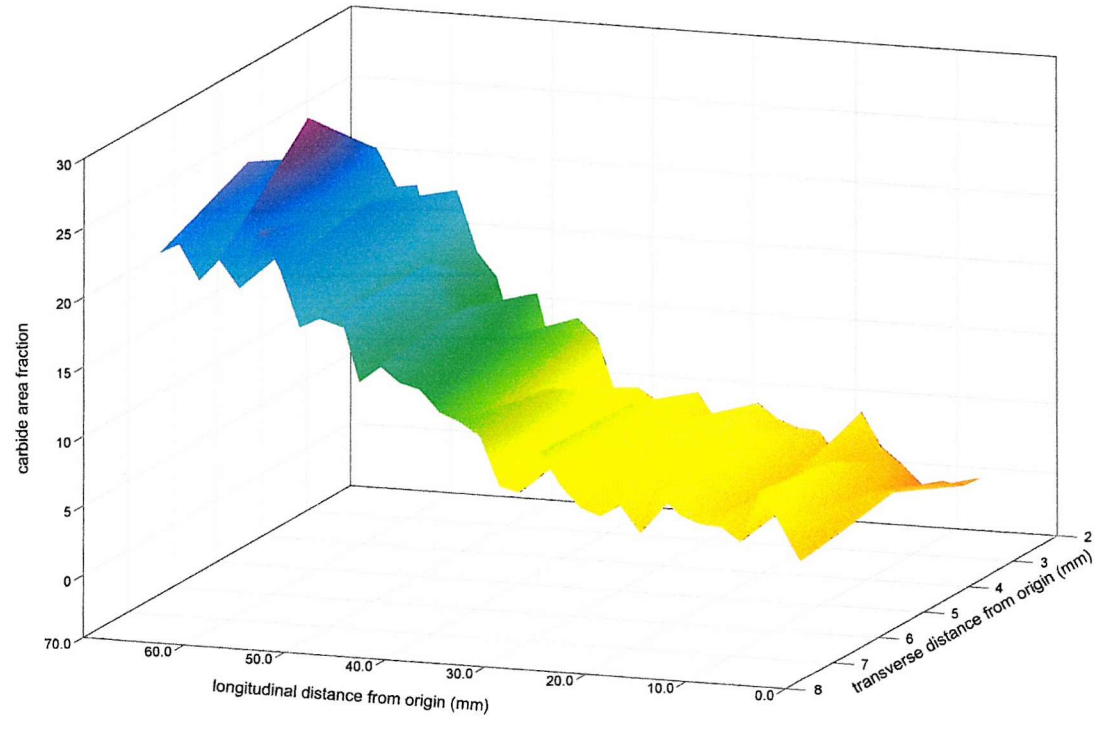

Figure 7.5: '800/260' carbide area fraction map.

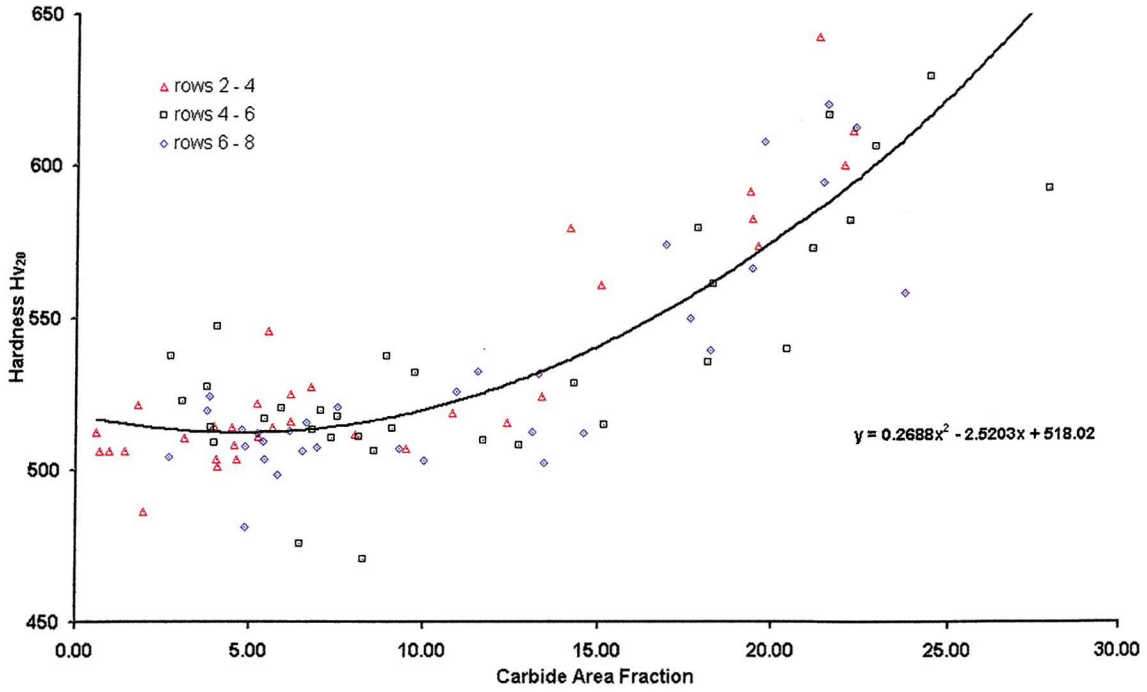

Figure 7.6: Hardness prediction from carbide area fraction.

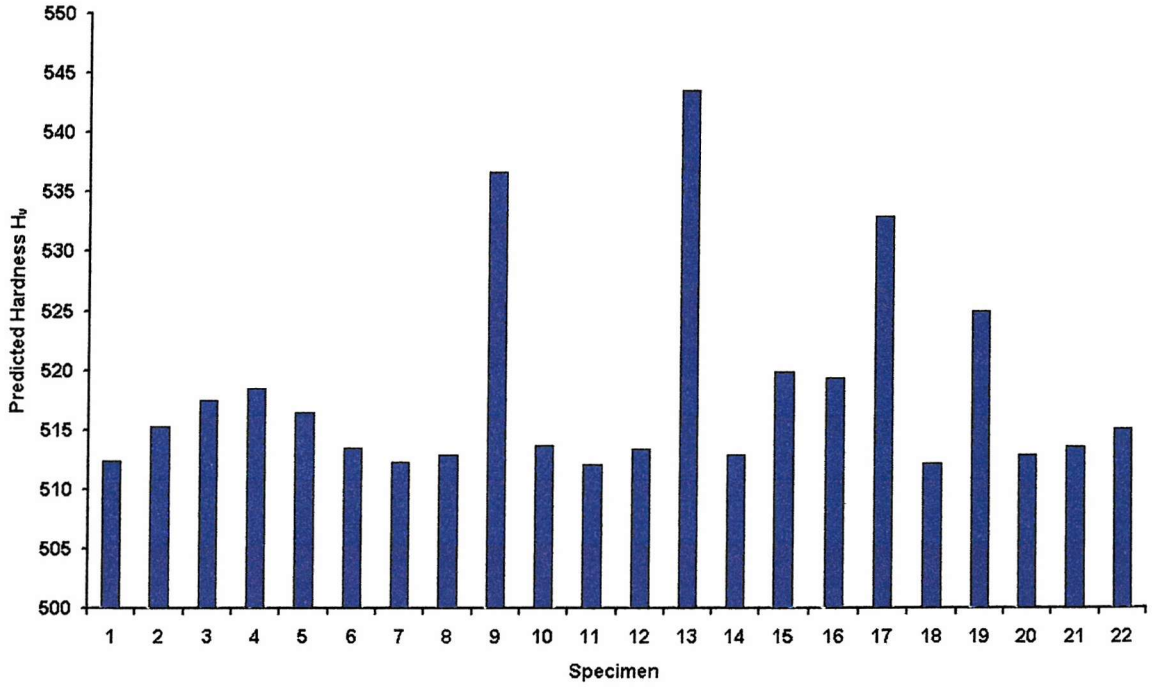

Figure 7.7: '800/260' hardness values predicted by comparison of hardness map values and eutectic carbide area fraction.

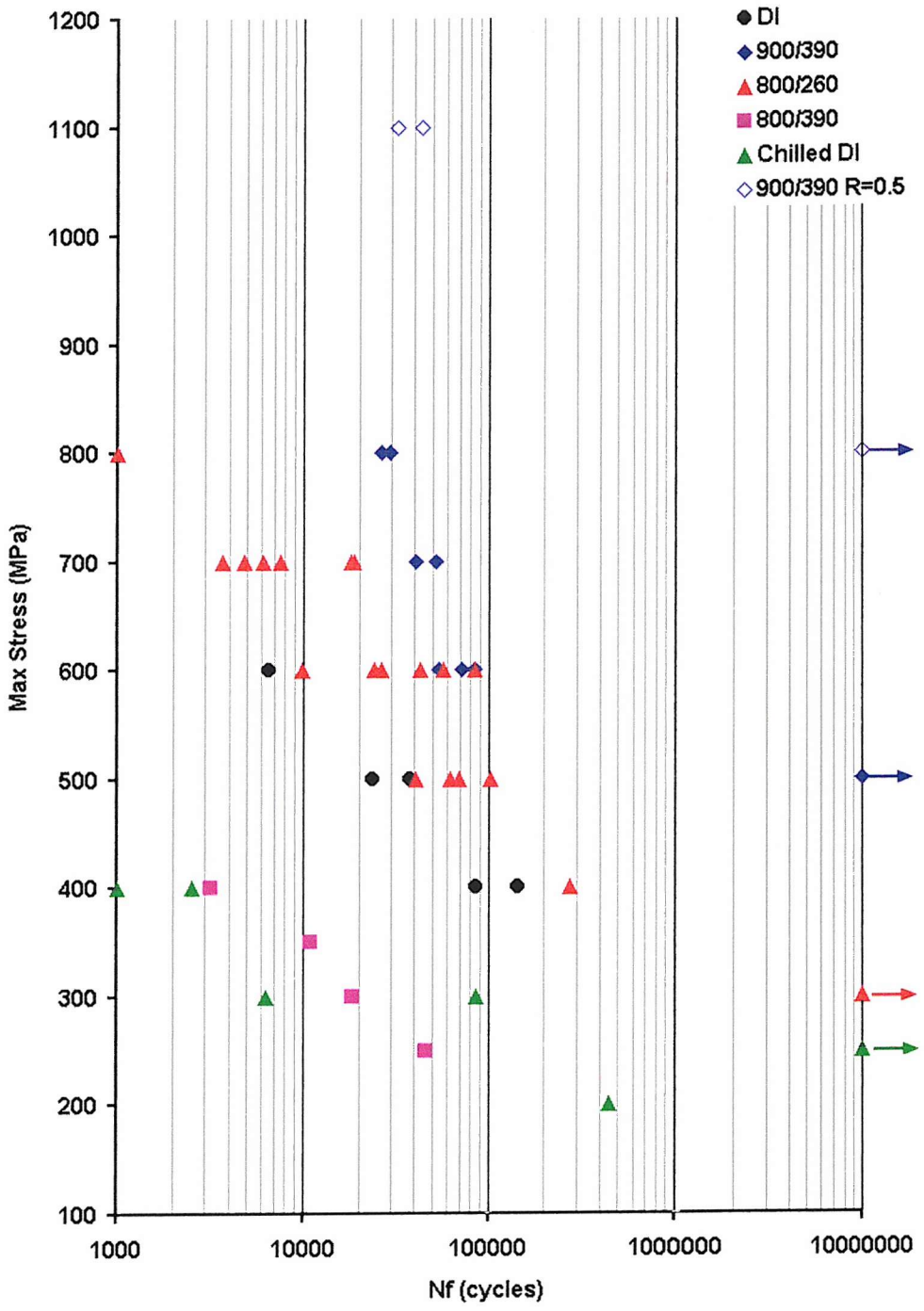

Figure 7.8: S-N curve for all short fatigue crack specimens in terms of the maximum applied stress.

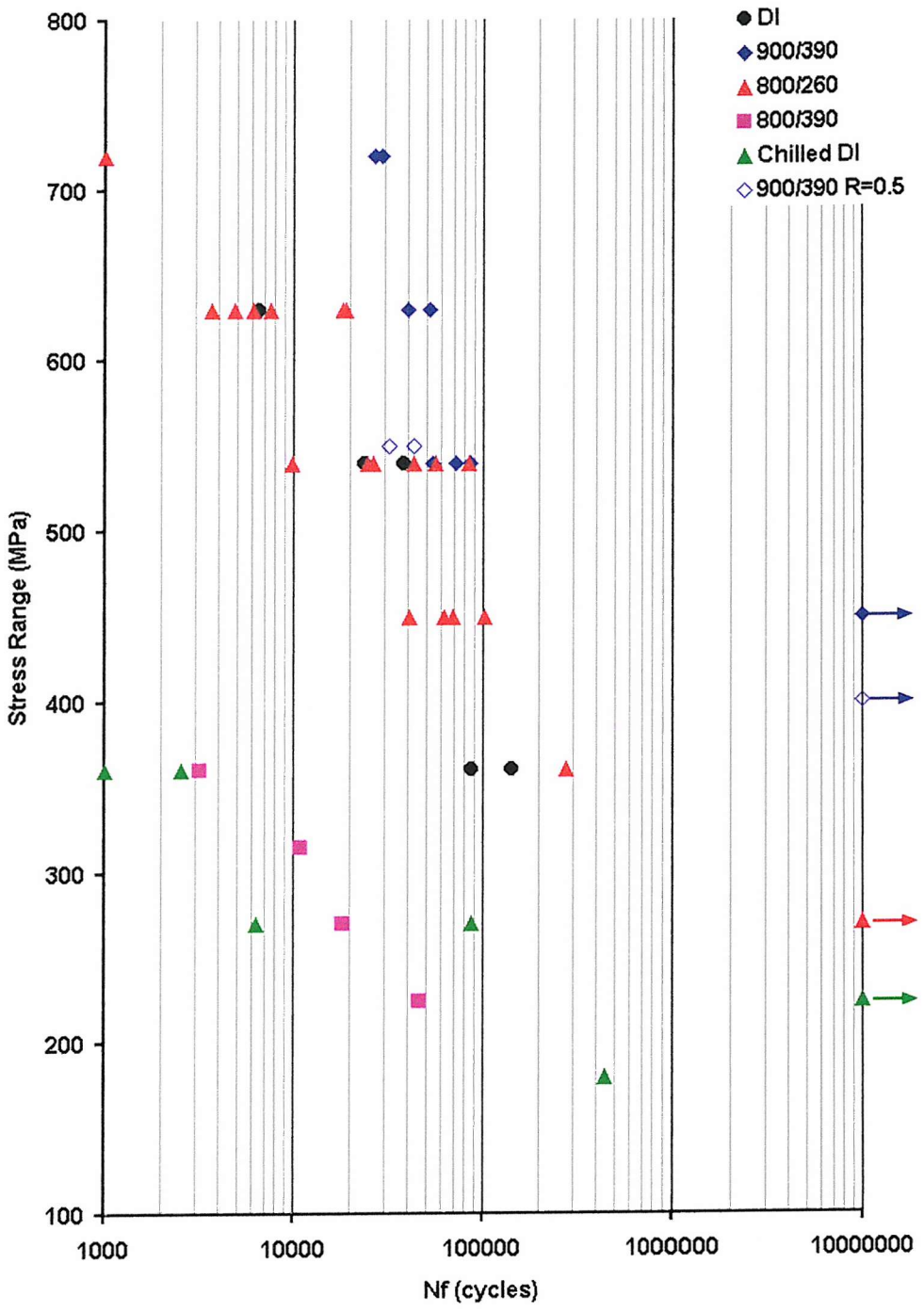

Figure 7.9: S-N curve for all short fatigue crack specimens in terms of the mean applied stress.

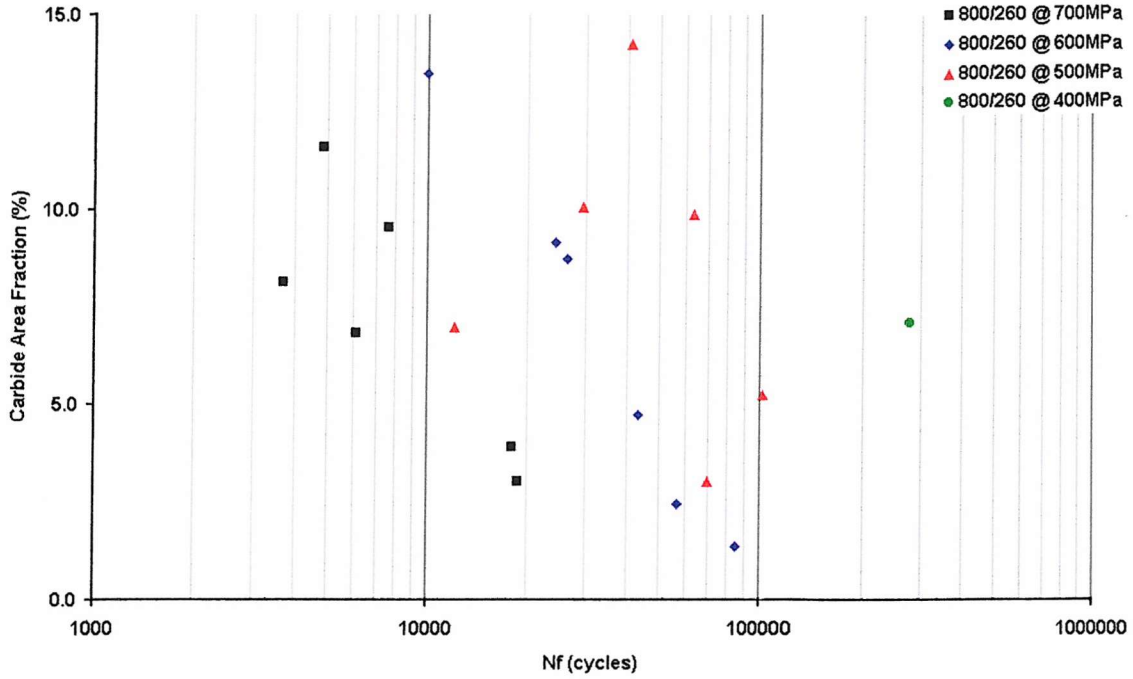

Figure 7.10: Relationship between carbide area fraction and fatigue lifetime for all '800/260' short fatigue crack specimens.

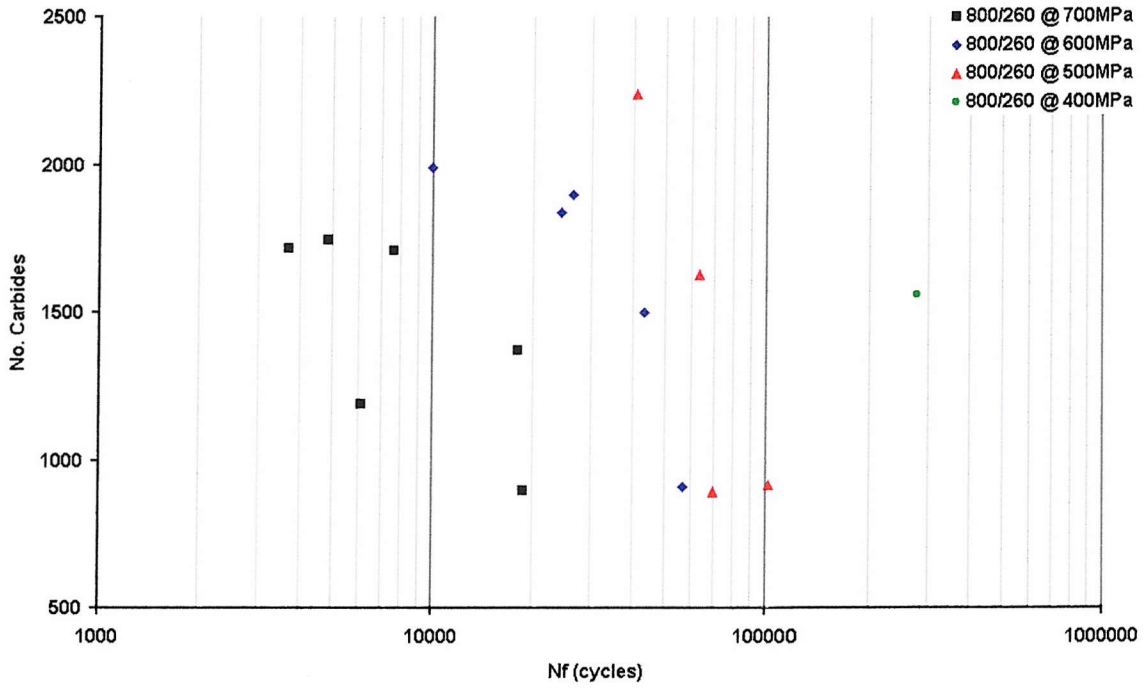

Figure 7.11: Relationship between number of individual carbides and fatigue lifetime for all '800/260' short fatigue crack specimens.

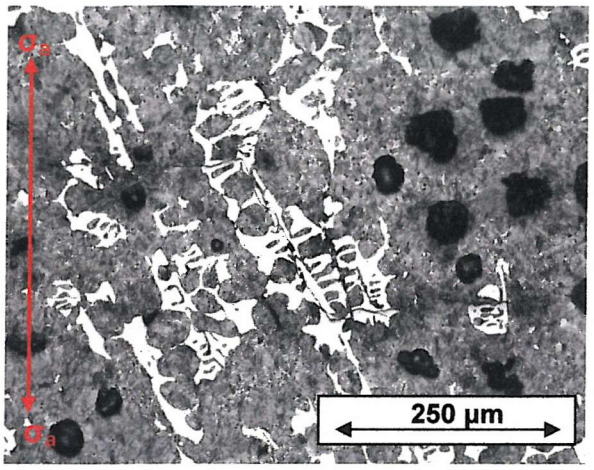

Figure 7.12: Example of fatigue crack initiation in '800/260' specimens. Note the direction of crack.

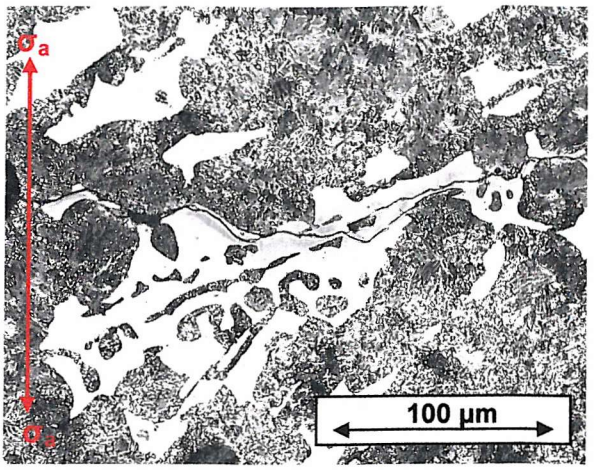

Figure 7.13: Example of fatigue crack initiation in '800/260' specimens.

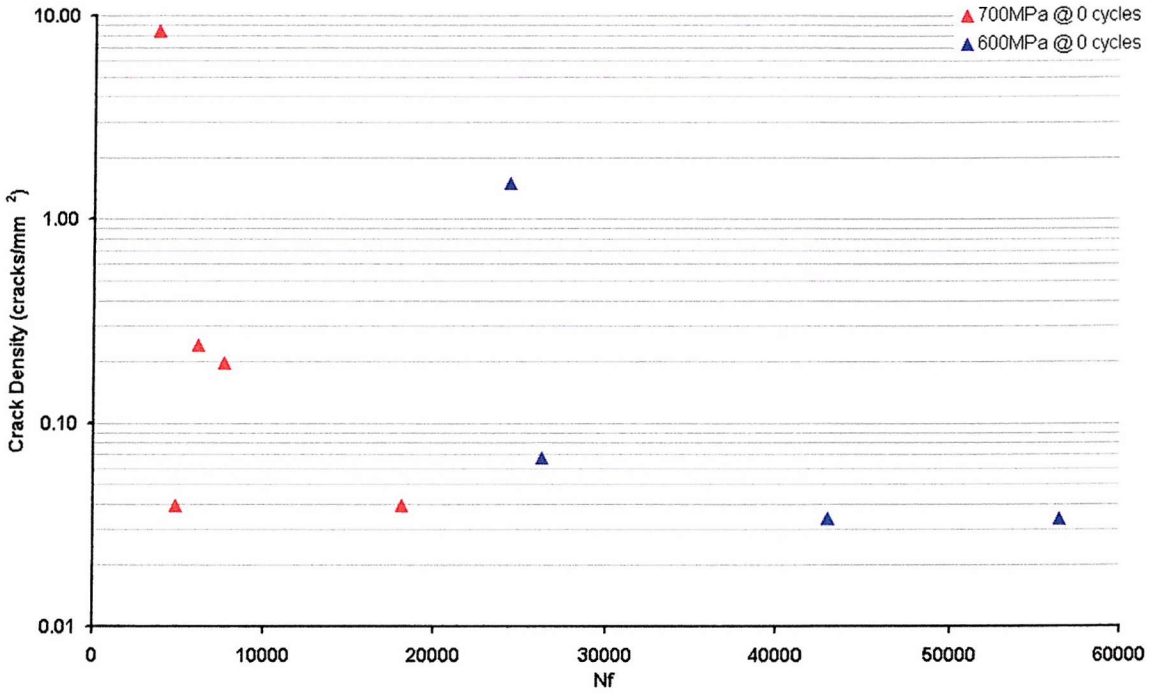

Figure 7.14: Extent of carbide cracking on initial loading for '800/260' short fatigue crack specimens.

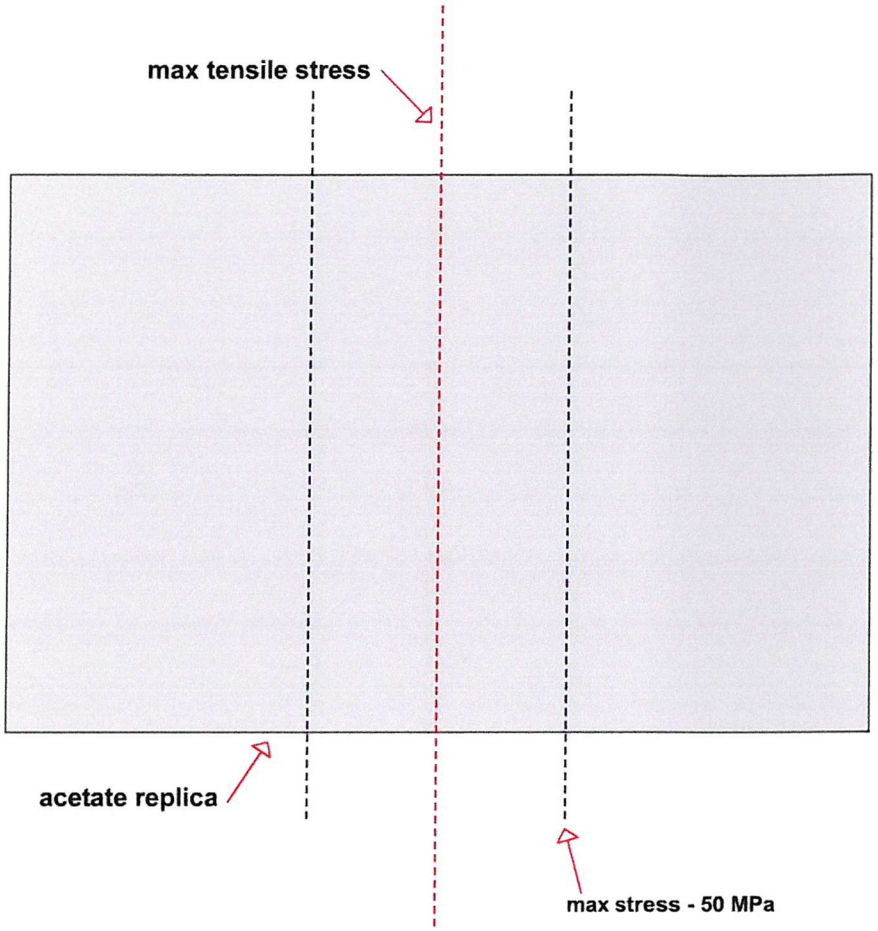

Figure 7.15: Diagram showing procedure for '800/260' short fatigue crack density measurement.

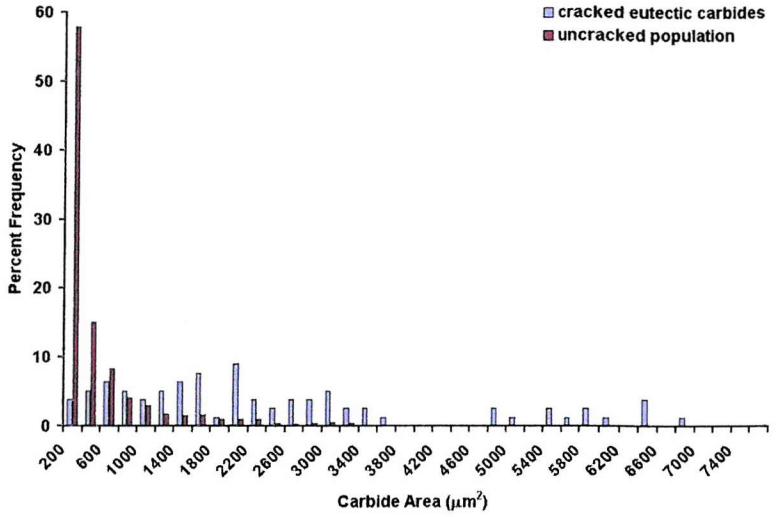

Figure 7.16: Characterisation of crack initiating eutectic carbides: Carbide area.

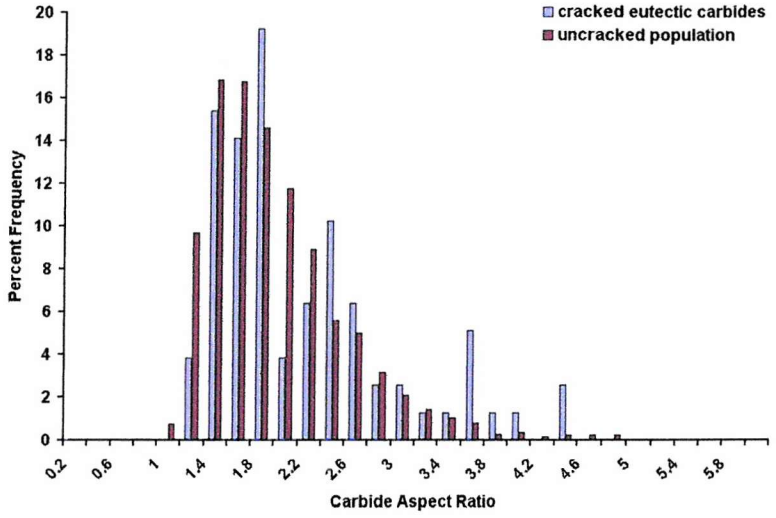

Figure 7.17: Characterisation of crack initiating eutectic carbides: Carbide aspect ratio.

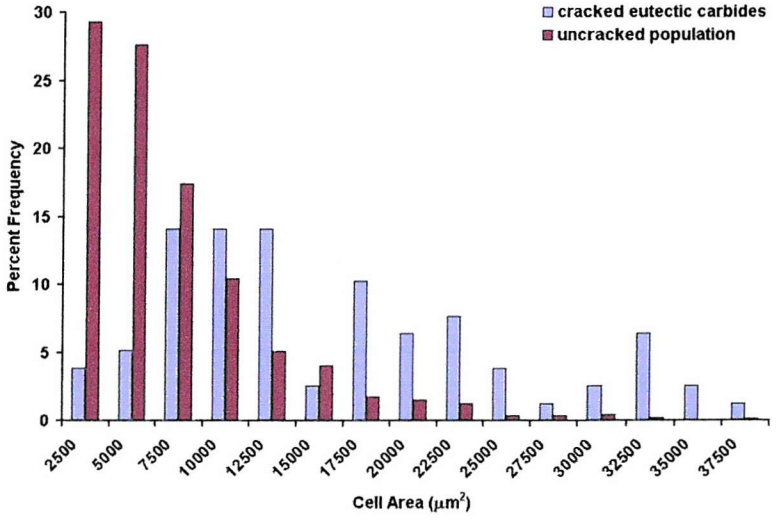

Figure 7.18: Characterisation of crack initiating eutectic carbides: Cell area.

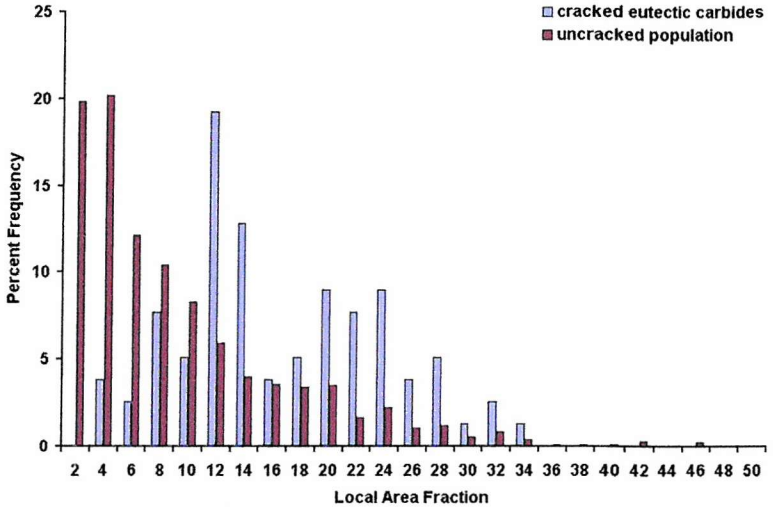

Figure 7.19: Characterisation of crack initiating eutectic carbides: Local area fraction.

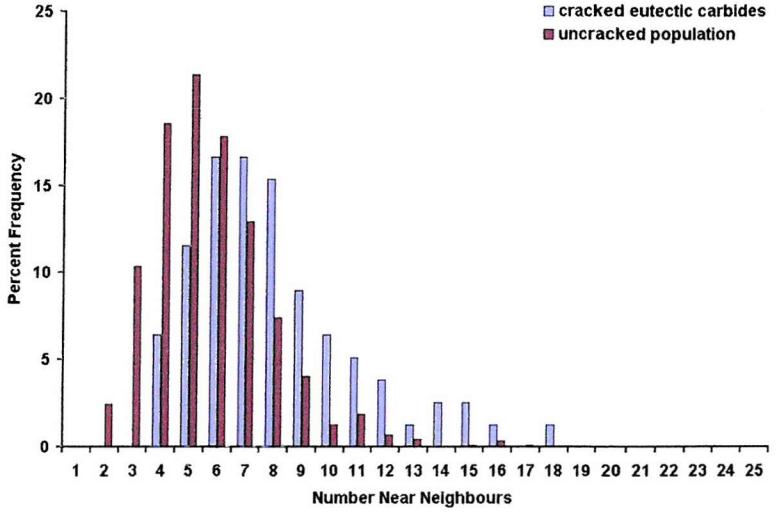

Figure 7.20: Characterisation of crack initiating eutectic carbides: Number of near neighbours.

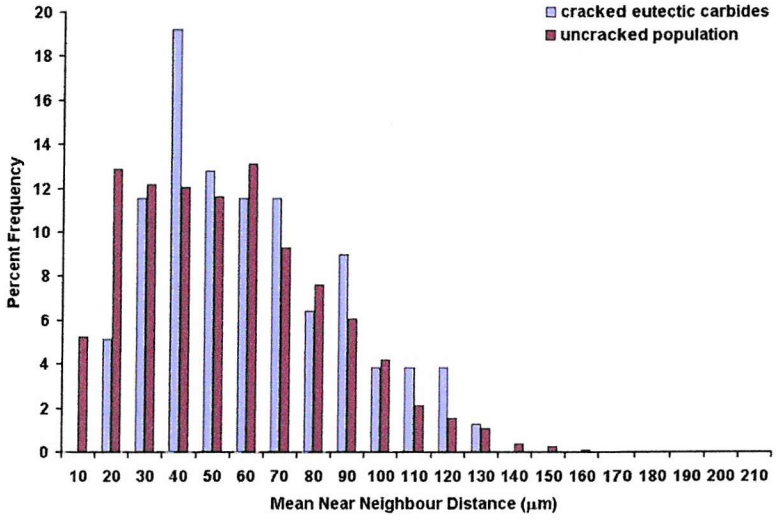

Figure 7.21: Characterisation of crack initiating eutectic carbides: Mean near neighbour distance.

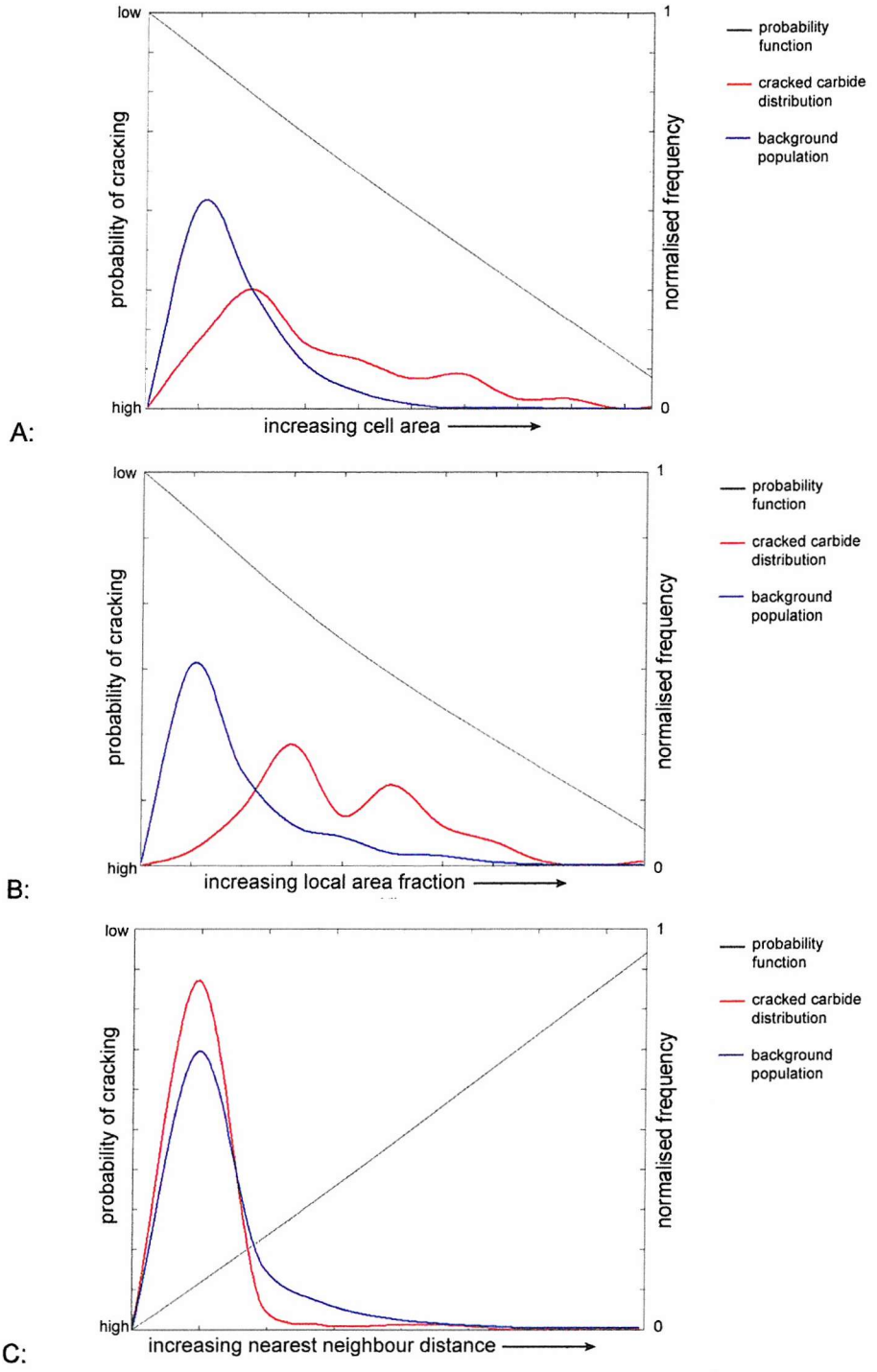

Figure 7.22: SUPANOVA generated univariate terms for classifcation of crack initiating carbides in '800/260' short fatigue crack specimens with associated data-spread. A: Cell area. B: Local area fraction. C: Neaest neighbour distance.

A:

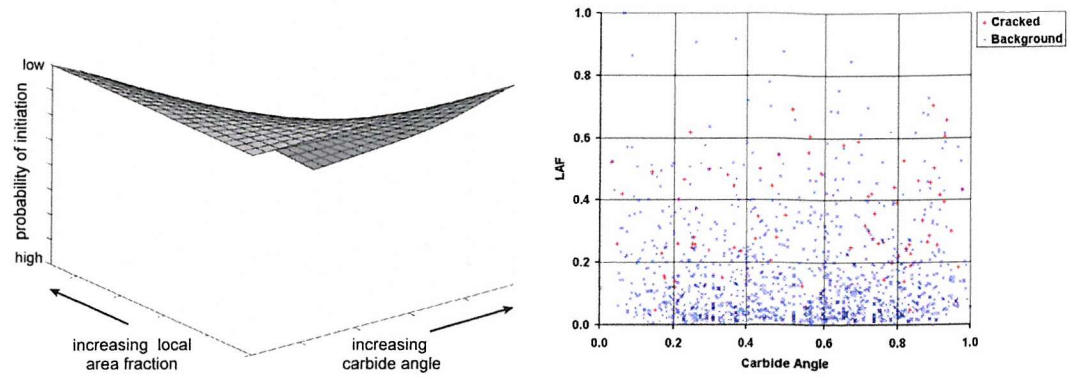

B:

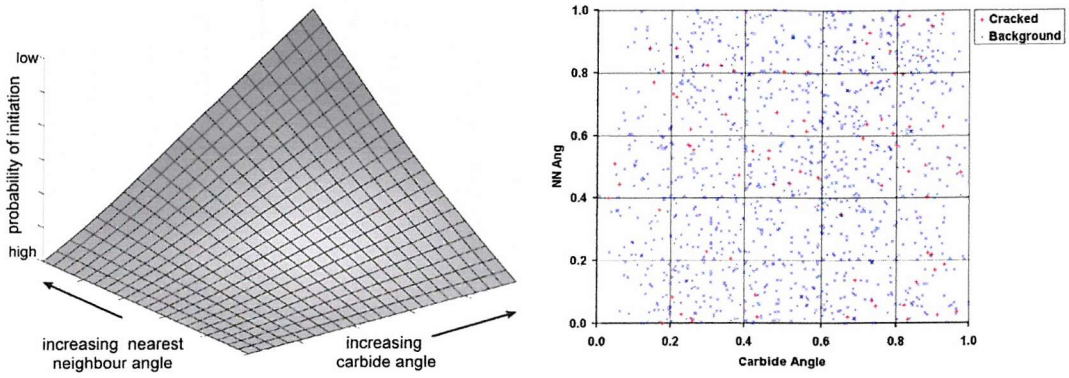

Figure 7.23: SUPANOVA generated bivariate terms for classification of crack initiating carbides in '800/260' short fatigue crack specimens. Spread of data for each term shown alongside. A: Carbide angle vs. local area fraction. B: Carbide angle vs. nearest neighbour angle.

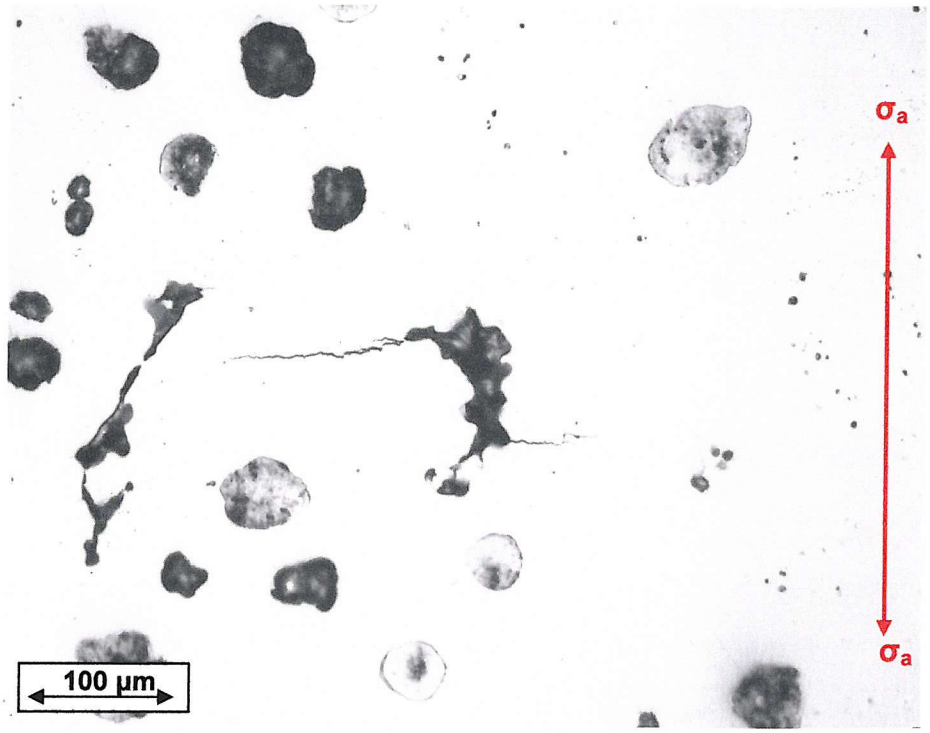

Figure 7.24: An example of short fatigue crack initiation at a surface pore in '900/390' specimens. Image captured digitally from an acetate replica.

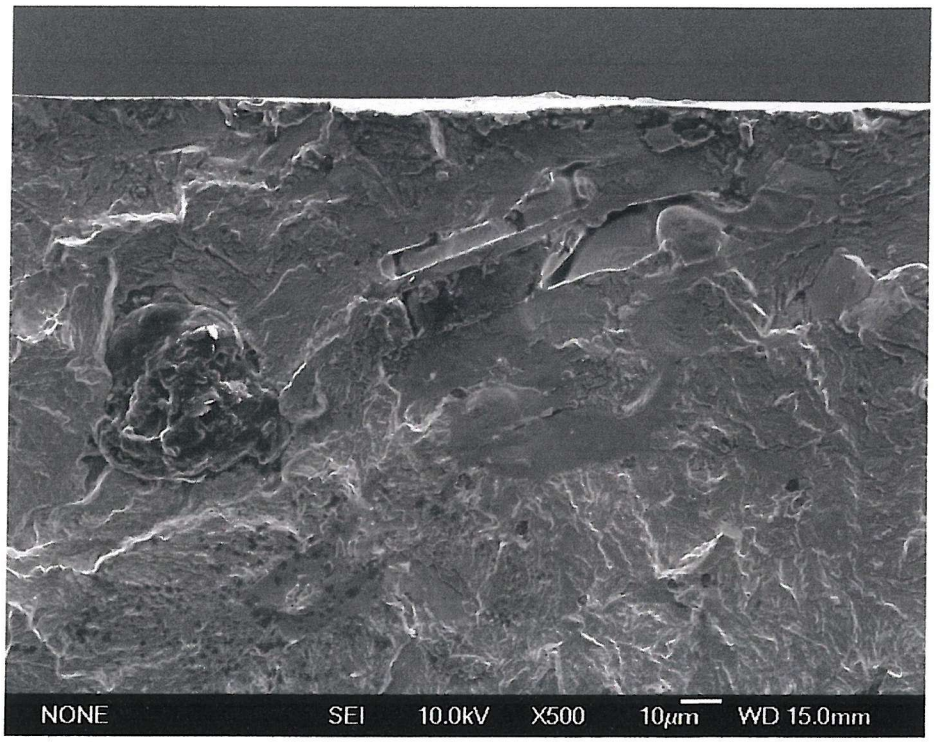

Figure 7.25: An example of short fatigue crack initiation at a sub surface pore in '900/390' specimens.

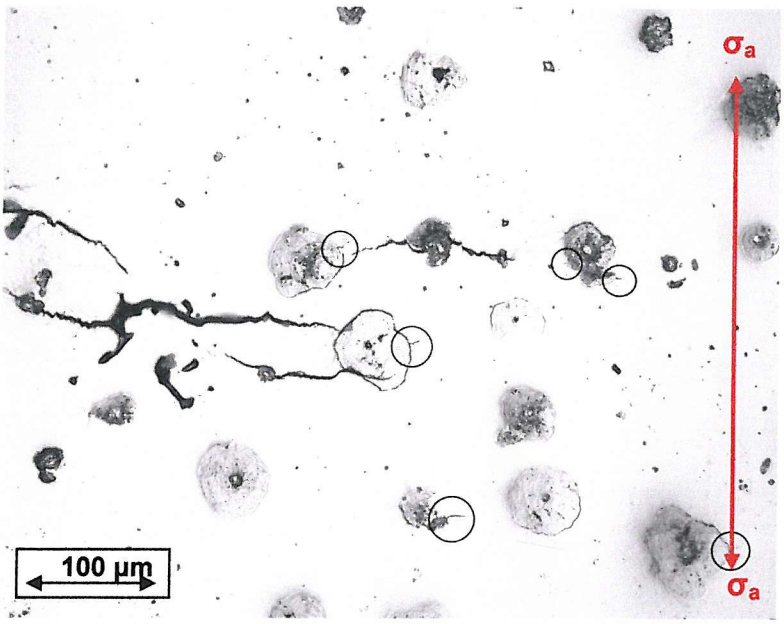

Figure 7.26: Image from '900/390' short fatigue crack replica records. Crack initiation ahead of advancing dominant crack tip.

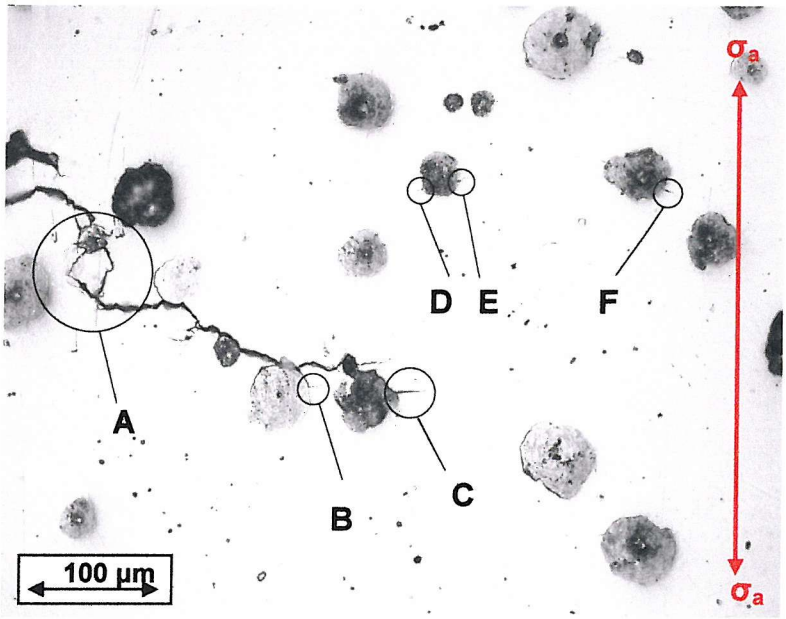

Figure 7.27: Image from '900/390' short fatigue crack replica records. Crack initiation ahead of advancing dominant crack tip and subsequent coalescence event.

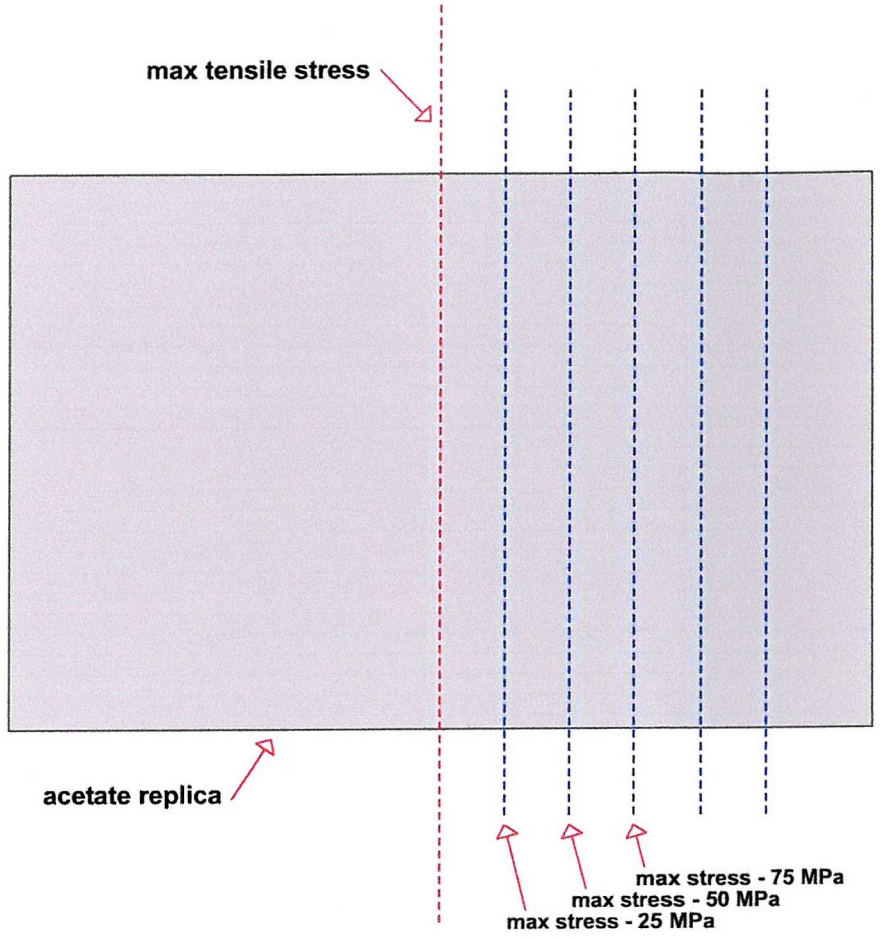

Figure 7.28: Stress regions on replica maps.

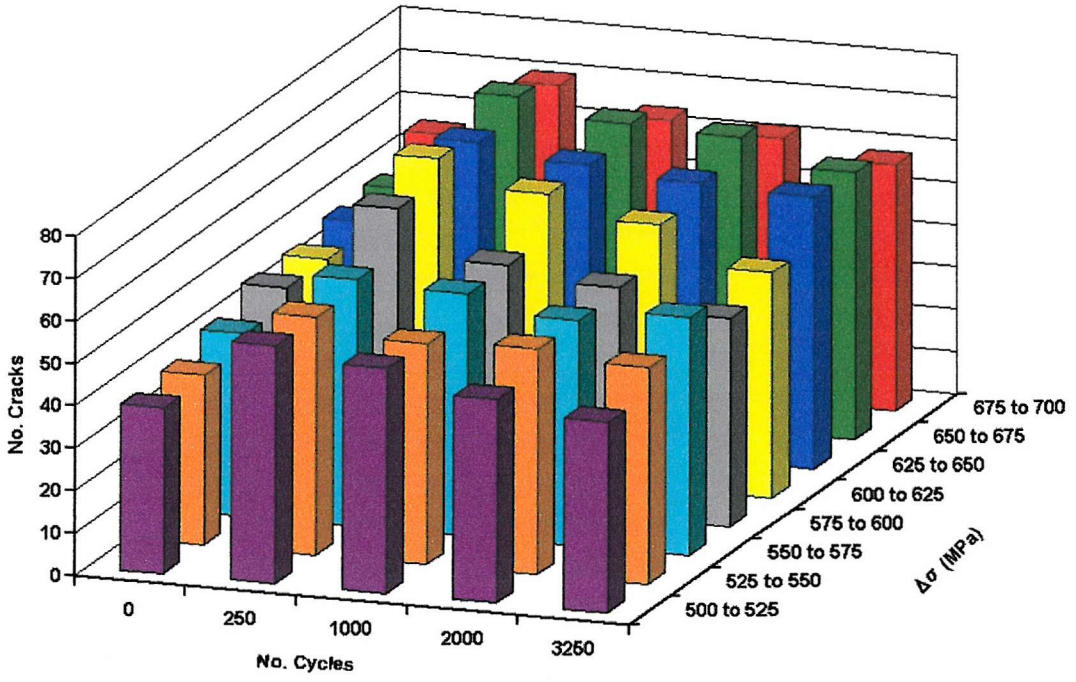

Figure 7.29: Number of cracks as a function of applied stress and number of elapsed fatigue cycles for '800/260' specimen showing greatest number of micro-cracks

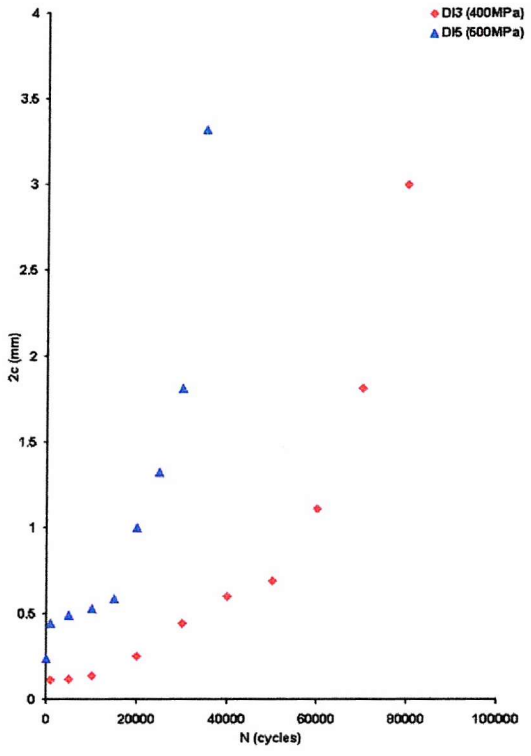

Figure 7.30: Crack length plotted as a function of the number of elapsed fatigue cycles for as-cast ductile iron specimens.

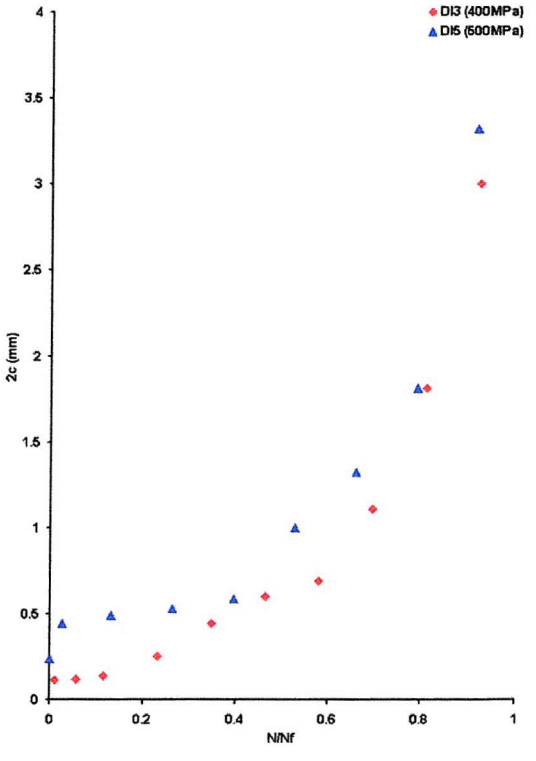

Figure 7.31: Crack length plotted as a function of normalised lifetime for as-cast ductile iron specimens.

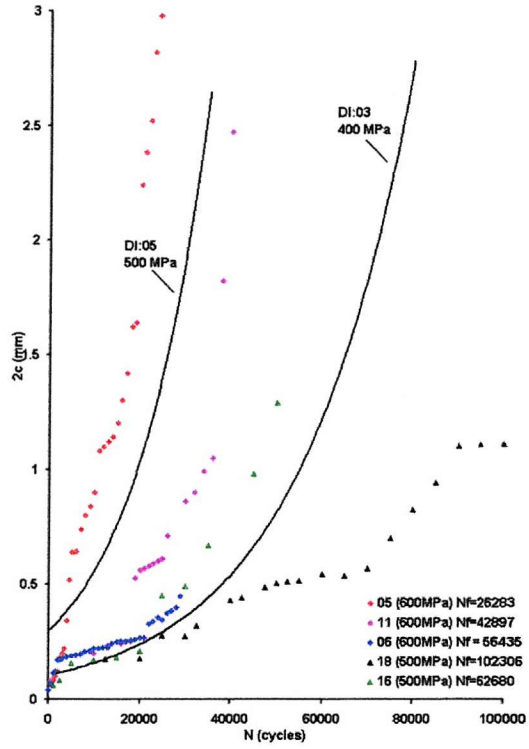

Figure 7.32: Crack length plotted as a function of the number of elapsed fatigue cycles for '800/260' specimens.

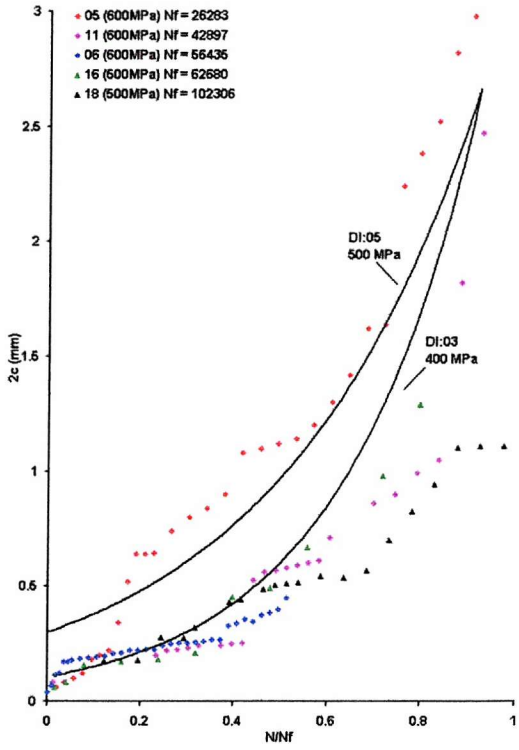

Figure 7.33: Crack length plotted as a function of normalised lifetime for '800/260' specimens.

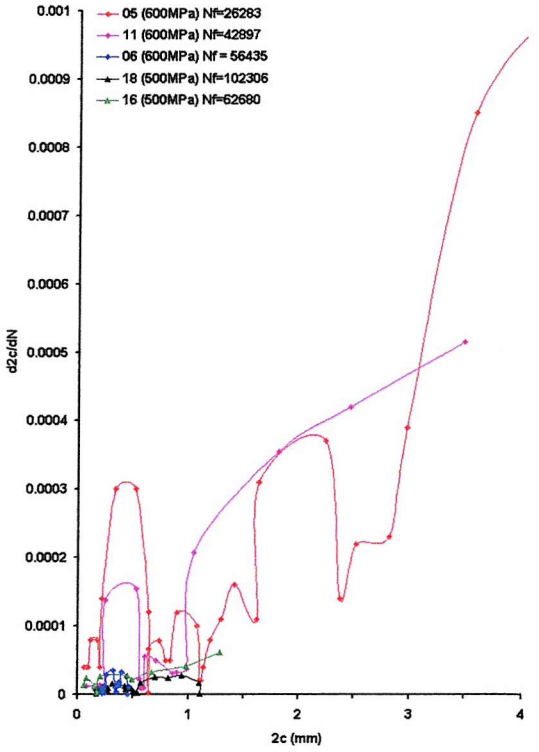

Figure 7.34: Crack growth rate plotted as a function of crack length for '800/260' short crack specimens.

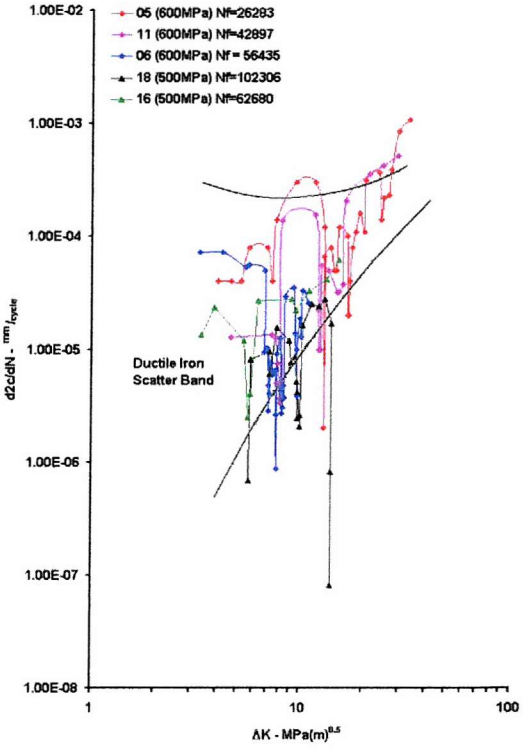

Figure 7.35: Crack growth rates plotted as a function of ΔK for '800/260' short fatigue crack specimens.

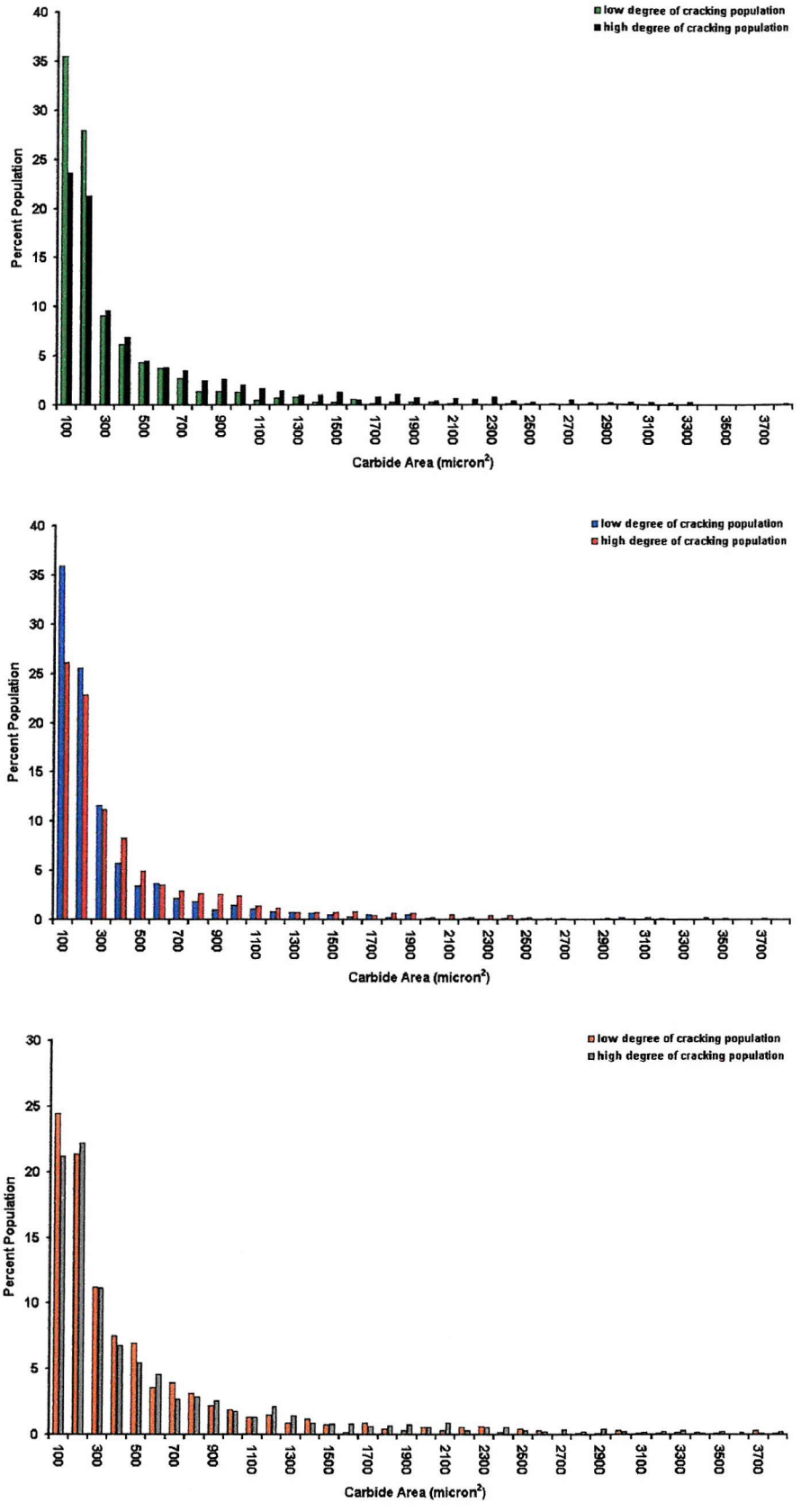

Figure 7.36: Carbide area (from top to bottom results from specimens tested at 700 MPa, 600 MPa and 500 MPa)

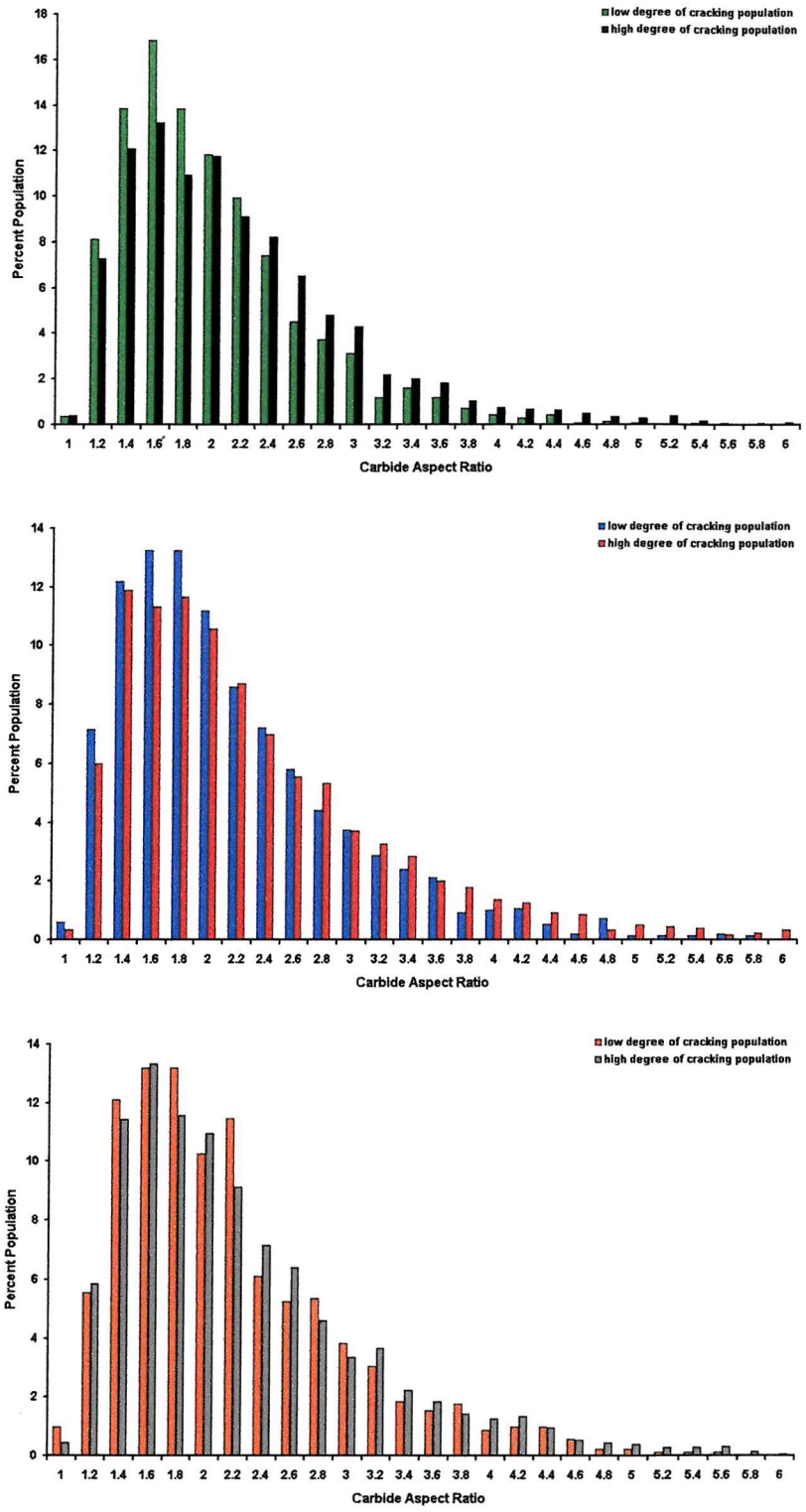

Figure 7.37: Carbide Aspect Ratio (from top to bottom results from specimens tested at 700 MPa, 600 MPa and 500 MPa)

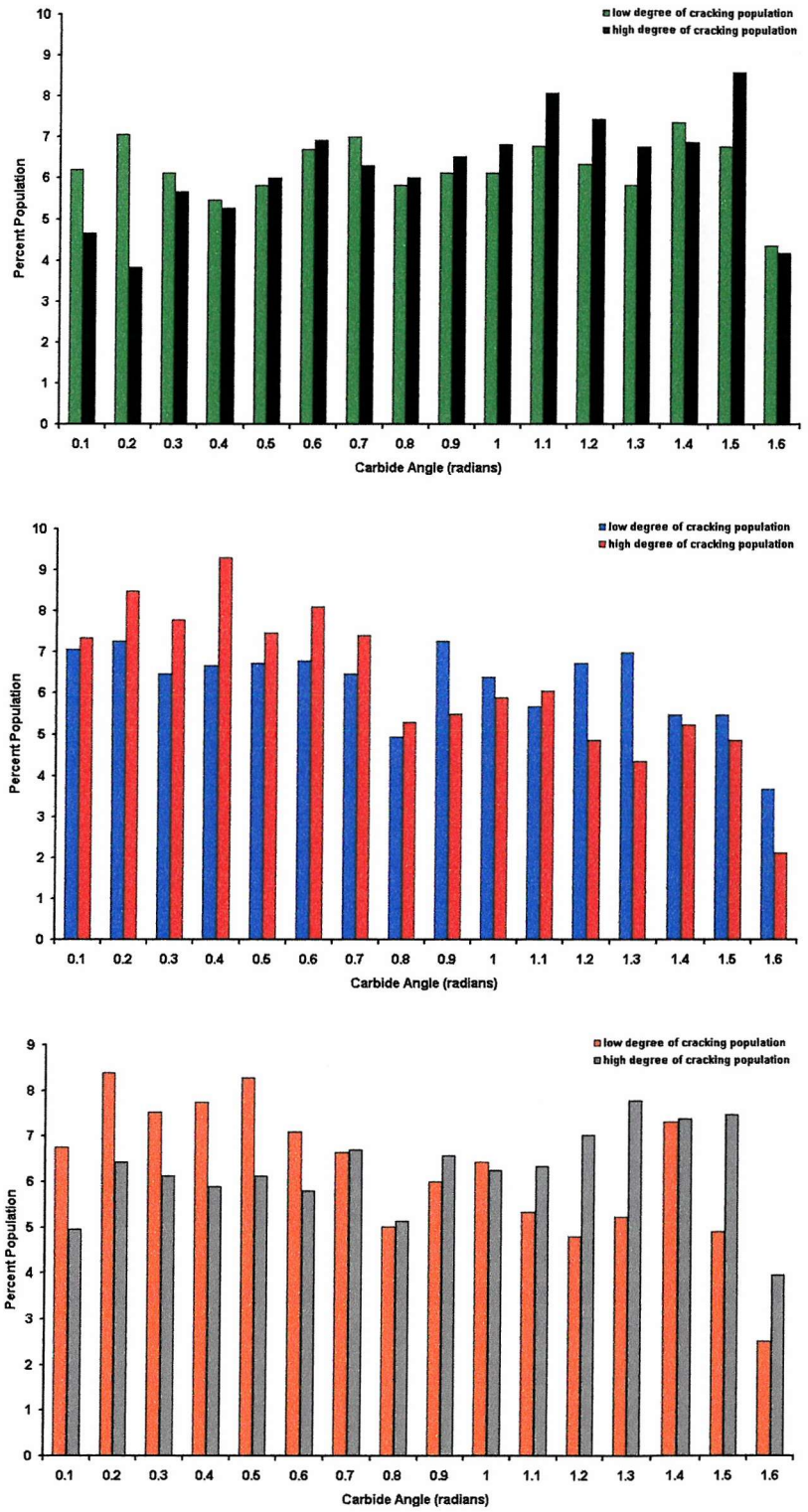

Figure 7.38: Carbide Angle (from top to bottom results from specimens tested at 700 MPa, 600 MPa and 500 MPa)

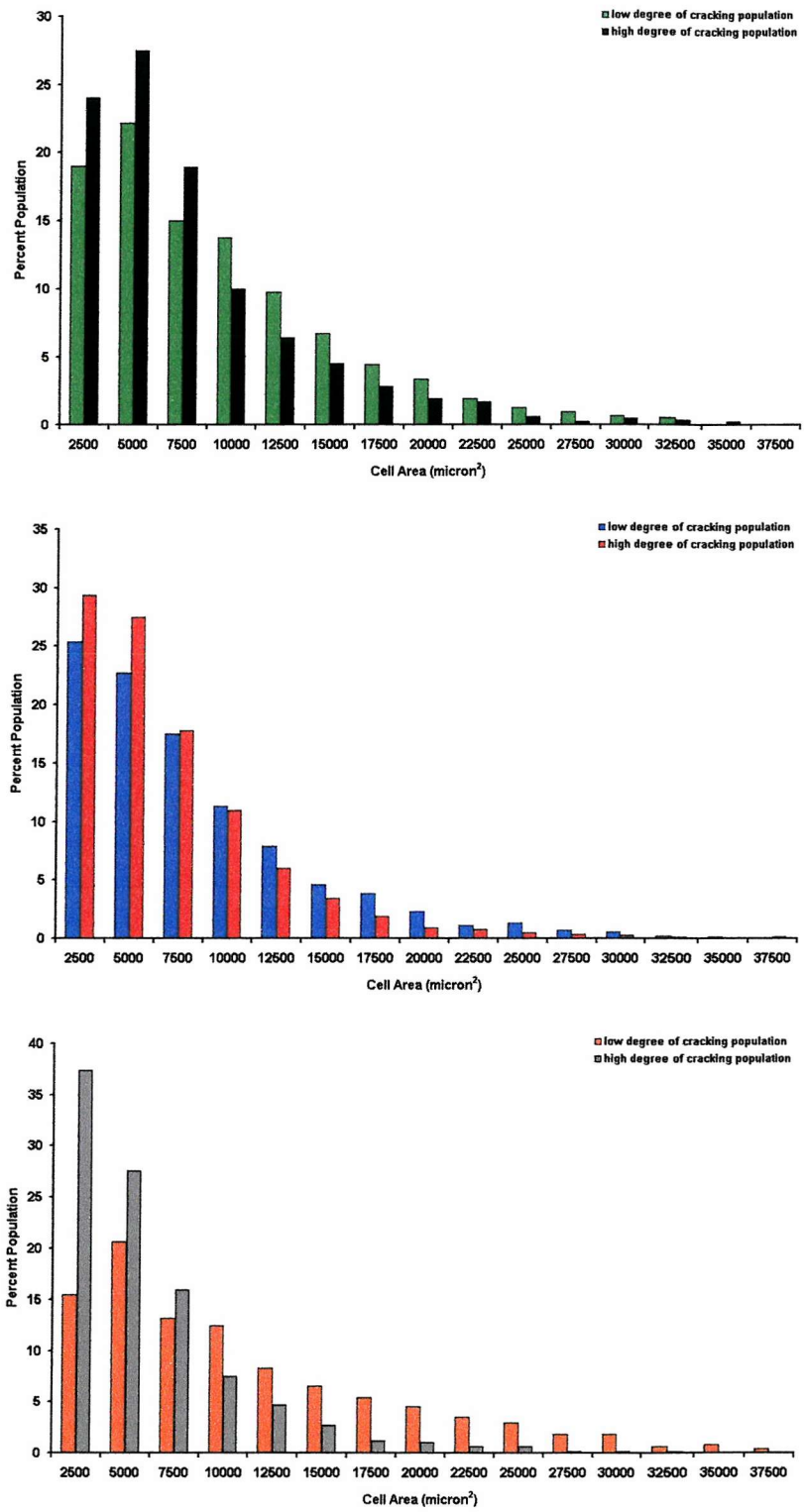

Figure 7.39: Cell Area (from top to bottom results from specimens tested at 700 MPa, 600 MPa and 500 MPa)

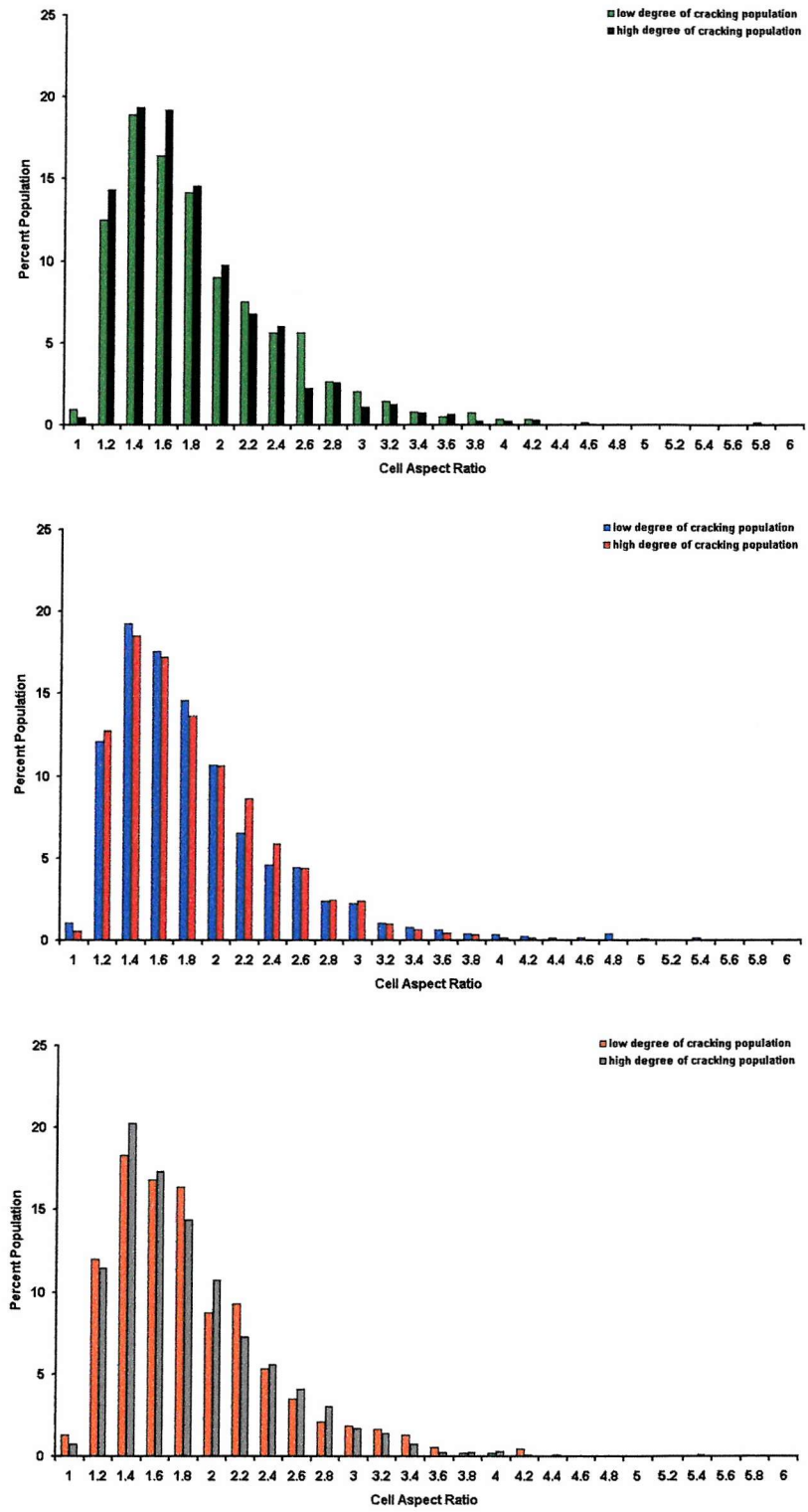

Figure 7.40: Cell Aspect Ratio (from top to bottom results from specimens tested at 700 MPa, 600 MPa and 500 MPa)

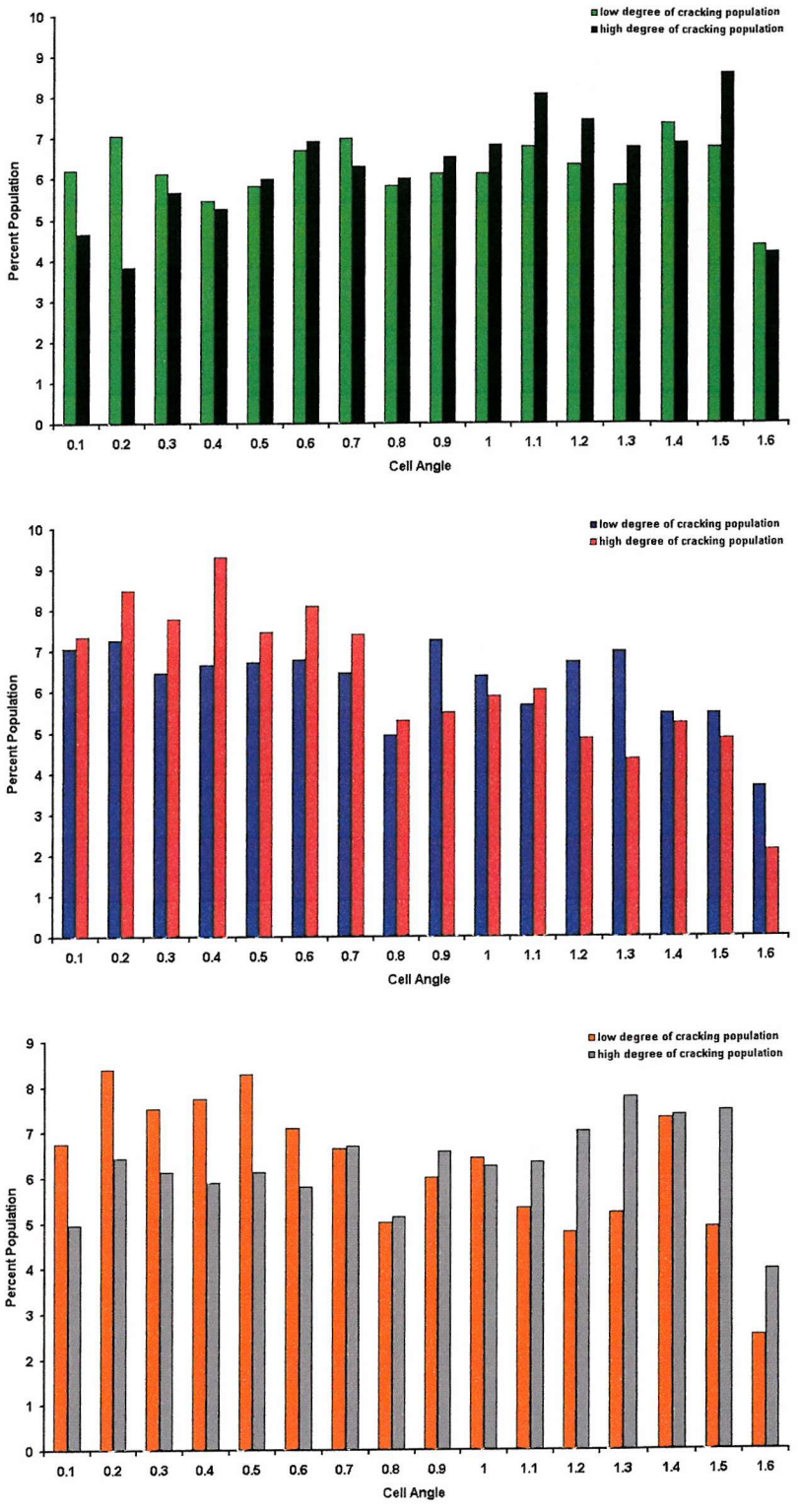

Figure 7.41: Cell Angle (from top to bottom results from specimens tested at 700 MPa, 600 MPa and 500 MPa)

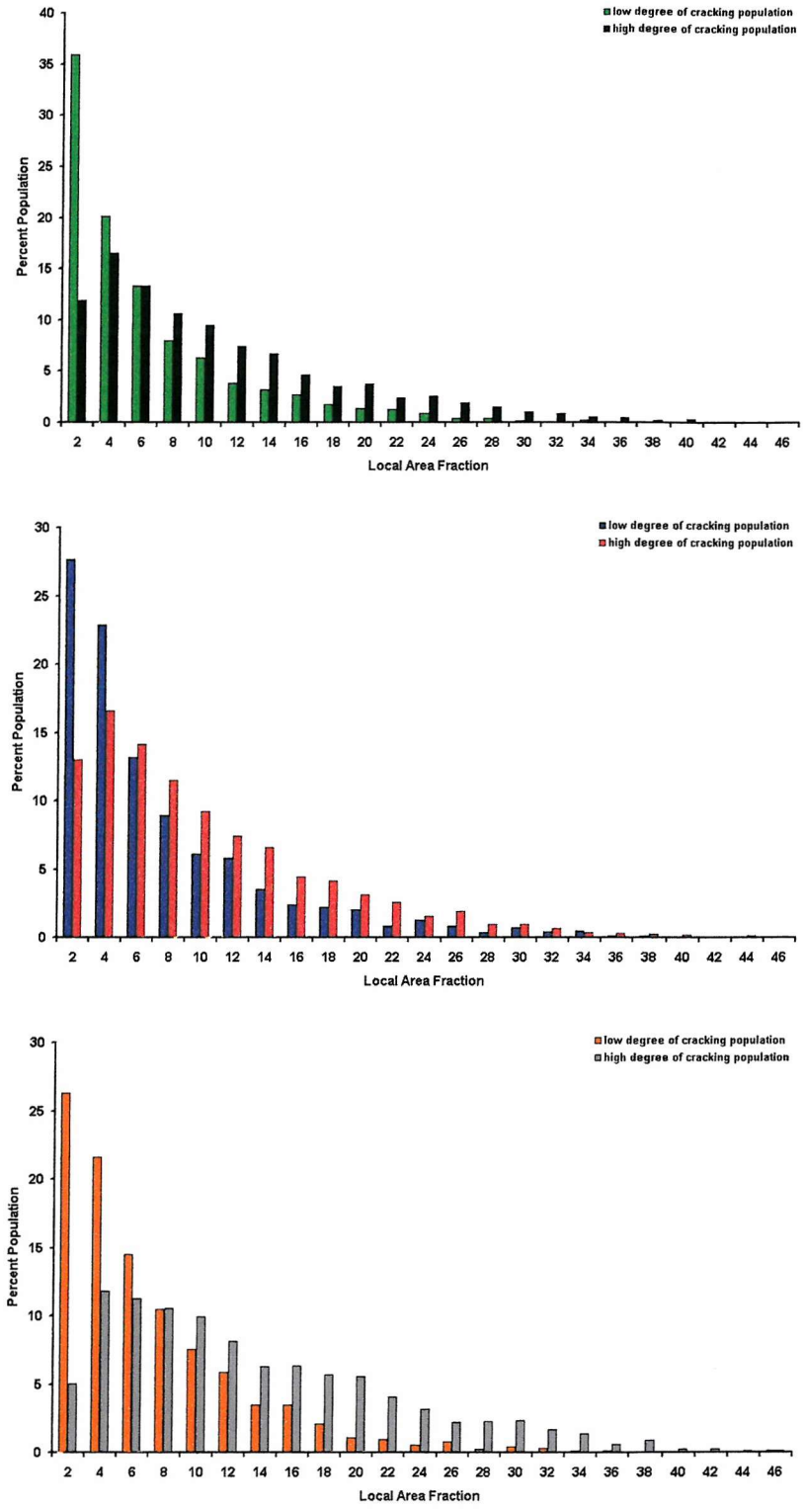

Figure 7.42: Local Area Fraction (from top to bottom results from specimens tested at 700 MPa, 600 MPa and 500 MPa)

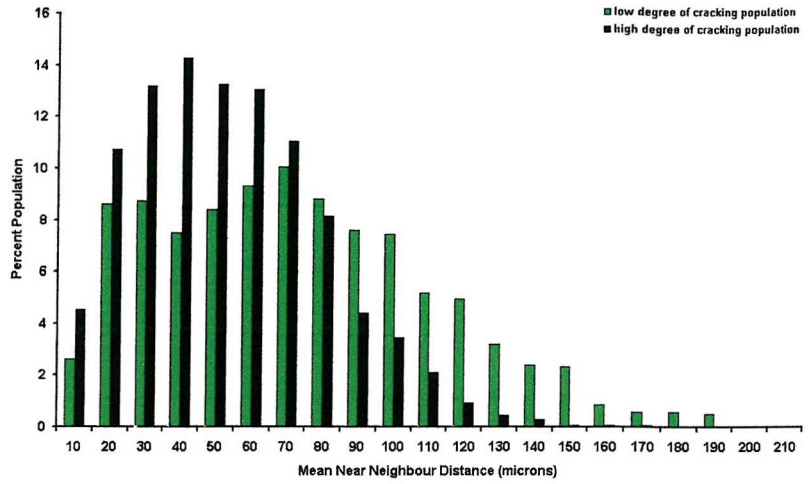

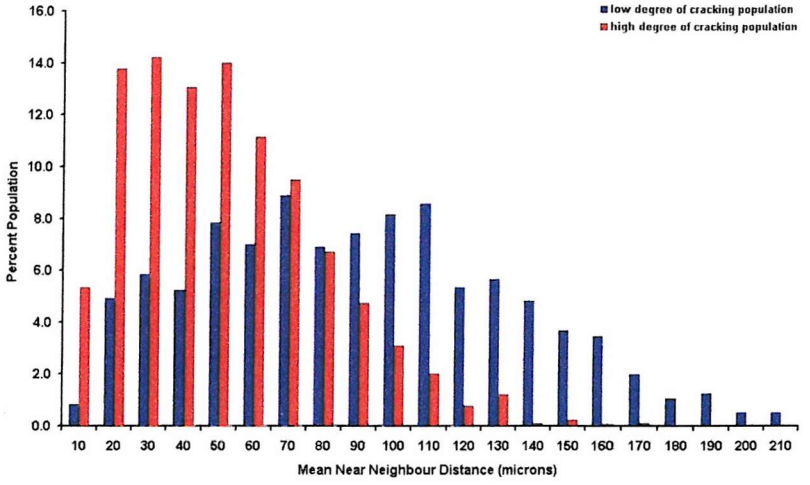

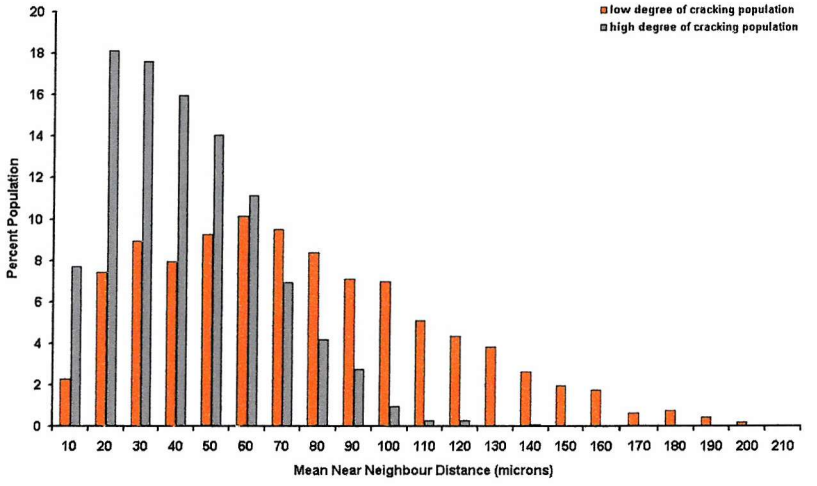

Figure 7.43: Number of Near Neighbours (from top to bottom results from specimens tested at 700 MPa, 600 MPa and 500 MPa)

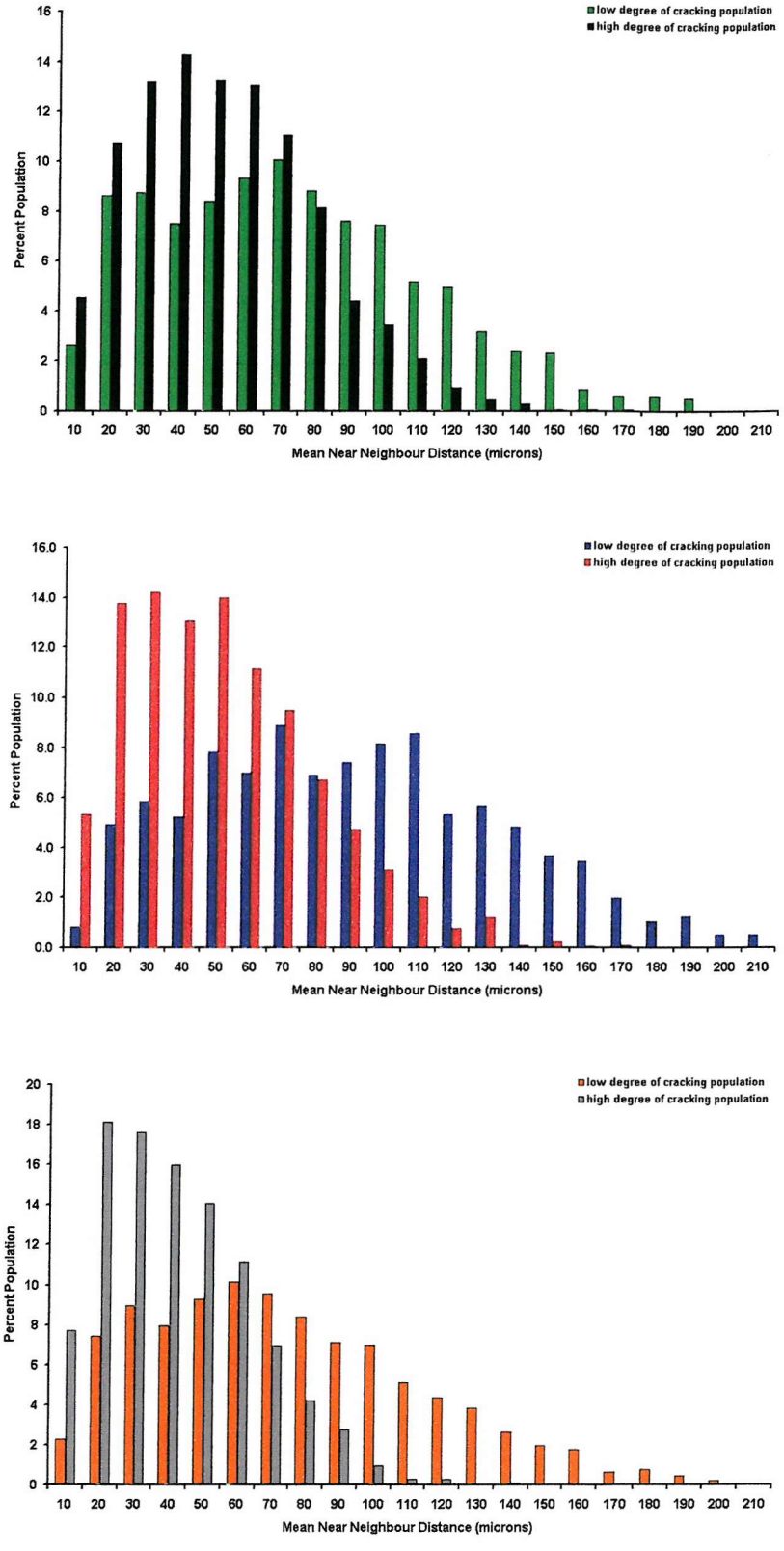

Figure 7.44: Mean Near Neighbour Distance (from top to bottom results from specimens tested at 700 MPa, 600 MPa and 500 MPa)

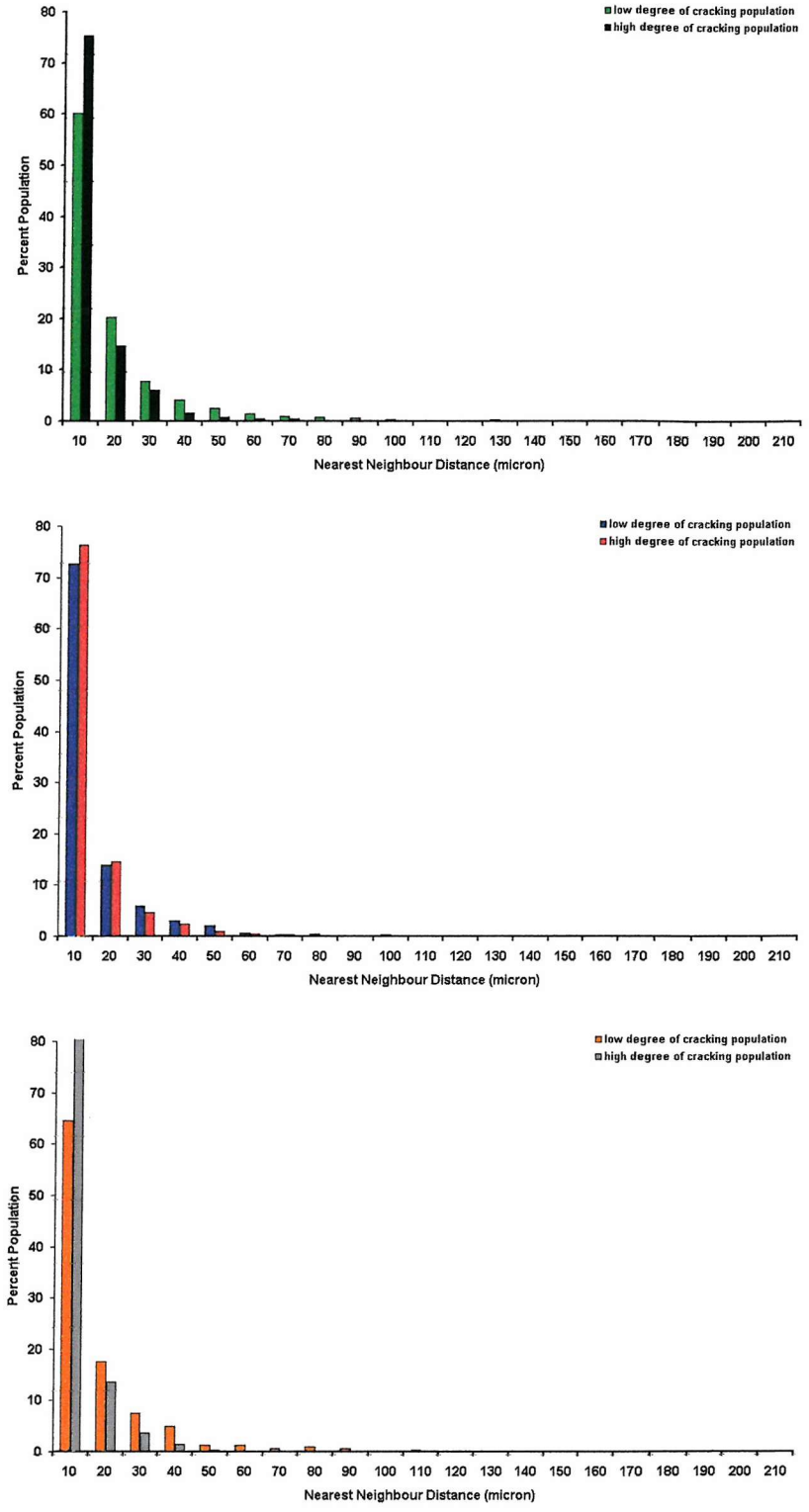

Figure 7.45: Nearest Neighbour Distance (from top to bottom results from specimens tested at 700 MPa, 600 MPa and 500 MPa)

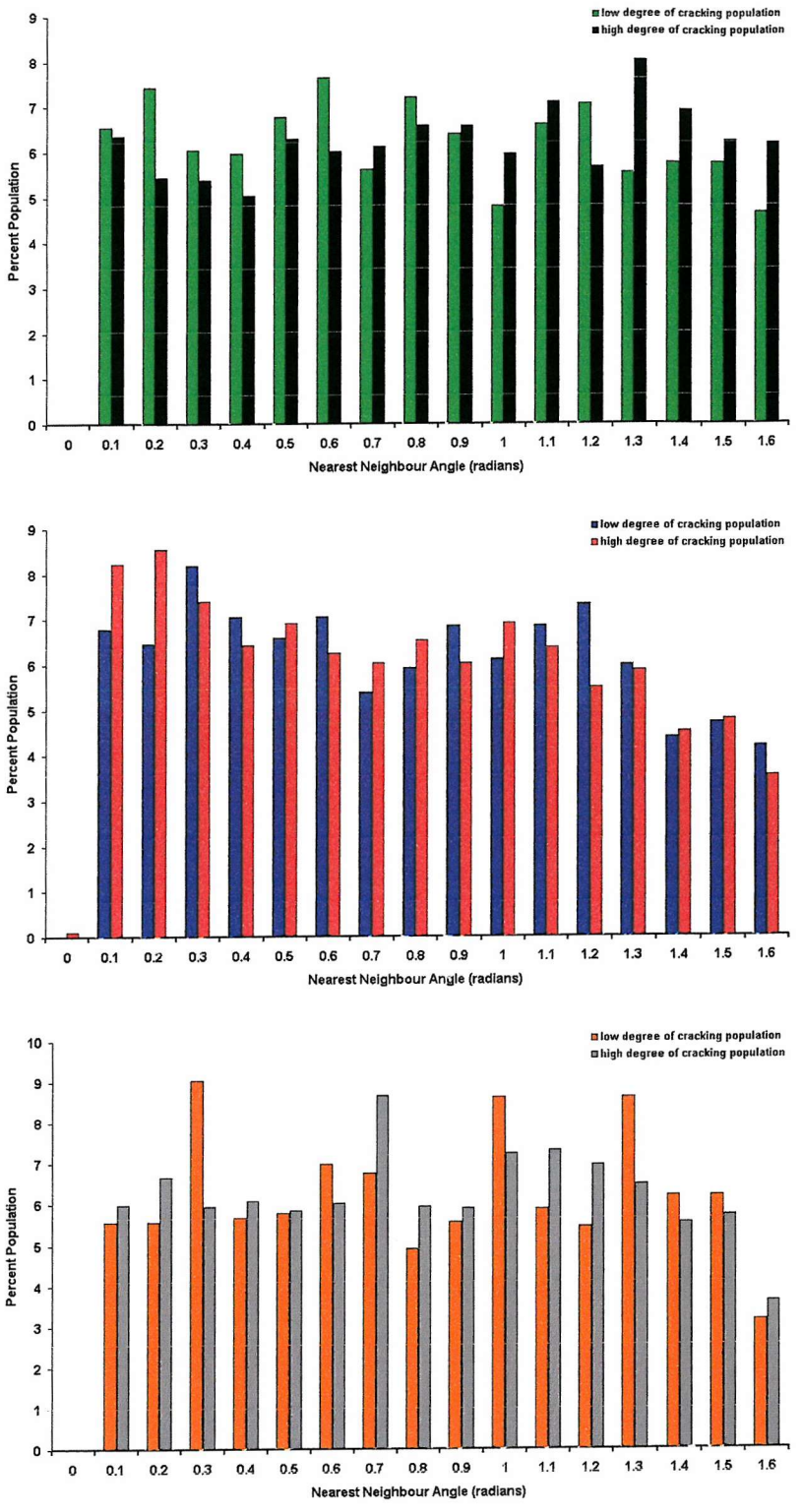

Figure 7.46: Nearest Neighbour Angle (from top to bottom results from specimens tested at 700 MPa, 600 MPa and 500 MPa)

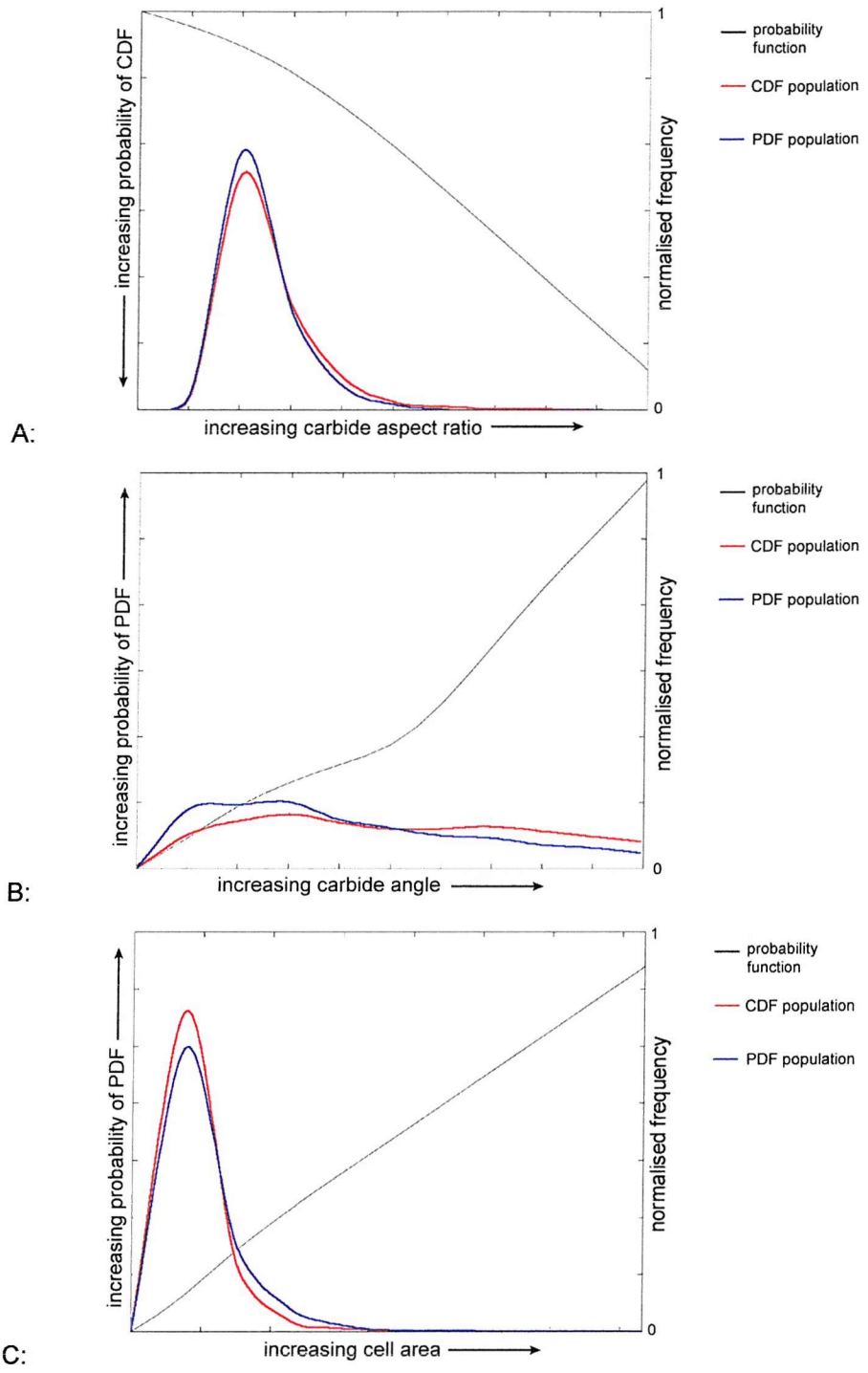

Figure 7.47: SUPANOVA generated univariate terms for classification of highly cracked carbide populations in '800/260' short fatigue crack specimens with associated data-spread. A: Carbide aspect ratio. B: carbide angle. C: Cell area.

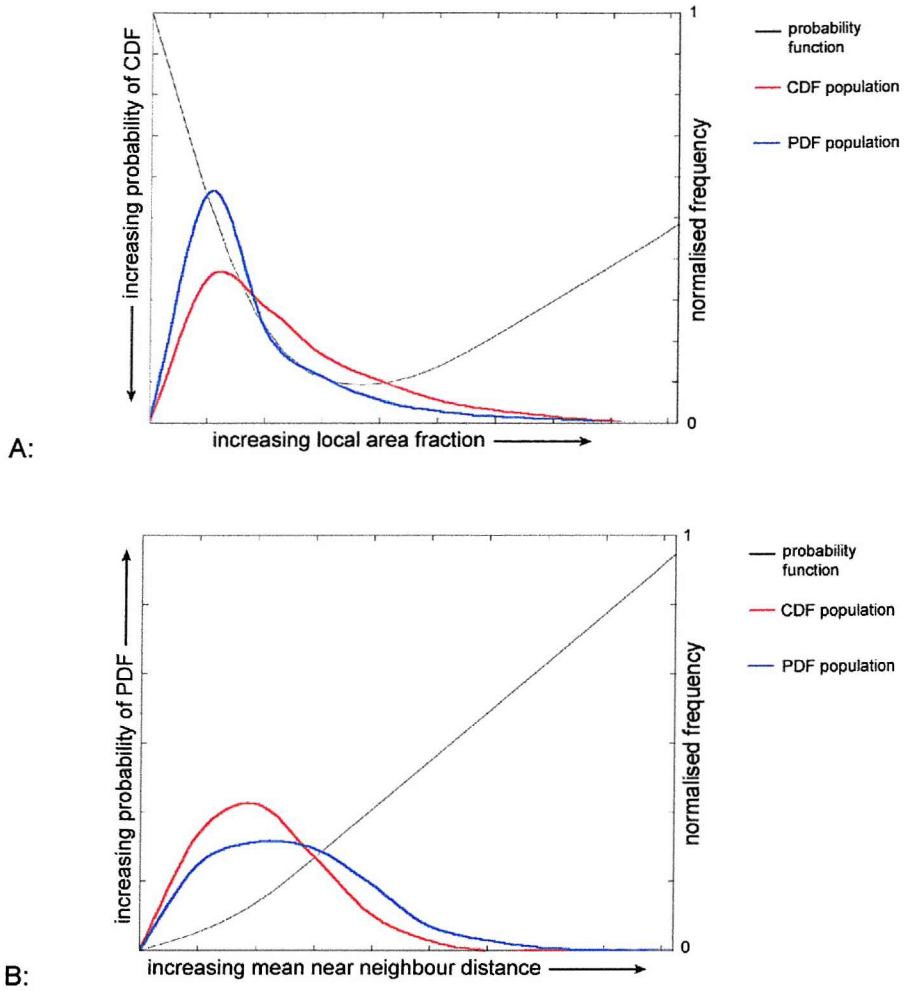

Figure 7.48: SUPANOVA generated univariate terms for comparison of carbide populations in '800/260' short fatigue crack specimens. A: Local area fraction. B: Mean near neighbour distance.

A:

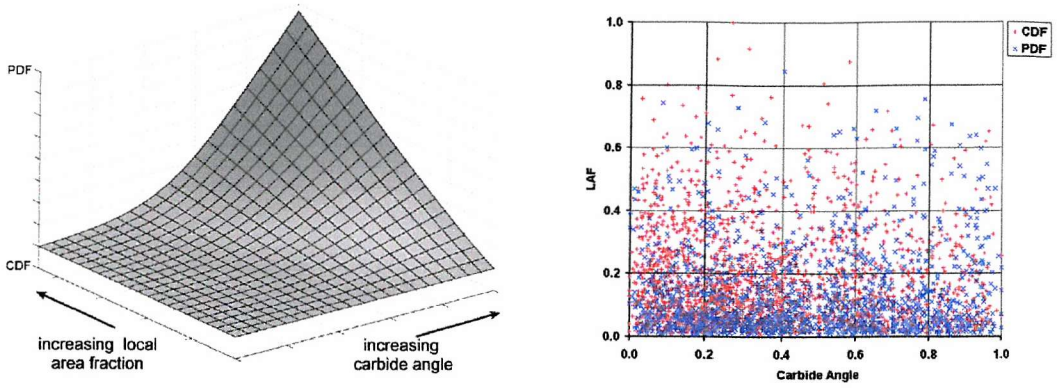

B:

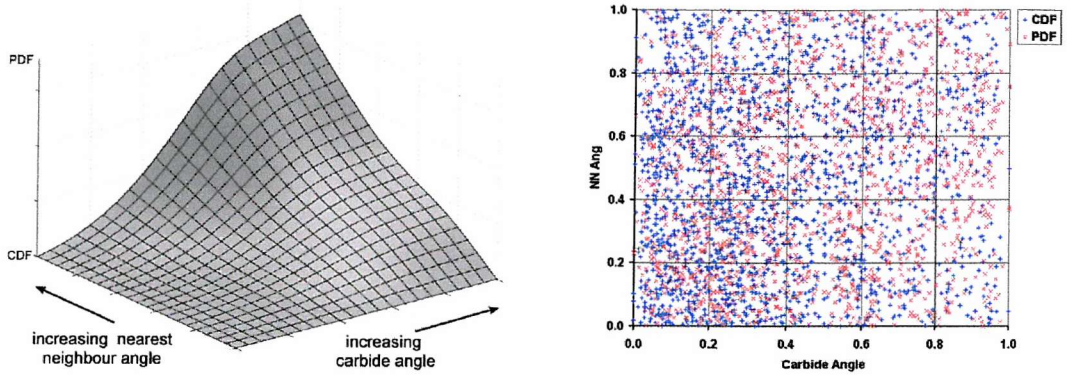

Figure 7.49: SUPANOVA generated bivariate terms for comparison of carbide populations in '800/260' short fatigue crack specimens. Spread of data for each term shown alongside. A: Local area fraction vs. carbide angle. B: Nearest neighbour angle vs. carbide angle.

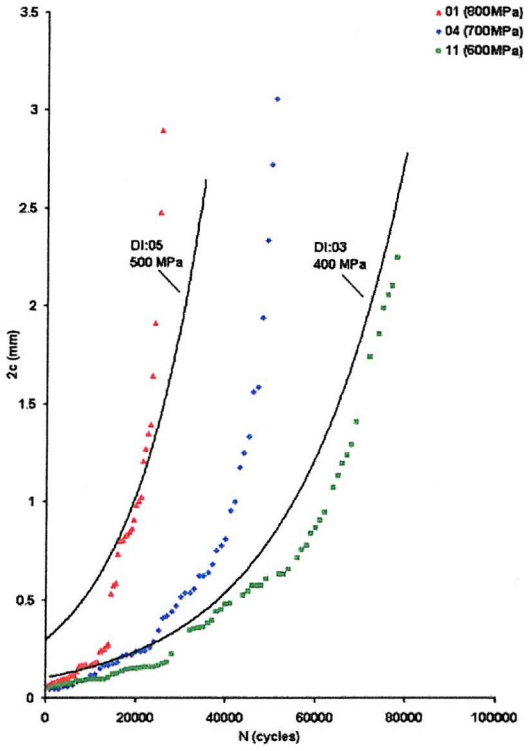

Figure 7.50: Crack length plotted as a function of the number of elapsed fatigue cycles for '900/390' specimens.

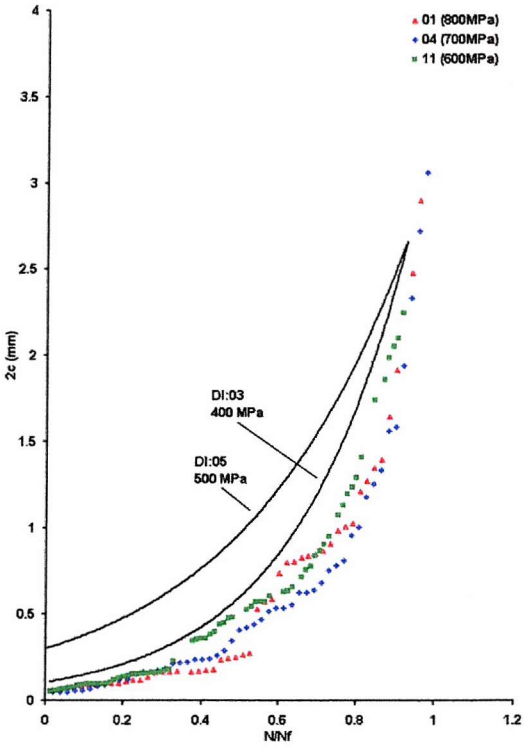

Figure 7.51: Crack length plotted as a function of normalised lifetime for '900/390' specimens.

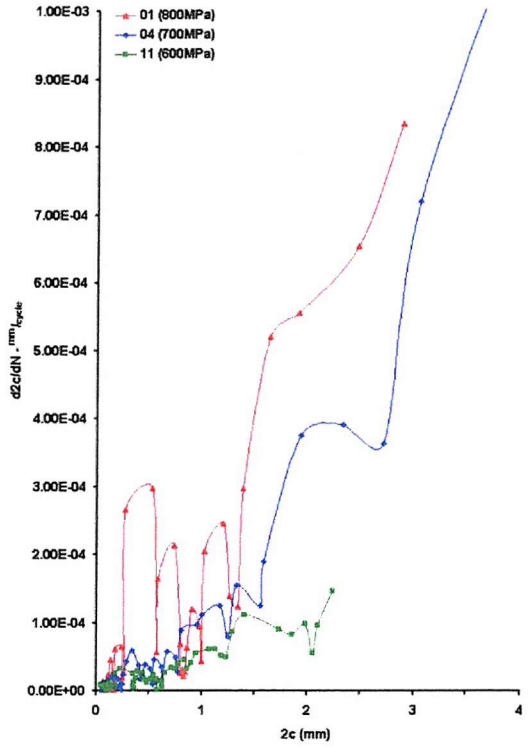

Figure 7.52: Crack growth rate plotted as a function of crack length for '900/390' short crack specimens.

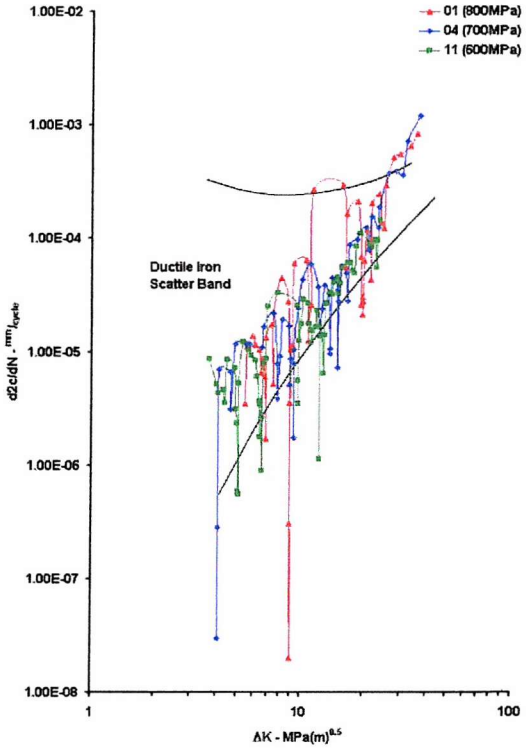

Figure 7.53: Crack growth rates plotted as a function of ΔK for '900/390' short fatigue crack specimens.

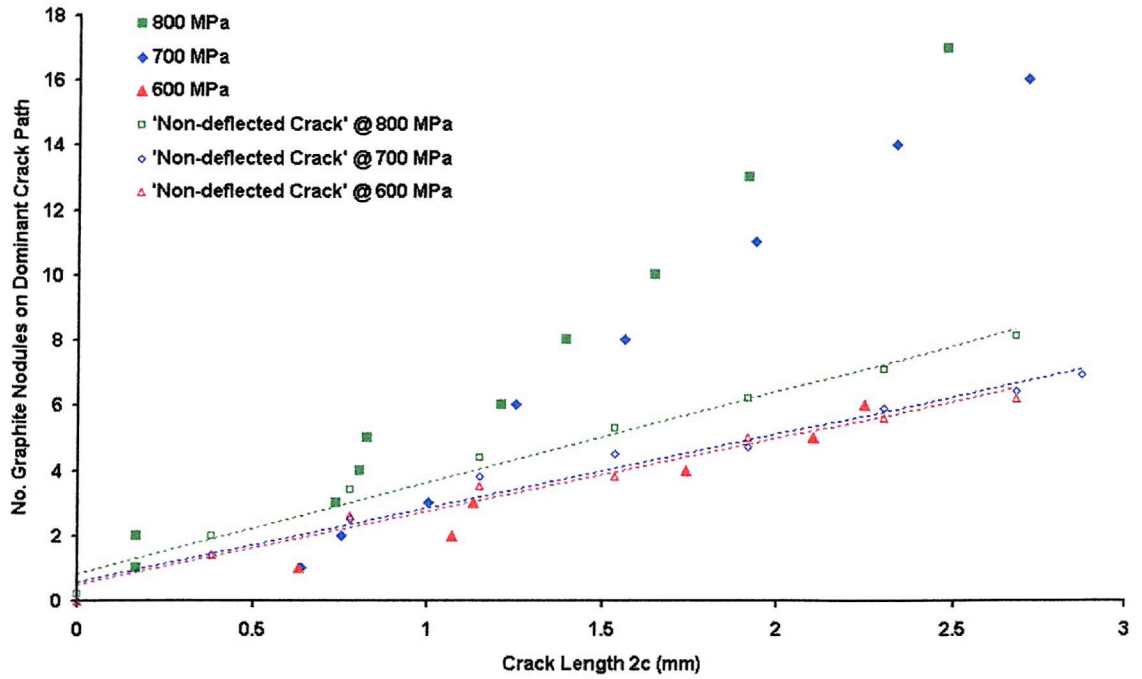

Figure 7.54: Investigation of the influence of graphite nodules on '900/390' fatigue crack propagation; the variation of the number of graphite nodules on the dominant crack path with crack length. Compared to simulated non-deflected cracks for each stress level.

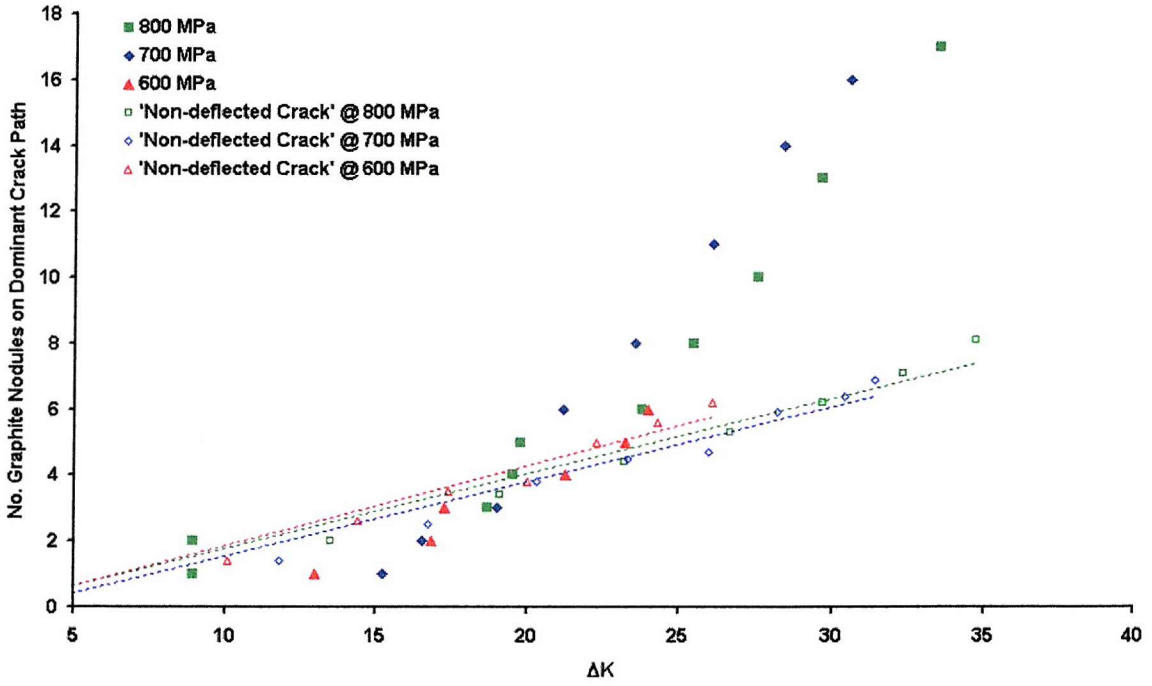

Figure 7.55: Investigation of the influence of graphite nodules on '900/390' fatigue crack propagation; the variation of the number of graphite nodules on the dominant crack path with ΔK. Compared to simulated non-deflected cracks for each stress level.

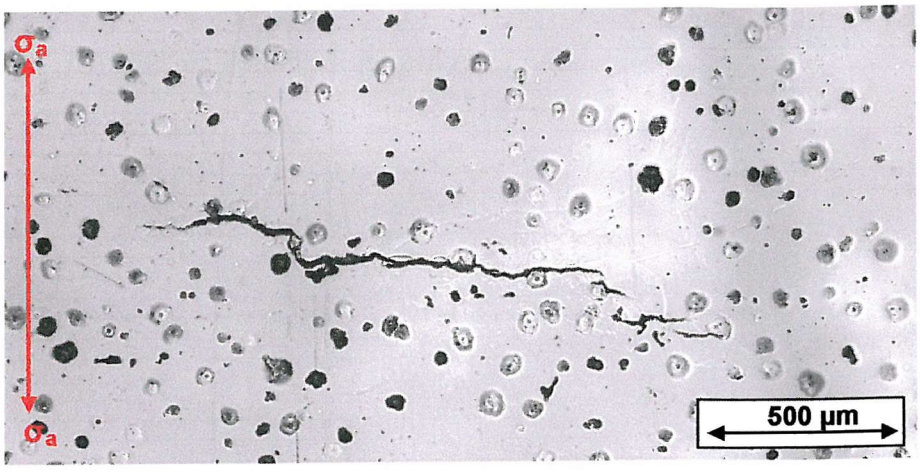

Figure 7.56: Dominant crack on short fatigue crack specimen '900/390:01' at 90% life. Specimen tested with σ_{max} = 800 MPa.

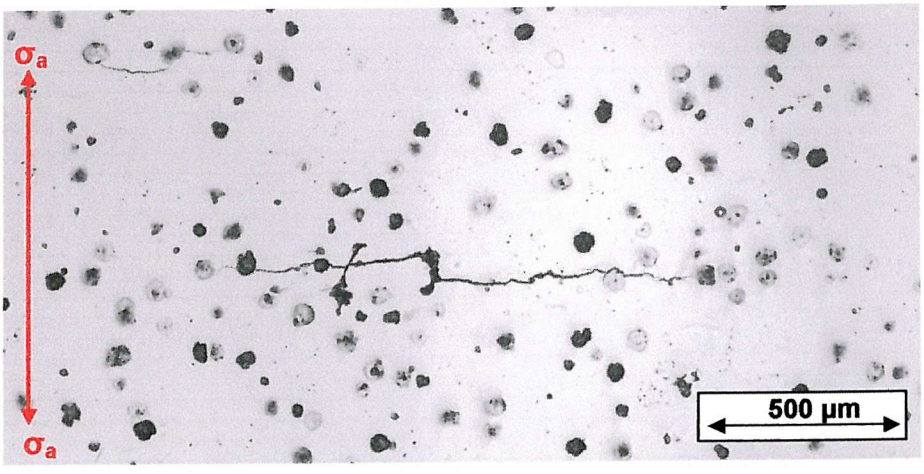

Figure 7.57: Dominant crack on short fatigue crack specimen '900/390:04' at 90% life. Specimen tested with σ_{max} = 700 MPa.

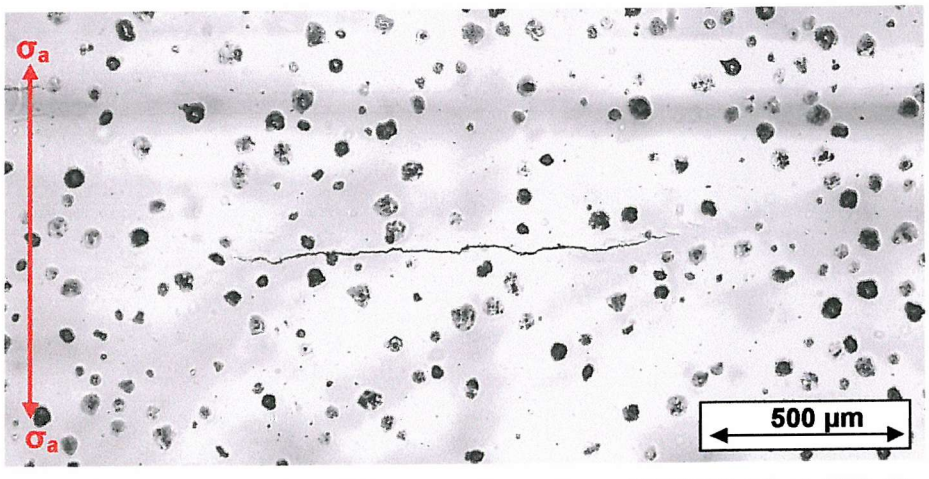

Figure 7.58: Dominant crack on short fatigue crack specimen '900/390:11' at 90% life. Specimen tested with σ_{max} = 600 MPa.

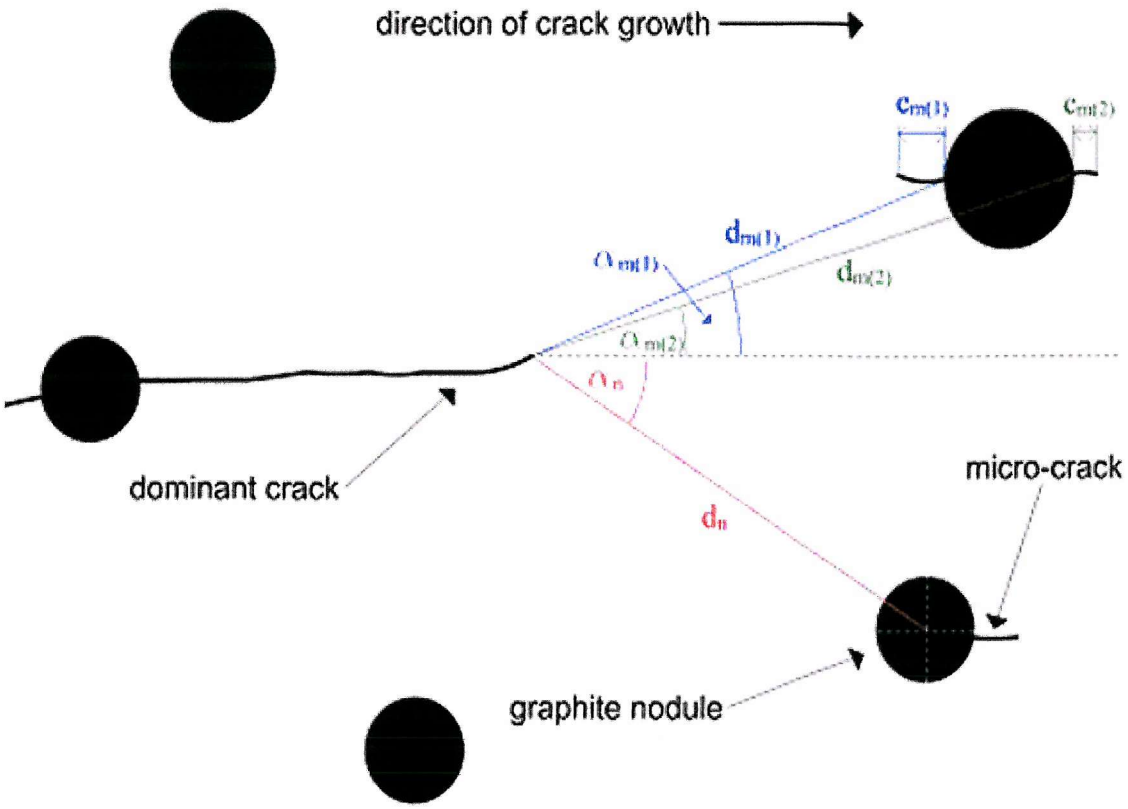

Figure 7.59: Schematic for measurement of micro-crack initiation ahead of the dominant crack tip.

N	=	No. Cycles
c_m	=	Length of micro-crack (µm)
d_m	=	Distance of micro-crack from dominant crack (µm)
d_n	=	Distance of graphite nodule from dominant crack (µm)
a_m	=	Angle of micro-crack from dominant crack (degrees)
a_n	=	Angle of graphite nodule from dominant crack (degrees)
ΔK	=	ΔK of dominant crack (MPa√m)
pz	=	Estimated plastic zone size ahead of crack tip

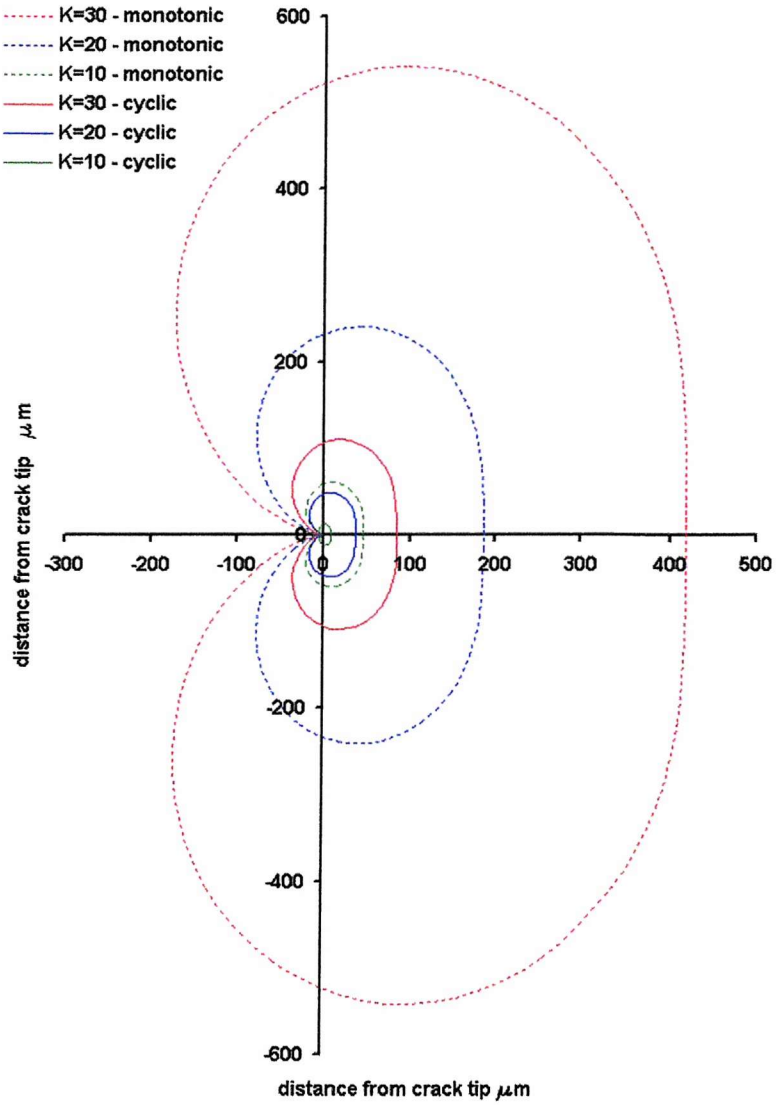

Figure 7.60: Monotonic and cyclic plastic zone shape and size for '900/390' short fatigue crack specimens. Estimated using:

$$r_y = \frac{1}{4\pi}\left(\frac{K_{MAX}}{\sigma_y}\right)^2\left[1+\cos\alpha+\frac{3}{2}\sin^2\alpha\right] \text{ and}$$

$$r_y = \frac{1}{4\pi}\left(\frac{\Delta K}{2\sigma_y}\right)^2\left[1+\cos\alpha+\frac{3}{2}\sin^2\alpha\right] \text{ respectively.}$$

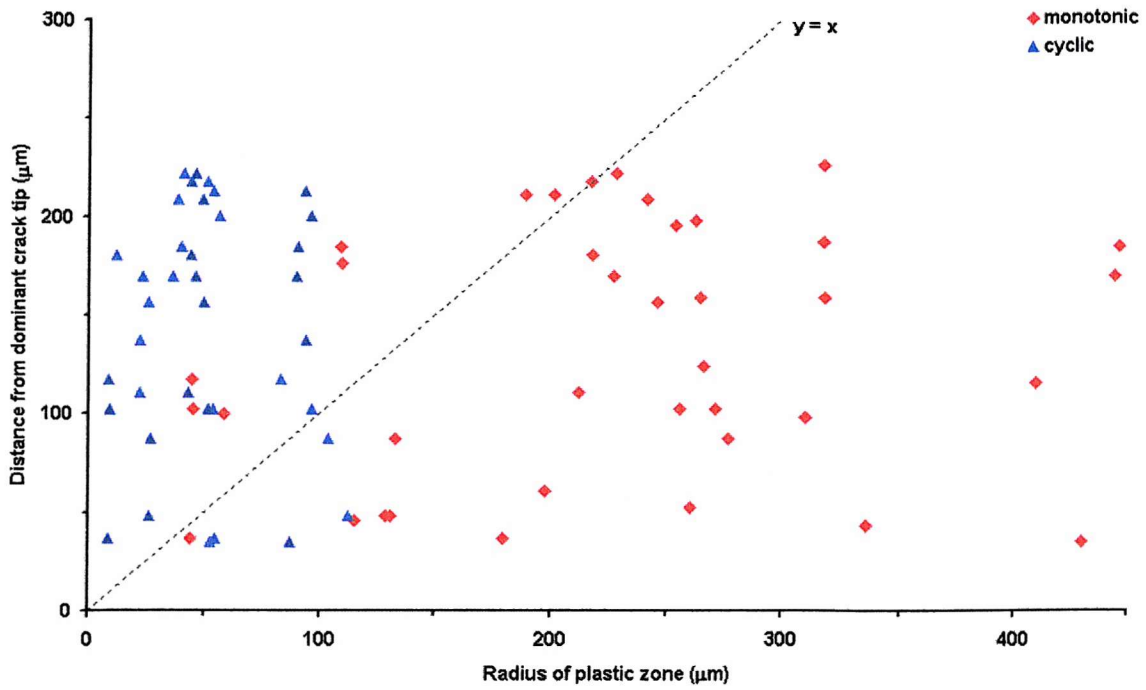

Figure 7.61: Comparison of monotonic and plastic crack-tip plastic zone size and proximity of micro-crack initiation events ahead of the advancing dominant macro-crack for short fatigue crack specimens '900/390:01' and '900/390:04'.

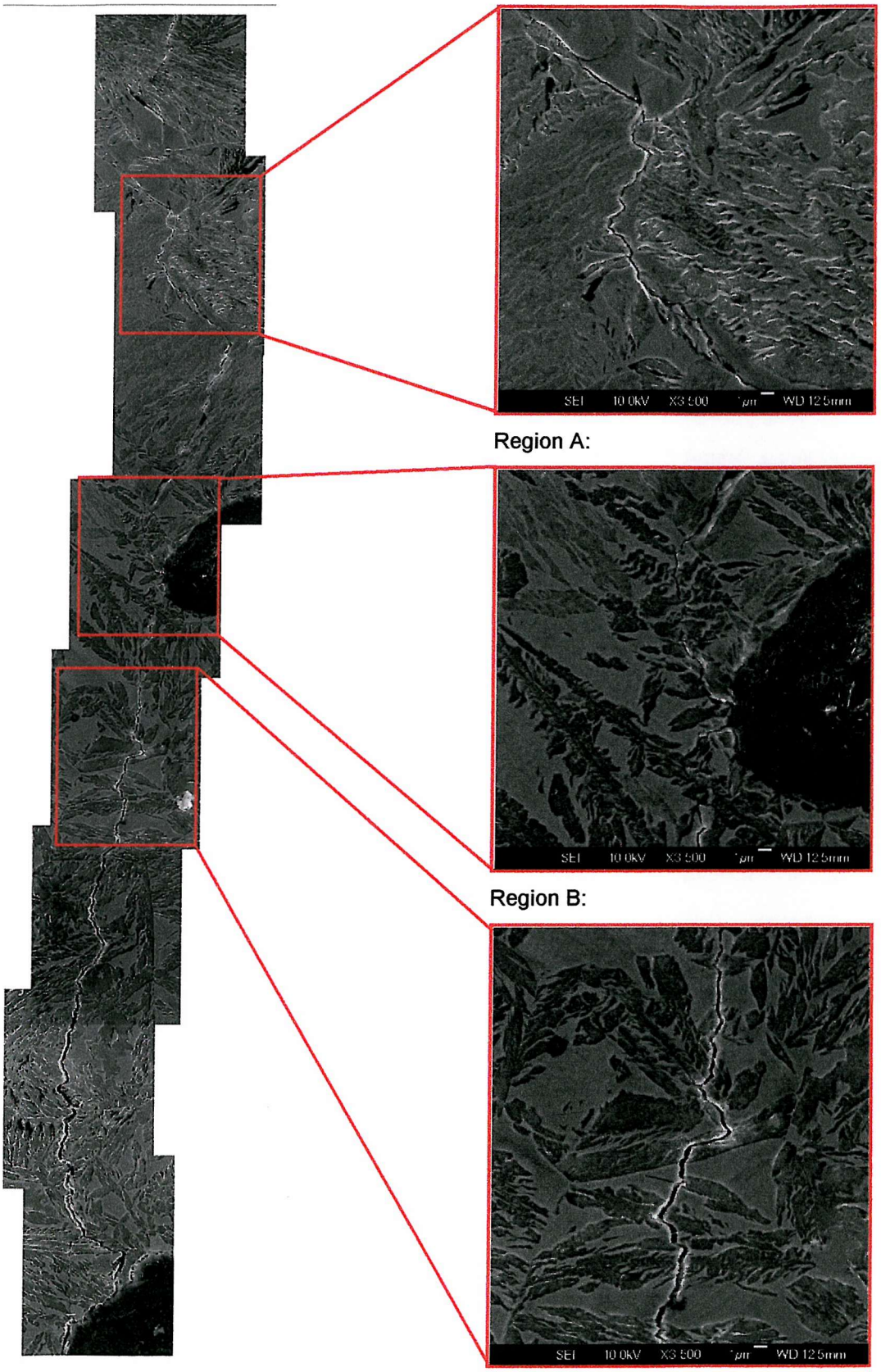

Figure 7.62: SEM images of '900/390:13' interrupted test specimen.

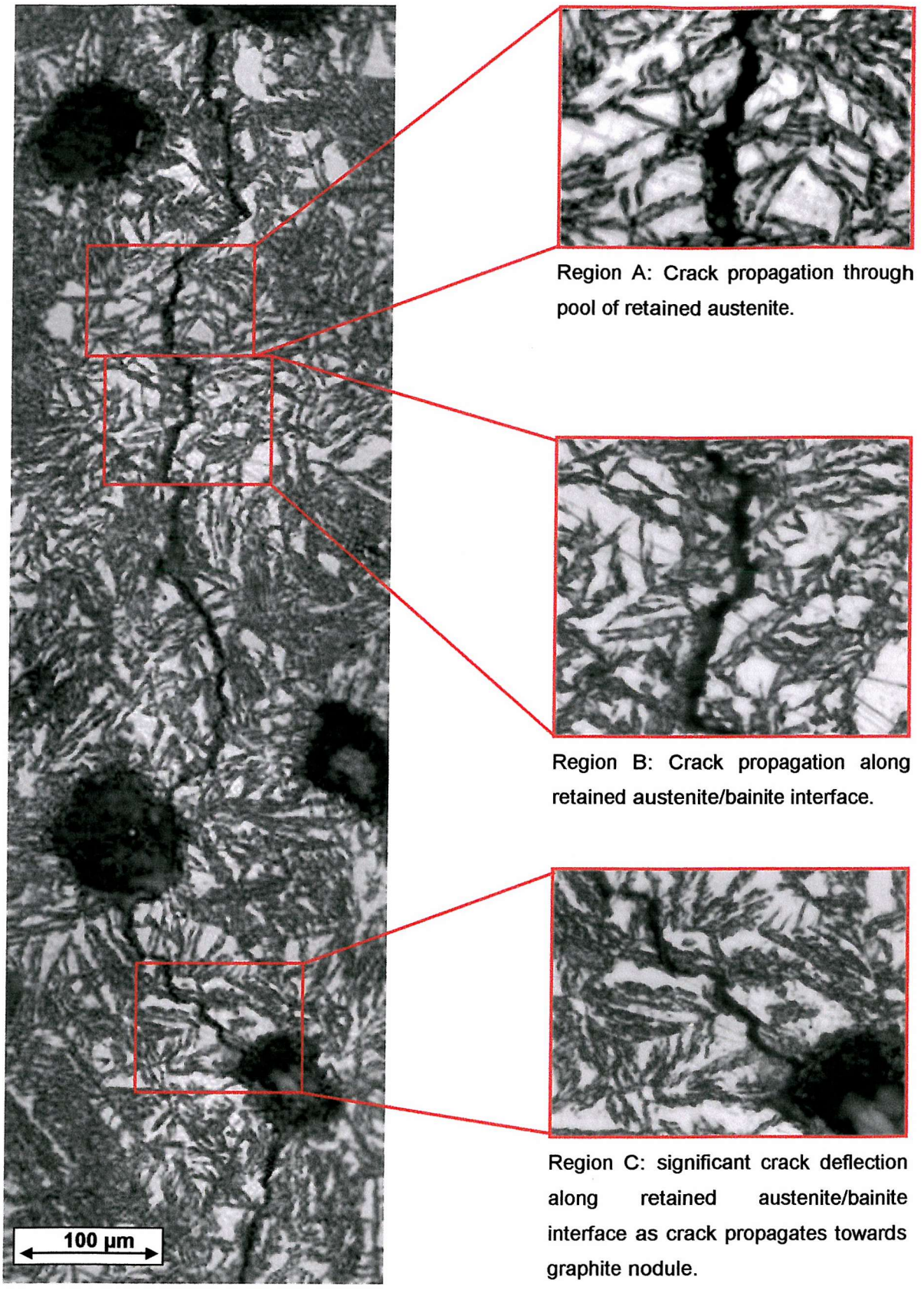

Region A: Crack propagation through pool of retained austenite.

Region B: Crack propagation along retained austenite/bainite interface.

Region C: significant crack deflection along retained austenite/bainite interface as crack propagates towards graphite nodule.

Figure 7.63: Micrographs showing deflected and non-deflected crack growth as a function of microstructure for a secondary crack in specimen '900/390:09'.

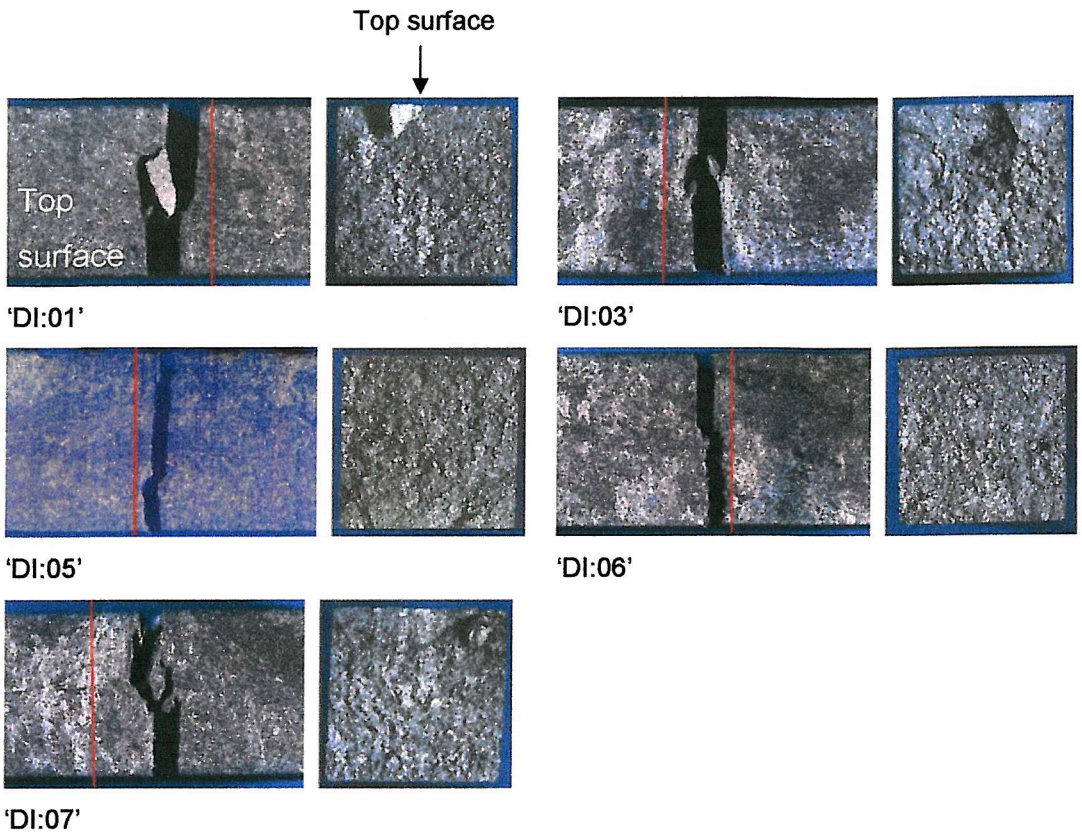

Figure 7.64: Fracture profiles and fracture surfaces for as-cast ductile iron ('DI') short fatigue crack specimens

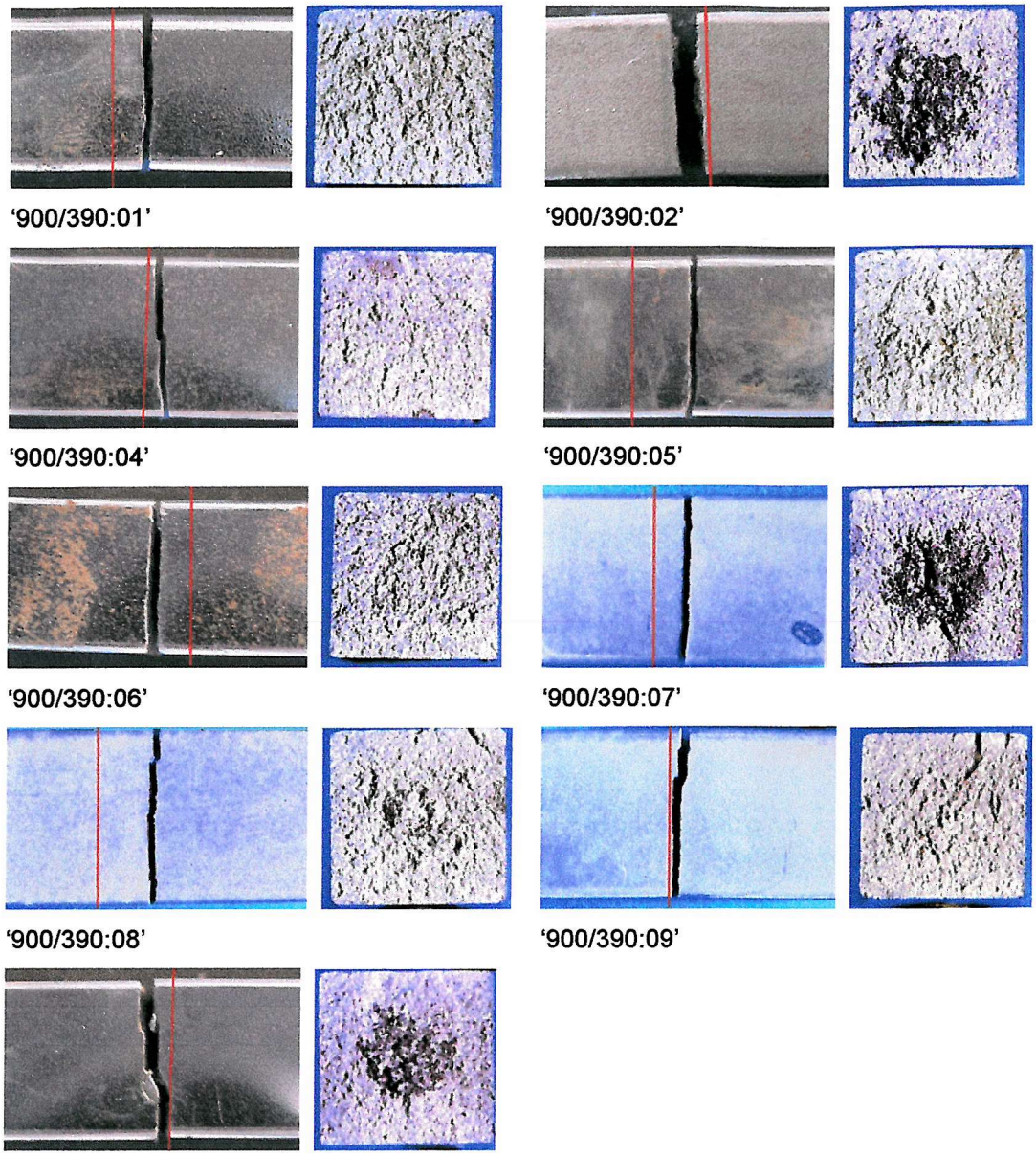

Figure 7.65: Fracture profiles and fracture surfaces for '900/390' short fatigue crack specimens. Note; specimens '900/390:03' and '900/390:10' did not suffer failure.

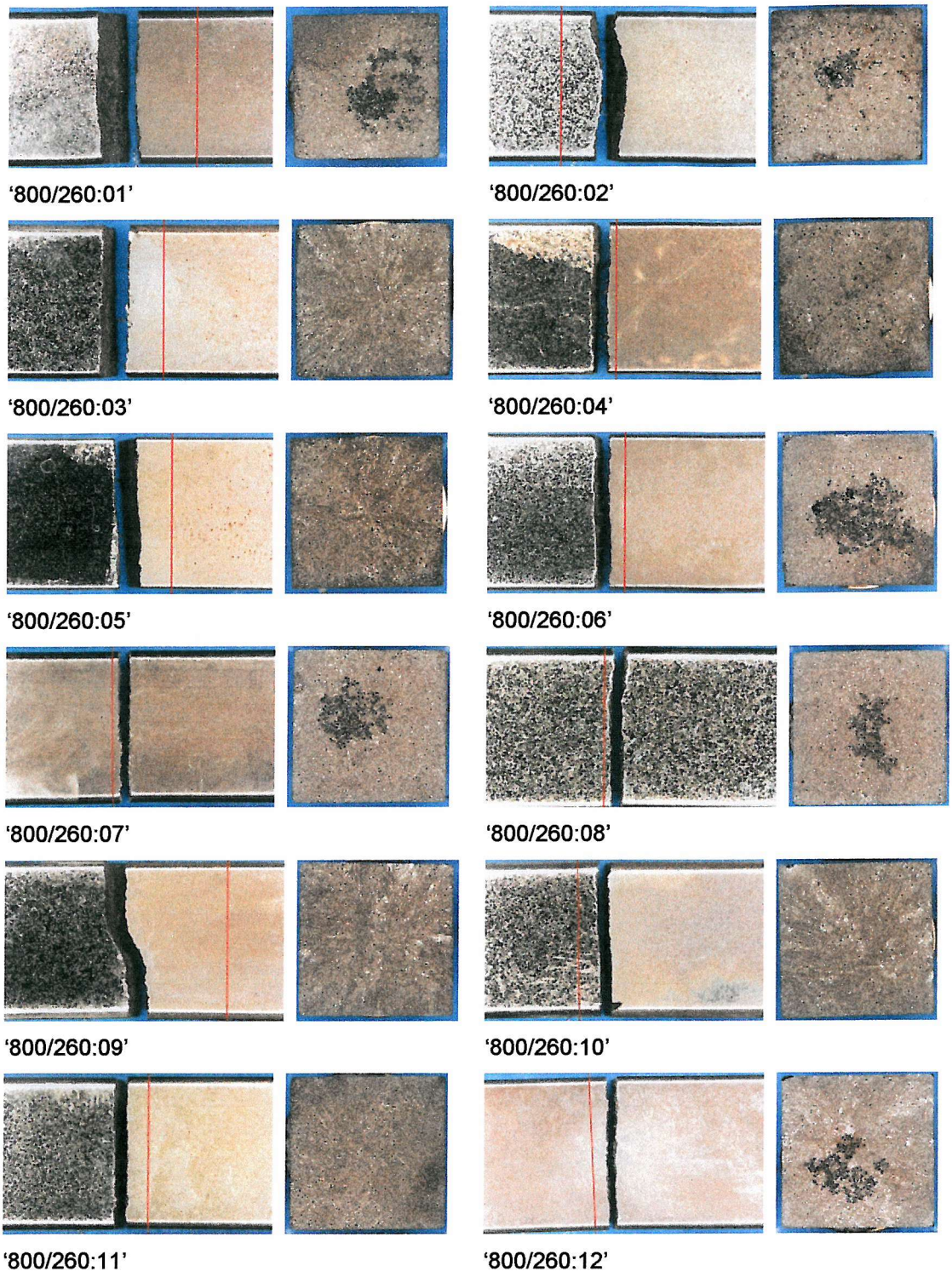

Figure 7.66: Fracture profiles and fracture surfaces for '800/260' short fatigue crack specimens 01 to 17

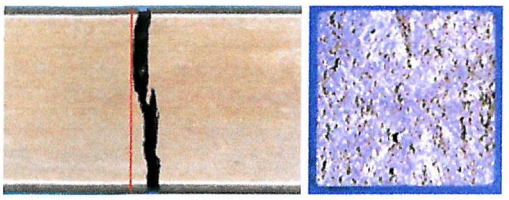

'800/260:16'

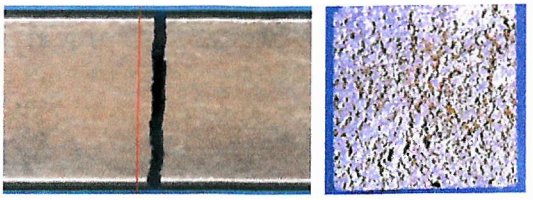

'800/260:17'

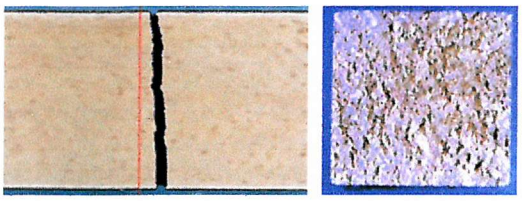

'800/260:18'

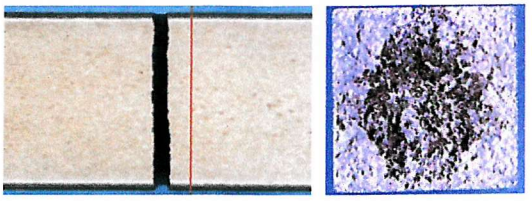

'800/260:19'

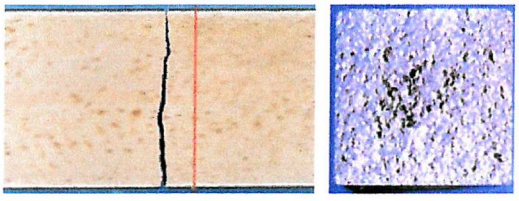

'800/260:20'

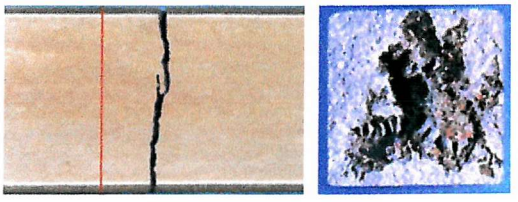

'800/260:21'

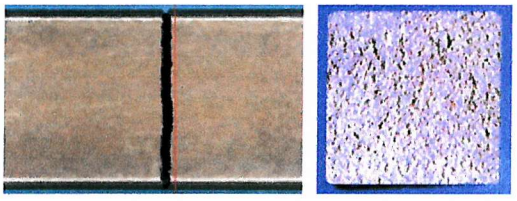

'800/260:22'

Figure 7.67: Fracture profiles and fracture surfaces for '800/260' short fatigue crack specimens 18 to 22

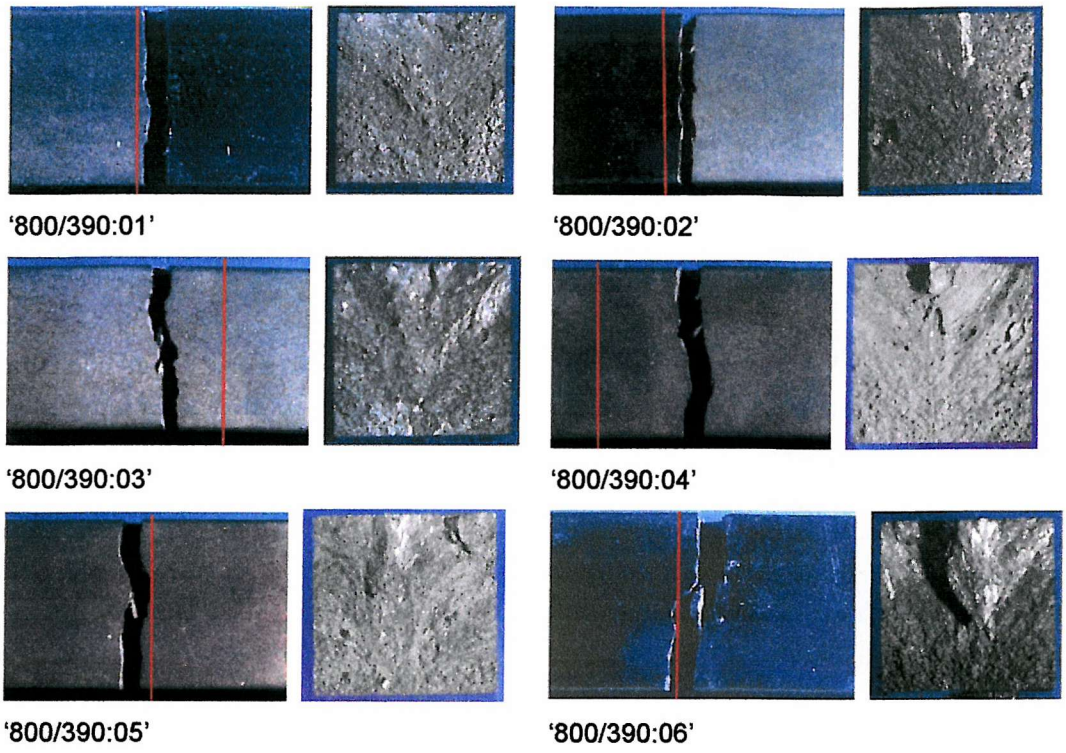

Figure 7.68: Fracture profiles and fracture surfaces for '800/390' short fatigue crack specimens

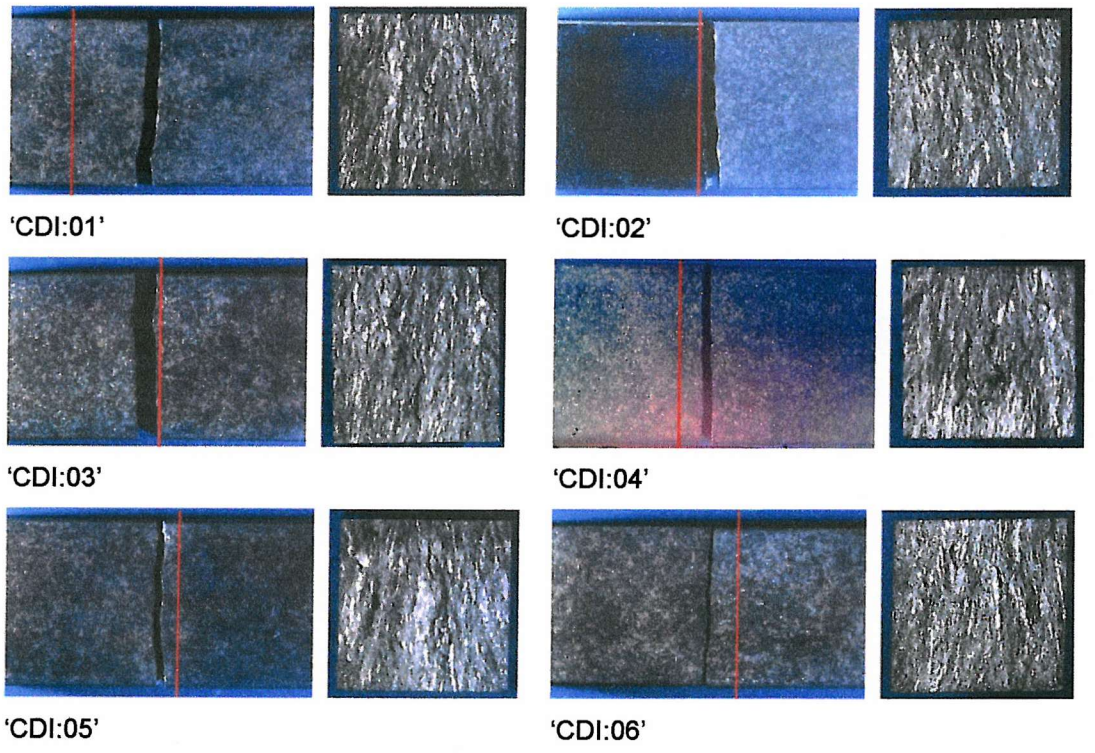

Figure 7.69: Fracture profiles and fracture surfaces for chilled ductile iron ('CDI') short fatigue crack specimens

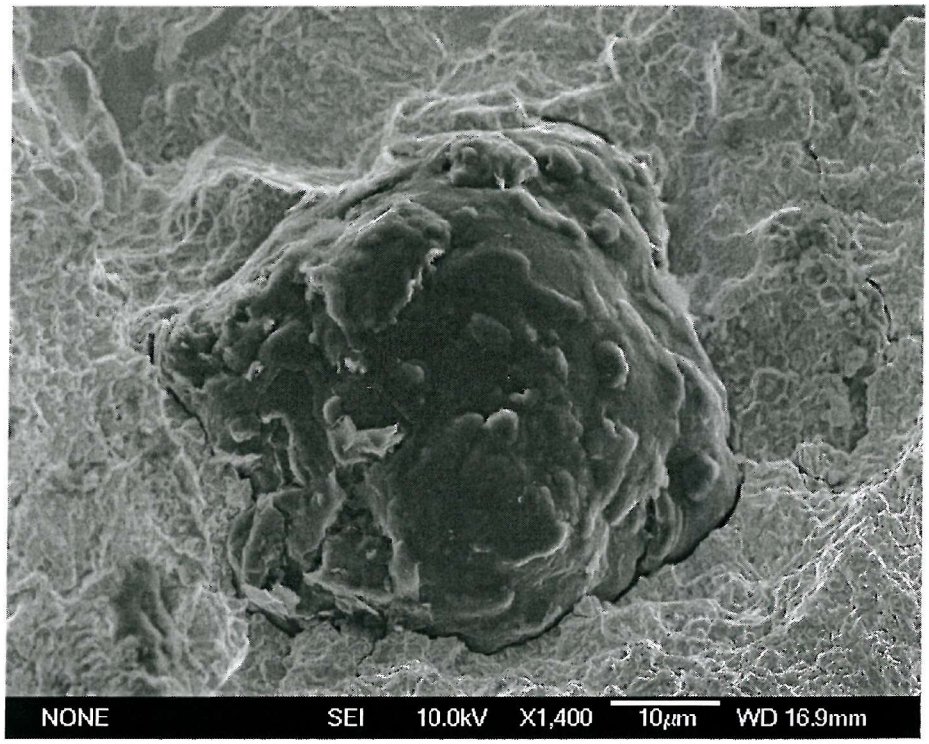

Figure 7.70: ADI fracture surface: example of a decohered graphite nodule.

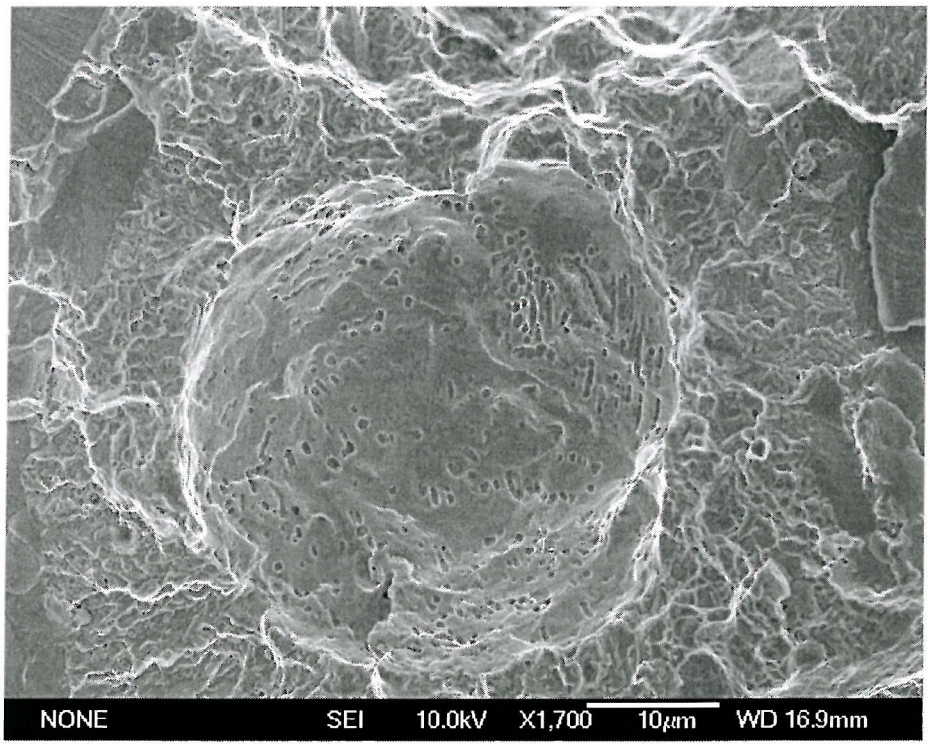

Figure 7.71: ADI fracture surface: example of a crater left from decohered graphite nodule.

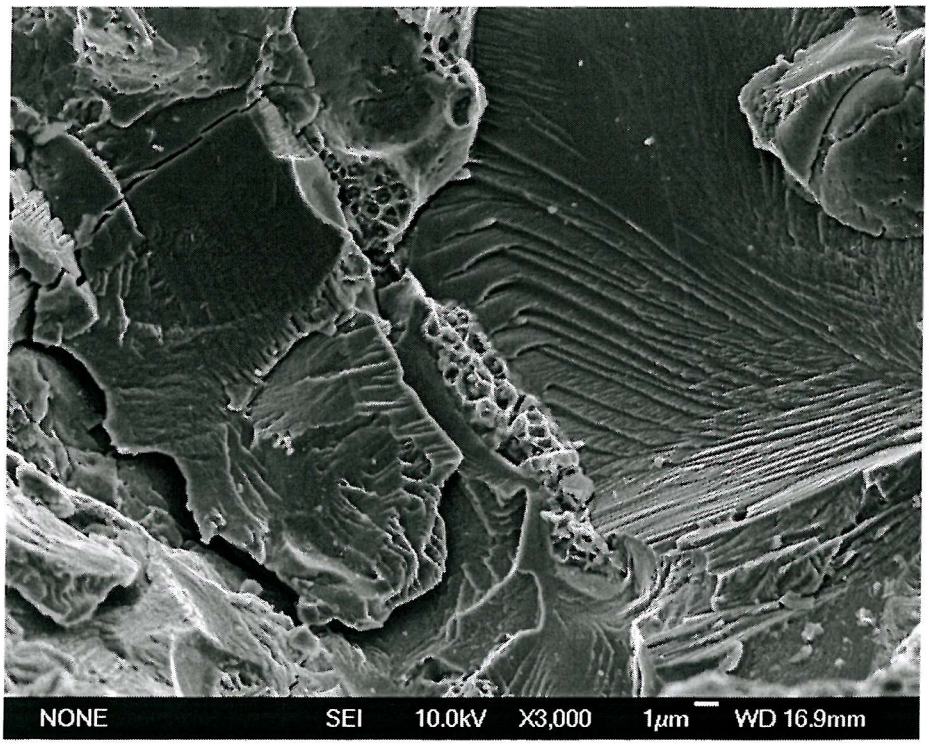

Figure 7.72: ADI fracture surface: example of a fractured eutectic carbide.

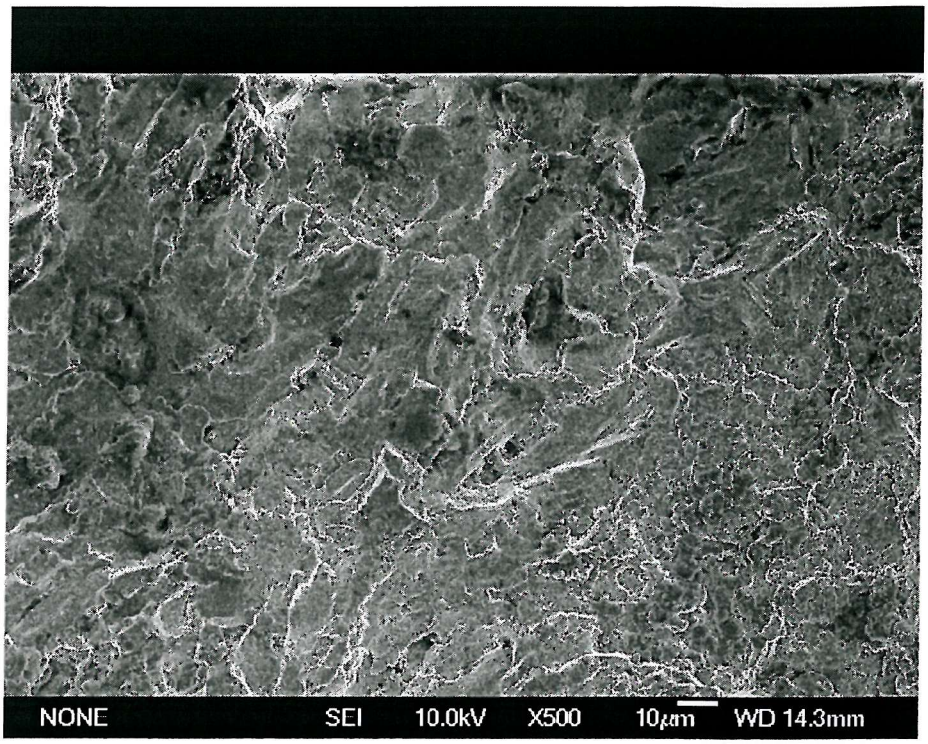

Figure 7.73: Fracture surface of short fatigue crack specimen '800/260:02'. Note the large number of brittle facets.

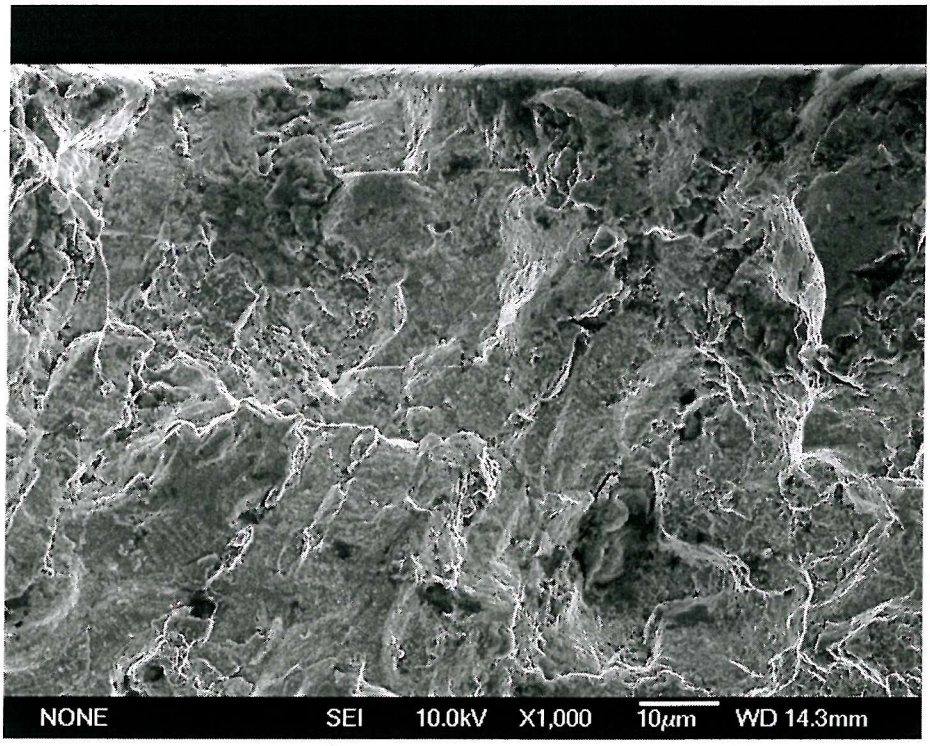

Figure 7.74: Fracture surface of short fatigue crack specimen '800/260:02'.

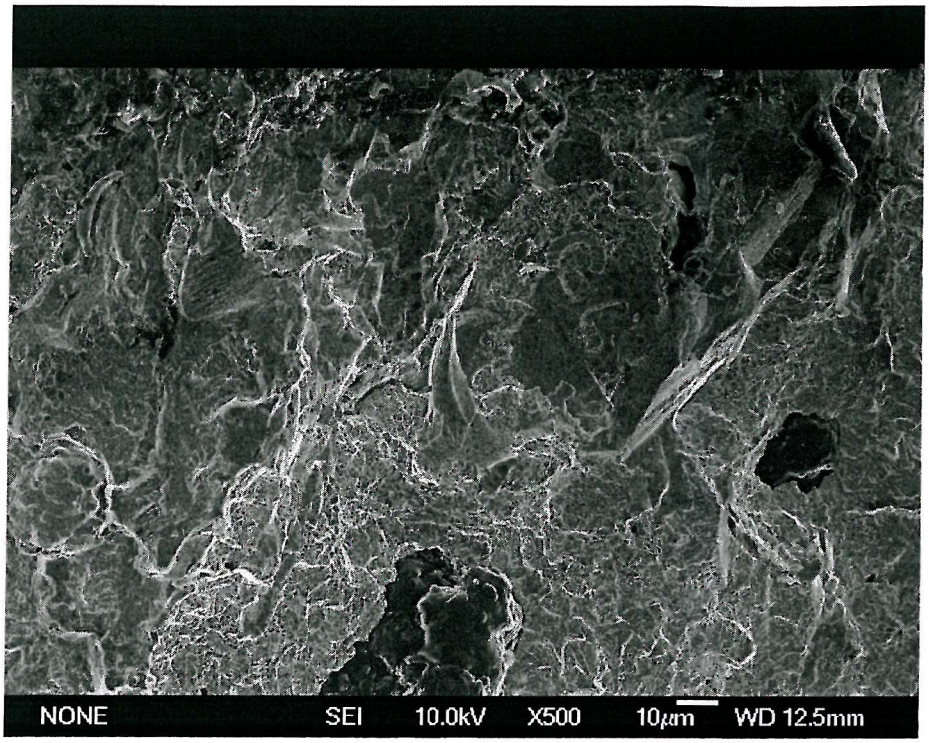

Figure 7.75: Fracture surface of short fatigue crack specimen '800/260:09'

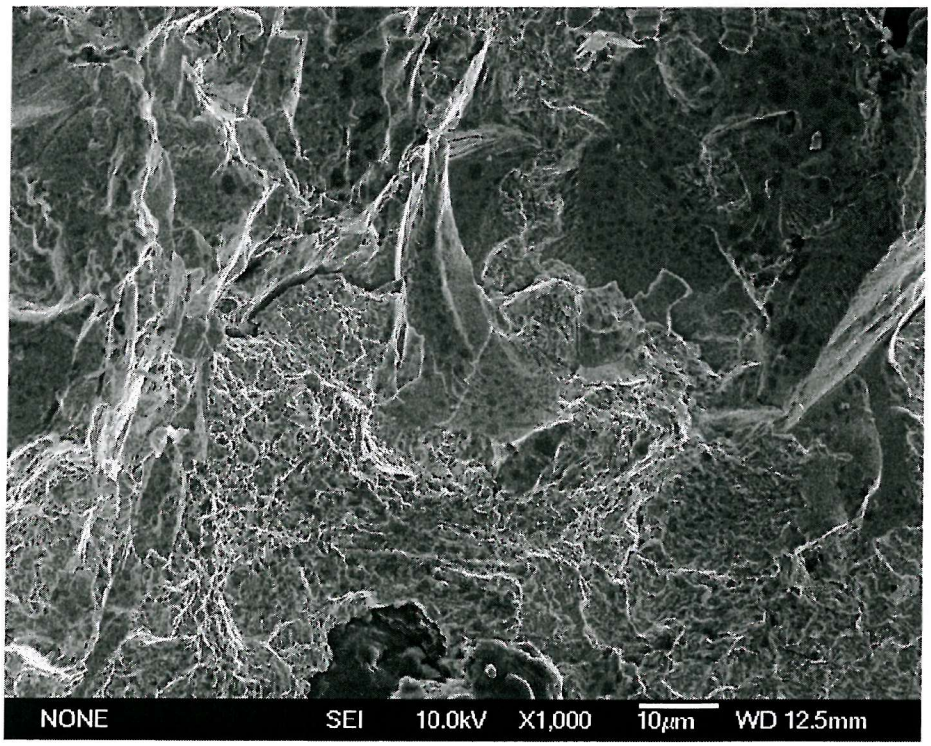

Figure 7.76: Fracture surface of short fatigue crack specimen '800/260:09'

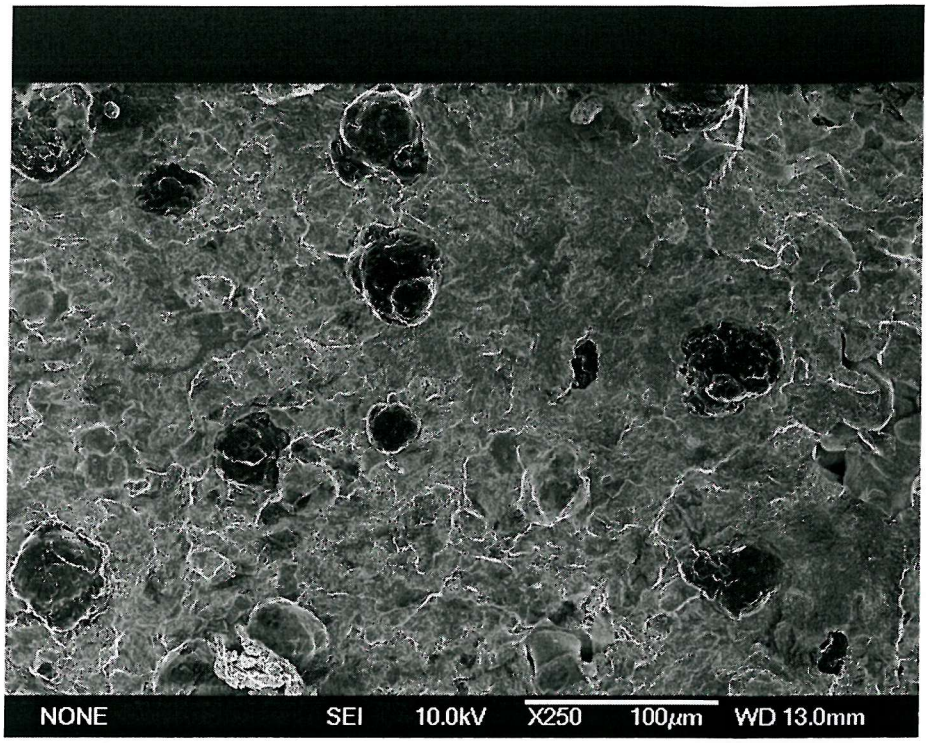

Figure 7.77: Fracture surface of short fatigue crack specimen '800/260:18'

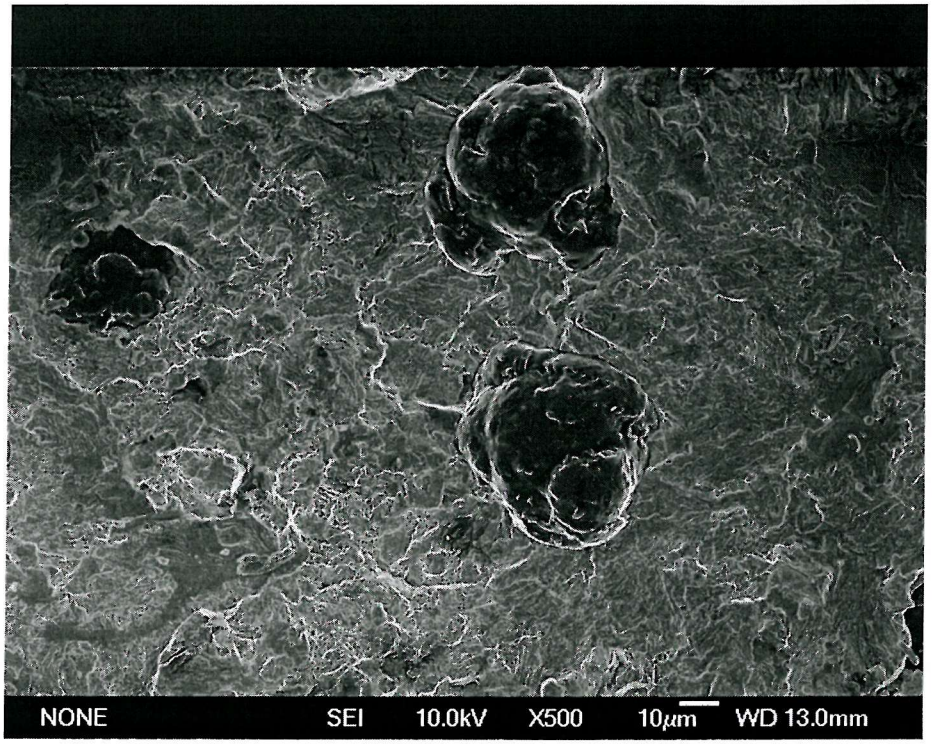

Figure 7.78: Fracture surface of short fatigue crack specimen '800/260:18'

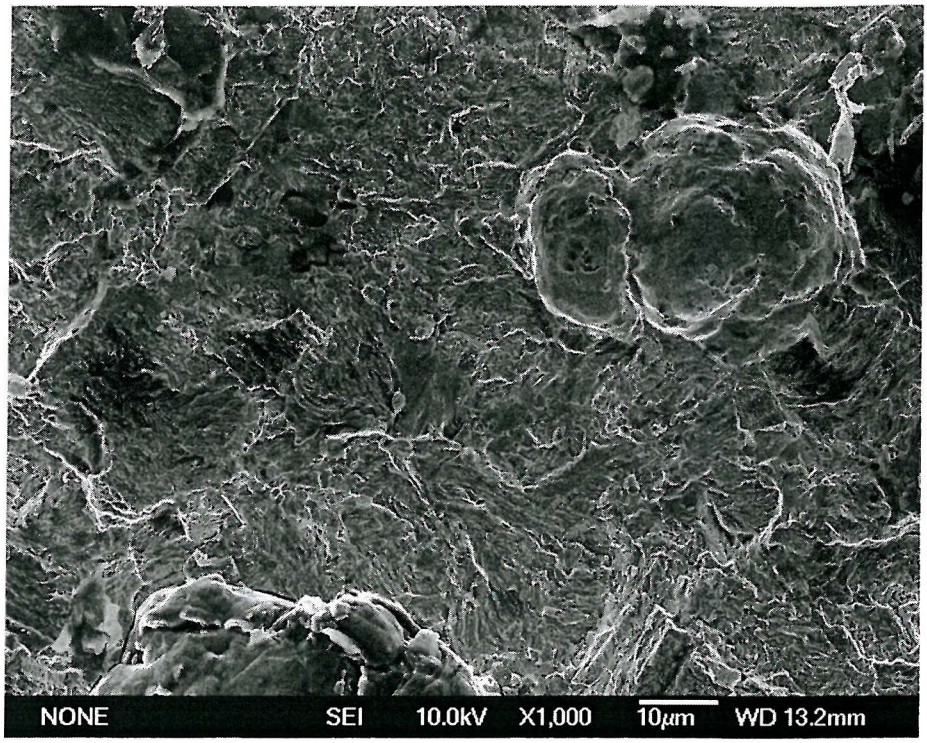

Figure 7.79: Fracture surface of short fatigue crack specimen '800/260:22'

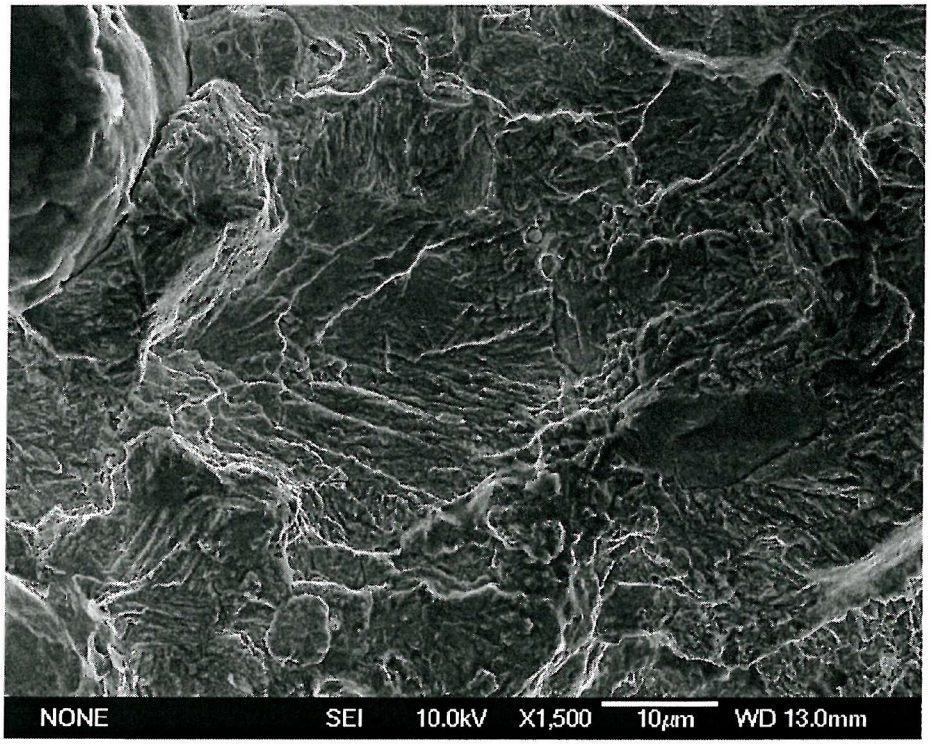

Figure 7.80: Fracture surface of short fatigue crack specimen '800/260:22'

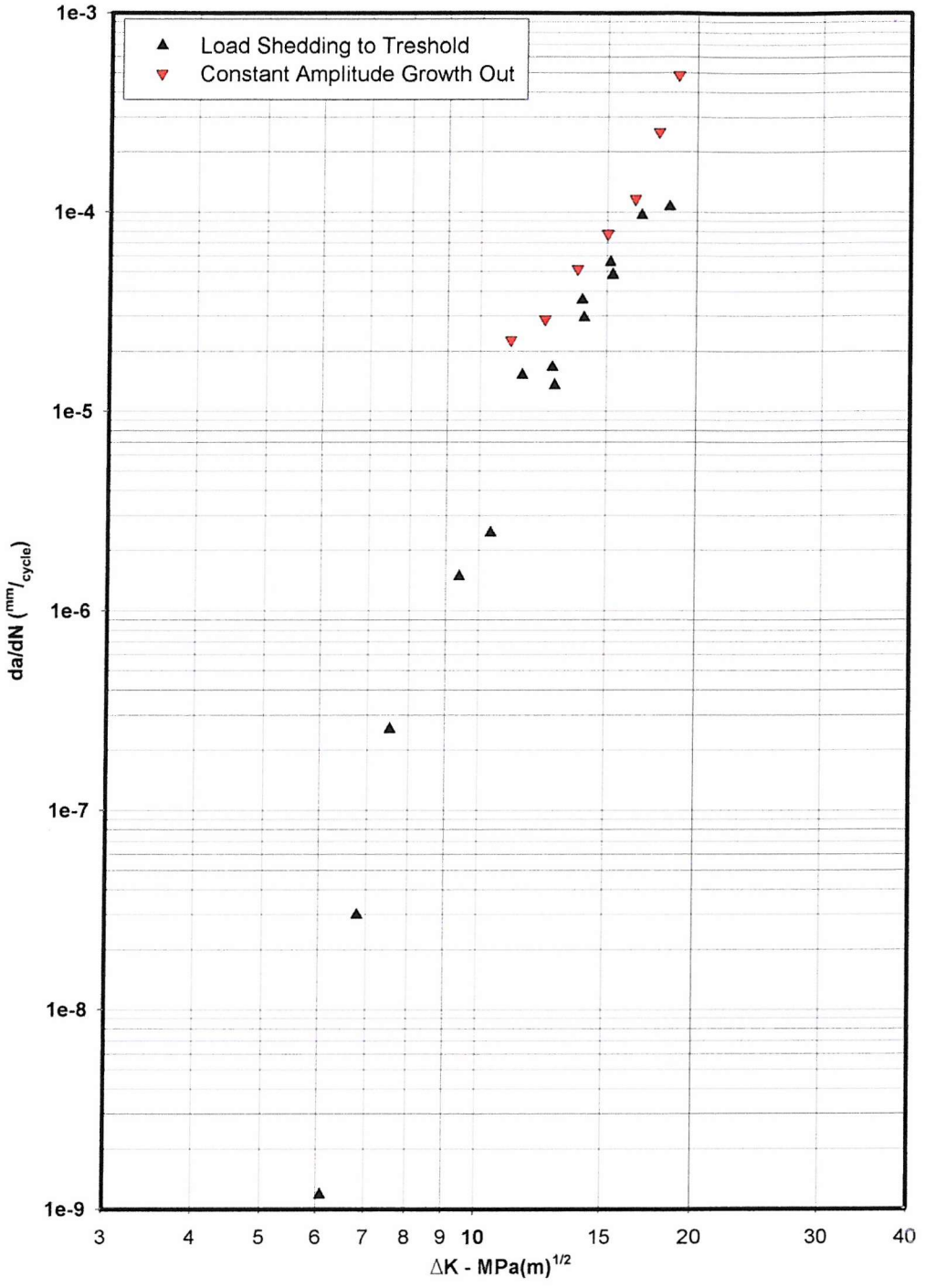

Figure 7.81: As-cast ductile iron fatigue crack propagation data from long crack testing.

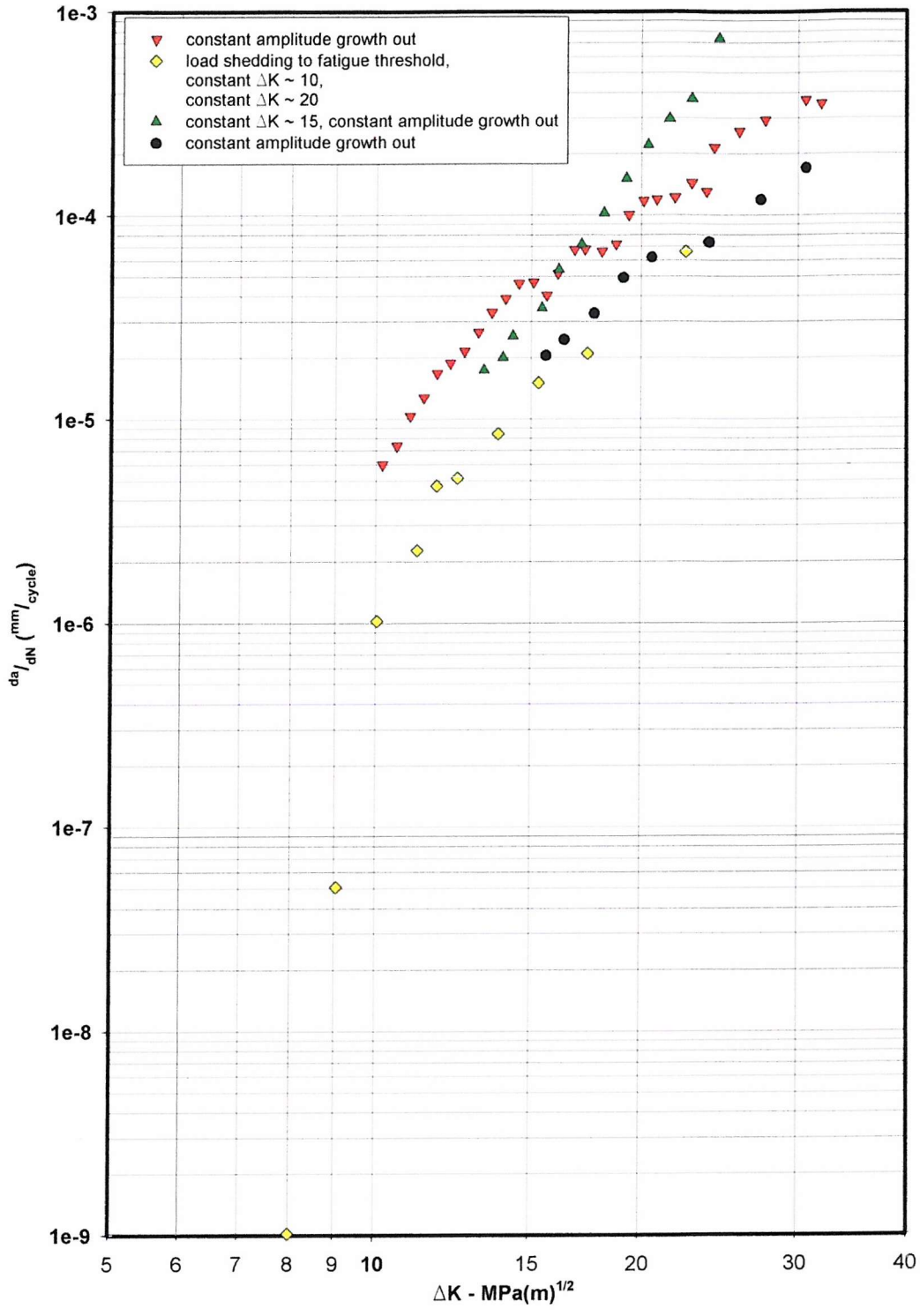

Figure 7.82: '900/390' fatigue crack propagation data from long crack testing.

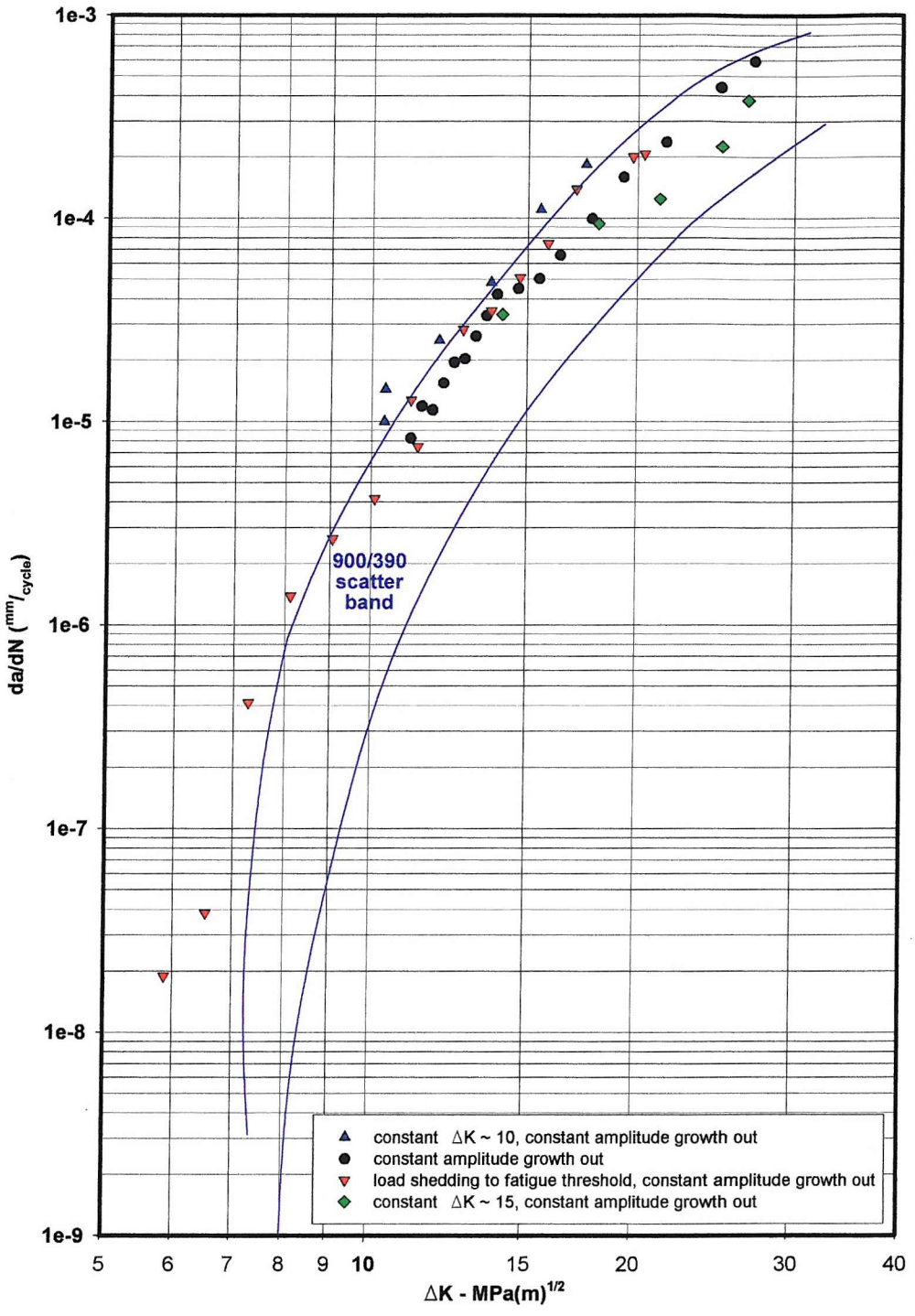

Figure 7.83: '800/260' fatigue crack propagation data from long crack testing.

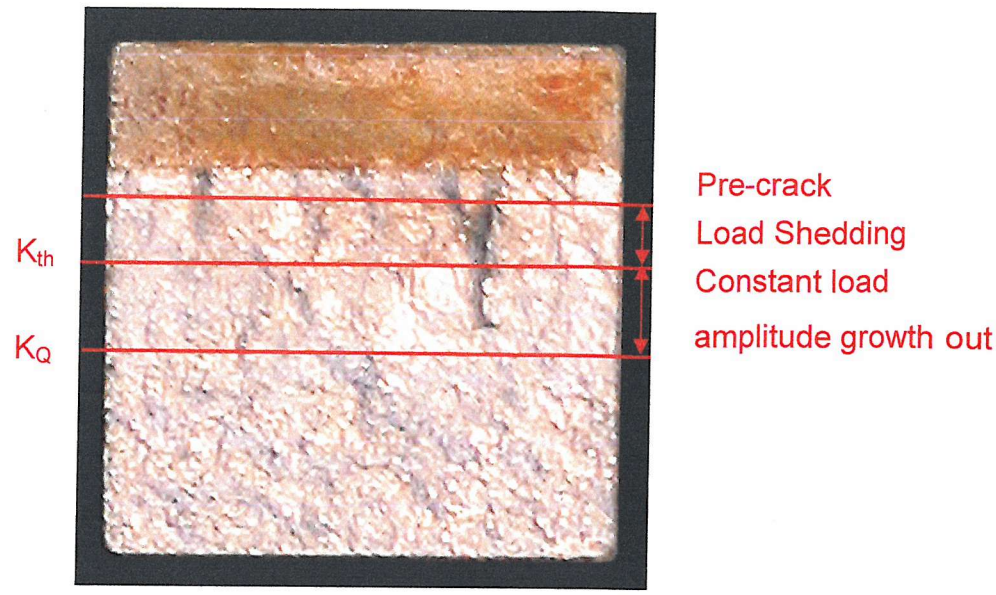

Figure 7.84: Fracture surface of DI:L1 showing pre-crack, load shedding, and constant load amplitude growth out regions.

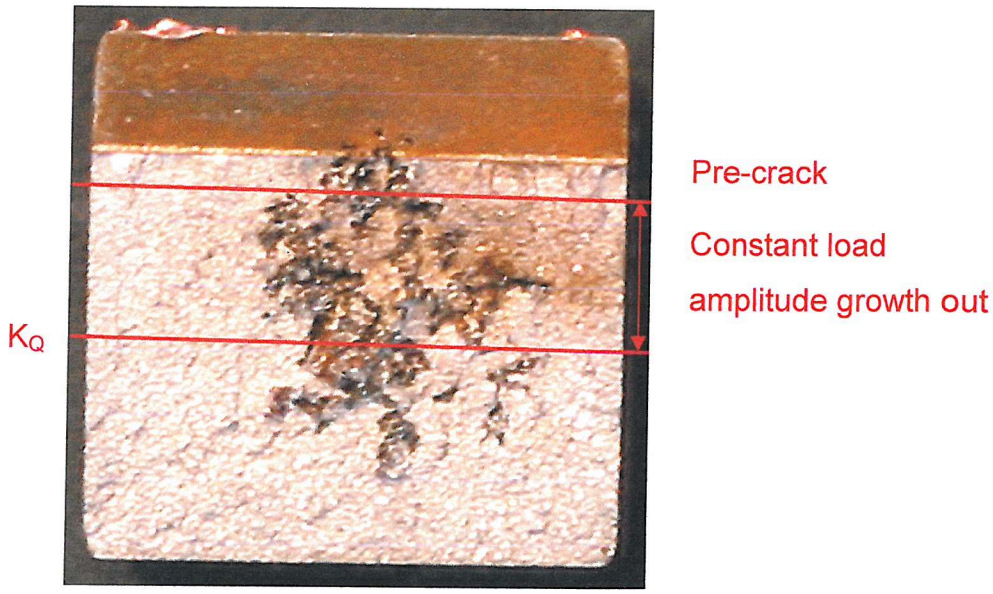

Figure 7.85: Fracture surface of '900/390:L3' showing pre-crack, and constant load amplitude growth out regions.

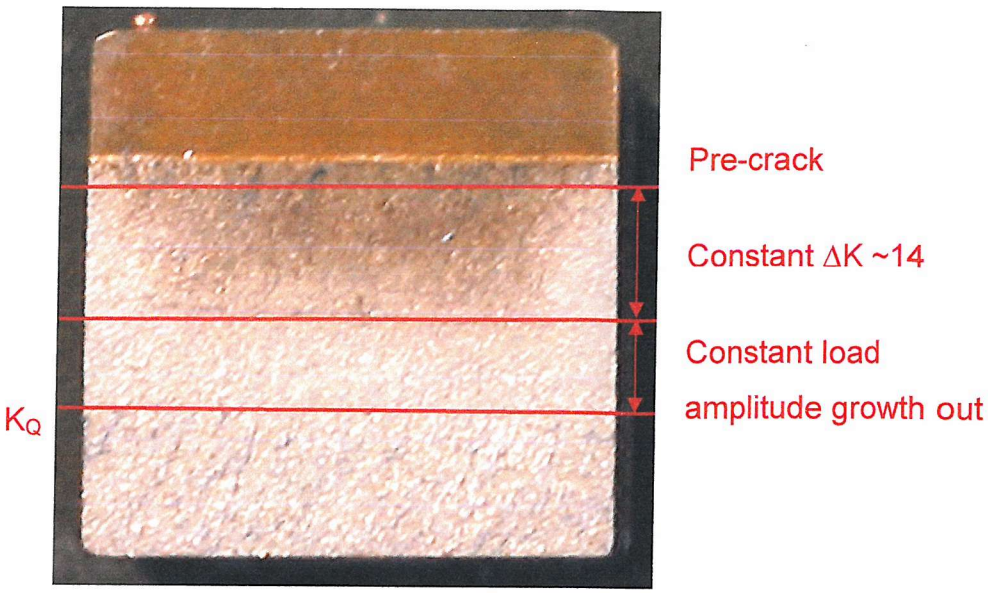

Figure 7.86: Fracture surface of '900/390:L4' showing pre-crack, constant ΔK, and constant load amplitude growth out regions.

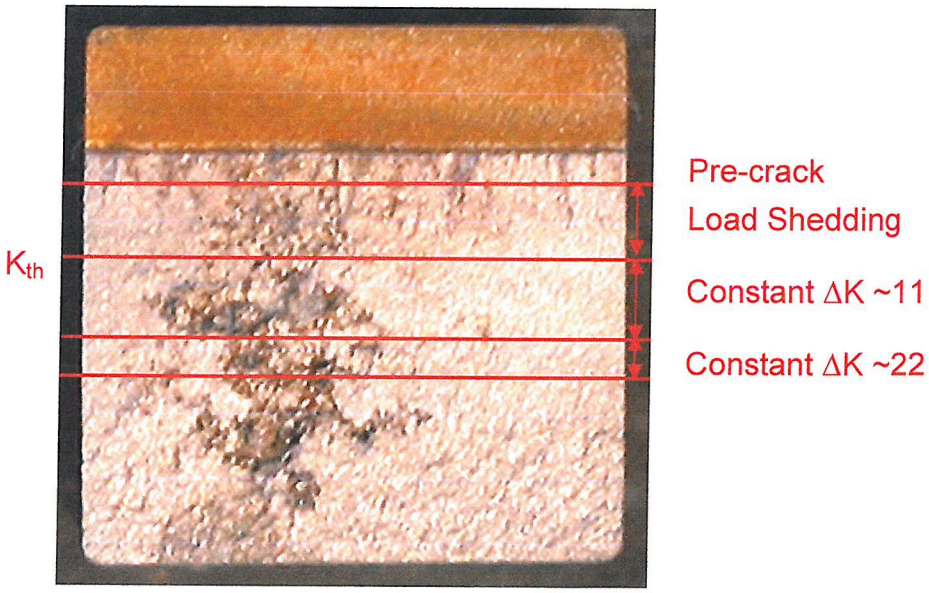

Figure 7.87: Fracture surface of '900/390:L6' showing pre-crack, load-shedding, and constant ΔK regions.

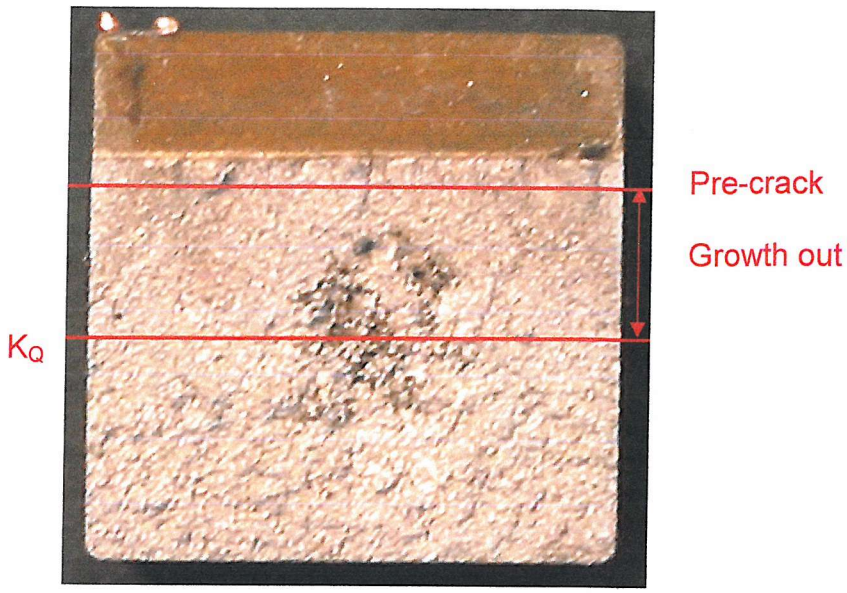

Figure 7.88: Fracture surface of '800/260:L1' showing pre-crack, and constant load amplitude growth out regions.

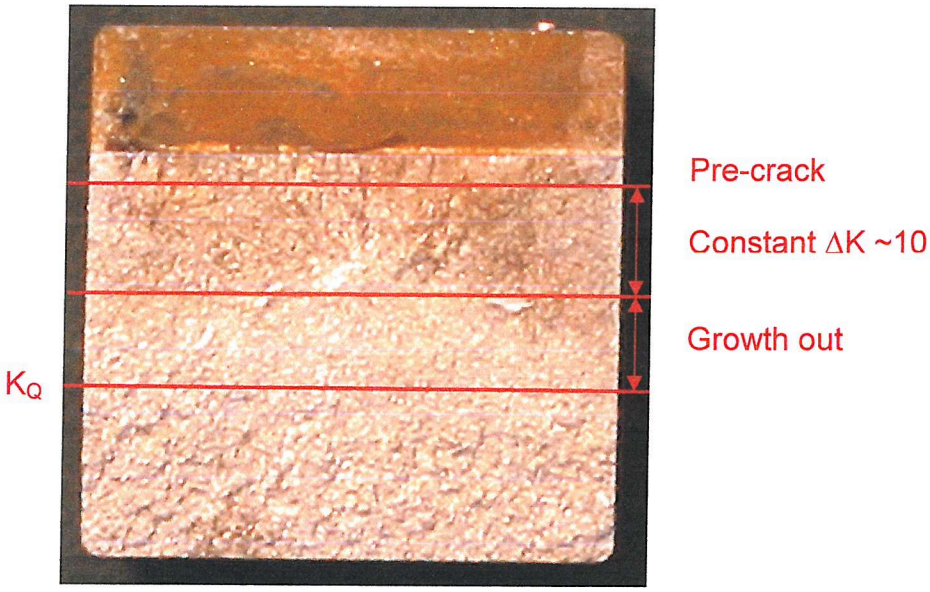

Figure 7.89: Fracture surface of '800/260:L2' showing pre-crack, constant ΔK, and constant load amplitude growth out regions.

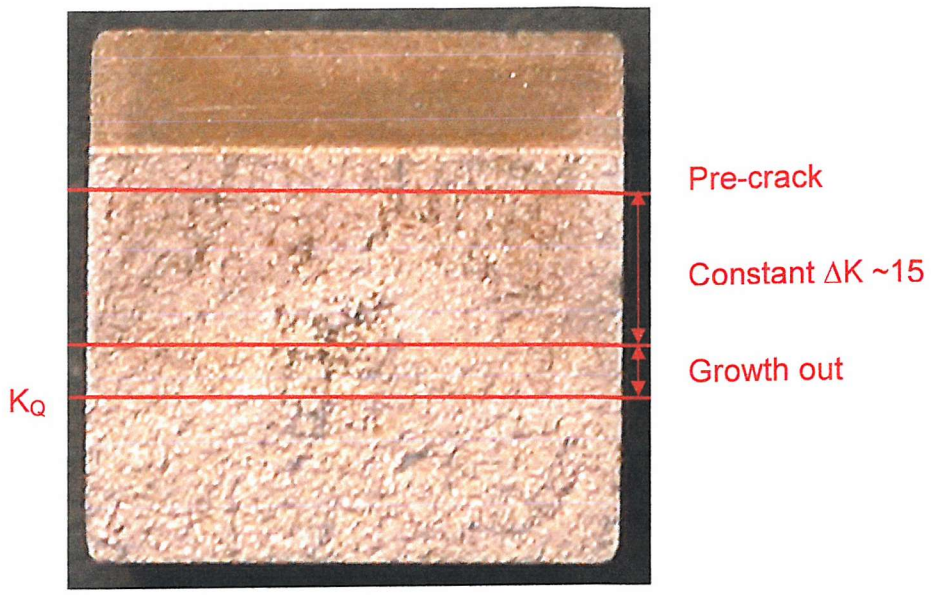

Figure 7.90: Fracture surface of '800/260:L3' showing pre-crack, constant ΔK and constant load amplitude growth out regions.

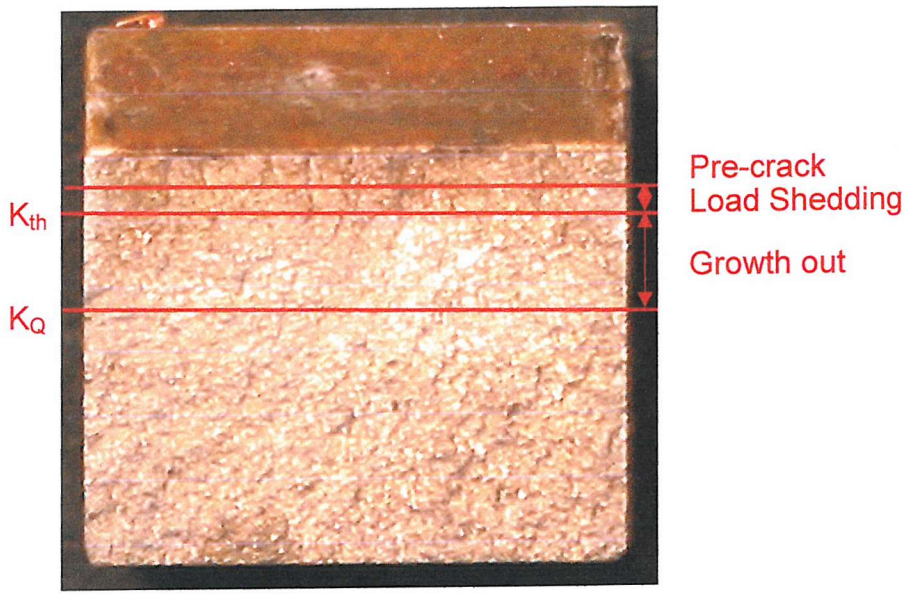

Figure 7.91: Fracture surface of '800/260:L4' showing pre-crack, and constant load amplitude growth out regions.

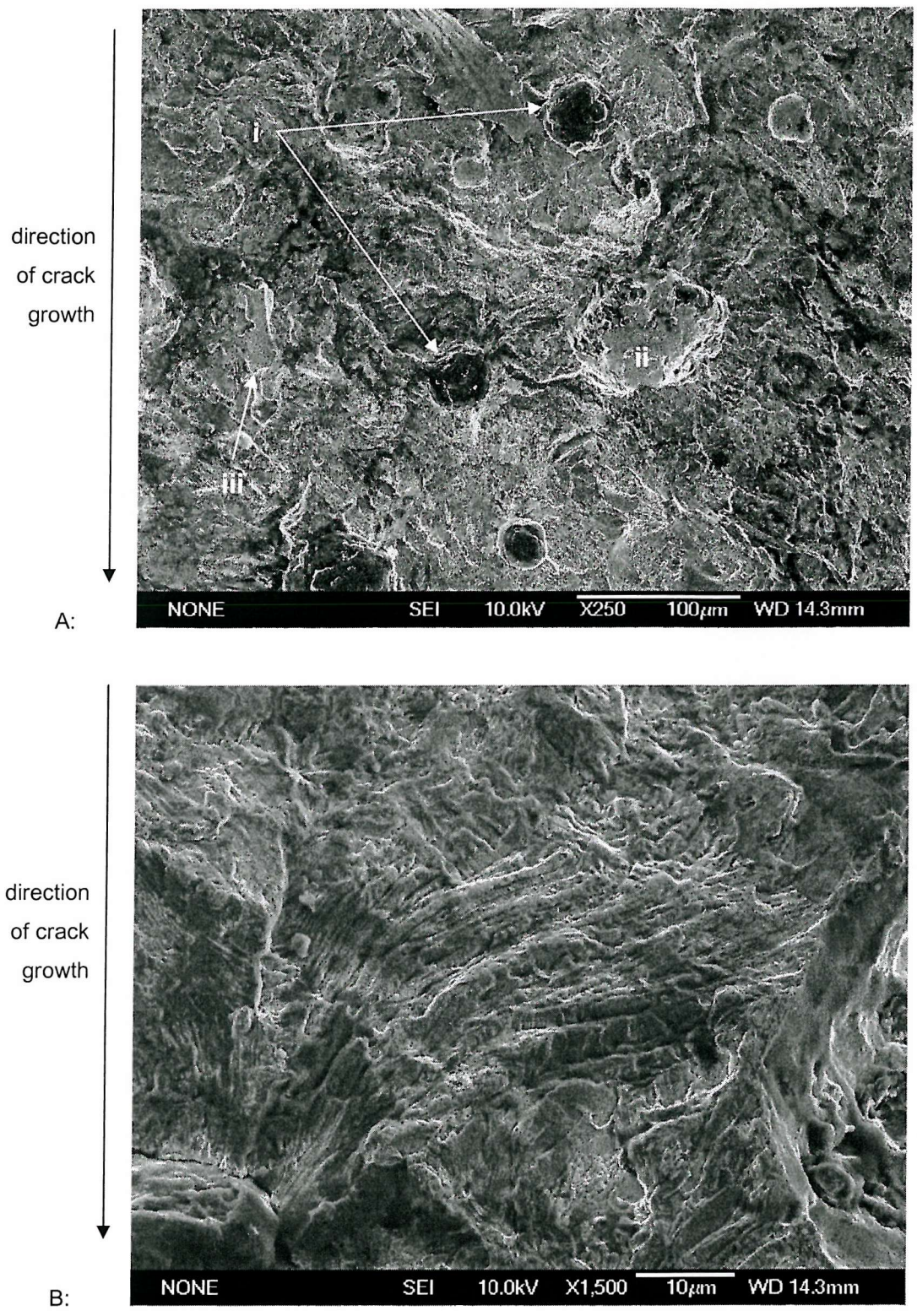

Figure 7.92: 'As cast ductile iron' Threshold and growth out test. Fracture surface: ΔK 7.5 ~ MPa√m.

Region i: Graphite nodules.

Region ii: Crater left by decohered graphite nodule.

Region iii: Brittle facet of fractured eutectic carbide.

direction of crack growth

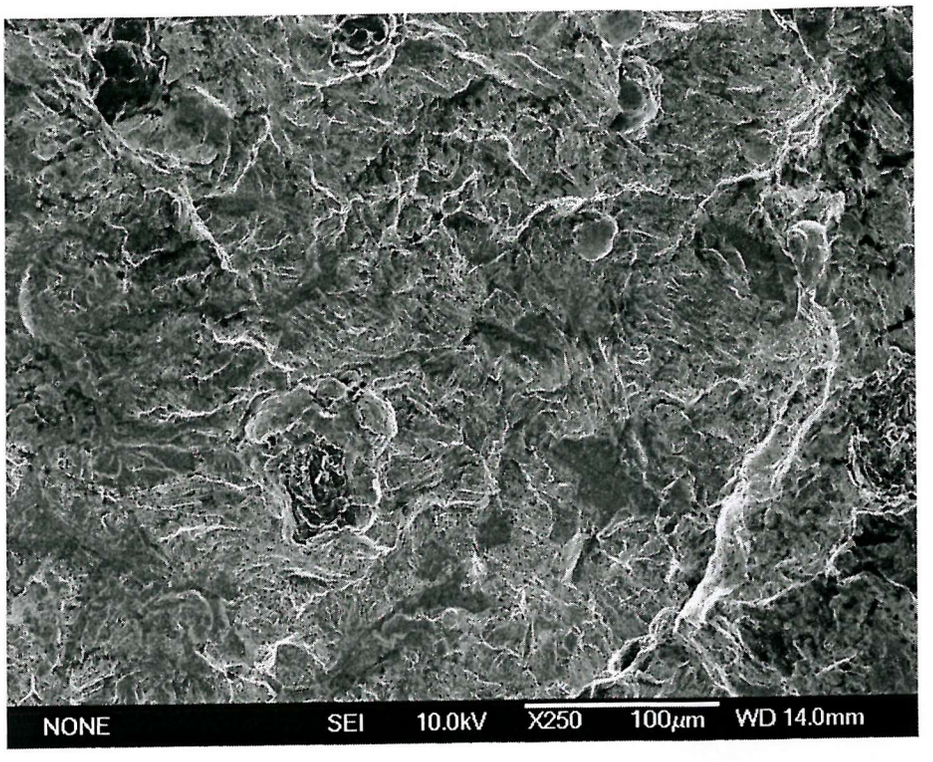

A:

direction of crack growth

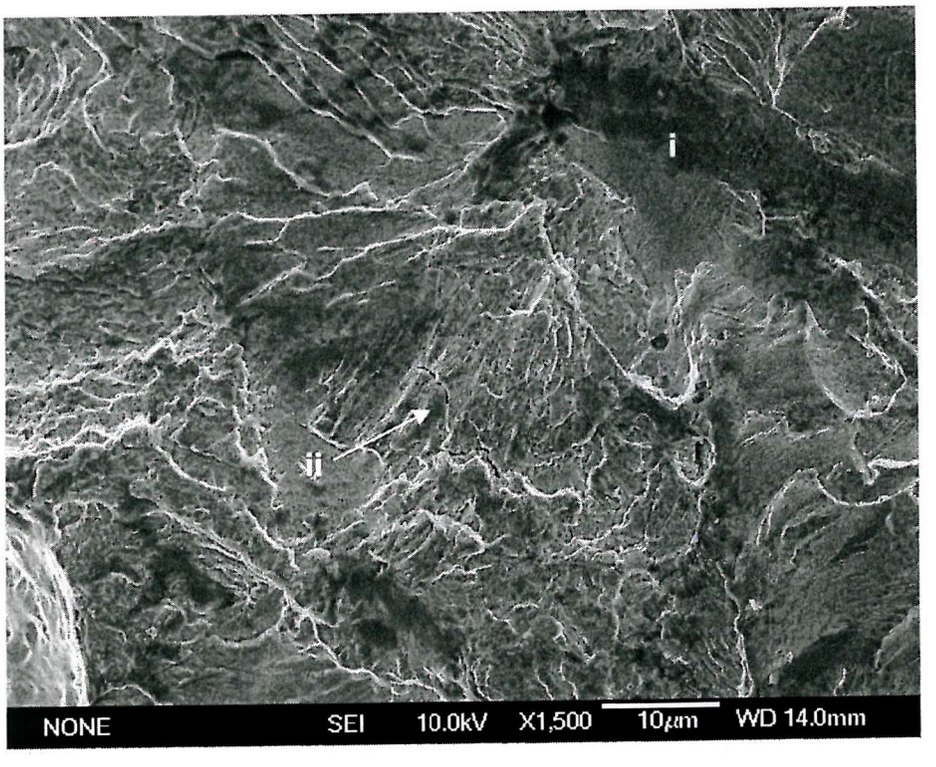

B:

Figure 7.93: 'As cast ductile iron' Threshold and growth out test. Fracture surface: ΔK 15 ~ MPa$\sqrt{m}$.

Region i: Brittle Facet of fractured eutectic carbide.

Region ii: Through thickness micro-crack.

direction of crack growth

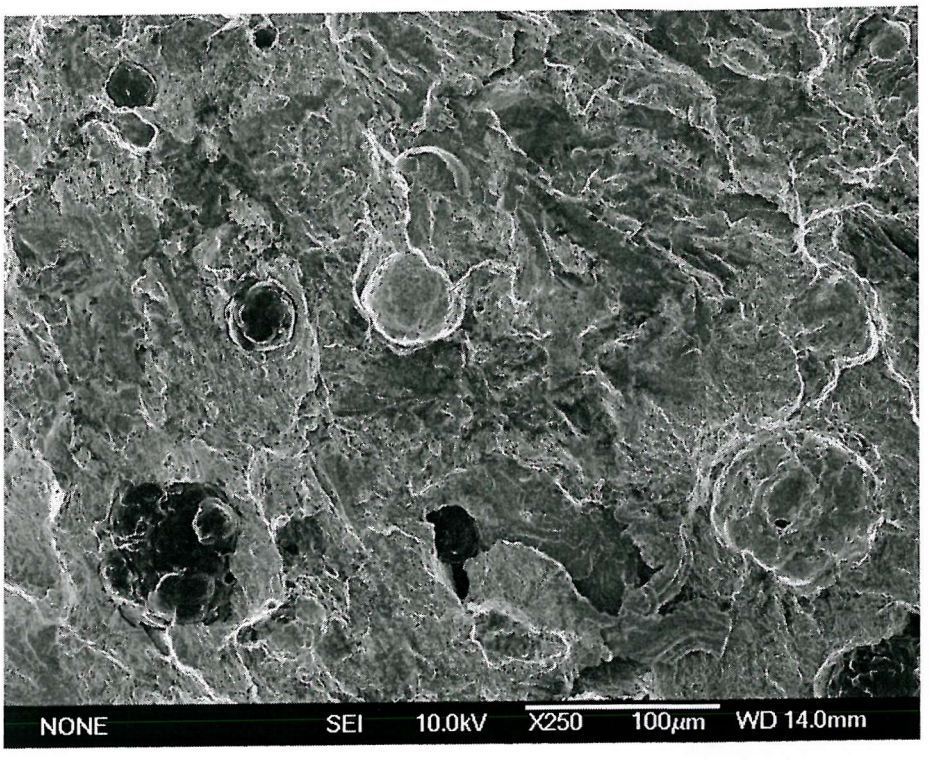

A:

direction of crack growth

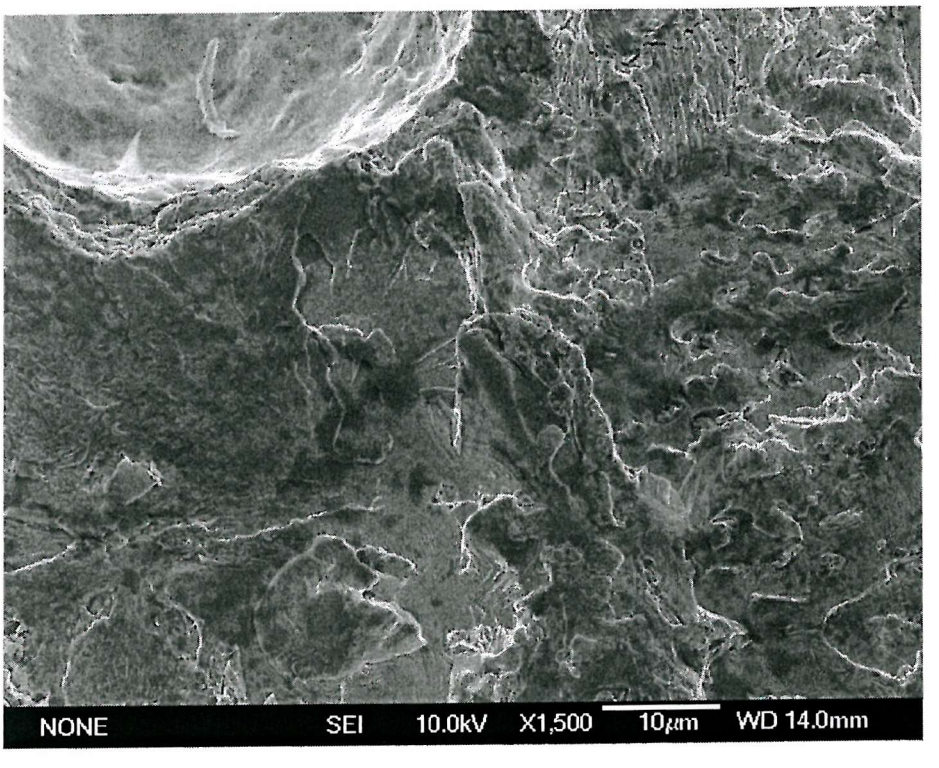

B:

Figure 7.94: 'As cast ductile iron' Threshold and growth out test. Fracture surface: ΔK 18 ~ MPa$\sqrt{m}$

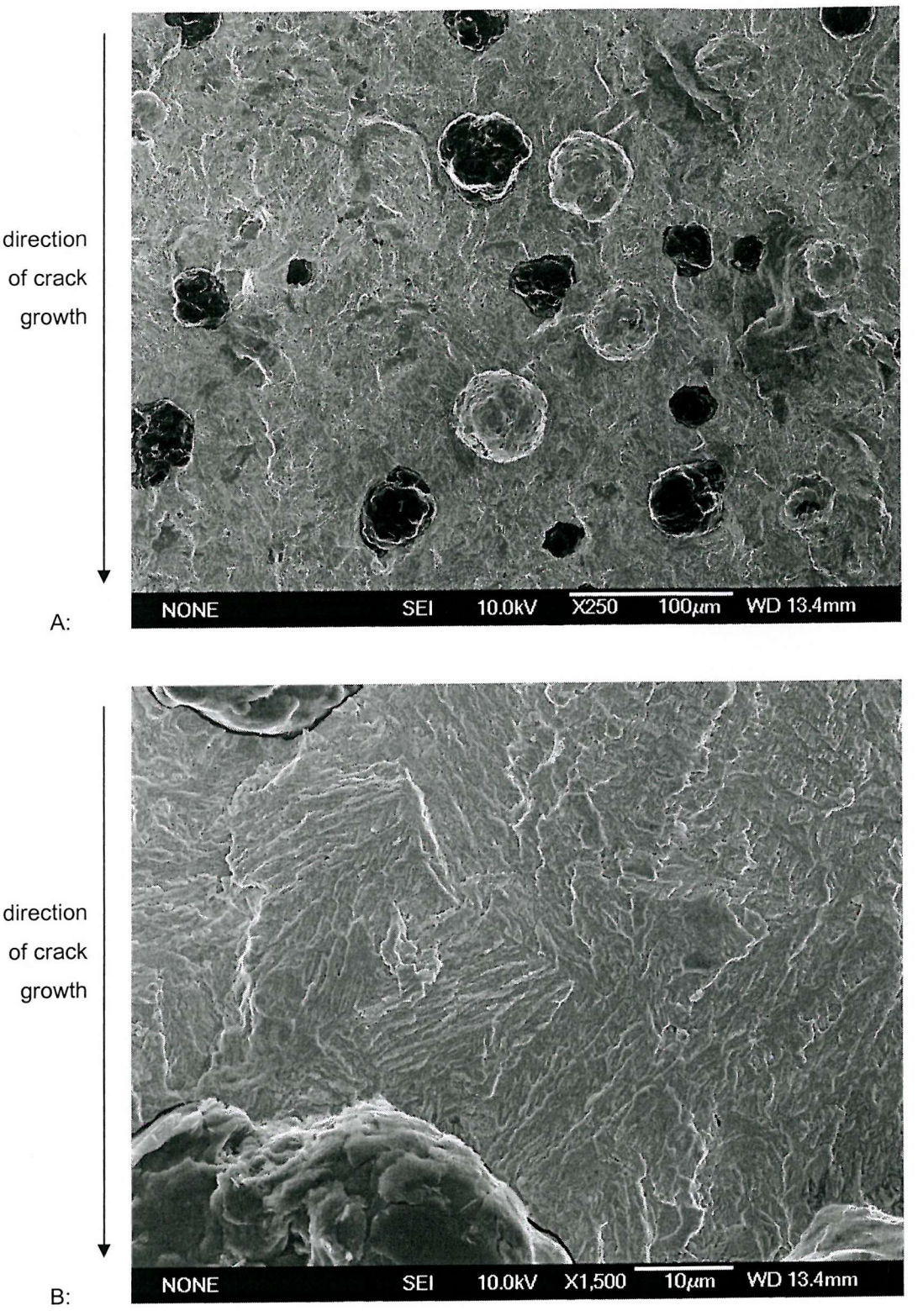

Figure 7.95: '900/390' Threshold and growth out test. Fracture surface: ΔK 8 ~ MPa$\sqrt{m}$. (Near threshold)

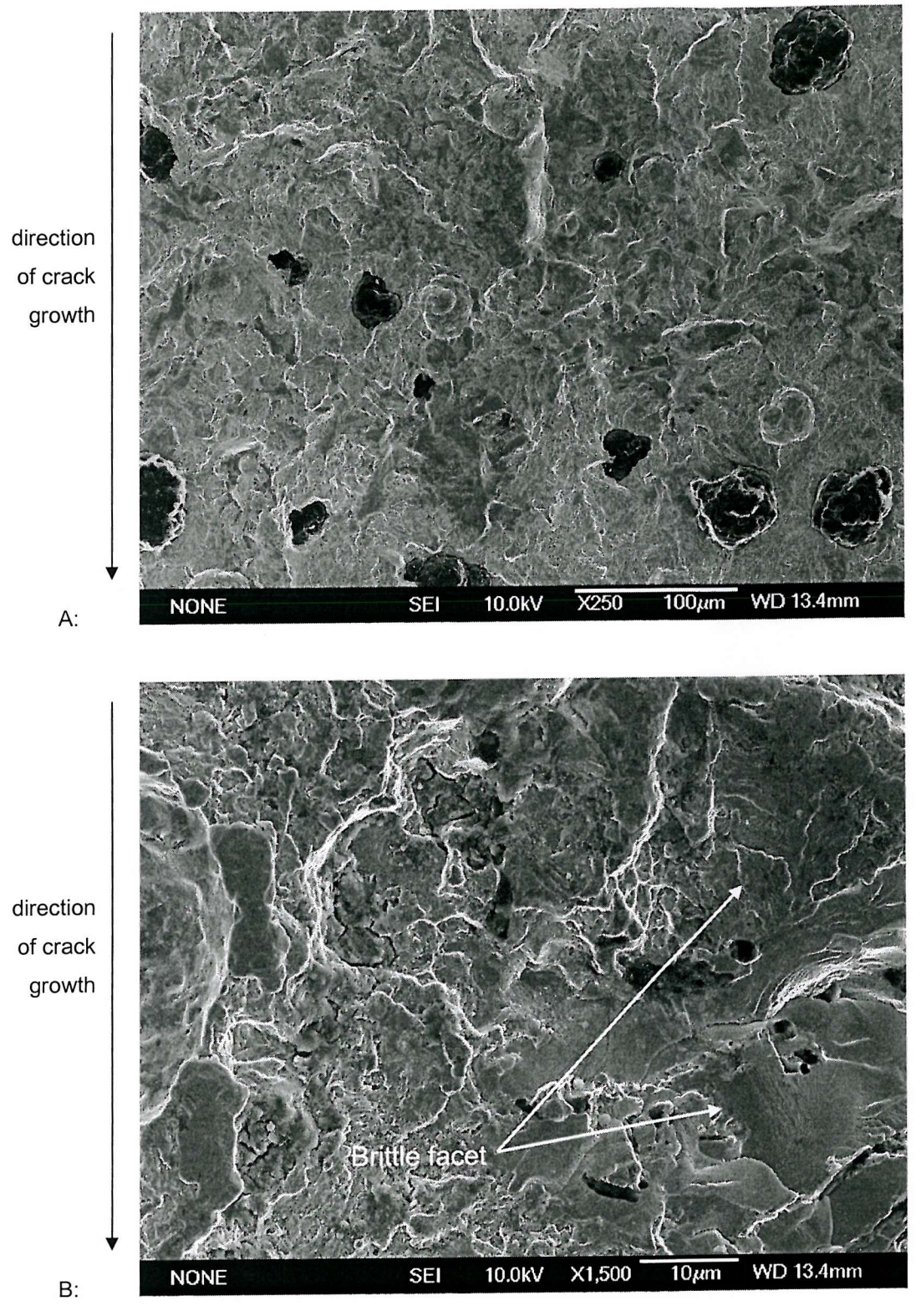

Figure 7.96: '900/390' Threshold and growth out test. Fracture surface: ΔK 15 ~ MPa$\sqrt{m}$

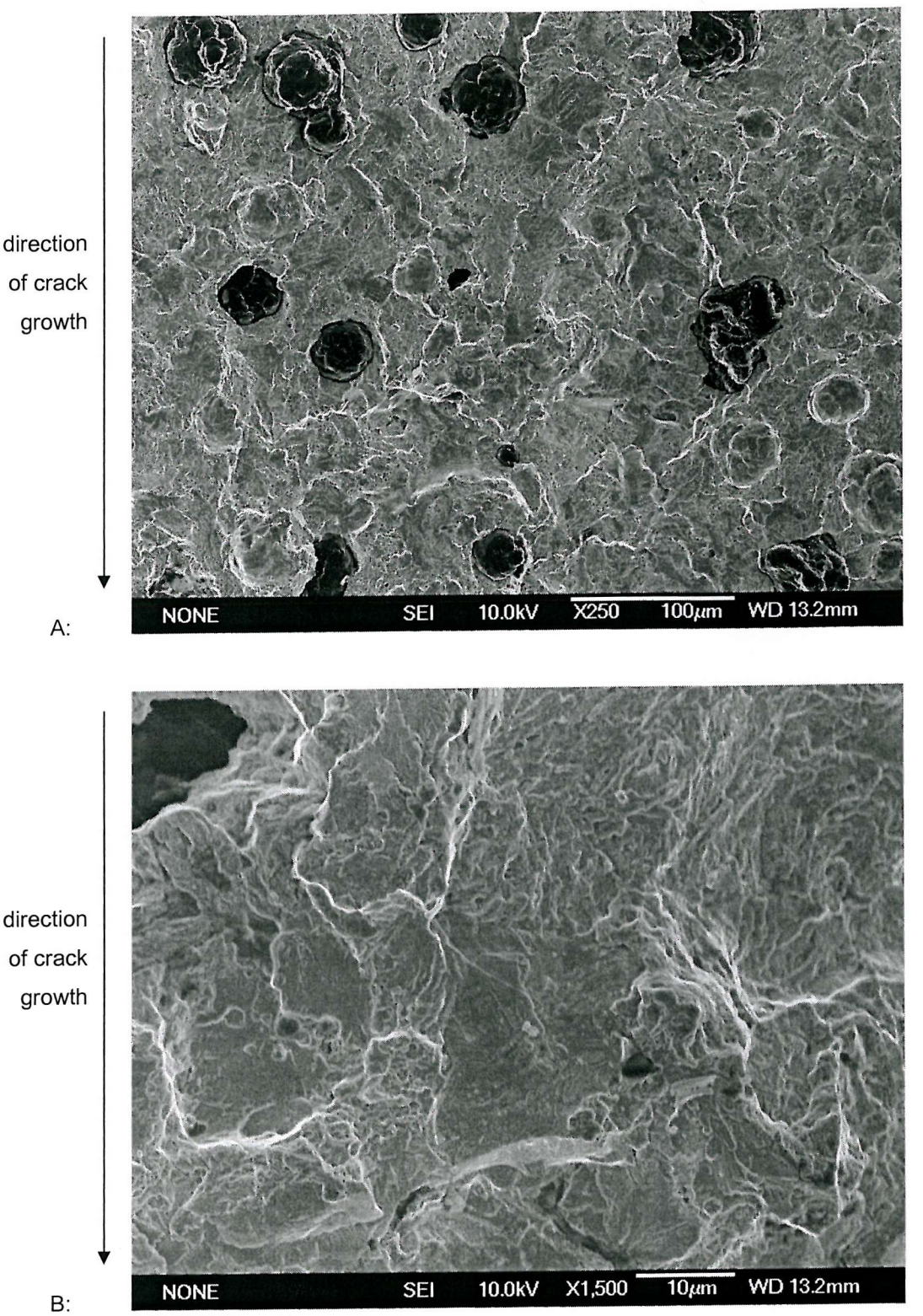

Figure 7.97: '900/390' Threshold and growth out test. Fracture surface: ΔK 20 ~ MPa$\sqrt{m}$.

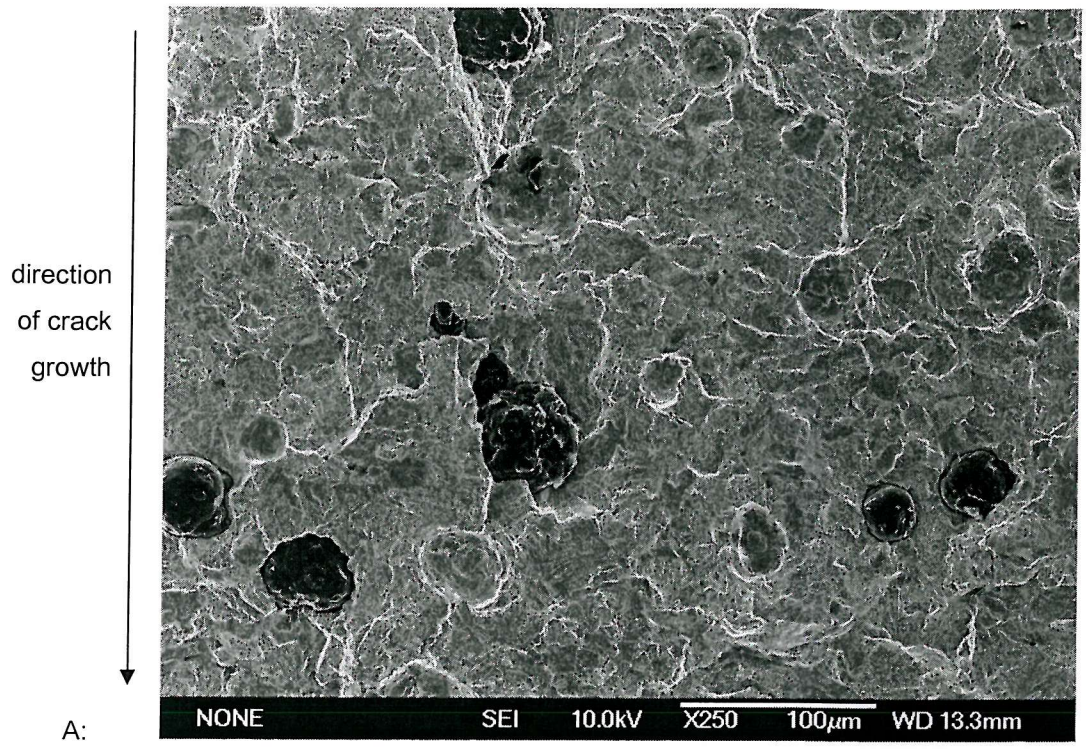

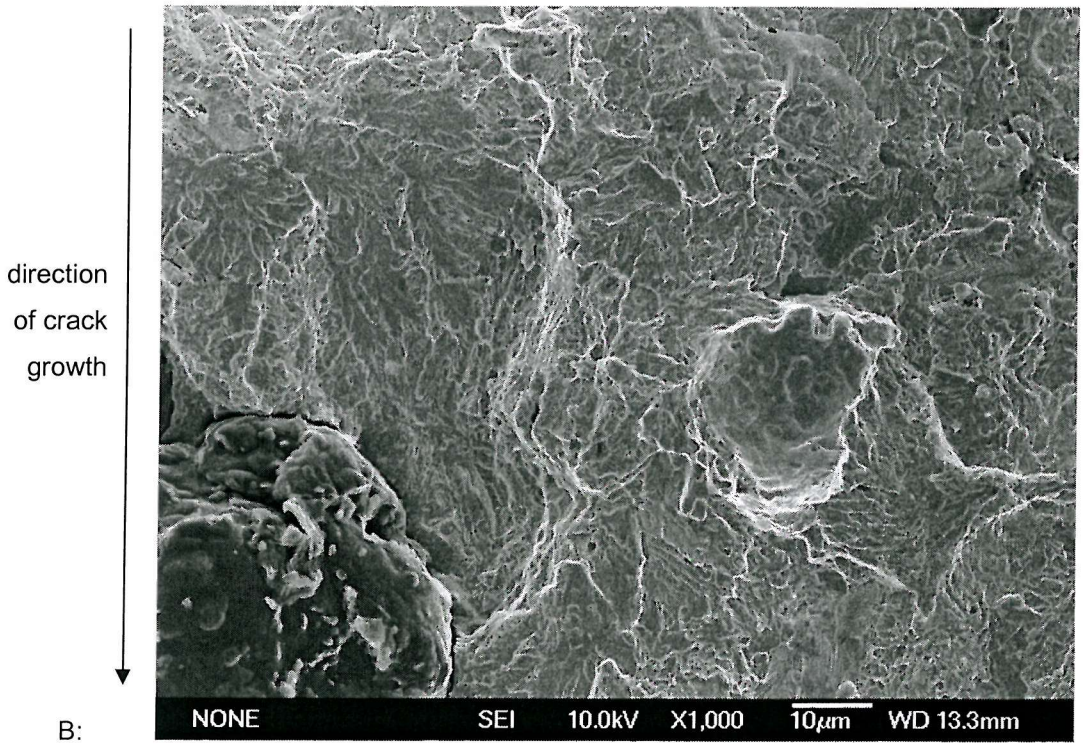

Figure 7.98: '900/390' Growth out test. Fracture surface: ΔK 25 ~ MPa$\sqrt{m}$

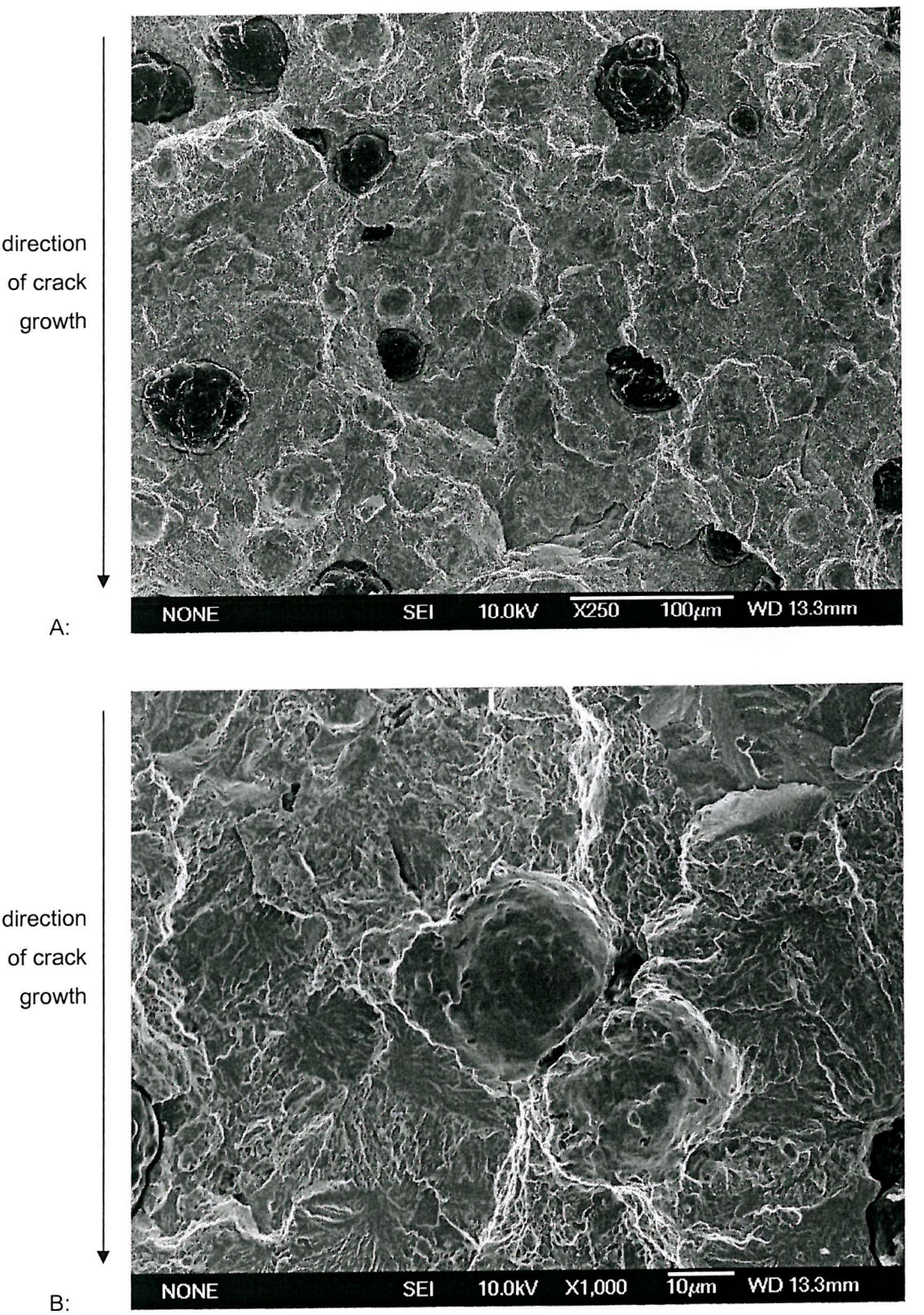

Figure 7.99: '900/390' Growth out test. Fracture surface: ΔK 30 ~ MPa$\sqrt{m}$

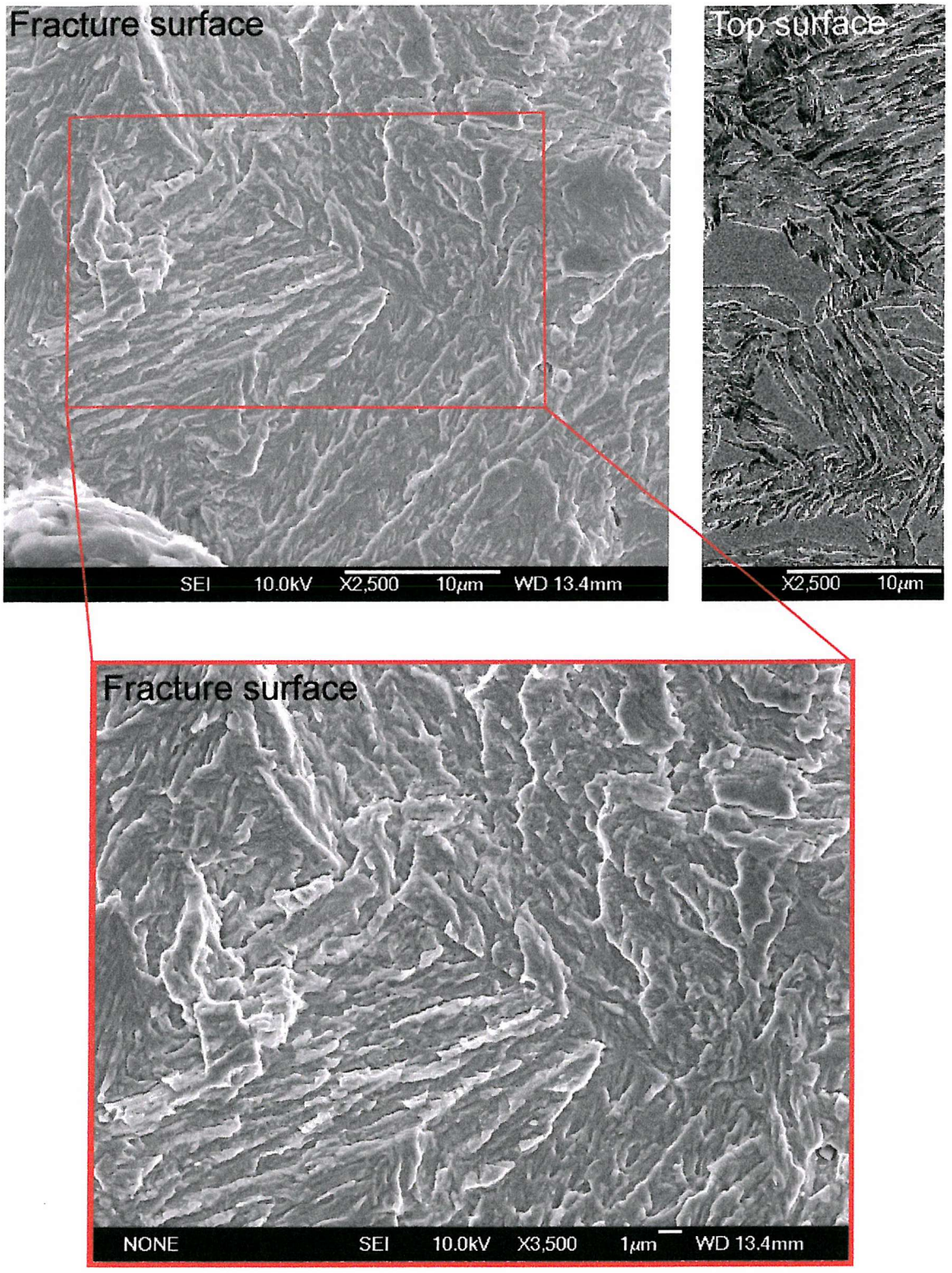

Figure 7.100: '900/390' Threshold and growth out test. Fracture surface: ΔK 8~ MPa√m. Higher magnification images revealing 'feathery' fracture surface. An image of the specimen top surface (top right) allows comparison with bainite morphology.

direction of crack growth

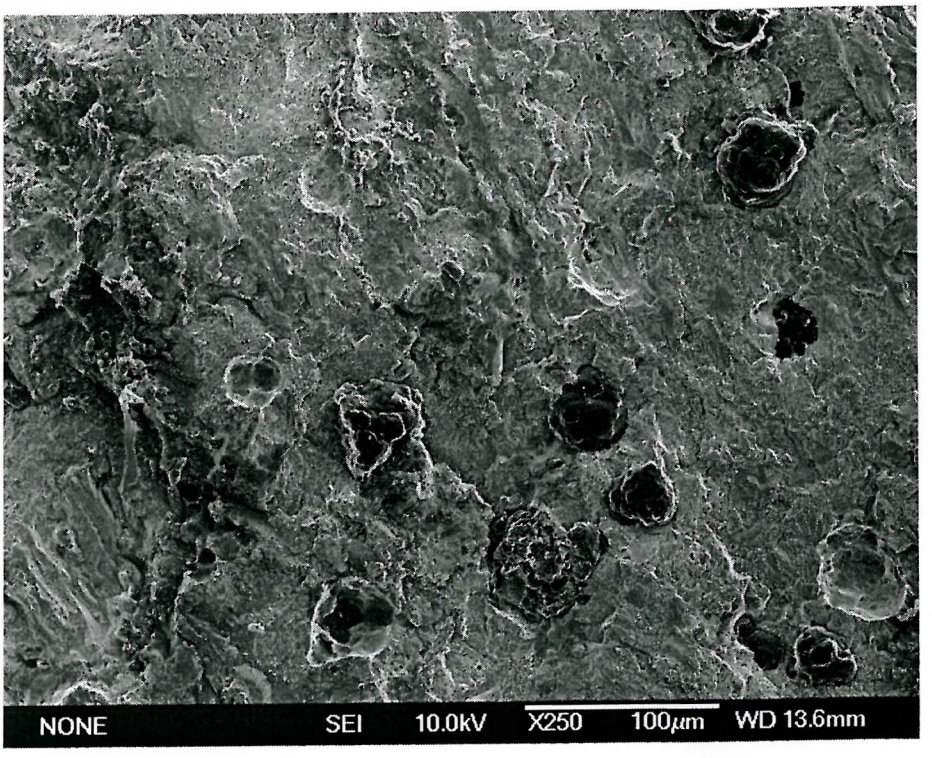

A:

direction of crack growth

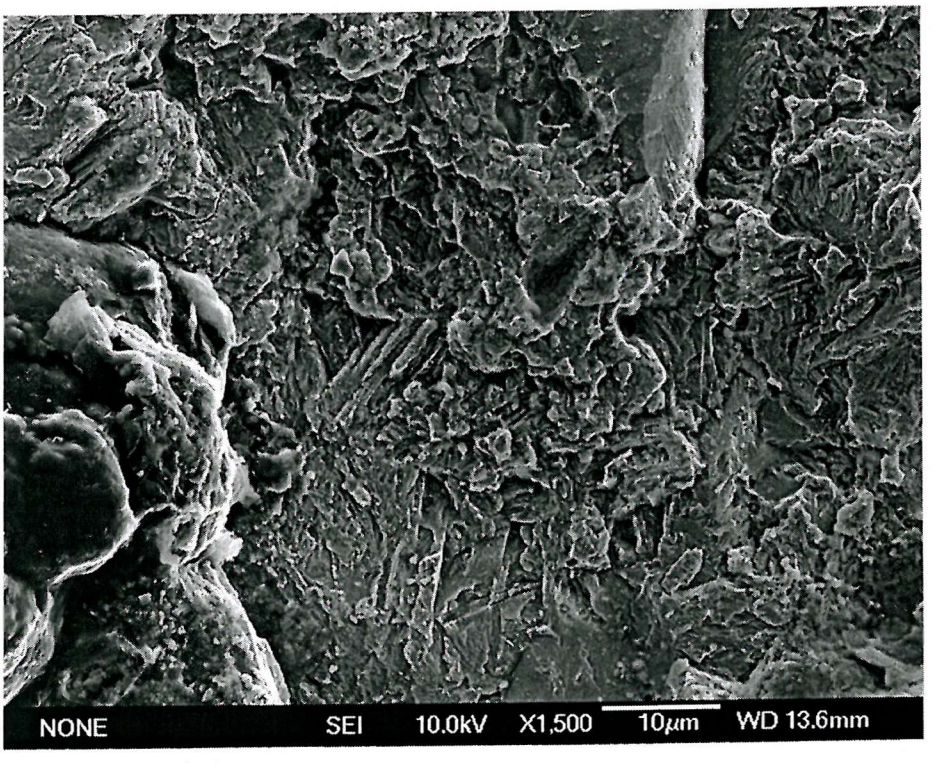

B:

Figure 7.101: '800/260' Threshold and growth out test. Fracture surface: ΔK 5.8 ~ MPa$\sqrt{m}$

direction of crack growth

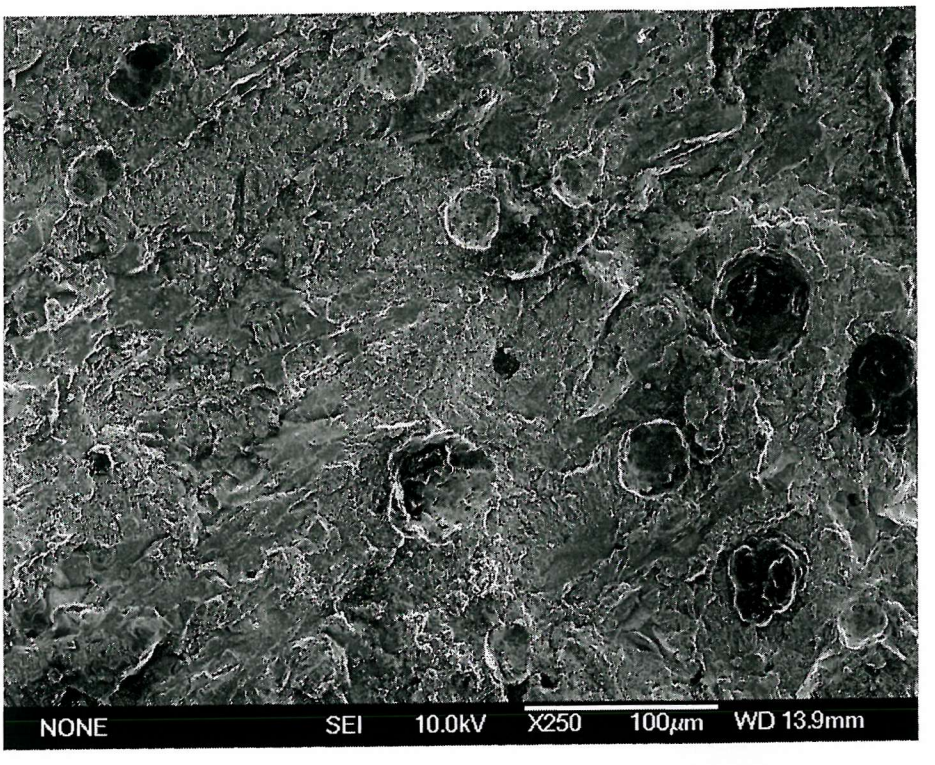

A:

direction of crack growth

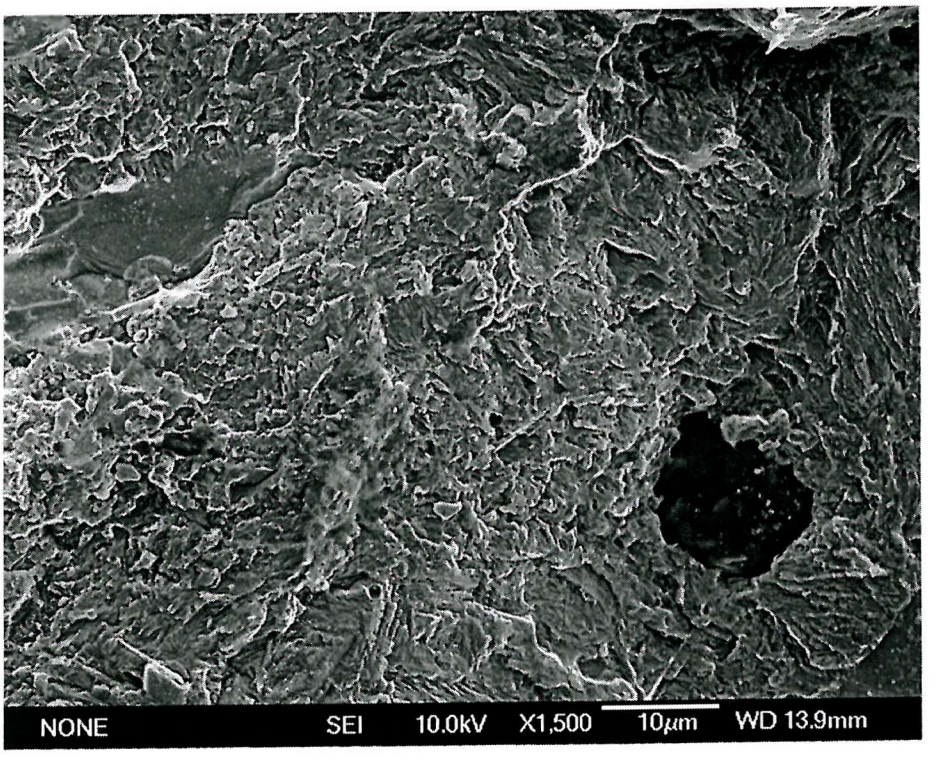

B:

Figure 7.102: '800/260' Threshold and growth out test. Fracture surface: ΔK 8 ~ MPa$\sqrt{m}$

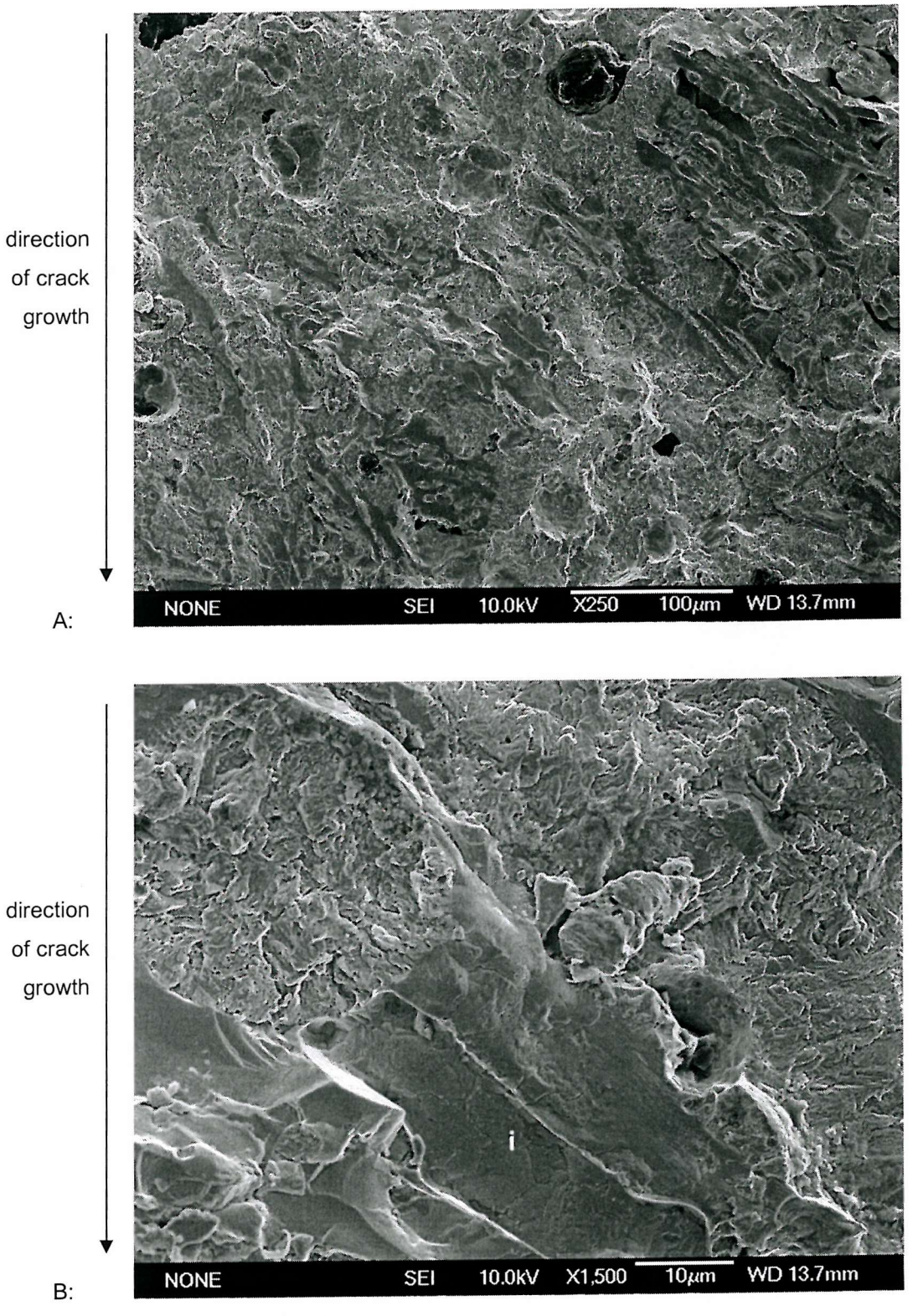

Figure 7.103: '800/260' Threshold and growth out test. Fracture surface: ΔK 15 ~ MPa$\sqrt{m}$
Region i: Brittle facet of fractured eutectic carbide.

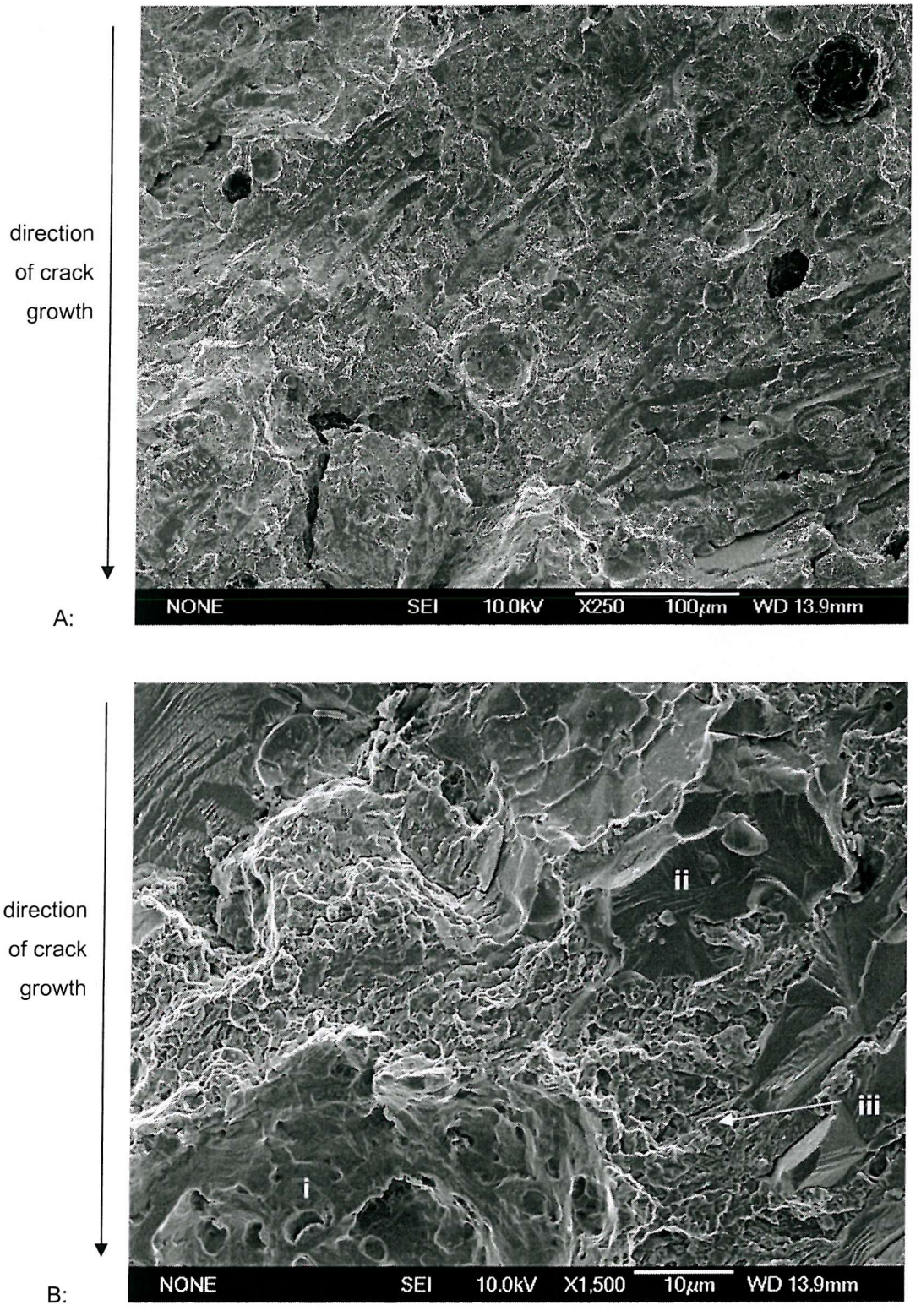

Figure 7.104: '800/260' Threshold and growth out test. Fracture surface: ΔK 20 ~ MPa$\sqrt{m}$.

Region i: Crater left by decohered graphite nodule.

Region ii: Brittle facet of fractured eutectic carbide.

Region iii: Micro-void coalescence representing ductile fracture.

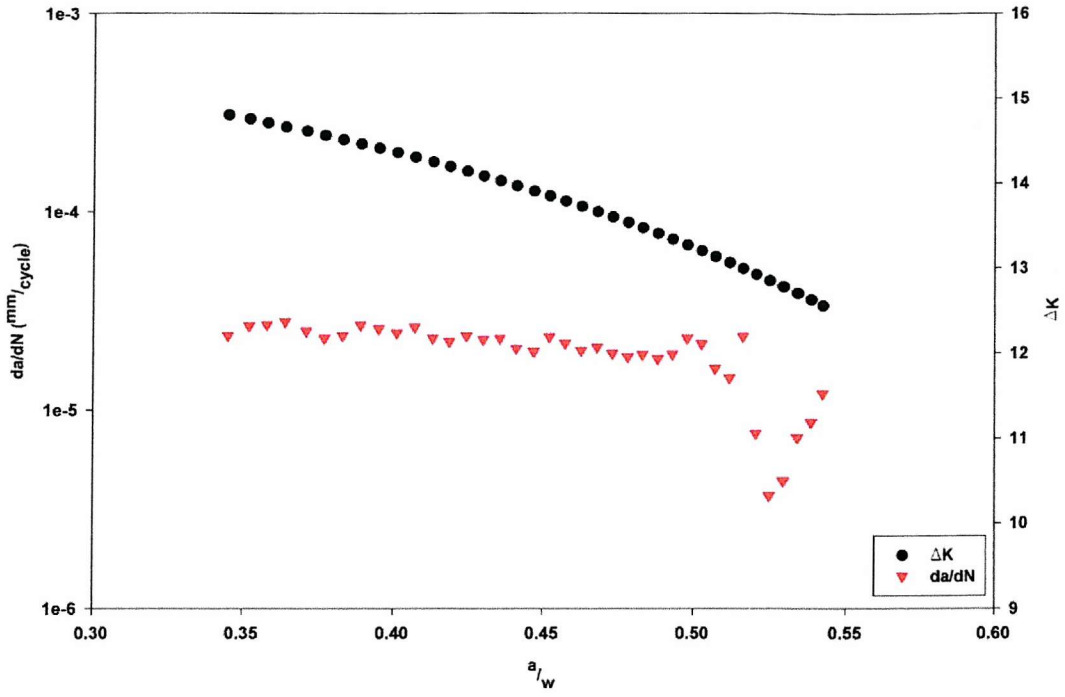

Figure 7.105: The variation of crack growth rates and ΔK as a function of $^{a}/_{w}$ for '900/390:L4'

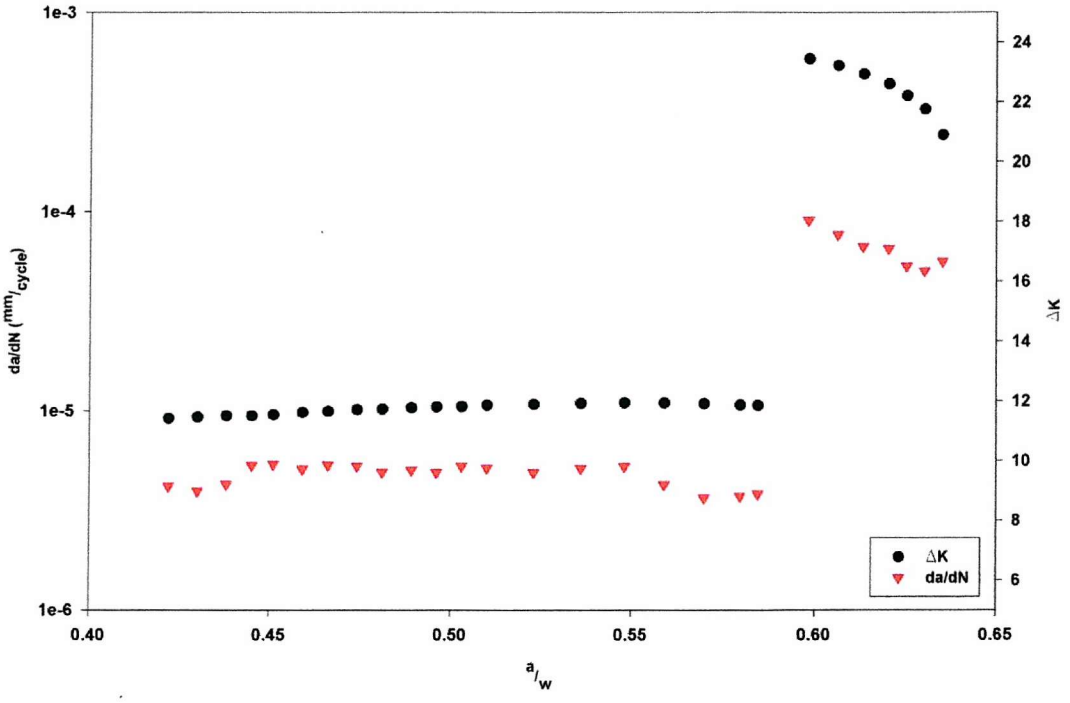

Figure 7.106: The variation of crack growth rates and ΔK as a function of $^{a}/_{w}$ for '900/390:L6'

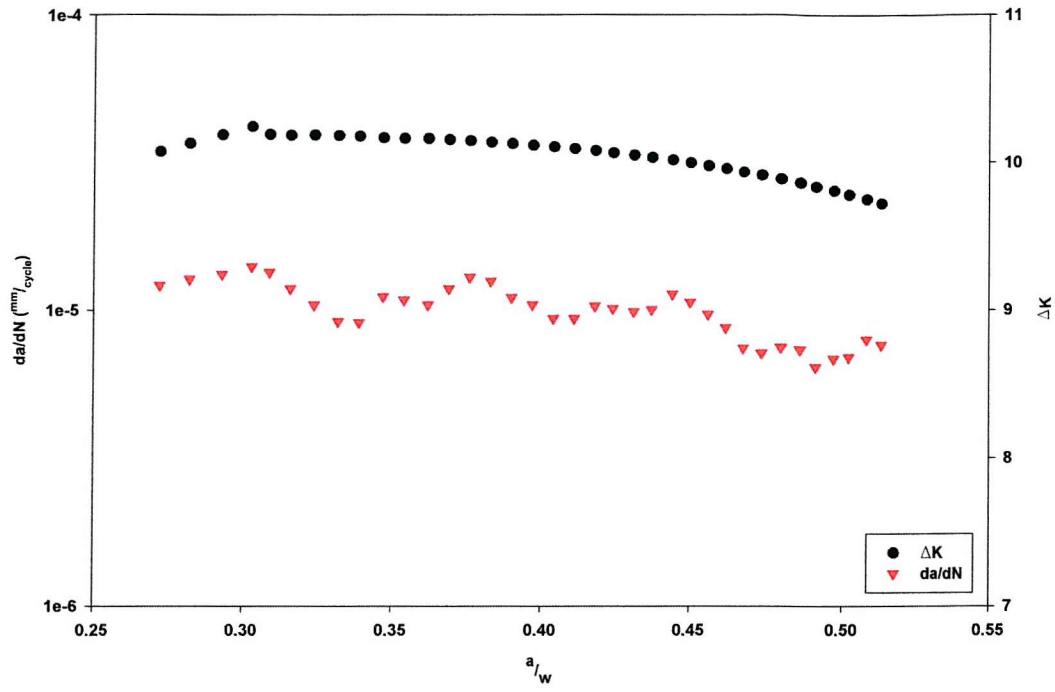

Figure 7.107: The variation of crack growth rates and ΔK as a function of $^{a}/_{w}$ for '800/260:L2'

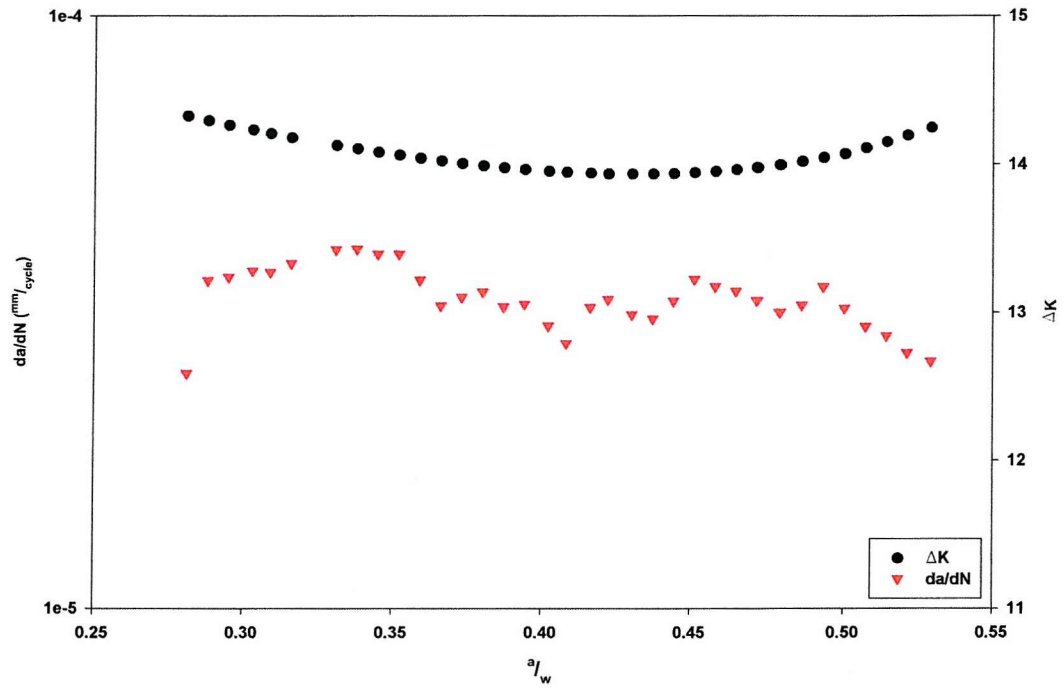

Figure 7.108: The variation of crack growth rates and ΔK as a function of $^{a}/_{w}$ for '800/260:L3'

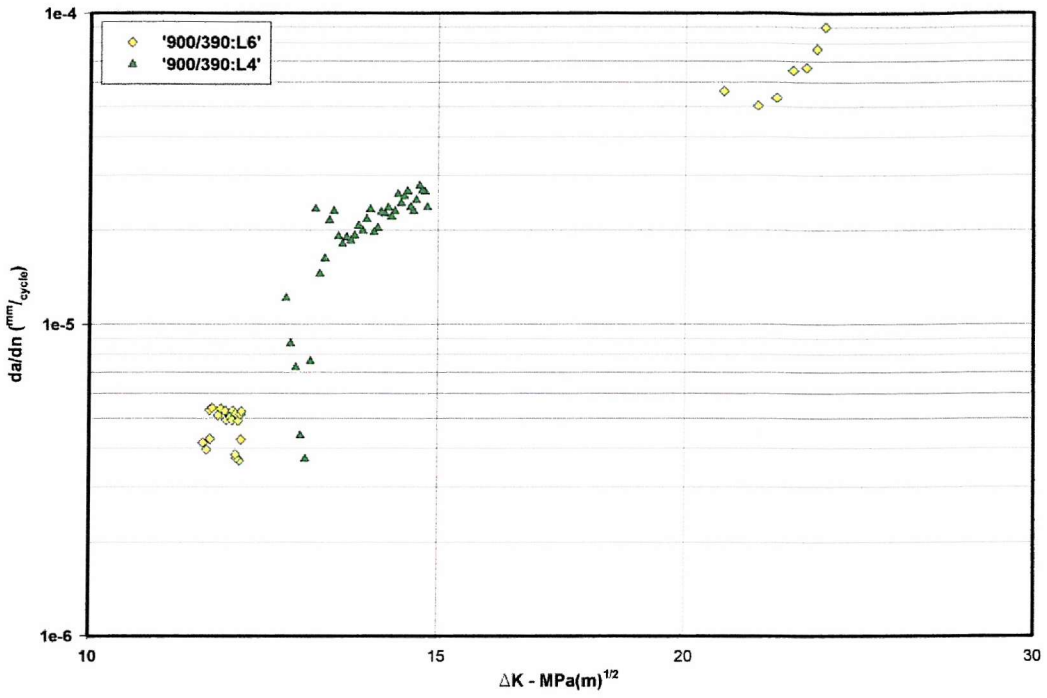

Figure 7.109: Comparison of da/dN vs. ΔK for '900/390' constant ΔK regions.

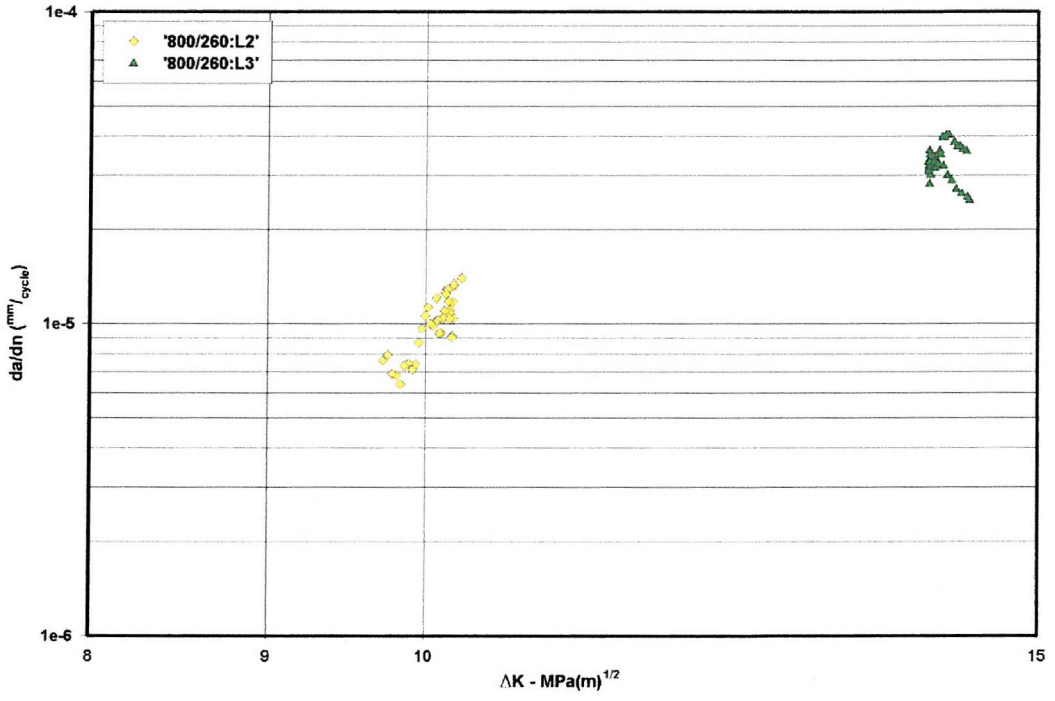

Figure 7.110: Comparison of da/dN vs. ΔK for '800/260' constant ΔK regions.

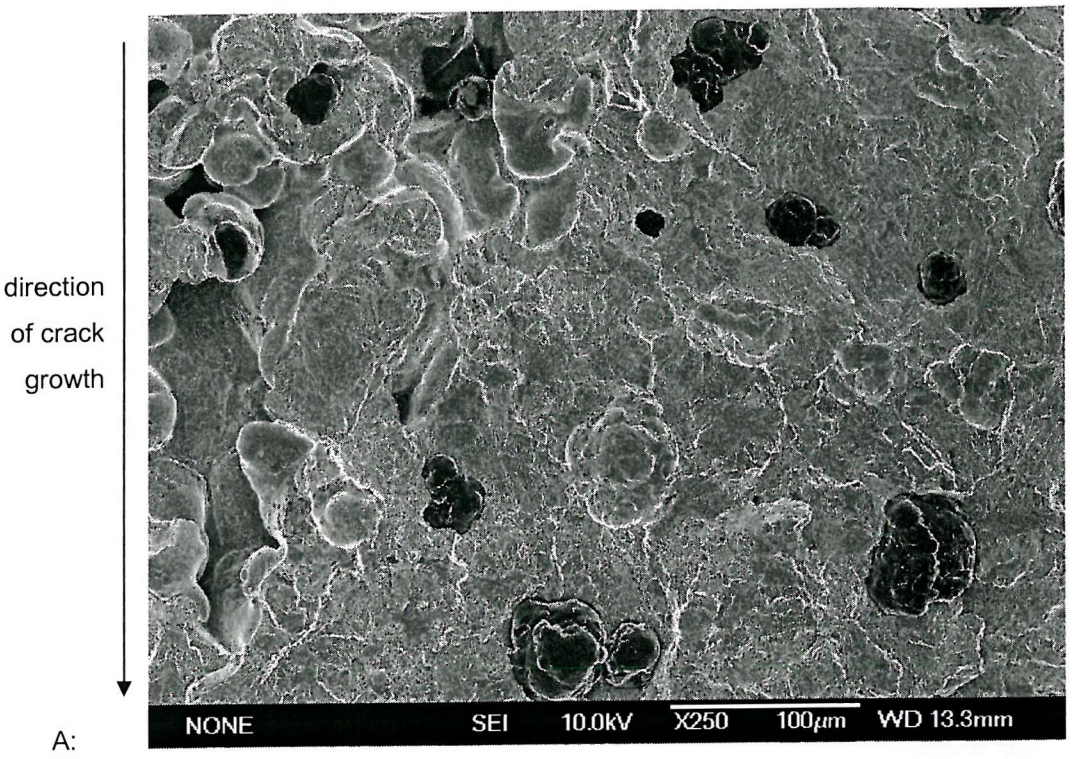

Figure 7.111: Fracture surface (900/390:L6) ΔK 11 ~ MPa$\sqrt{m}$, da/dN = 3.7×10^{-5} mm/cycle.

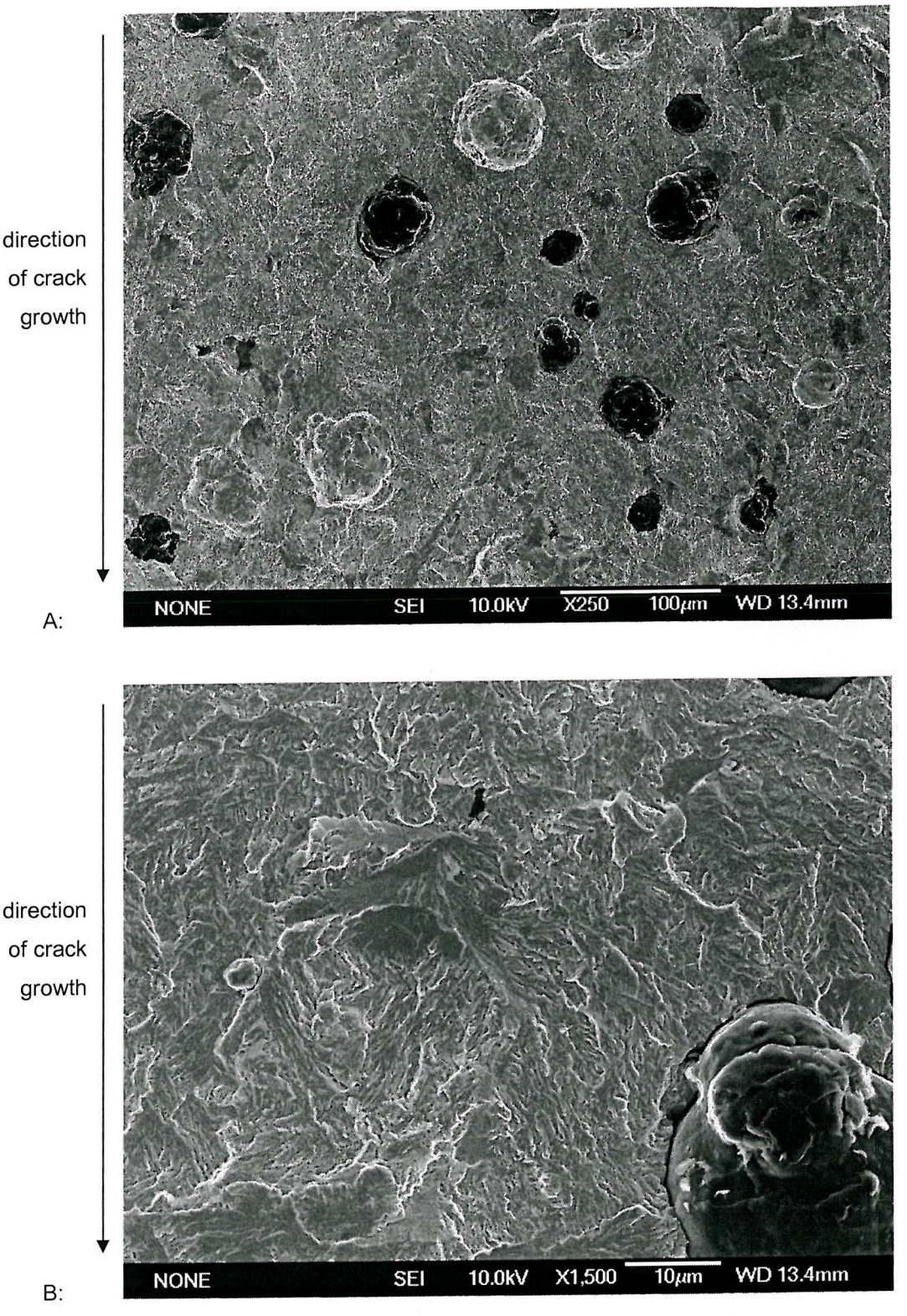

Figure 7.112: Fracture surface (900/390:L6) ΔK 11 ~ MPa$\sqrt{m}$, da/dN = 4.0×10^{-5} mm/cycle.

direction of crack growth

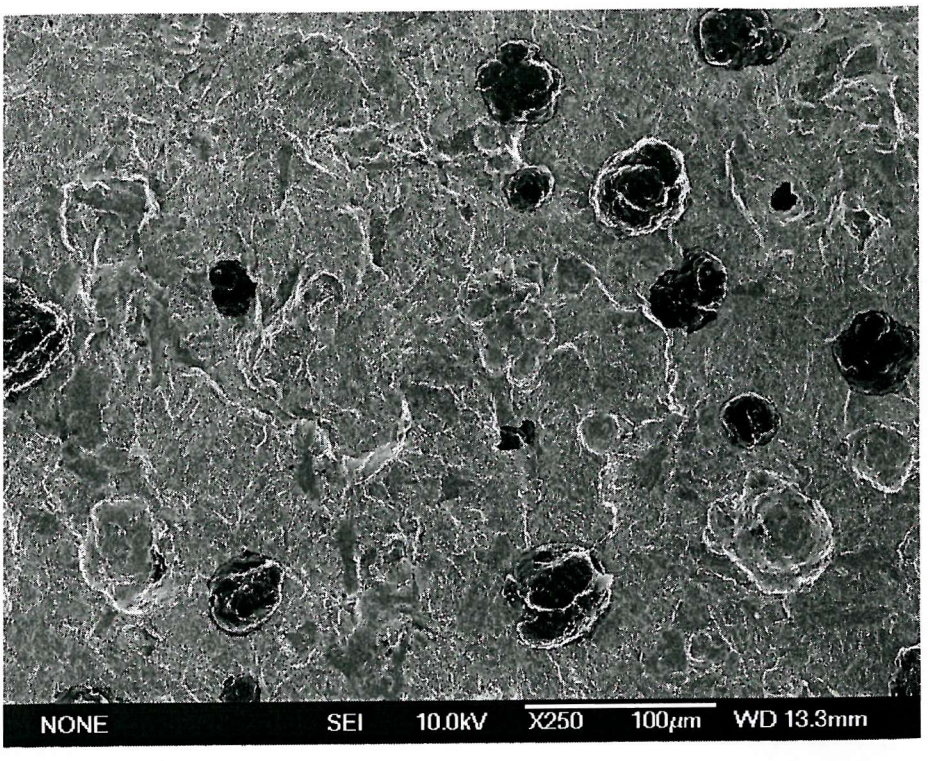

A:

direction of crack growth

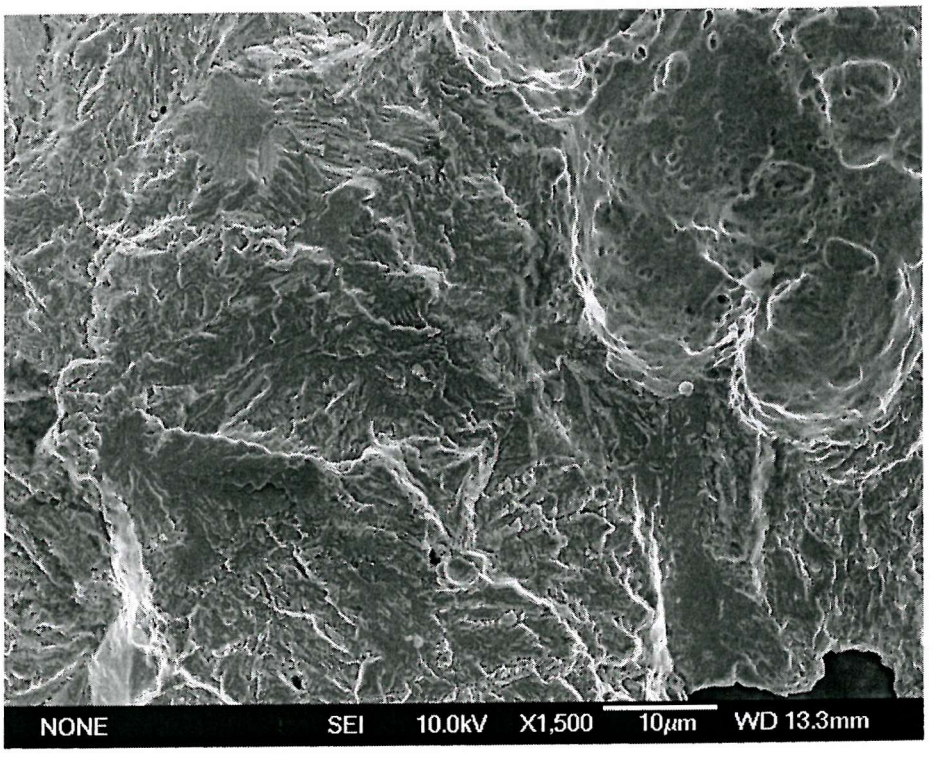

B:

Figure 7.113: Fracture surface (900/390:L6) ΔK 11 ~ MPa$\sqrt{m}$, da/dN = 4.9×10^{-5} mm/cycle.

direction of crack growth

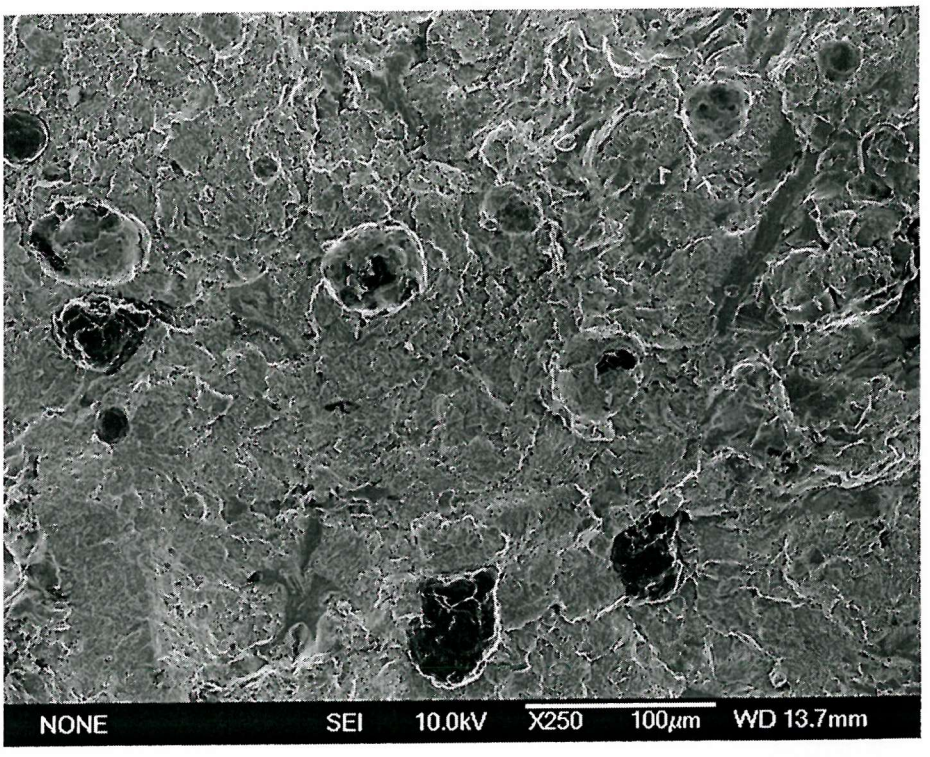

A:

direction of crack growth

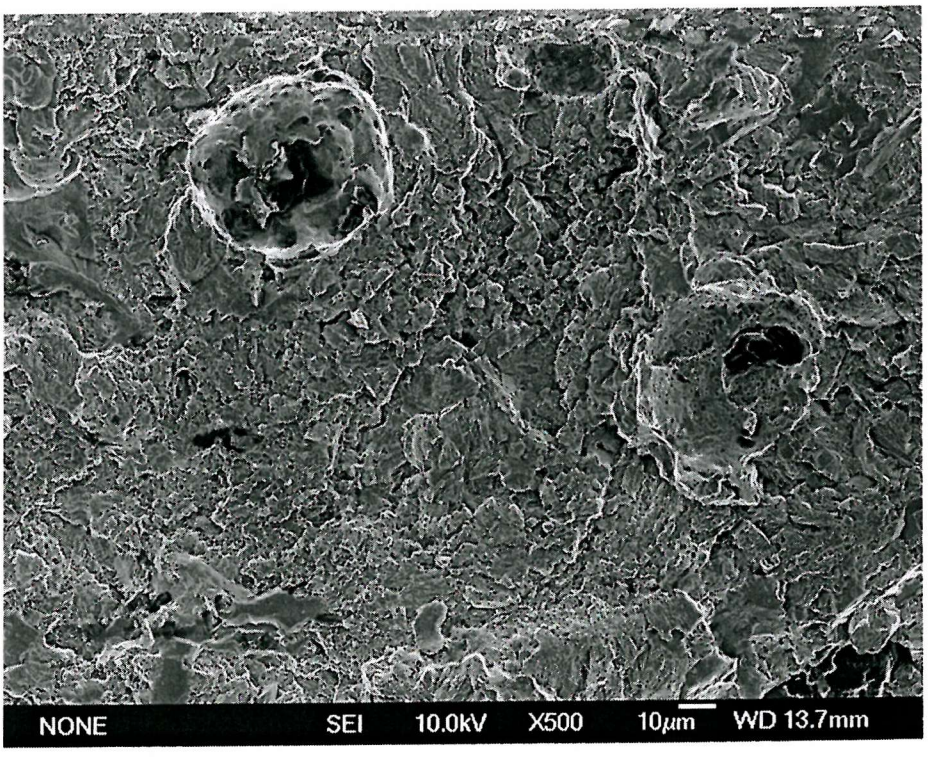

B:

Figure 7.114: Fracture surface (800/260:L3) ΔK 14 ~ $MPa\sqrt{m}$, $^{da}/_{dN}$ = $2.6x10^{-5}$ mm/cycle.

direction of crack growth

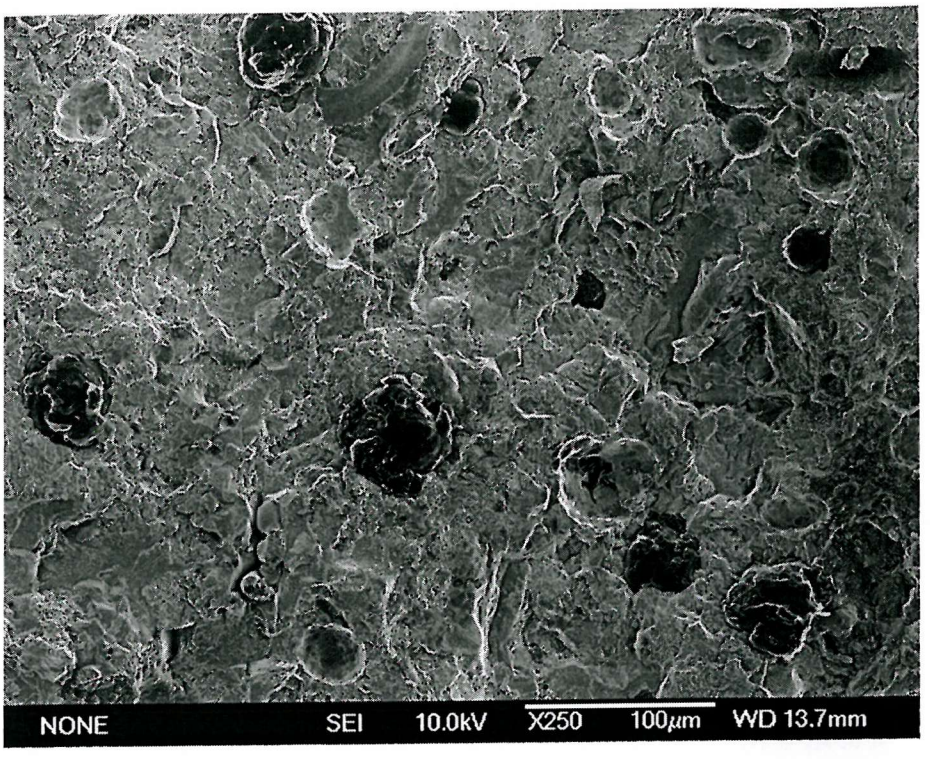

A:

direction of crack growth

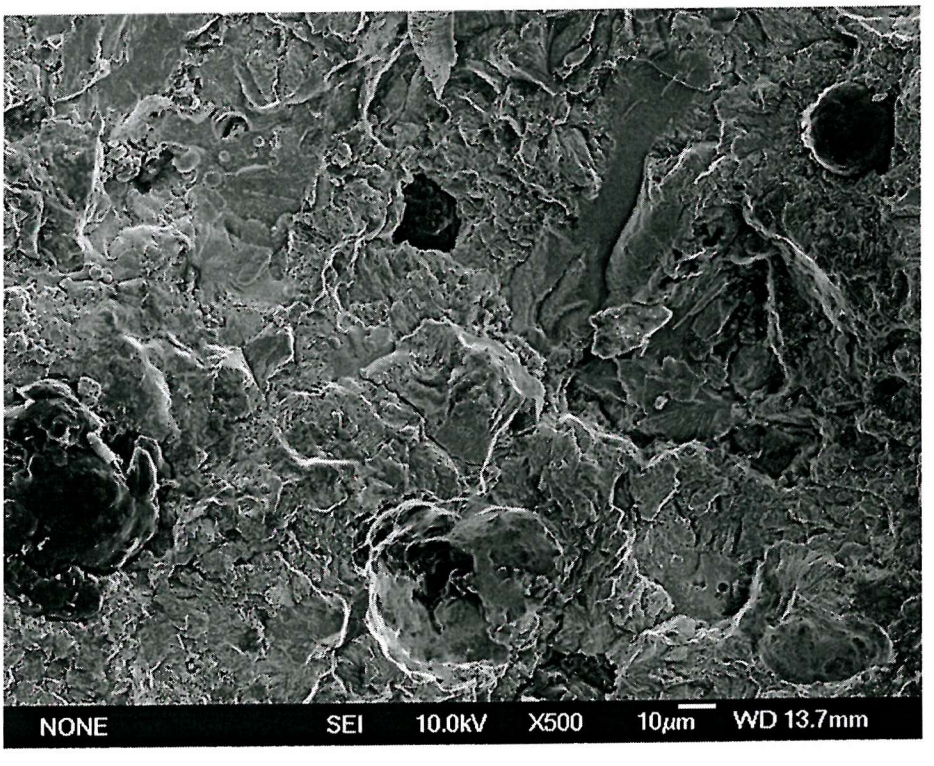

B:

Figure 7.115: Fracture surface (800/260:L3) ΔK 14 ~ MPa$\sqrt{m}$, $^{da}/_{dN}$ = 3.2x10^{-5} mm/cycle.

direction of crack growth

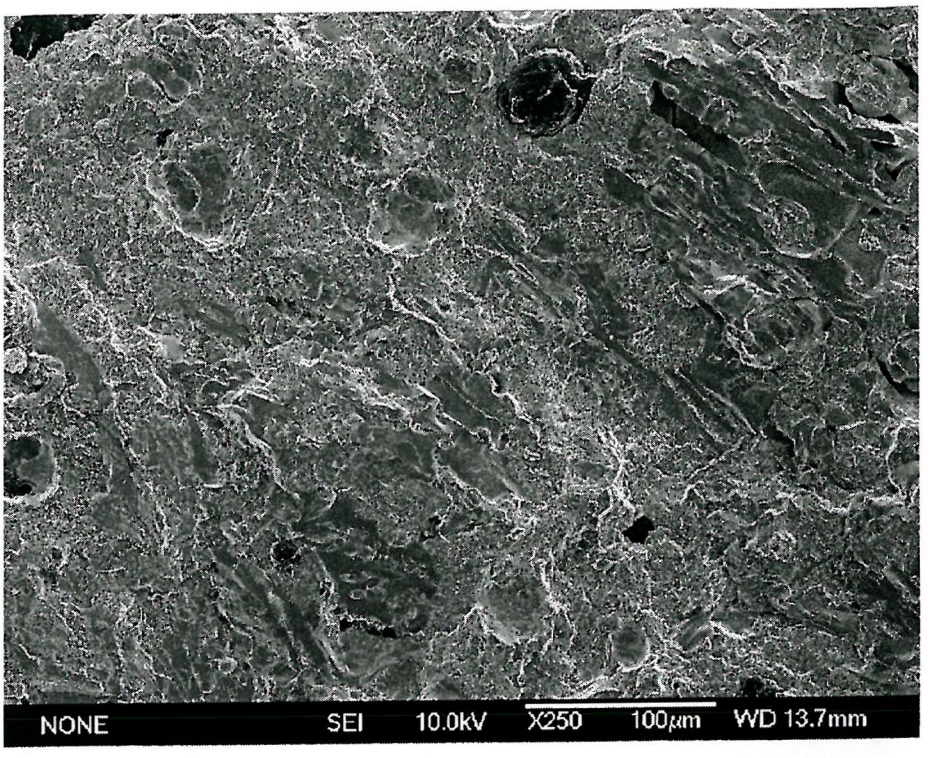

A:

direction of crack growth

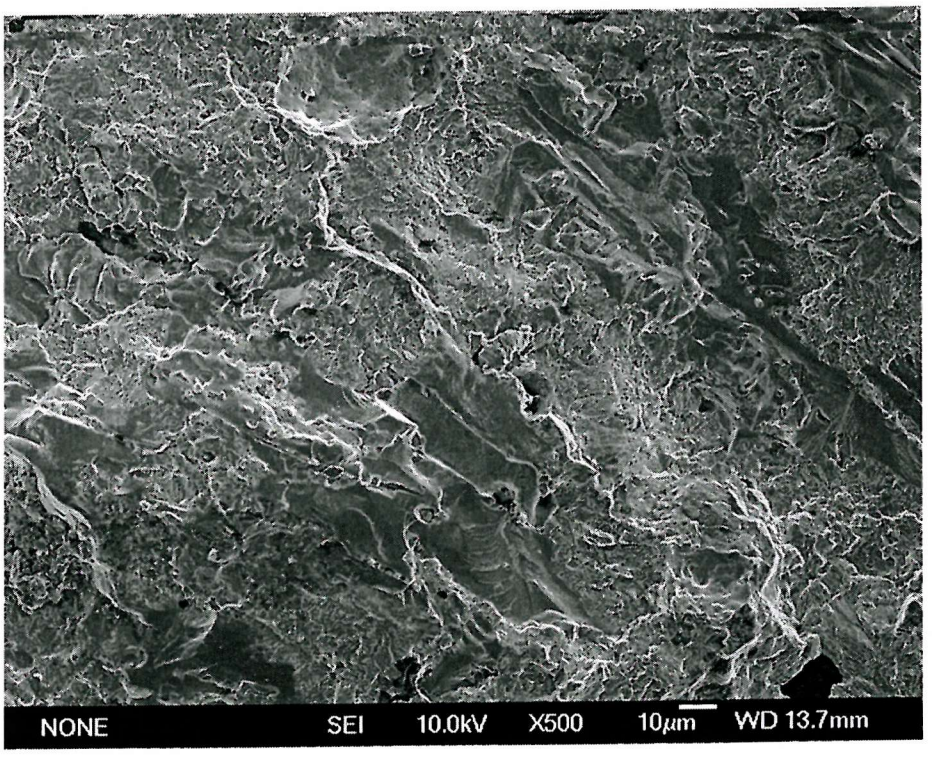

B:

Figure 7.116 Fracture surface (800/260:L3) ΔK 15 ~ $MPa\sqrt{m}$, $^{da}/_{dN}$ = $5.1x10^{-5}$ mm/cycle.

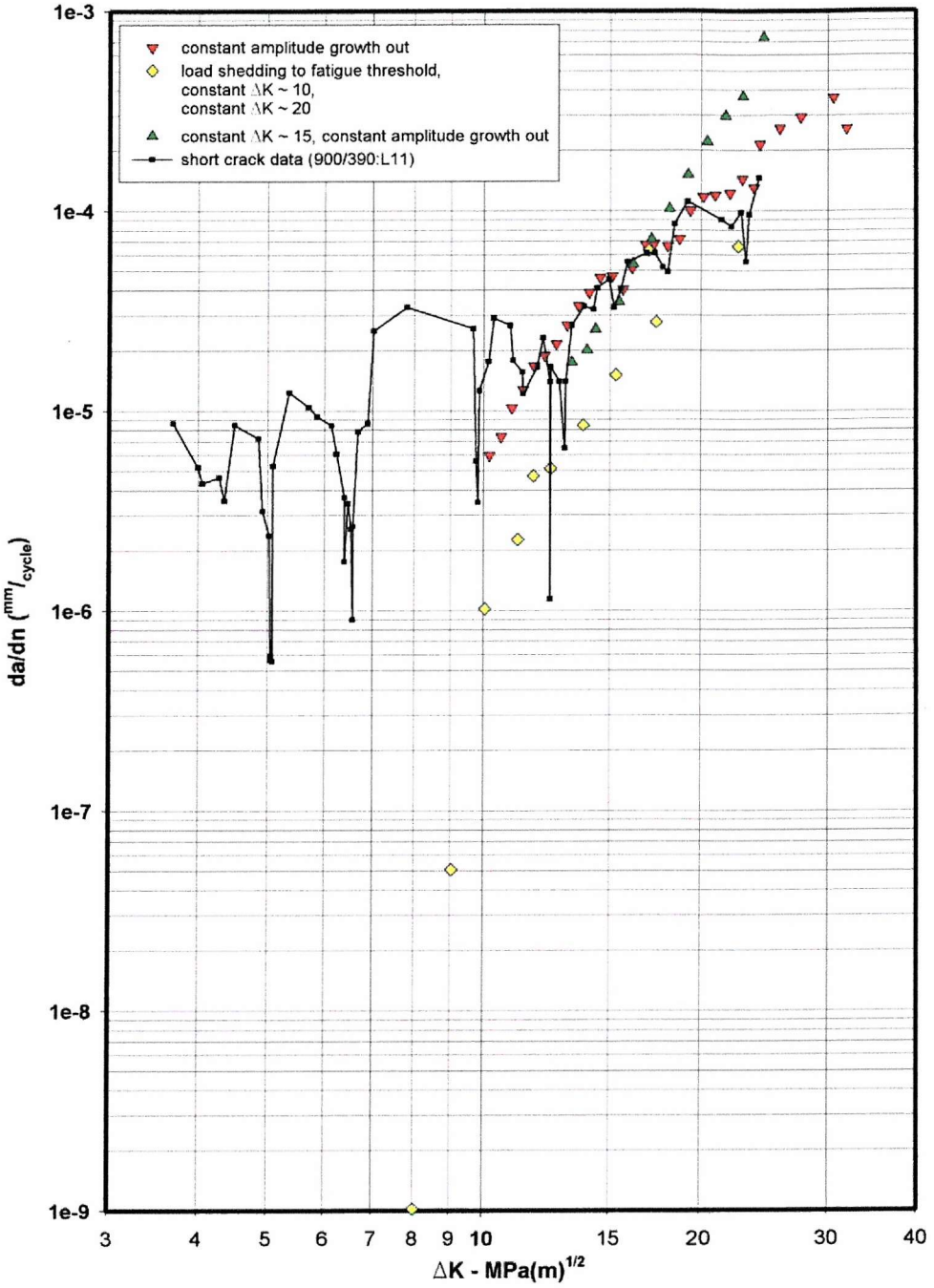

Figure 7.117: Comparison of '900/390' long and short fatigue crack data

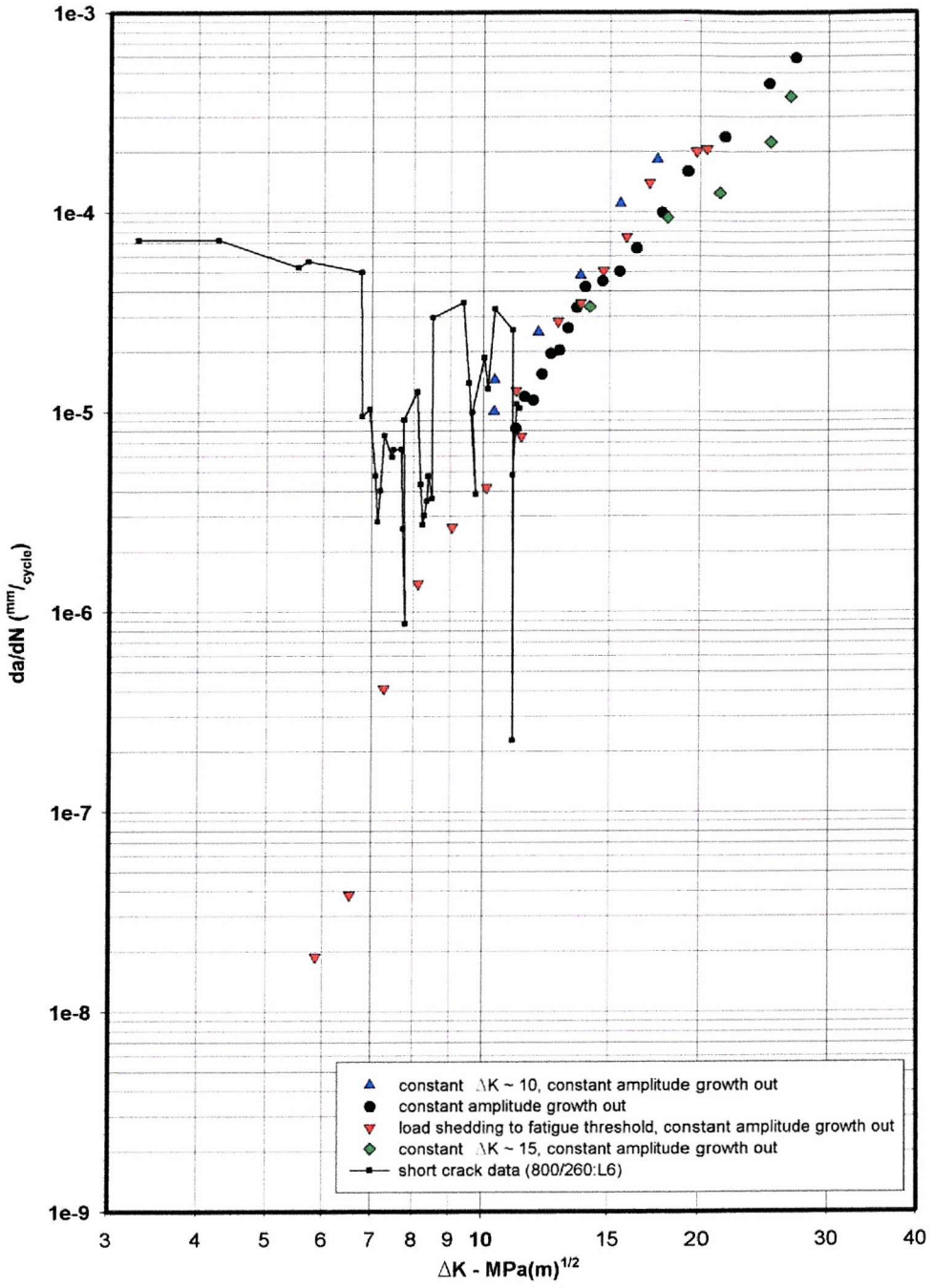

Figure 7.118: Comparison of '800/260' long and short fatigue crack data.

8 Discussion

8.1 Hardness Testing

Figure 7.1 shows the hardness values of all the alloy conditions considered by this study and previous work at Southampton University [2,3,4]. The two chilled alloy variants are clearly the hardest. This is expected since the purpose of chilling a material is to promote the formation of hard carbidic structures. The ADI heat treatments austempered at 250^0C – 260^0C show higher hardness values than those austempered at 390^0C – 400^0C. This relationship between austempering temperature and hardness concurs with data found in the literature [59,66,67]. It is thought however, that the intrinsic relationship lies between the hardness of an ADI heat treatment and the microstructure promoted by these austempering conditions.

8.2 Hardness as a Function of Microstructure

It is reasonably apparent from the graph (Figure 7.2) that the hardness of an ADI alloy is inversely related to the predicted retained austenite volume fraction. Since bainite contains Fe_3C precipitates within or between sheaves it is generally the harder phase within the ADI matrix. It is therefore reasonable to expect that microstructures with lower retained austenite and corresponding higher bainite volume fractions to exhibit higher values of hardness. This relationship appears to be generally true for all the seven ADI heat treatments. The anomalous hardness value for the '850/250' heat treatment is explained by the formation of Widmanstatten ferrite in the matrix microstructure, as discussed in section 6.2. The presence of Widmanstatten ferrite can be seen in Figure 6.2 as white sheaves and as a relatively soft phase is expected to lower the hardness. Values of hardness for the '800/390' and '850/400' heat treatments are expected to be comparable due to similar predicted proportions of retained austenite and bainite. Observation of Figure 7.1 however, shows the '800/390' heat treatment is significantly harder. The increase in the hardness of approximately one third over the '850/400' condition is likely to be caused by the presence of eutectic carbides. Micro-hardness testing identified the hardness of these carbides to be approximately 750 H_V. These carbides are not predicted by the Loughborough

microstructural evolution model which assumes all the carbon in the as-cast DI is in the form of graphite nodules. In the case of the '800/390' heat treatment eutectic carbides represent on average 23% of the surface area and are 140% harder than the values predicted for the surrounding matrix. The presence of eutectic carbides, with mean specimen area fractions of 6.9% and 7.2% for the as-cast ductile iron and '800/260' heat treatment respectively, is expected to have less of an effect on the mean hardness values of these alloy variants. The following summation was used to give a simple comparison between predicted and measured values of hardness whilst considering the comparative hardness and area fraction of eutectic carbides.

$$Hv_{(carbide-measured)}\left(Af_{(carbide)}\right)+Hv_{(microstructure-predicted)}\left(1-Af_{(carbide)}\right)\approx Hv_{(microstructure-measured)}$$

Equation 8.1

For the '800/390' heat treatment:

$$750(0.23)+311(0.77)=412Hv \text{ whilst } Hv_{(microstructure-measured)}=420Hv$$ *Equation 8.2*

Similarly, for the '800/260' heat treatment:

$$750(0.072)+461(0.928)=482Hv \text{ whilst } Hv_{(microstructure-measured)}=529Hv$$ *Equation 8.3*

In the case of the '800/390' heat treatment, the summation above gives a reasonable correlation between predicted and measured values of microstructure hardness. This is not so for the '800/260' heat treatment, where the measured value of hardness is still significantly higher than that calculated by the summation. However, since the presence of carbides in the as-cast DI of the current ADI heat treatments is not addressed by the microstructure evolution model (as discussed in section 6.1), the values of retained austenite volume fraction used in Figure 7.2 may not be wholly representative of the current ADI heat treatments. The same caveat should be applied to the prediction of mechanical properties (Table 7.1) and may explain the variation between experimental and predicted values of hardness.

8.2.1 Variability in Hardness on a Macroscopic Scale

The values of standard deviation and coefficient of variance presented in Figure 7.1 indicate the consistency of hardness measurement differs from one heat treatment to another. It is reasonable to assume that the measured hardness values of alloy conditions with low values of coefficient of variance are representative of the bulk material. This would imply the scale of the indent for these tests is larger than any variability in the microstructure which might cause a macroscopic inconsistency in hardness measurement. With the exception of the as-cast DI and the '800/260' heat treatment, this is the case for all tested alloy conditions. Since the '800/390' microstructure shows a relatively low coefficient of variance, the presence of eutectic carbides in the as-cast DI and the '800/260' heat treatment cannot be solely responsible for the variability in hardness. It is possible the variability of distribution of the carbides in these two alloy conditions with respect to the more homogeneous distribution found in the '800/390' heat treatment is responsible for the scatter in hardness values. The variability in hardness within the '800/260' heat treatment is explored more fully in section 8.2.3.

8.2.2 Variability in Hardness on a Microscopic Scale

The complexity of the cast iron microstructure is such that a significant variation in hardness is expected throughout the microstructure on a microscopic scale. For the case of the ADI microstructure, graphite nodules are comparatively very soft with respect to the matrix. The matrix itself is formed by two main constituents (retained austenite and bainite), the hardness values of which are quite different. Furthermore, when considering austempering kinetics, it is expected there will [9] be a possible hardness gradient between neighbouring graphite nodules. As discussed in section 6.2.4, the growth of bainite sheaves away from the graphite nodules, leave regions of supersaturated austenite in areas remote from nodules. Therefore, as the distance from the graphite nodules increases, the proportion of austenite increases. Since retained austenite is a softer phase than bainite the hardness value is expected to decrease in these areas. The variation in hardness due to the distribution of retained austenite and bainite is on too small a scale to be investigated with Vickers hardness indents and would ideally require a series of nano-hardness indents between graphite nodules. This was beyond the scope

of this work. The presence of constituent segregation and eutectic carbides in the austenitised microstructure may further increase the complexity of this hardness gradient. Constituent segregation and the formation of primary eutectic carbides are discussed in section 6.2.4. The variation in hardness due to the distribution of primary eutectic carbides can be assessed with Vickers hardness indents and is discussed in the following section.

To summarise, bainite is harder than retained austenite, and primary eutectic carbides are harder still. The distribution and proportion of these constituents therefore has a great significance on hardness. This local microstructural variation in hardness may be a significant factor when considering crack initiation in or propagation through such a region.

8.2.3 Hardness Mapping

The hardness value mapping of an '800/260' plain bend bar specimen revealed a longitudinal variation in hardness which correlated with a similar gradient in the local eutectic carbide area fraction of the same specimen. The higher the eutectic carbide area fraction; the greater the local hardness value. This is not unexpected since the hardness of individual carbides (~750 H_{v20}) is 55% greater than that of the surrounding matrix. As discussed in section 6.2.4, the variability in the quantity of eutectic carbide within a specimen is likely to be caused by the variation in cooling rate experienced throughout the casting: A greater amount of carbide formation is likely to occur in the faster to cool areas. The data collected from the hardness testing allows a simple prediction of hardness from carbide area fraction. This allows an estimation of hardness without needing to damage a specimen inspection area with hardness indents.

8.3 Summary of Fatigue Performance

In terms of the number of fatigue cycles to failure at a given stress level, the '900/390' heat treatment showed the best short crack fatigue performance. Furthermore, this ADI heat treatment resisted failure at a higher stress (500 MPa) than any other alloy condition of this work. A number of '800/260' specimens showed comparable fatigue lifetimes to the '900/390' condition. However, this represented only a small percentage of '800/260' specimens, the majority of which showed shorter lifetimes at comparable stress levels than the '900/390' condition. At worst, the '800/260' heat treatment showed no improvement over the as-cast DI. The poorest performers in terms of short crack fatigue lifetime were the '800/390' and chilled ductile iron specimens. This is not an inverse ranking of the variant hardness values as was observed during previous work at Southampton University. The '800/260' heat treatment is harder than the '800/390' treatment yet exhibits a greater resistance to short fatigue crack cycling. Indeed the '800/390' specimens failed under monotonic loads lower than the mean load applied to either the other two ADI heat treatments. This believed to be related to the carbidic structures of these two ADI heat treatments and the associated mechanism of fatigue failure. This is discussed further in section 8.4.5.

Figure 8.1 compares all the short fatigue crack specimens from the current batch of alloy conditions with those previously tested at Southampton University. It is apparent from this S-N curve that the '850/400' and '950/400' heat treatments show longer fatigue lifetimes at comparable values of maximum applied stress than all other heat treatments. The as-cast, '800/260' and '900/390' conditions showed longer fatigue lifetimes at comparable values of maximum applied stress than the '850/250' heat treatment. Finally, the '950/250' and '900/390' showed comparable lifetimes at given values of maximum applied stress. The current batch of ADI heat treatments perhaps should not be directly compared in this fashion to those previously tested, due to the differing compositions of the respective as-cast material and varying austenitisation times. More suitable comparison can be made using relative predicted amounts of microstructure constituents, particularly retained austenite and bainite. However, as with the hardness tests the presence of eutectic carbides in the '800/260' and '800/390'

heat treatments must be considered. Figure 8.2 compares the number of fatigue cycles to failure with predicted retained austenite volume fraction for short fatigue crack tests performed with a maximum applied stress between 800 MPa and 1000 MPa. Despite the obvious limited data, there appears as a first approximation, to be a relationship between predicted retained austenite volume fraction and short fatigue crack lifetime. For these tests, an increased retained austenite volume fraction leads to increased fatigue resistance. The '800/260' heat treatment shows relatively poor performance for the predicted retained austenite volume fraction. This is possibly due to the presence of brittle eutectic carbides. The unconventional ADI microstructure (presence of large numbers of eutectic carbides) of the current alloy heat treatments prevents comparisons based purely on predicted retained austenite and bainite volume fractions. In general, the short fatigue crack performance of the alloy conditions subject to the current studies appears directly related to the mechanism of failure both in terms of crack initiation and subsequent growth of short fatigue cracks. This in turn would seem dependent on microstructure and applied stress levels. Furthermore, this appears to be applicable not just to the differing performance between alloy conditions, but also to the variability within a particular heat treatment. This is discussed further throughout this chapter.

Figure 8.13 compares fatigue crack propagation data generated by long fatigue crack testing. The '900/390' heat treatment showed an improvement in performance over the as-cast ductile iron in terms of ΔK_{th}, K_Q, and slower crack growth rates at comparable values of ΔK. The '800/260' heat treatment showed no real increase in performance over the as-cast ductile iron. Values of ΔK_{th} were comparable, as were crack growth rates at a given value of ΔK.

8.4 Initial Assessment of Short Fatigue Crack Failure Mechanisms

Analysis of short crack fatigue interval test replica records revealed that at either end of the performance scale we are observing one of two extremes of fatigue failure; coalescence or propagation dominated failure. The majority of failures occur somewhere between these two extremes, with both regimes coexisting. The mechanism of failure for an individual specimen appears dependent on the number of primary, and to a lesser extent secondary, initiation sites.

8.4.1 Primary Initiation of Short Fatigue Cracks

The number of primary initiation sites has a profound impact on the mechanism of failure and ultimately the lifetime of the specimen as discussed in the following sections of this chapter.

For many of the interval tests performed at an R-ratio of 0.1 on '900/390', '800/390' and '800/260' heat treatments, cracks were observed on the first interval acetate replica. Indeed, replicas taken on application of mean load greater than 275 MPa before fatigue cycling for '800/260' tests also revealed the presence of crack initiation sites. This would indicate a rather easy initiation stage for all microstructures. The location of the fracture surface profiles of all short fatigue crack specimens (see Figure 7.64 to Figure 7.69) suggests primary initiation is dependent on local microstructure rather than the maximum applied stresses. Additionally, micro-crack initiation events were observed throughout the lifetime and appeared dependent on one or more of the following: microstructure, load ratio and stress range.

Primary crack initiation in the '900/390' microstructure occurred exclusively at pores, either surface or sub-surface. The angular nature of the crack initiating pores clearly acts as points of stress concentration. Other authors [59,67,72] have observed initiation of this type. It is suggested that in the absence of pores and other such defects, primary initiation occurs at graphite nodules (as seen in previous work by this university [2,3,4]). With the exception of specimen '900/390:09' which suffered extensive surface porosity and consequentially crack initiation the number of crack initiating pores in the '900/390' heat treatment was low. Whilst porosity existed in the as-cast DI, '800/260' and '800/390' microstructures, the primary crack initiators were eutectic carbides in these microstructures. For the case of the ADI variants these carbides remain from the as-cast material after insufficient austenitisation. These carbides are very hard (in excess of 750 Hv) and brittle. Indeed, the micro hardness indenter fractured a number of carbides during testing.

A large variability in the number of carbides cracking on initial loading to a mean stress of 385 MPa and 330 MPa (σ_{max} = 700 MPa and 600 MPa respectively) was

observed for '800/260' specimens. For the most damaged specimen ('800/260:02' – σ_{max} = 700 MPa, σ_{mean} = 385 MPa) over 400 eutectic carbides cracked on initial loading to mean stress. This is compared to figures of less than ten for the least damaged specimens. No cracked carbides were observed on loading to a mean stress of less than or equal to 275 MPa. It is therefore reasonable to assume an applied stress between 275 MPa and 330 MPa is required to cause eutectic carbide fracture in this microstructure. Indeed, the presence of cracked carbides on replicas taken at the first interval for all tests with a mean stress of 275 MPa or less indicate the increase to maximum stress during first fatigue cycle is sufficient to cause carbide fracture. The variability on crack initiation due to carbide fracture has been investigated quantitatively and is discussed in section 8.4.3.

8.4.2 The Principle of Load Transfer

The system of brittle carbides in a relatively ductile matrix found in the as-cast DI, '800/260' and '800/390' heat treatments can be compared to that of typical discontinuously reinforced Metal Matrix Composite (MMC). Common discontinuous MMCs are Al based alloys reinforced with SiC or Al_2O_3 particles. A great deal of research has been undertaken on these alloys and is cited for comparison for the analysis of crack initiating carbides. The objectives of any composite material are to combine the qualities of the distinct materials without seriously accentuating their shortcomings. The size of the particles (1-100 μm^2) and the volume fraction (5-40%) in discontinuous MMCs create a situation where there is a significant amount of load transfer to the reinforcement from the matrix [92]. The principle of load transfer is fundamental to the understanding of the mechanical properties of MMCs. As the specimen is subjected to applied stress the load is shared by the matrix and the carbides. The proportion of the external load borne by each of these phases can be gauged by volume averaging the load within them such that at equilibrium:

$$\sigma_A = (1-f)\overline{\sigma}_m + f\overline{\sigma}_i \qquad \textit{Equation 8.4}$$

Where σ_A , represents the external stress, while $\overline{\sigma}_m$ and $\overline{\sigma}_i$ are the volume averaged stress of the matrix and inclusion respectively. The inclusion volume fraction is represented by f.

Therefore a certain proportion of the load is carried by the inclusion (carbides) and the remainder by the matrix. Under elastic conditions this proportion will be independent of applied load and represent an important characteristic of the material.

8.4.2.1 Eshelby Calculation of Internal Stresses in Loaded Composites

Methods based on the work of Eshelby, examine the partitioning of stress between the constituents of composites subjected to external loads by considering the *misfit* between the shapes of constituents in mechanically inhomogeneous materials. For example a relatively stiff inclusion tends to deform less than the surrounding matrix under mechanical loading. This is particularly pertinent to the elastic mismatch between reinforcement and matrix material in discontinuous MMCs. Only the basics of the Eshelby theory are described in this section since more detailed descriptions are readily available in literature [92,93].

Eshelby evaluated the stress and strain field in a homogeneous material in which a sub-region is cut from the matrix and subjected to a 'stress free' shape change such that it no longer fits into its previous space in the parent material. This shape change creates a transformation strain ϵ^T. The region is then placed back into the matrix. However, in order for it to fit into the hole from which it was cut surface tractions need to be applied. On removal of the surface tractions equilibrium is reached between the matrix and the inclusion at a constrained strain ϵ^C of the inclusion relative to its initial shape before removal. By considering Hooke's law, the stress in the inclusion can be expressed in terms of the elastic strain.

$$\sigma_I = C_M\left(\varepsilon^C - \varepsilon^T\right) \qquad \textit{Equation 8.5}$$

If the inclusion is ellipsoidal the stress within it is uniform and the calculation of the elastic strain becomes analytically tractable. Therefore, the relation between constrained and transformation strains is given by the following equation.

$$\varepsilon^C = S\varepsilon^T \qquad \textit{Equation 8.6}$$

where S is the Eshelby tensor. The Eshelby tensor therefore relates the final constrained inclusion shape to the original shape mismatch between the matrix and inclusion. Combining Equation 8.5 and Equation 8.6:

$$\sigma_I = C_M(S - I)\varepsilon^T \qquad \textit{Equation 8.7}$$

where I is the identity matrix.

It is possible to expand this theory to typical MMCs where the matrix and inclusion have differing elastic constants (C_M and C_I represent the elastic constants of the matrix and inclusion respectively). Consider the cut and weld approach detailed above. An inclusion stiffer than the matrix would resist being forced back to the natural shape of the hole more strongly than an inclusion that is elastically equivalent to the matrix. However, with ellipsoidal inclusions it is possible to represent the real inclusion with a region of matrix material – a *ghost inclusion*. It is required that the *ghost inclusion* has undergone a stress-free transformation giving it an identical shape to the real inclusion at an equivalent constrained stress. Using this approach it can be shown that the transformation strain of a real inclusion in a loaded composite is given by:

$$\varepsilon^T = -\{(C_M - C_I)[S - f(S - I)] - C_M\}^{-1}(C_M - C_I)\varepsilon^A \qquad \textit{Equation 8.8}$$

Where the applied strain is:

$$\varepsilon^A = C_M{}^{-1}\sigma^A \qquad \textit{Equation 8.9}$$

With the transformation strain established the mean inclusion (particle) and matrix stresses may be calculated:

$$\langle\sigma\rangle_I = (1 - f)C_M(S - I)\varepsilon_T \qquad \textit{Equation 8.10}$$

$$\langle\sigma\rangle_M = -fC_M(S - I)\varepsilon_T \qquad \textit{Equation 8.11}$$

The mean internal stresses are defined as the difference between the average constituent stresses and the applied external stress such that:

$$\overline{\sigma}_I = \langle \sigma \rangle_I + \sigma^A \qquad \textit{Equation 8.12}$$

$$\overline{\sigma}_m = \langle \sigma \rangle_M + \sigma^A \qquad \textit{Equation 8.13}$$

Hence, the proportion of the external load borne by each of the phases determined by Equation 8.4 can now be solved. A large negative mean matrix stress is desirable and indicates that the load has been transferred elastically from the matrix to the reinforcement. The limitation of the Eshelby method is that it is only realistically applicable to spheroid and ellipsoidal inclusions that are either parallel (prolate) or perpendicular (oblate) to the tensile axis. Evaluating the effect of particle orientation is extremely complex.

The Effect of Particle Volume Fraction

As the volume fraction of composites increases, the greater proportion of the applied load is experienced by the reinforcement. However, the volume averaged stress within individual reinforcement particles decreases (see Figure 8.3).

The Effect of Particle Aspect Ratio

Using the Eshelby technique it is possible to evaluate the effect of increasing particle aspect ratio on inclusion stress. In Figure 8.4 an increase in aspect ratio for prolate particles generates an increase in inclusion stress. Initially an increase in oblate particle aspect ratio gives rise to a decrease in inclusion stress. The stress in an oblate inclusion reaches a minimum value at an aspect ratio of approximately 2, after which an increase in aspect ratio brings about an increase in inclusion stress.

8.4.2.2 Estimation of Carbide Fracture Stress

The identification of a threshold value of stress, above which carbide cracking is seen to occur, allows the estimation of a minimum carbide fracture stress. Since inclusion stress is approximately independent of size [92], fracture stresses have been evaluated for cracked carbides of various aspect ratio and alignment. Finite Body Tessellation (FBT) data from the specimen containing the largest number of

cracked carbides was used for this analysis. Fracture stresses for cracked carbides with the highest and lowest aspect ratios are evaluated using the Eshelby approach. Additionally, carbides with the highest aspect ratio perpendicular (oblate) and parallel (prolate) to the tensile axis are considered. Carbides of low, mid and high values of aspect ratio were selected that deviated from the prolate and oblate orientations as little as possible. Values of 190 GPa and 160 GPa were taken from literature [80,94,95] for the Young's modulus of the eutectic carbides (Fe_3C) and bulk ADI respectively. Additionally, Poisson's ratios of 0.27 and 0.3 were taken from literature [80,94] for Fe_3C and ADI respectively. Inclusion stresses were calculated for the upper and lower estimations of applied stress required for carbide fracture (330 MPa and 275 MPa) and are summarised in Table 8.2.

The lowest inclusion stresses (~302 MPa) are shown by oblate particles with aspect ratios 1.73 to 2.37. The highest inclusions stresses are shown by prolate particles with stress increasing with aspect ratio. However, it should be remembered that the orientations of the eutectic carbides are not exactly prolate or oblate. Additionally, since the average carbide geometry is far from ellipsoidal these figures can only be regarded as first approximations of carbide fracture stress.

Despite the fact that inclusion stress is approximately independent of size, it is widely accepted that fracture at a given stress level occurs only when the particle contains a critical flaw, which is more likely for large particles [92]. The probability of a given flaw distribution containing this critical flaw increases with inclusion stress (as the critical flaw size will decrease). It is reasonable to propose that the probability of carbides containing a critical flaw is increased for large carbides and carbides with geometry and orientation that induces higher inclusion stresses by more efficient load transfer.

8.4.3 Interpretation of '800/260' Crack Initiating Carbide Classification

These relationships predicted by the classifier were interpreted with caution, with particular attention being paid to the data spread and effective weighting. The effective weighting represents the highest or lowest value of the probability axis ('y-axis' for univariates and 'z-axis' for bivariates) where there is a reasonable

spread of data. This provides an indication of the relative importance of the relationships. A schematic of the terms selected by each of the data set runs can be seen in Appendix 11.3.

When looking for significant differences in data distribution it is important to assess data correlation and input space distribution. One method to achieve this is to look at pair-wise scatter plots. These are presented for all the FBT parameters in Appendix 11.5 and Appendix 11.6. Correlation between inputs can prove troublesome for determining classification functions and should be considered when interpreting the relationships generated by the SUPANOVA model. There is observable correlation between a number of the terms in Appendix 11.5 and Appendix 11.6 (e.g. D_{min} vs. O_a and D_{mean} vs. C_a). It can also be seen that there is clustering of data in some of the pair-wise plots (e.g. O_{ar} vs. O_a). It should be noted that the plots which feature number of nearest neighbours reflect the fact the term is an integer before normalising, giving bands of data.

8.4.3.1 Univariate Relationships

Simple comparison of mean values between crack initiating carbides and the background population (Table 7.4) suggest that the propensity of individual carbides to fracture is promoted by the following features:

- Large carbide area
- Large cell area
- Large local area fraction (LAF)
- Small mean near neighbour distance

The application of the SUPANOVA model also identified cell area and LAF as significant factors governing fatigue crack initiation. Both terms were selected by all of the data set runs. The good spread of data for these two terms supports the suggested relationships; there are visibly more cracked carbides with higher cell areas and local area fractions than the background population. Whilst the data is relatively sparse for highest and lowest values of cell area and LAF, there appears to adequate data to allow for confidence in the model prediction for the rest of the data range. The effective weightings for cell area and LAF were -5.0 and -2.8

respectively. This suggests cell area is the dominant feature in carbide fracture. Carbide area and mean near neighbour distance were not identified by the model. The fact that increasing cell area and increasing LAF (which also implies increasing carbide area since LAF = carbide area / cell area) is selected by the classifier and not carbide area is unexpected. Carbide area has been plotted as a function of both cell area and LAF in Figure 8.5 and Figure 8.6 respectively. It is noticeable that in general cracked carbides with a large cell area or LAF tend themselves to also be large. A large cell area or LAF in the background carbide population however, does not have such a strong correlation with a large carbide area. Interestingly Figure 8.7 shows that there is no appreciable correlation between cell area and LAF. This would suggest the univariates selected by the SUPANOVA model are independently significant for the process of carbide fracture. Appendix 11.5:

The SUPANOVA model identifies the decrease in the likelihood of crack initiation with increasing nearest neighbour distance. This perhaps suggests the location of the nearest carbide is influential in determining the susceptibility of individual carbides to cracking and acting as fatigue initiation sites. The data spread for this term is weighted to relatively low values of nearest neighbour distance and with an effective weighting of 1.5 is perhaps the least influential of the univariate relationships. However, the suggested relationship appears to a reasonable one within the range where there is a significant amount of data.

8.4.3.2 Bivariates Relationships

With SUPANOVA we are also able to identify higher order interactions that are not easily identified by simple comparison of mean values.

Carbide Angle vs. Local Area Fraction

The first bivariate (see Figure 7.23:A) suggests the likelihood of fracture is increased with increasingly locally clustered particles orientated at a high angle to the tensile axis. It is significant that this relationship was selected by all of the data set runs and had the strongest effective weighting at -1.7 suggesting it is a significant factor in determining the likelihood of carbide fracture.

Carbide Angle vs. Nearest Neighbour Angle

The other bivariate suggests that the likelihood of crack initiation is decreased if the nearest neighbour of oblate carbides is situated perpendicularly to the carbide with respect to the tensile axis (see Figure 7.23:B). This was selected by 60% of the data set runs and with an effective weighting of 1.12 appeared to have a lesser influence.

8.4.3.3 Summary

Therefore to summarise, large or long and thin carbides on the whole appear to be susceptible to fracture. Carbides that are locally clustered and aligned at a high angle to the tensile axis are particularly susceptible to fracture except when the nearest neighbour is situated perpendicularly to that carbide with respect to the tensile axis. This perhaps suggests the presence of possible stress shielding effects in local populations showing a high degree of alignment. The comments made in section 6.2.3 regarding the application of FBT to complex carbide geometries and the significance of the parameters generated should be considered when interpreting the FBT data. The same caveat is applicable to the relationships generated by the SUPANOVA model. Modelling of actual carbide geometry would require extremely complex finite element analysis which is beyond the scope of this study. Nonetheless, the FBT approach provides a reasonable first approximation of the influence of carbide geometry and distribution.

As discussed earlier it is possible to relate this system of brittle carbides in a relatively ductile matrix to a MMC where reinforcement particle cracking has been identified as the main damage mechanism [96,97,98,99,100,101]. Additionally, it is reported in the literature that incidence of particle cracking in a range of MMCs is related to aspect ratio and size of the ceramic reinforcement such that particles with high aspect ratio or volume are more easily fractured [102,103]. These effects have been explained using Weibull statistical distribution for the strength of reinforcement particles [97,99,102,104], the Griffith criterion for particle fracture stress [105], and the load transferring mechanism between particle and matrix. Additionally, clustering of particles has been observed to promote cracking [103,98,106,107,108,109]. Reasons for this phenomenon include increased local or tri-

axial stress levels with clusters owing to the constraint of matrix material between closely spaced particles [110,111].

Summarising, fracture occurs when the carbide contains a sufficiently large flaw, which is more likely for large particles. Furthermore, the probability of any flaw being critical is likely to be dependent on the magnitude of internal stress experienced by that carbide, which following load transfer arguments is related, amongst other parameters to aspect ratio, orientation and local clustering of carbides.

8.4.4 Secondary Initiation of Short Fatigue Cracks

As described in section 8.4.6 further crack initiation was observed for both the '900/390' and the '800/260' heat treatments throughout the specimens' lifetime. Initiation events occurred ahead of advancing crack tips. For the '900/390' specimens secondary crack initiators were graphite nodules. Decohesion of the interface between the graphite nodules and matrix is likely to be caused by mechanical property mismatch occurring in the stress field ahead of the advancing crack leads to the subsequent initiation of micro-cracks. Greno et al. [72] identified the irregular surface of the graphite-matrix interfaces (sharp micro-notches) as high stress concentrators. These act as preferential initiation sites in the increased ΔK region in the vicinity of the advancing crack tip. Further tests at progressively lower maximum stresses showed fewer crack initiation events ahead of the crack tip. As a direct result there were fewer coalescence events visible for these specimens until the failure mechanism was almost exclusively propagation controlled. It is reasonable therefore to suggest that decohesion and subsequent crack initiation is in fact sensitive to the crack tip stress intensity factor and hence the locally raised stress field experienced by the graphite nodules, fitting in with the observations of Greno et al. [72] outlined above. The plastic zone ahead of the advancing crack increases with increasing stress intensity factor. The larger the plastic zone ahead of the crack tip, the greater number of graphite nodule interfaces will be subjected to the increased stress and strain values associated with this region. It has been identified that initiation ahead of the crack tip almost exclusively occurs within the monotonic crack-tip plastic zone (as seen in Figure 7.61). This indicates that graphite nodule decohesion does not require globally reversed plasticity to occur, although the local stress state around the

nodules is likely to be complex. Not every nodule that is encompassed by the monotonic crack-tip plastic suffers decohesion and micro-crack initiation. What causes one graphite nodule to decohere and lead to the subsequent initiation of micro-cracks whilst others remain mechanically unaffected is undetermined. Possible significant factors such as nodule size, magnitude of nodule clustering, and nodule distribution can be assessed using finite body tessellation techniques (the nature of the individual nodule interface is also thought to be important). This is beyond the scope of the current work but is a topic for suggested further work.

Micro-crack initiation ahead of the crack-tip was identifiable on the replica records of '800-260' interval tests showing propagation dominated failure. Crack initiation on specimens exhibiting coalescence dominated failure was so widespread it was not possible to identify secondary initiation sites as being caused exclusively by the proximity of a dominant crack. Initiation from graphite nodules was rare and the more common sites for secondary initiation were eutectic carbides. It is thought that this is a reflection of the brittle nature of the eutectic carbides which appear to provide the 'weakest link'.

8.4.5 Coalescence Dominated Short Fatigue Crack Failure (CDF)

This mechanism of failure is principally crack growth from linking through coalescence events, where large numbers of micro-cracks initiate on or shortly after initial loading. This condition is related to shorter fatigue lifetimes and is associated with the '800/390' heat treatment and a number of as-cast and '800/260' specimens. The consequence of the significantly higher volume fraction of eutectic carbide in the '800/390' microstructure when compared to the as-cast ductile iron and the '800/260' condition is an increase in the extent of fatigue crack initiation and subsequent coalescence events. This goes some way to explain the relatively short fatigue lifetimes of this particular ADI composition and heat treatment.

The large number and close proximity of cracks (initiating from the primary eutectic carbides) prevents significant propagation relative to the initial length of the crack before coalescence. Therefore, the linking of numerous micro-cracks governs the growth of a dominant crack and gives rise to fast and generally erratic crack propagation rates. Analysis of interval test replica records suggests

segregated regions rich in retained austenite remote from graphite nodules within the microstructure provide the preferential crack path between fractured eutectic carbides. The presence of bainite in these segregated regions tends to be relatively sparse, resulting in a generally ductile austenitic local microstructure. Observations of '800/260' fracture surfaces generated by coalescence dominated failure (Figure 7.73 to Figure 7.76) identified regions of micro-void coalescence between the brittle facets of fractured carbides and perhaps represent an increase in static failure modes as the specimen approaches fracture. Furthermore, the close proximity and the large number of micro-cracks suggest that crack shielding effects play an important role in the failure mechanism. It is reasonable to assume that the stress experienced by individual micro-cracks is quite different to global applied stress.

The fracture surface of specimen '800/260:02' (Figure 7.73) is relatively devoid of graphite nodules. This is not completely unexpected due to the mechanism of failure. The number and density of cracked carbides was so large that limited propagation was required for crack coalescence. The position of the eutectic carbides in the microstructure is such that they are remote from graphite nodules. Additionally, crack growth between carbides has been observed to occur in the segregated regions of the microstructure which again are inherently remote from graphite nodules. Therefore, the location of the crack initiation events and the limited propagation needed for crack coalescence significantly reduces the probability of a micro-crack being proximate to a graphite nodule. It can therefore be suggested that a feature of coalescence dominated failure is the minimal influence of graphite nodules on crack growth. This is markedly different from 'conventional' ADI fatigue crack growth.

The mechanism of crack linking via coalescence has, on a number of occasions promoted a coarse fracture profile. This is clearly illustrated with specimens '800/260:02' and '800/260:09' (Figure 7.66). These two specimens exhibited the highest magnitude of coalescence dominated failure and greatest deflection on the fracture profile. It should be noted that large sheared ligaments are not necessarily representative of coalescence dominated failure. Conversely the behaviour often associated with large sheared ligaments is the coalescence on

final failure of two or more large dominant cracks. It is possible that these cracks may have experienced significant propagation prior to the failure of the specimen.

8.4.6 Propagation Dominated Short Fatigue Crack Failure (PDF)

Propagation dominated failure exhibits behaviour more akin to classic short fatigue crack growth. Coalescence events are small in number or, on some occasions non-existent. For an ADI alloy to suffer this failure mechanism the number of primary initiation events must be limited and well dispersed. Certain as-cast ductile iron, '800/260' and most '900/390' specimens demonstrate this fatigue behaviour. Once initiated, crack advance commonly involves propagation through the matrix microstructure with little influence from neighbouring micro-cracks. The propagation of an individual micro-crack is large when compared to its initial length. Coalescence with other relatively large micro-cracks may occur, though often not until final failure. If certain conditions are fulfilled (see section 8.4.4), crack initiation may occur ahead of an advancing dominant crack tip. In the case of the '900/390' heat treatment, fatigue crack initiation may occur at the interface of decohered graphite nodules within the near tip monotonic plastic zone. The cracking of eutectic carbides provides crack initiation sites ahead of the crack tip in the as-cast and '800/260' microstructures. The coalescence of selected micro-cracks with the dominant crack may occur and result in observable crack deflection. In the case of the '900/390' heat treatment, crack growth appears to occur by the connection of graphite nodules. This is the more commonly observed fatigue failure mechanism for ADI alloys as seen in literature [59,66,67,72].

As identified in Figure 7.54 the number of graphite nodules on the dominant crack with a '900/390' microstructure appears to decrease with a corresponding decrease in the applied stress level. When compared to the 'simulated non-deflected cracks' it is clear that the dominant crack for tests at 800 MPa and 700 MPa intersected a greater number of graphite nodules. This suggests that at these stress levels, the dominant crack was 'seeking' out graphite nodules. Identification of whether all these graphite nodules decohered ahead of the crack-tip before intersection was prevented by the frequency of the replica records for these tests. The data summarised in Table 7.8 shows that for the test performed at 800 MPa, only 47% of the graphite nodules on the crack profile were seen to decohere ahead of the crack-tip. This falls to 25% for the test performed at 700

MPa. It is expected however, that these figures are an underestimation, with the decohesion of graphite nodules, micro-crack initiation and subsequent coalescence occurring in the period between replicas. The test performed at 600 MPa showed no increase in the number of graphite nodule intersected by the dominant crack over the 'simulated non-deflected crack'. This would suggest that the path of the dominant crack was not influenced by graphite nodules at this lower stress level. The lower number of coalescence events before fracture for the 600 MPa maximum stress test may be the reason for the relatively stable crack growth rates shown for this specimen in Figure 7.50 to Figure 7.53. It is also reasonable to suggest that the fewer number of initiation events and subsequent crack coalescence is responsible for the less deflected dominant crack path shown in Figure 7.58. The crack growth data for the 800 MPa short-crack test shows considerably more scatter than the tests at lower stress levels, and this may be directly attributable to the numerous coalescence events experienced by this specimen. Determination of the stress intensity factor for each of these micro-cracks and for the dominant crack as a whole is rather ambiguous due to the very complex overlapping stresses experienced. This possibly indicates that ΔK may not adequately describe crack tip driving force for this specimen. However, for general comparisons the use of a nominal ΔK to describe crack growth behaviour is justified. The tests at lower stress levels produced fewer numbers of cracks, and hence less complex overlapping stress states were likely to be generated. In these instances the use of ΔK allows a more unambiguous determination of short fatigue crack growth.

Figure 7.55 suggests the number of graphite nodules intercepted by a dominant crack is a factor of ΔK. At values of ΔK above 18-20 MPa$\sqrt{m}$ the dominant crack intercepts a greater number of graphite nodules than the corresponding 'simulated non-deflected cracks'. Furthermore, observation of long and short fatigue crack fracture surfaces shows increased numbers of graphite nodules and surface roughness with increasing values of ΔK. It is reasonable to suggest this reflects the increase in size of monotonic crack tip plastic zone associated with increasing ΔK. More graphite nodules will be encompassed by the plastic zone effectively giving the crack tip a greater 'sampling area'. The greater extent of the near tip plastic zone is likely to increase the probability of graphite nodule decohesion and

micro-crack initiation ahead of the crack-tip and in turn, subsequent deflection of the dominant crack by coalescence events. Therefore, it is reasonable to propose higher stress intensity factors cause the advancing dominant crack to 'seek out' graphite nodules. This may cause increased crack deflection and fracture surface roughness and consequently may decrease global crack growth rates by roughness induced closure mechanisms and shielding effects. At lower values of ΔK fewer initiation events are observed ahead of the crack tip.

Greno et al. [72] investigated the mechanism of micro-crack initiation ahead of the advancing crack tip by means of a 2D elastic computational model developed using the Boundary Element Method. A graphite nodule was modelled as having nucleated micro-cracks fore and aft with respect to the dominant crack at varying positions along the nodule perimeter. Additionally, the graphite nodule was considered at three positions and distances from the dominant crack. Stress intensity factors were calculated for the dominant crack and the micro-cracks nucleated from the graphite nodule. The effect of interaction between crack and nodule is more marked for the micro-cracks emanating from graphite nodules than for the dominant crack with the greatest increase observed for the micro-crack facing the dominant crack. The value of stress intensity factor for this crack increases ten-fold and approaches that of the dominant crack. The crack facing away from the dominant crack showed an increase in stress intensity factor, although to a lesser extent. Predictably, the nearer the nodule to the dominant crack tip, the greater the increase in stress intensity factor. It was also shown that the angular position of the graphite nodule with respect to the dominant crack-tip has only a minor influence on any increase in stress intensity factor.

Additionally Greno et al. investigated the effect of crack initiation from various orientations around the graphite nodule (θ). The greatest increase in stress intensity factor for micro-cracks initiating and propagating towards the dominant crack occurred when θ is between 15 and 30 degrees. The increase in stress intensity factor for micro-cracks initiating and propagating in the same direction as the dominant crack was less pronounced and varied less with θ. It was noticed in this study that crack initiation from the interface between graphite nodules and matrix did in fact occur at various orientations around the graphite nodule. The

orientation of crack initiation from graphite nodules with respect to the nodule is summarised in Figure 8.8. It is reasonable to suggest that the majority of crack initiation events facing the advancing dominant crack tip occur at an orientation of 15 to 30 degrees from the tensile axis. This agrees with the work of Greno et al. There is a greater variability in orientation for micro-cracks that initiated and propagated in the same direction to the dominant crack which is suggested by Greno et al.. Not all micro-cracks initiating from decohered nodules coalesce with the advancing dominant macro-crack. It is not clear at the present time why one crack should coalesce with the dominant crack whilst another does not. It is believed that the matrix microstructure between two cracks and the crack spacing are significant factors in selecting coalescence events. This is a suggested subject for further work.

If the numbers of crack initiating carbides are low and the distribution of micro-cracks is large the as-cast ductile iron and '800/260' specimens are likely to show a certain degree of propagation dominated behaviour. This is due to increased propagation through the microstructure being required for an individual micro-crack to interact with other cracks. Associated with the presence of propagation dominated behaviour is an increase in fatigue lifetime over coalescence dominated failure at comparable stress levels. However, even when there is a significant amount of propagation, comparison of Figure 7.35 and Figure 7.53 shows that the as-cast ductile iron and '800/260' data exhibit faster crack growth rates at comparable values of ΔK to the '900/390' specimens. The fluctuations in the crack growth seen in Figure 7.32 to Figure 7.34 are attributable to coalescence events in a similar manner to the '900/390' test at 800 MPa. The comments regarding the validity of ΔK that were raised for the '900/390' 800 MPa test are equally applicable for these tests. When considering fracture surfaces of '800/260' specimens showing a greater degree of crack propagation (see Figure 7.77 to Figure 7.80) fewer numbers of brittle facets are observed. This is likely to be symptomatic, in part due to the lower carbide area fractions shown by these specimens, and to the fewer number of initiation events. It is clear however, that these two factors are related. In some occasions as shown in Figure 7.80, regions of the microstructure with few brittle facets show a lath-like relief similar in nature to the structure of bainite.

8.4.7 Coalescence vs. Propagation Dominated Failure

Observation of the short-crack replica tests for both the '800/260' and the '900/390' specimens reveals that the two mechanisms of failure described above are not mutually exclusive. The extent of either regime is dependent upon the number of initiation sites, both on initial loading and during subsequent crack propagation. These two regimes can be visualised as extreme ends of a scale. When the number density of initiation events is low (~10^1 per specimen) crack propagation is the principal cause of failure. With a large number of initiation events (~10^3) crack growth by coalescence occurs. Under the right conditions a specimen may, to some extent show both failure mechanisms. For example not all of the '800/260' specimens suffered widespread crack initiation as described in the coalescence dominated failure mechanism. Indeed a number of the '800/260' specimens suffered relatively low numbers of primary initiation events and hence exhibited significant amounts of propagation, although none quite approaching that observed with the '900/390' heat treatment. The mechanism of failure has a distinct effect upon the specimen lifetime. On a large scale, the greater the extent of crack propagation, the longer the lifetime of the specimen. However, a limited number of coalescence events directly attributable to initiation ahead of the crack tip may lead to extended fatigue life by creating a more tortuous crack path. Mechanisms such as roughness induced crack closure may occur as a result of this. At the other end of the scale, an extensive number of coalescence events lead to rapid failure. Therefore, the fatigue life of a specimen is dependent on the failure mechanism, which in turn is dependent on the number of initiation events. For '900/390' specimens this is ultimately dependent on the applied stress and the amount of surface porosity, whilst the exact relationship for the '800/260' is rather less defined. When tested at 600 MPa a number of '800/260' specimens exhibited lifetimes comparable to the '900/390' heat treatment. When showing comparable fatigue performance to the '900/390' specimens, the higher hardness of the '800/260' condition makes this heat treatment a more likely candidate for camshaft applications.

8.4.8 '800/260' Carbide Population Comparison

A schematic of the terms selected by each of the data set runs can be seen in Appendix 11.4. Additionally, pair-wise scatter plots for all the FBT parameters can

be seen in Appendix 11.7 and Appendix 11.8. These were checked for correlations between individual FBT parameters as discussed in section 8.4.3. It should be remembered this comparison which was based purely on any dissimilarities between carbide populations showing PDF and CDF. No distinction was made between cracked and un-cracked carbides.

8.4.8.1 Univariate Relationships

The effect of carbide population on determining the mechanism of failure was investigated for the '800/260' heat treatment. The simple comparison of carbide population histograms (Figure 7.40) suggested coalescence dominated failure (CDF) was promoted by the following features:

- Large carbides
- Long and thin (large aspect ratio) carbides
- Small cell area
- Small mean near neighbour distance

The univariates generated by the SUPANOVA classification of carbide populations also identify the importance of carbide geometry in determining the fatigue failure mechanism. CDF appears to be promoted by carbide populations with higher proportions of carbides with large carbide aspect ratios (Figure 7.47:A) or carbides orientated at a low angle to the tensile axis (Figure 7.47:B). Carbide aspect ratio was selected by all the data set runs and showed the highest effective weighting (-4.2). This suggests carbide aspect ratio is particularly influential in determining the failure mechanism. Since there is little data for carbides that have relatively low or high aspect ratios the relationship predicted by the SUPANOVA model should be regarded as interpolation within these regions. The selection of carbide angle and the implied effect on crack initiation is interesting since the classification of individual crack initiating carbides suggests carbides aligned perpendicularly to the tensile axis have a greater propensity to initiate fatigue. There is a good data spread for this term which appears to support the relationship proposed by the SUPANOVA model. This feature was however, only selected on seven out of the ten data set runs and showed the lowest effective weighting (~1.1). it is interesting to note that when the data set run did

not select carbide angle was not as a univariate it appeared in a bivariate relationship (Appendix 11.4).

Decreasing cell area (Figure 7.47:C) and mean near neighbour distance (Figure 7.48:B) were selected by the SUPANOVA model as likely to increase the probability of multiple crack initiation and crack growth by coalescence. It is not surprising that both these FBT terms were selected by the classifier since mean near neighbour distance is distinctly related to cell area. An increased mean near neighbour distance is generally expected with an increase in cell area since mean near neighbour distance is a measure of the intercellular region between carbides (although local area fraction has an obvious effect). This phenomenon can be seen for these carbide populations in Appendix 11.7. When considering the influence of large carbides identified by the simple comparison of specimen populations it seems reasonable to suggest that the selection of cell area, local area fraction and mean near neighbour implies local clustering of carbides promotes CDF. The relationship described in Figure 7.47:A would appear to suggest that carbide populations with generally low local area fractions (sparsely distributed) have a greater propensity to suffer PDF. CDF then appears to be promoted by a locally clustered population (increasing local area fraction). After a threshold value a further increase in local area fraction actually decreases the propensity for CDF. The data spread however, in this region is relatively low.

8.4.8.2 Bivariate Relationships

Carbide Angle vs. Nearest Neighbour Angle

The most commonly occurring bivariate describes the relationship between carbide angle, nearest neighbour angle and failure mechanism. Figure 7.49:B suggests oblate carbides increase the likelihood of PDF when the nearest neighbour is situated perpendicularly to the carbide with respect to the tensile axis. The mechanism of failure becomes increasingly coalescence dominated with a decrease in either carbide angle or nearest neighbour angle. Indeed prolate carbides appears to promote CDF irrespective of the position of the nearest neighbouring particle. Similarly, when the nearest neighbour is aligned parallel the carbide with respect to the tensile axis promote CDF whatever the carbide orientation. This perhaps suggests the presence of possible stress shielding

effects in local populations showing a high degree of carbide alignment and was a feature selected in the classification of individual crack initiating carbides.

Carbide Angle vs. Local Area Fraction

The other bivariate identifies the significance of carbide alignment in determining the failure mechanism. A carbide population that has a large number of oblate carbides with high local area fractions (Figure 7.49:A) promotes PDF. A decrease in carbide angle or local area fraction promotes CDF. A large number of prolate carbides promote CDF regardless of the local area fraction. This may explain the univariate function described in section 8.4.8.1 where only the highest values of local area fraction encourage PDF which is otherwise promoted by low values of local area fraction (see Figure 7.47:A).

8.4.8.3 Summary

CDF appears to be promoted by a large number of prolate carbides irrespective of the orientation of the nearest neighbour, or degree of local clustering. Additionally, a high aspect ratio or a large mean carbide area appears to increase the propensity of CDF. As discussed in section 8.4.3.3 the susceptibility of a particle to fracture is increased at high aspect ratios and large volumes. Furthermore, load transfer is more efficient to carbides that have high aspect ratios or prolate orientations. These factors are likely to increase the extent of carbide cracking and hence encourage CDF.

Carbides orientated at a high angle to the tensile axis promote PDF. As carbide orientation become increasingly oblate PDF is further promoted with a simultaneous increase in nearest neighbour angle or local area fraction. PDF may be promoted when oblate carbides show a high level of clustering, or aligned perpendicularly to the tensile axis. The requirements for PDF appear more stringent than CDF. PDF is only promoted by carbides that show a large degree of alignment, both individually and as a population, in a direction perpendicular to the tensile axis.

8.4.9 Porosity Effects on Short Fatigue Crack Behaviour

A feature of many of the short fatigue crack specimens is the presence of porosity. As previously discussed, crack initiation in the '900/390' heat treatment

occurs exclusively at pores. It is expected in the absence of porosity, graphite nodules would act as crack initiators. What effect this would have on the fatigue lifetime of these specimens is uncertain, although previous work suggests the number of fatigue cycles before the first initiation event would increase.

Porosity can be seen on the fracture surfaces of many of the short crack specimens. However, with the exception of specimen '800/260:21', it is unlikely that the location of the porosity in these samples has any significant effect on the short crack fatigue behaviour which is essentially restricted to the top 2-3 mm of the specimens. This is particularly pertinent to the '800/260' specimens where eutectic carbides act as crack initiators in preference to pores. This would suggest that porosity is less significant in crack initiation in this heat treatment than in the '900/390' condition. Furthermore, it is believed that porosity would not significantly affect a camshaft in service since pores have only been found in significant quantities in the centre region of castings. Contact fatigue is generally a surface phenomenon.

8.4.10 Crack Interaction and Coalescence Effects

Crack interaction and subsequent coalescence is to varying extent a feature of all the short fatigue crack failure mechanisms of this study. What follows is a summary of literature on the subject of multiple fatigue cracks, interaction and coalescence. Parallels to the current work are made although extensive analysis is beyond the scope of the thesis. In general, the types of coalescence events observed in the current study are as follows:

- The rapid formation of a dominant macro-crack by the early-life coalescence of two or more micro-cracks that initiated in close proximity. Micro-crack dimensions at coalescence are typically less than 100μm.
- The coalescence of numerous micro-cracks throughout the lifetime of the specimen as seen in CDF.
- Mid-life coalescence of relatively large micro-cracks as seen in '800/260' specimens. Both micro-cracks are typically of comparable length (250 μm to 500 μm) at coalescence.

- Crack initiation ahead of an advancing dominant crack-tip as seen in '900/390' specimens at stress intensity values greater than 14 MP$\sqrt{m}$.
- The coalescence of two large parallel offset non-coplanar dominant cracks of at least 1000μm on failure.

Kamaya et al. [112] proposed the influence of the interaction between multiple cracks on crack growth behaviour greatly depends on the relative position of the cracks. Interaction is influenced not only by the relative position but also by the relative lengths of cracks. The influence is strongest when the crack lengths are equal and decreases as the difference in crack length increases. If the difference in crack length is greater than a certain level the interaction is sufficiently small to allow the influence of interaction to be ignored. The critical ratio in crack lengths was shown to be related to the magnitude of offset between the two cracks. The greater the offset, the greater the requirement for similitude in crack length for there to be interaction. Crack interaction in '900/390' short fatigue crack specimens was between the dominant macro-crack and micro-cracks that initiated ahead of the crack-tip. The difference in crack lengths for this mechanism is significant (generally c_1/c_2 = 0.01). The dominant macro-crack and micro-cracks were typically offset by 10 μm to 140 μm. The work summarised above suggests the interaction between the dominant macro-crack and micro-cracks is negligible. Coalescence in '800/260' specimens was typically of cracks of more comparable length and crack interaction is therefore likely to be more significant. However, this approach considers only pairs of cracks. Crack initiation ahead of the crack tip for the '900/390' heat treatment generally involves numerous micro-cracks. Greno et al. [72] and J Ortiz et al. [74] proposed crack initiation ahead of the crack tip and subsequent crack interaction and coalescence **is** significant and responsible for low propagation rates and high threshold values for ADI alloys when compared to steels. These phenomenon were attributed the redistribution and reduction of the average near-tip stresses by micro-cracks ahead of the advancing dominant macro-crack.

Work has been carried out on pairs of coalescing cracks in steels with initial separations in the range of 10 mm. Three dimensional FE models produced by Soboyejo et al. [113] predicted parallel offset non-coplanar semi-elliptical cracks

would grow independently until adjacent crack tips overlap. Subsequent growth in the region of overlap is associated with deviations of the adjacent crack tips. The deviations do not appear to significantly affect crack growth outside the region of overlap. Although separations were notably smaller than in the work by Soboyejo et al., similar behaviour for parallel offset non-coplanar cracks was observed in some '900/390' short crack specimens. Figure 8.9 is an image taken from the replica record of specimen '900/390:11'. The deviation of the adjacent crack tips is clear. Furthermore, any deviation does not appear to take place until the adjacent crack tips overlap. Figure 8.10 and Figure 8.11 show the crack-tip separation and overlap compared with the crack length and growth rates respectively of the two cracks in Figure 8.9. Reducing crack-tip separation appears to have little effect on crack growth rate. Soboyejo et al. suggested offset cracks may coalesce at depth positions without coming into contact at the surface. Additionally, it is suggested in the literature that there is a sudden increase in stress intensity factor as cracks coalesce [114114,115,116]. The stress intensity factor then decreases as the crack forms a semi-elliptical shape [114114,116]. The high stress intensity factors in the region of coalescence result in a rapid transition to a semi-elliptical crack.

Parallel collinear non-coplanar semi-elliptical cracks are very sensitive to crack-tip shielding [113]. Larger cracks shield the tips of smaller cracks(s) from the applied stress or stresses until the latter become non-propagating. The fatigue crack growth of larger cracks does not appear to be significantly affected by the presence of smaller cracks. This effect has been observed in '800/260' specimens showing PDF. The three longest cracks of specimen '800/260:05' grew in parallel, with the longest in the region of maximum applied stress. The crack growth data for these cracks is presented in Figure 8.12. The length of these cracks and a number of other smaller cracks decreased as the distance from the central roller position decreased in such a fashion that when observed from above a diamond pattern could be observed. As the specimen approached failure the central crack grew rapidly as the other cracks were effectively shielded and exhibited little growth.

When the '800/260' heat treatment suffers CDF the number of micro-cracks and subsequent interaction and coalescence events is large. The multiplicity of

initiation events and diversity of separation distances and relative positions does not allow for tractable models describing coalescence behaviour on a crack-by-crack basis. Multiple fatigue crack initiation and growth have been observed in steel weld structures [117]. As the initial surface cracks propagate adjacent cracks coalesce into fewer cracks of lower aspect ratio. Once a dominant surface crack has formed by coalescence of numerous coplanar micro-cracks, growth occurs predominantly in the depth direction. It is expected a similar mechanism occurs during CDF. J. Stolarz [118] proposed the increase in surface crack length due to coalescence has no effect on crack growth rate until the crack reaches its equilibrium aspect ratio which occurs exclusively in the depth direction. It was also suggested for low cycle fatigue, crack coalescence of this nature at the surface has no significant influence on the kinetics of fatal crack growth. It therefore seems reasonable to suggest the critical factors for CDF is the extent of damage (number of cracked carbides) on loading to maximum stress and crack growth in the depth direction following coalescence not the nature of coalescence on the surface.

8.5 Long Crack Behaviour

The propagation behaviour of the as-cast ductile iron, the '900/390' and '800/260' heat treatments has been assessed using long crack fatigue testing. Values of ΔK_{th} and K_Q for each of these alloy conditions can be seen in Table 8.1. Additionally a comparison of propagation data for these heat treatments is displayed in Figure 8.13. The changes in the as-cast microstructure generated by the '900/390' heat treatment appear to have resulted in improved fatigue crack propagation performance. No such improvement was promoted by the '800/260' heat treatment. The '900/390' heat treatment is tougher and has a higher fatigue threshold than other two variants. Crack growth rates for the as-cast ductile iron and '800/260' are generally faster than the '900/390' for comparable values of ΔK (the propagation data for these two alloy conditions lie in the upper range of the '900/390' scatter band). The improvement in toughness may in part be due to the lack of eutectic carbides in the '900/390' microstructure. This is supported by the variation in K_Q shown by the '800/260' heat treatment, where an increase in toughness appears to be promoted by a reduction in carbide area fraction (see Table 7.10). It is likely the brittle eutectic carbides decrease the toughness of a

microstructure by increasing the proportion of static failure modes. Evidence of an increase in the number of brittle facets (and hence static failure modes) visible on the fracture surface has been observed with a corresponding increase in values of both ΔK and crack growth rate within constant ΔK regions (see Figure 7.114 to Figure 7.116). Furthermore, as values of ΔK approach K_Q regions of micro-void coalescence can be seen on the fracture surface. These areas are perhaps further evidence of an increase in static failure modes as the specimen approaches fracture and can be compared to similar fracture surface observations of short crack specimens suffering coalescence dominated failure. It is therefore reasonable to suggest that the faster crack growth rates shown by the as cast ductile iron and the '800/260' ADI may in some part be related to increased numbers of static failure modes associated with the presence of eutectic carbides.

It may be seen in Table 8.1 that the '900/390' specimens show higher values of ΔK_{th} and K_Q than other ADI more conventional (lacking eutectic carbides) heat treatments in the literature. This may be related to the coarse microstructure inherent to this heat treatment. Observations of near threshold regions on '900/390' fracture surface (Figure 7.100) reveal lath like features of a similar scale to the bainite morphology associated with this heat treatment. These observations, together with short fatigue crack observations suggest crack growth along the interface between retained austenite and bainite. Observations in the literature [7,9,55] have suggested the presence of a ductile retained austenite film surrounding bainite sheaves. It is reasonable to propose that bainite sheaves (retained austenite films) are causing deflected crack propagation in near threshold conditions and therefore promoting roughness-induced closure and or crack shielding via crack deflection. It is likely this would lead to an increase in the value of ΔK_{th}. Furthermore, it has also been reported in the literature [59,66,67,69] that ADI microstructures containing significant amounts of retained austenite in large blocky pools undergo stress induced phase transformation to martensite in the vicinity of the crack tip. This process, known as the TRIP effect has been observed to reduce crack growth rates due to compressive stress at the crack tip, and raise threshold levels via phase transformation induced closure effects. Observation of the '900/390' microstructure reveal large quantities of blocky austenite pools.

Even though constant ΔK conditions were not satisfactorily achieved for two out of three regions (ΔK~15 MPa$\sqrt{m}$ and ΔK~20 MPa$\sqrt{m}$), some interesting behaviour may be observed in the propagation data shown in Figure 7.109. Little variation in crack growth rate can be observed for the ~12 MPa$\sqrt{m}$ region. A constant ΔK~15 MPa$\sqrt{m}$ region was not achieved and what we have is a gradual increase in ΔK from 12 to 15 MPa$\sqrt{m}$. Within this region there appears to be little variation in crack growth rate for values of ΔK of 14 to 15 MPa$\sqrt{m}$. However, for values of ΔK between 12 and 14 MPa$\sqrt{m}$ there is significant scatter in crack growth rates. Furthermore there is a noteworthy increase in crack growth rate from of $1.6x10^{-5}$ mm/cycle at 12 MPa$\sqrt{m}$ to $1.8x10^{-4}$ mm/cycle at 14 MPa$\sqrt{m}$ possibly suggesting a transition in the fatigue failure mechanism. Comparisons may be made to the short fatigue crack observations where the rate of graphite nodules intercepted by the dominant crack showed a marked increase above 14 MPa$\sqrt{m}$. It is possible this is associated to an increase of near tip micro-crack initiation events. Also noteworthy, is the merging of long and short fatigue crack data at this level of stress intensity factor. Additionally, estimates of monotonic plastic zone size at this magnitude of stress intensity factor are of the order of mean nodule spacing. Further observation of the '900/390' fatigue threshold and growth out test fracture surface reveal an increase of surface roughness, as ΔK increases (see Figure 7.95 to Figure 7.99). This may be indicative of increased crack deflection related to the seeking out of graphite nodules by the advancing crack front via the mechanism described in the propagation dominated short fatigue crack analysis.

8.5.1 Porosity Effects on Long Fatigue Crack Behaviour

A feature of some of the long fatigue crack specimen fracture surfaces is the presence of porosity. The '900/390' test with the least amount of porosity (Figure 7.86) exhibited the fasted crack growth rates during the constant load amplitude growth out region. This possibly suggests porosity retards crack propagation by crack-tip blunting mechanisms. There was little porosity in the fatigue threshold region of '900/390:L6' (see Figure 7.87) suggesting a reasonably porosity unaffected value was recorded. Additionally, it can be seen in Figure 7.86 the 15 MPa$\sqrt{m}$ constant ΔK region showed no porosity on the fracture surface. This would imply the phenomenon of a sudden increase in crack growth rate outlined

in section 8.5 is a genuine observation. Only one of the '800/260' long fatigue crack test fracture surfaces showed any significant amount of porosity (Figure 7.88). This appeared to have no effect on the crack propagation rates of this specimen.

Heat Treatment	ΔK_{th} (MPa$\sqrt{m}$)	K_Q (MPa$\sqrt{m}$)
DI	6	19
900/390	8	24-32
800/260	5.8	18-27
950/400	4.7	28
950/250	4.4	20
850/400	4.7	22
850/250	3.7	17

Table 8.1: Comparison of long crack data for current and previously tested heat treatments.

Carbide Aspect Ratio	Carbide Area (μm^2)	Inclination wrt Tensile Axis		Assumed Orientation	Deviation from Actual Orientation		Inclusion Stress - σ_I (MPa)	
		radians	degrees		radians	degrees	σ^A = 275 MPa	σ^A = 330 MPa
1.04	2737	1.14	65.4	Oblate	0.43	24.6	304.8	365.7
1.73	2701	1.46	83.7	Oblate	0.11	6.3	301.8	362.2
2.05	5711	0.07	4.0	Prolate	0.07	4.0	314.3	377.2
2.05	668	1.37	78.5	Oblate	0.20	11.5	301.7	362.0
2.32	2369	0.04	2.3	Prolate	0.04	2.3	316.1	379.4
3.9	1354	0.26	14.9	Prolate	0.26	14.9	323.0	387.6
2.37	1178	1.47	84.3	Oblate	0.10	5.7	301.8	362.1
3.52	6784	1.40	80.3	Oblate	0.17	9.7	303.6	363.8

Table 8.2: Summary of inclusion stresses for selected cracked carbides.

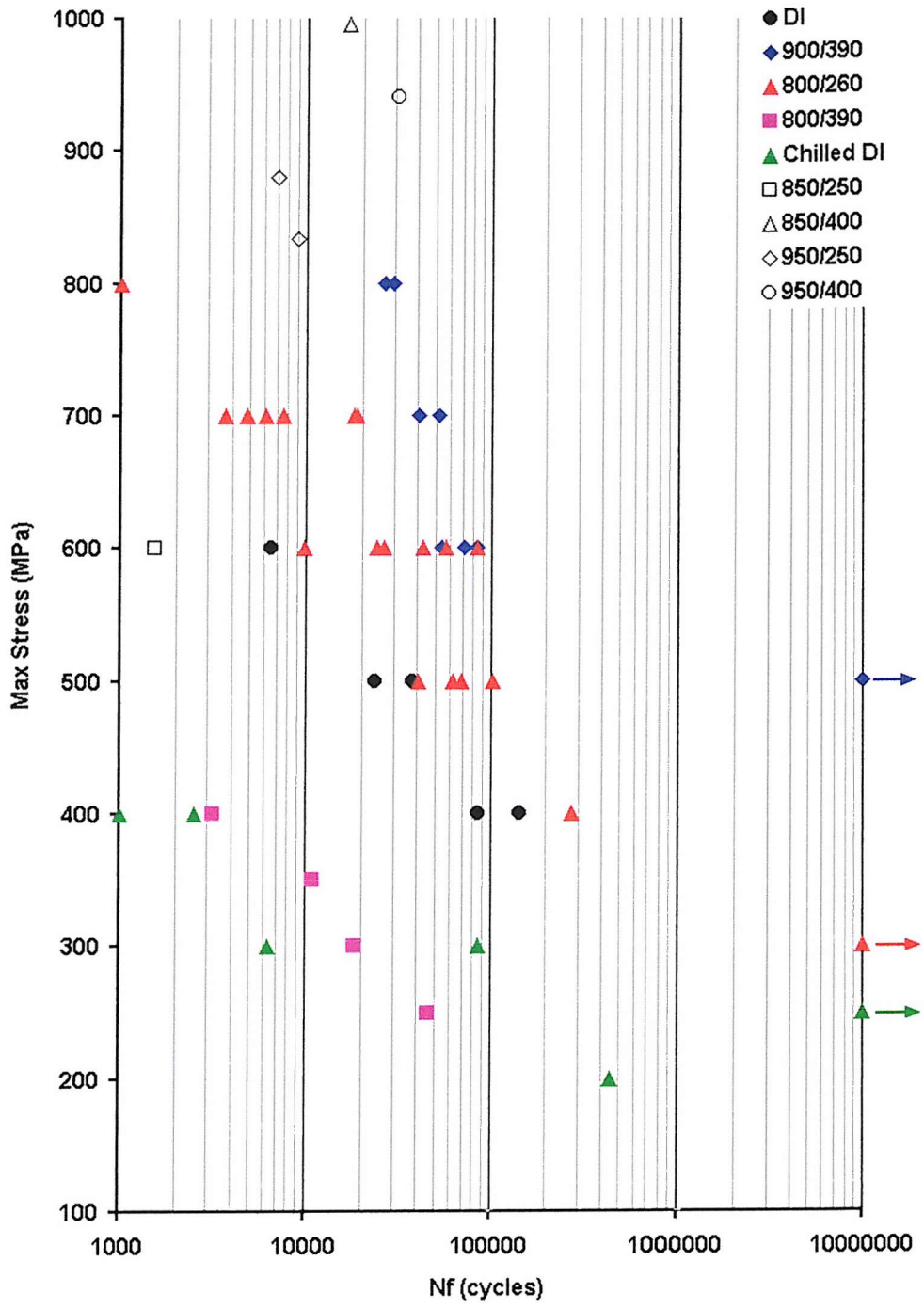

Figure 8.1: S-N curve comparing all short fatigue crack specimens from the current batch of alloy conditions with those previously tested at Southampton University.

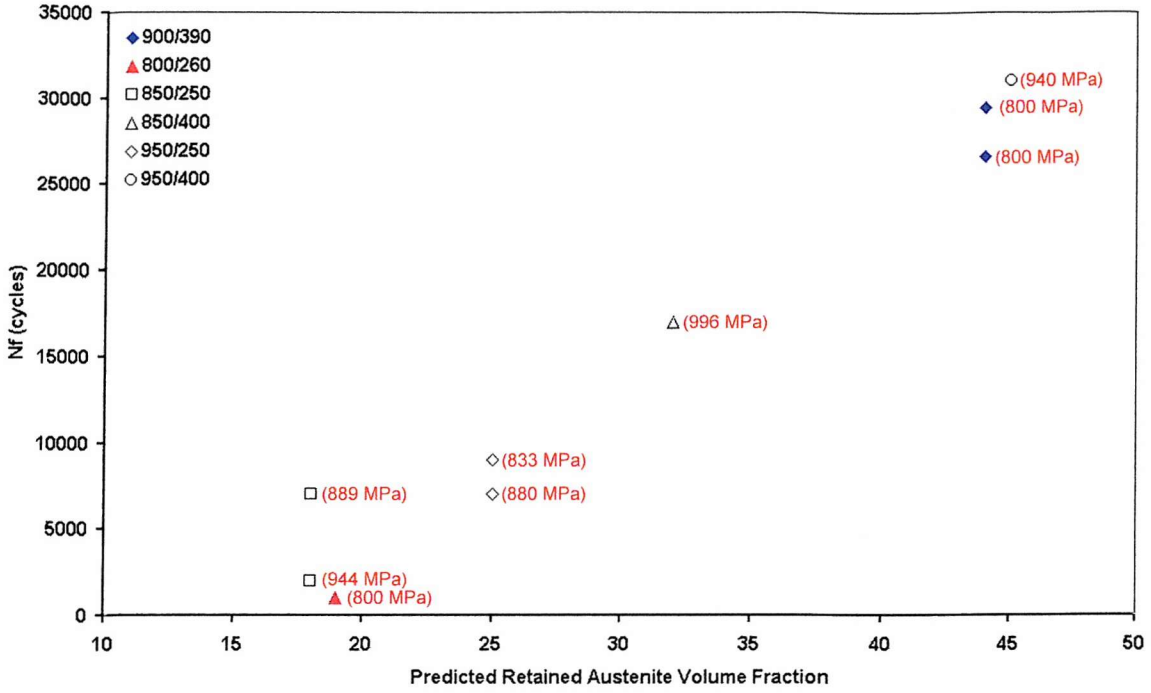

Figure 8.2: Comparison of short fatigue crack lifetime with predicted retained austenite volume fraction. Values in brackets indicated maximum applied stress.

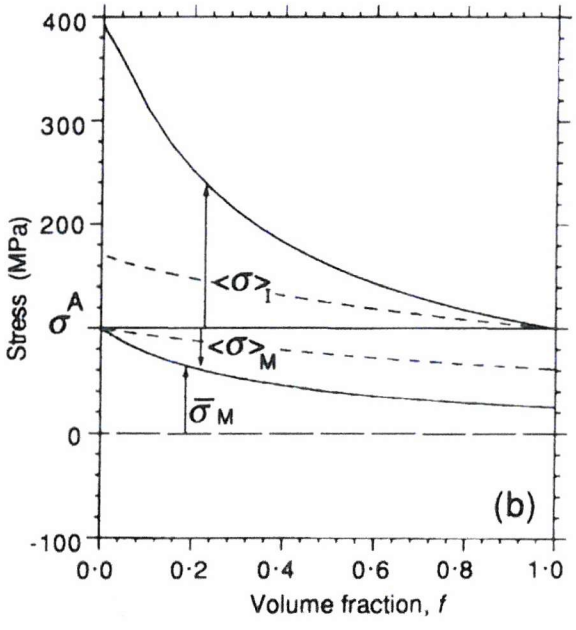

Figure 8.3: Effect of composite volume fraction on mean and volume averaged stresses.

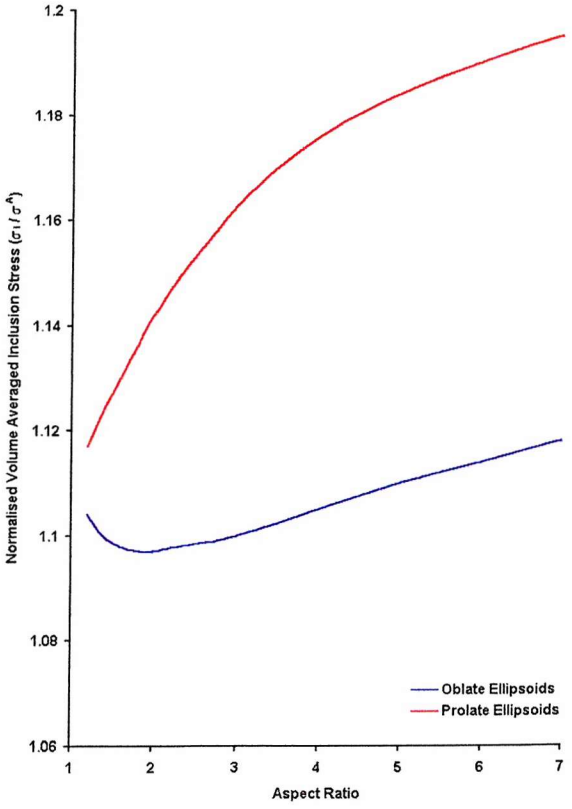

Figure 8.4: Effect of particle aspect ratio on inclusion stress for prolate and oblate orientations.

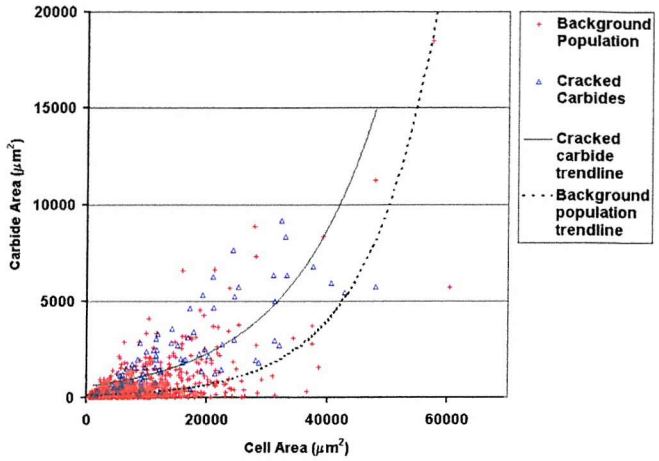

Figure 8.5: Comparison of carbide area and cell area for '800/260' specimen used for SUPANOVA classification of cracked carbides.

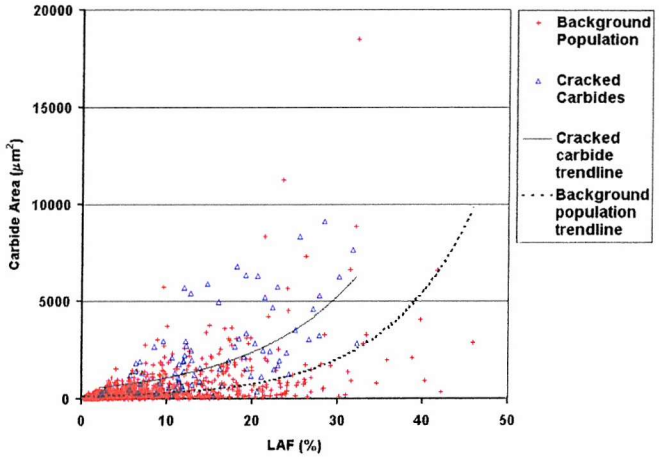

Figure 8.6: Comparison of carbide area and local area fraction for '800/260' specimen used for SUPANOVA classification of cracked carbides.

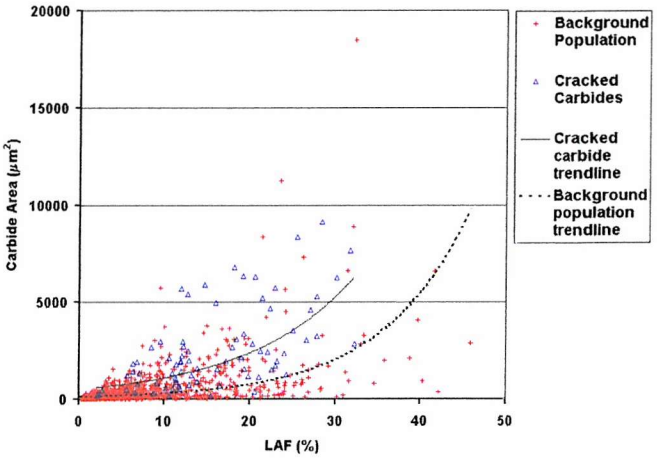

Figure 8.7: Comparison of cell area and local area fraction for '800/260' specimen used for SUPANOVA classification of cracked carbides.

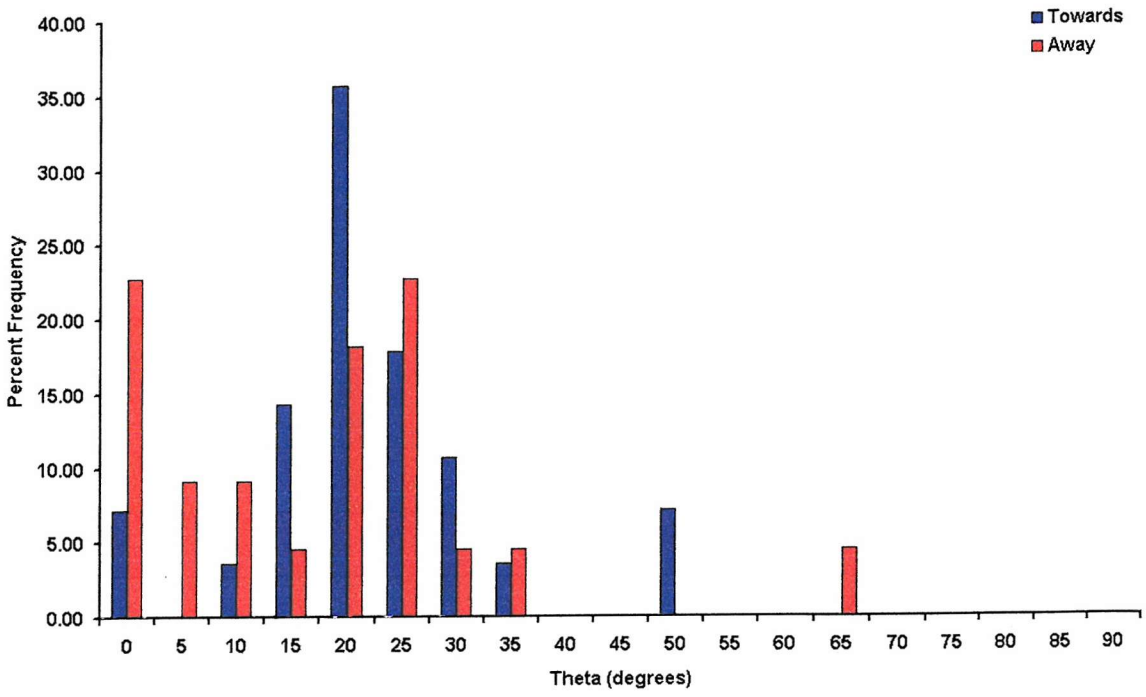

Figure 8.8: Crack initiation from graphite nodules ahead of the advancing dominant crack tip. Investigation into the orientation of micro-cracks with respect to the graphite nodule.

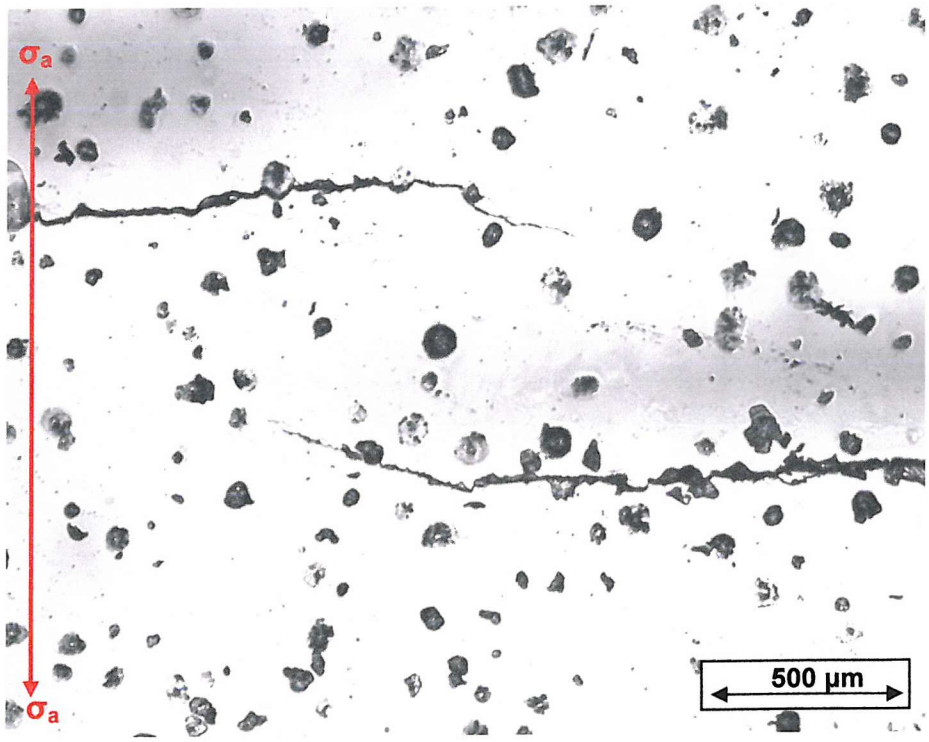

Figure 8.9: Crack coalescence in specimen '900/390:11'.

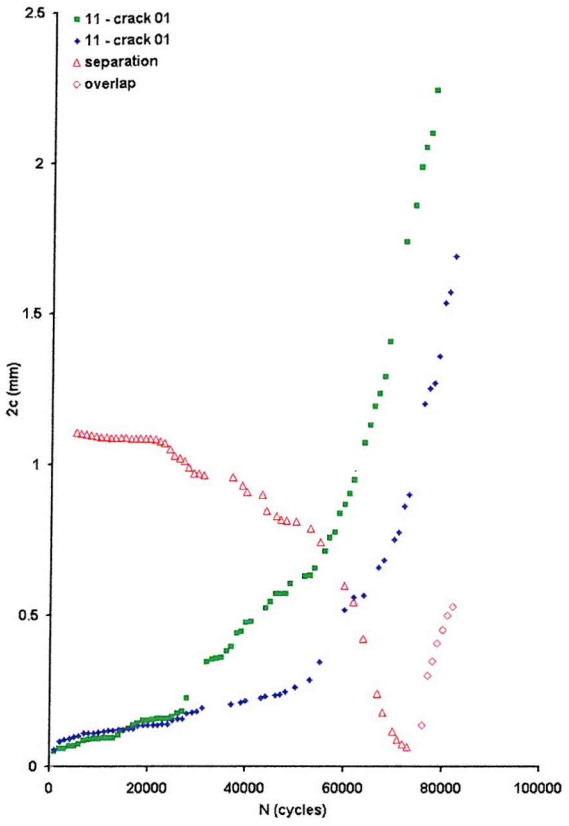

Figure 8.10: Crack length and crack-tip separation as a function of number of fatigue cycles for specimen '900/390:11'

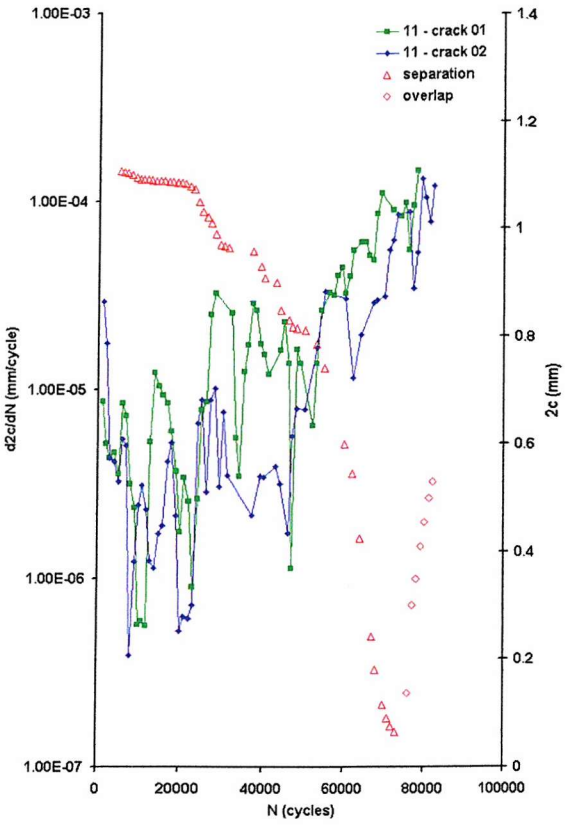

Figure 8.11: Crack growth rates and crack-tip separation as a function of number of fatigue cycles for specimen '900/390:11'.

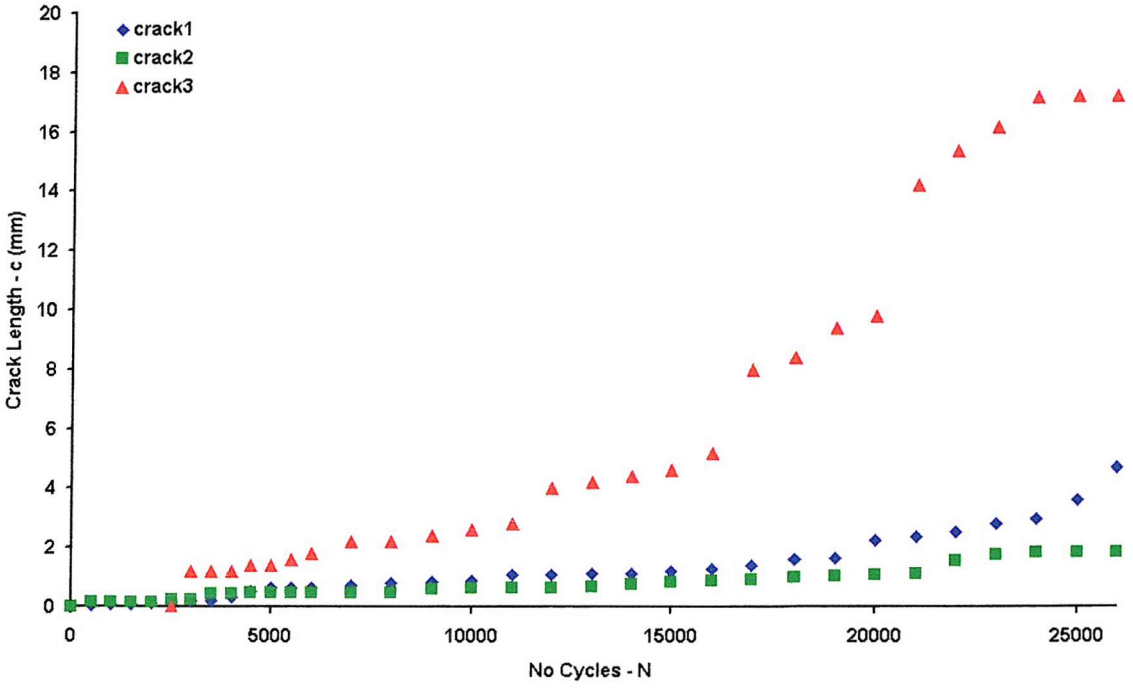

Figure 8.12: Short fatigue crack growth rates for specimen '800/260:05'

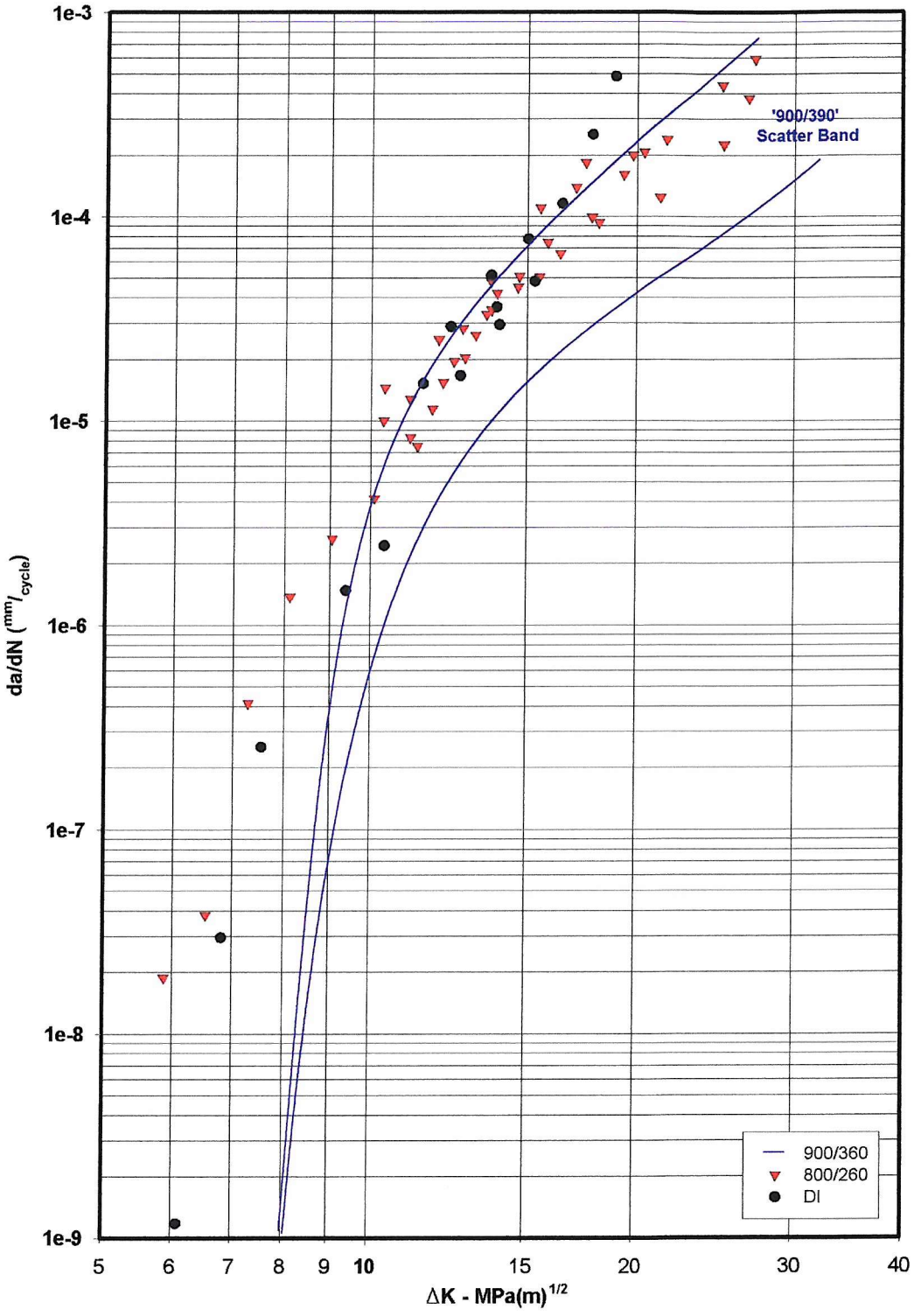

Figure 8.13: Comparison of fatigue crack propagation data from long crack testing.

9 Summary and Conclusions

The as-cast ductile iron is used as a benchmark against which all alloy derivatives are compared. The purpose of this is to identify the effect on mechanical properties that each of the heat treatment procedures generates. The '800/260' and '800/390' ADI heat treatments and the chilled alloy variants showed improved hardness with respect to the as-cast ductile iron. However, only the '900/390' and '800/260' showed an increase in fatigue performance.

The as-cast ductile iron is characterised by the presence of large eutectic carbides in a pearlitic microstructure. Austenitising at 900^0C for two hours was sufficient for the dissolution of these carbides where as austenitising at 800^0C was not (only a minimal amount of carbide dissolution occurred). This phenomenon resulted in the near complete dissolution of eutectic carbides for one ADI heat treatment ('900/390') whilst significant numbers remained in the other two ('800/260' and '800/390'). The presence or lack of eutectic carbides generated a range of fatigue failure processes. Furthermore, the variable distribution of the carbide structures throughout the microstructure of the '800/260' variant produced a range of fatigue failure behaviour from coalescence to propagation dominated failure.

The '900/390' microstructure is relatively soft and tough due to the relatively high quantity of retained austenite. Short fatigue crack behaviour is generally propagation dominated and leads to improved lifetimes when compared to all other alloy variants. At high values of stress intensity factor short cracks have been observed to 'seek' graphite nodules. Other authors have also observed this behaviour in ADI alloys. Investigation revealed that graphite nodules decohere and initiate micro-cracks in the **monotonic** crack-tip plastic zone ahead of the dominant crack. This fits in with the suggestions by Greno et al. that nodule decohesion ahead of the crack tip is a quasi-static phenomenon. Some of these micro-cracks may subsequently coalesce with the dominant crack thereby causing crack deflection. It is this deflection that gives the impression the dominant crack is seeking graphite nodules. A rise in the rate of increase in the number of graphite nodules on the dominant crack was observed above a stress intensity factor of 14 MPa$\sqrt{m}$. This related to a monotonic plastic zone of equivalent size to

the average graphite nodule spacing for this microstructure. This would suggest that at values of ΔK above this threshold value there is an increased probability of a graphite nodule being present within the monotonic plastic zone. Furthermore, long and short fatigue crack data merge at 14 MPa√m. Observations of crack propagation data in both constant ΔK and increasing ΔK tests have revealed a significant increase in crack growth rate above a stress intensity factor of 14 MPa√m. It is probable this is related to an increase in crack initiation ahead of the crack tip similar to that observed for short fatigue cracks at comparable values of ΔK. An increase in roughness for long fatigue crack fracture surfaces was observed with a corresponding increase in stress intensity factor. It is reasonable to suggest this reflects an increase in graphite nodule decohesion and crack initiation ahead of the crack-tip and ensuing dominant crack deflection. Greno et al. identified an increased likelihood of micro-crack initiation towards a dominant crack at an orientation around a graphite nodule perimeter of between 15 and 30 degrees. This is supported by the observations in this study. Initiation away from the dominant crack appears less dependent on orientation around the nodule. Long fatigue crack tests have identified crack deflection by bainite sheaves at near threshold values of stress intensity factor. Other authors [7,9,55] have noticed a retained austenite film surrounding bainite sheaves. It is possible this ductile film provides a sufficient barrier to cause crack deflection at these low values of ΔK. It is believed this feature causes roughness induced crack closure and therefore is responsible for the elevated fatigue threshold compared to the as-cast ductile iron and the '800/260' heat treatment.

The '800/260' microstructure is hard and (sometimes) very brittle. The microstructure is typified by a fine lower bainitic matrix with variable quantities and distributions of eutectic carbides. The application of finite body tessellation to short fatigue crack specimens has revealed the presence of a longitudinally graduated carbide distribution which is closely related to a hardness gradient over the same region. A higher local carbide area fraction has been related to a higher local hardness value. It was observed that the location of the increased local hardness and carbide area fraction related to positions in the original casting that were likely to experience the fasted cooling rates.

This heat treatment shows a range of short fatigue crack performance from coalescence to propagation dominated behaviour. Coalescence dominated failure is defined as crack growth via the coalescence of a large number of micro-cracks and is associated with shorter fatigue lifetimes. Propagation of individual cracks is relatively slow with the majority of growth occurring in the depth direction. Propagation dominated failure is defined as crack growth via the propagation of a small number of individual micro-cracks through microstructure and is associated with longer fatigue lifetimes. The mechanism of failure is determined by the number and position of initiation sites, which for the '800/260' heat treatment was identified as cracked eutectic carbides. Carbide cracking occurred when short fatigue crack specimens were subjected to a load of 275 – 330 MPa. Estimations of carbide fracture stress have been made using the Eshelby approach. CDF is typified by a large number of cracked carbides and therefore individual micro-cracks. Fatigue lifetimes are relatively short and show no improvement over the as-cast ductile iron. Crack growth is by the linking of a large number of surface micro-cracks which subsequently grow in the depth direction. It is suggested [117] that crack interaction associated with coalescence of this nature does not significantly reduce fatigue lifetimes. If this is the case, the relatively poor fatigue lifetimes shown by this failure mechanism are probably related to the extensive damage caused by carbide cracking on loading above 275 MPa. PDF is associated with longer lifetimes, that are comparable to the '900/390' heat treatment. Fewer cracked carbides (compared to CDF) at applied stresses above 275 MPa lead to a smaller number of individual micro-cracks. Crack coalescence remains a significant feature and leads to rapid and sudden increases of crack growth rate. Consequently, the improved short fatigue crack performance for this failure mechanism is probably related to the comparatively small extent of damage (carbide cracking) suffered in early life. In general high carbide area fractions promote CDF whilst low area fractions promote PDF. It is believed carbide geometry and distribution are influential in determining the mechanism of short crack fatigue failure for an individual specimen. The effect of carbide geometry and distribution has been investigated by two approaches:

- Classification of the features that cause individual carbides to crack (and subsequently initiate micro-cracks).
- Comparison of carbide populations that experience CDF and PDF.

The application of finite body tessellation (FBT) and SUPANOVA techniques have identified the following features:

- Cracking of individual carbides appears more likely if the carbide is large and locally clustered.
- The effect of orientation on both individual carbides and the nearest neighbour is unclear.
- The probability of a specimen suffering PDF appears to be increased by carbide alignment (both individually and as a population) in a direction that is perpendicular to the tensile axis.
- The requirements for CDF, appear to be less stringent than for PDF.
- The likelihood of CDF is increased in populations with a high number of carbides with a high aspect ratio or a large mean carbide area.
- CDF is promoted by a large number of prolate carbides irrespective of the orientation of the nearest neighbour, or degree of local clustering.
- Specimens are particularly likely to suffer CDF if the carbide population is characterised by a significant number of large prolate carbides aligned parallel to the tensile axis.

The probability of individual carbide fracture is defined by carbide size (probability of containing a critical sized flaw which increases with carbide size), and the magnitude of internal stress (probability of any flaw being critical). The nature of load transfer in carbide populations controls the internal stresses experienced by individual carbides. Load transfer mechanisms are influenced by the geometry and alignment of both the individual carbide and the overall population in addition to the carbide volume fraction. The failure probability distribution for all carbides within a population defines the extent of carbide fracture and hence the subsequent mechanism of failure.

The approach developed in this project for characterising multiple fatigue initiation sites is equally applicable to a number of other multiple cracking situations. Aluminium-silicon-tin alloys used for bearing applications and MMC whisker reinforced alloys often exhibit multiple fatigue cracks initiating from second phase particles.

Long fatigue crack testing has identified decreasing toughness and increasing crack propagation rates with higher carbide area fractions. It is likely this is associated with an increase in brittle static failure modes. Summarising, the '800/260' heat treatment is harder than the '900/390' and can show comparable fatigue performance at certain stress levels. Short crack fatigue performance is dependent on failure mechanism, which in turn is dependent on the characteristics of the carbide population. In general PDF should be encouraged as it is associated with longer short fatigue crack lifetimes.

The '800/390' heat treatment has significantly larger amounts of eutectic carbides than the '800/260', although with less variability between specimens. Short crack fatigue failure was entirely coalescence dominated with a larger number of micro-cracks than any of the '800/260' specimens.

9.1 Industrial Relevance

It is doubtful that conventional austempered ductile iron alloys will ever be suitable for rolling contact fatigue applications such as automotive camshafts. It is cited in the literature [77], that the good resistance of ADI alloys to fatigue propagation does not overcome the poor resistance to crack initiation. Crack initiation in the '900/390' microstructure was indeed rapid, although it is not known what effect the absence of porosity would have. Hardening of the surface by chilling was recommended in the literature [77]. Due to the presence of severe quench cracking in the chilled ADI specimens the effect of a chilled surface could not be identified. The ADI conditions austenitised at 800^0C contained carbidic structures, which had the effect of increasing the hardness of the material. These carbides are brittle and even though variability was observed, crack initiation under short fatigue crack conditions was generally rapid. It is likely that these ADI heat treatments are also unsuitable for rolling contact fatigue applications. However the combination of

high hardness and reasonable resistance to fatigue crack propagation is likely to prove attractive for other service applications. Under certain conditions the '800/260' heat treatment can provide both of these mechanical properties. The magnitude of hardness and fatigue resistance are both dependent on carbide populations. High hardness is promoted by a large carbide volume fraction, whilst extensive carbide cracking is highly detrimental to fatigue resistance. With careful control of both alloy content (i.e. thermodynamic driving forces) and cooling conditions it may be possible to retain a significant volume fraction of carbides without compromising the resistance to multiple fatigue crack initiation by promoting PDF.

10 Recommendations for Further Work

The following areas of further work have been identified as being potentially beneficial:

- Expansion of thermodynamic theory based microstructural evolution model to predict quantities of eutectic carbides.
- Investigation of the possible hardness variation between graphite nodules using nano-hardness indentation.
- Evaluation of matrix dependent crack growth in the '900/390' microstructure. Effect of stress intensity factor and bainite sheave morphology.
- Finite element modelling of the near crack-tip micro-crack initiation process.
- SUPANOVA comparison of carbide populations showing propagation and coalescence dominated failure at other applied stress levels.
- Modelling the effects of carbide orientation on inclusion stresses.
- Determine probability distribution of carbide cracking for CDF and PDF.
- Development of a solidification theory based model to predict carbide distribution with the aim of producing favourable carbide distributions.

11 Appendix

Austenitising Temp (^{0}C)	Austempering Temp (^{0}C)	Austempering Time (min)	Retained Austenite (%)	Predicted Retained Austenite (%)	Bainite (%)	Predicted Bainite (%)
900	280	15	-	49	-	51
		30	-	31	-	69
		60	7	31	93	69
		90	9	31	91	69
		120	9.5	31	90.5	69
	400	15	17	51	68	49
		30	20	41	80	59
		60	27	41	73	59
		90	37	41	63	59
		120	36	41	64	59
1050	280	15	15	79	65	21
		30	30	62	52	38
		60	40	47	60	53
		90	45	41	55	59
		120	51	40	49	60
	400	15	9	81	56	19
		30	16	69	84	31
		60	19	64	81	36
		90	22	64	78	36
		120	29	64	71	36

Appendix 11.1: Comparison of matrix constituent volume fractions claimed by Shanmugam et al. [68] and predicted by Loughborough University microstructure prediction model (Graphite not considered and figures based on relative volume fraction of matrix for purpose of comparison).

Capture image:	Using image capture techniques described in 5.3.1.
Calibrate image:	A graticule was used to determine the number of microns per pixel at all microscope magnifications. These ratios were saved as calibration files.
Define region of interest	Create a 5-pixel border around the binary image.
Produce a binary image using a greyscale threshold	A greyscale value is chosen for which every value below is regarded as binary 0 or black and every value above is regarded as binary 1 or white. Careful adjustment of the threshold level allows the required microstructural objects to be picked out and analysed. Once chosen the same 'threshold level' is used for all images with a batch.
Filter small objects:	A certain amount of noise is expected on all capture images. The careful removal of this noise is required to obtain accurate measurements of the material microstructure. The minimum size of objects to be analysed is determined by referral to the original captured image and careful judgement. Once chosen the same 'size call' is used for all images with a batch.
Open objects:	This removes irregular rough edges associated with slight imperfection in image focusing.
Close objects:	Closes any 'gaps' in the binary image.
Edit manually:	Even after all these processes a certain amount of manual editing may be required.
Filter small objects:	Re-clean the image after editing
Tessellate Image:	Apply distance transform and watershed. Create network of cells. Gather cells and objects to generate the final tessellation image.
Measure cells:	
Ignore edge cells:	Those objects whose cell area is restricted by the edge of the captured image are not statistically representative of the global microstructure and are ignored.

Appendix 11.2: FBT procedure.

Term	Data set 1	Data set 2	Data set 3	Data set 4	Data set 5	Data set 6	Data set 7	Data set 8	Data set 9	Data set 10
CA	•	•	•	•	•	•	•	•	•	•
LAF	•	•	•	•	•	•	•	•	•	•
Dmin	•	•	•	•		•	•	•		•
Oang vs. LAF	•	•	•	•	•	•	•	•	•	•
Oang vs. NNang	•		•	•	•				•	•

Appendix 11.3: FBT terms selected by the ten SUPANOVA data set runs for comparison of individual carbides.

Term	Data set 1	Data set 2	Data set 3	Data set 4	Data set 5	Data set 6	Data set 7	Data set 8	Data set 9	Data set 10
Oar	•	•	•	•	•	•	•	•	•	•
Oang	•			•	•	•		•	•	•
CA	•	•		•	•	•	•	•	•	
LAF	•	•	•	•	•	•	•	•	•	•
Dmean	•	•	•		•	•	•	•	•	•
Oang vs. LAF		•			•	•	•	•		•
Oang vs. NNang		•	•		•	•	•		•	•

Appendix 11.4: FBT terms selected by the ten SUPANOVA data set runs for comparison of carbide populations.

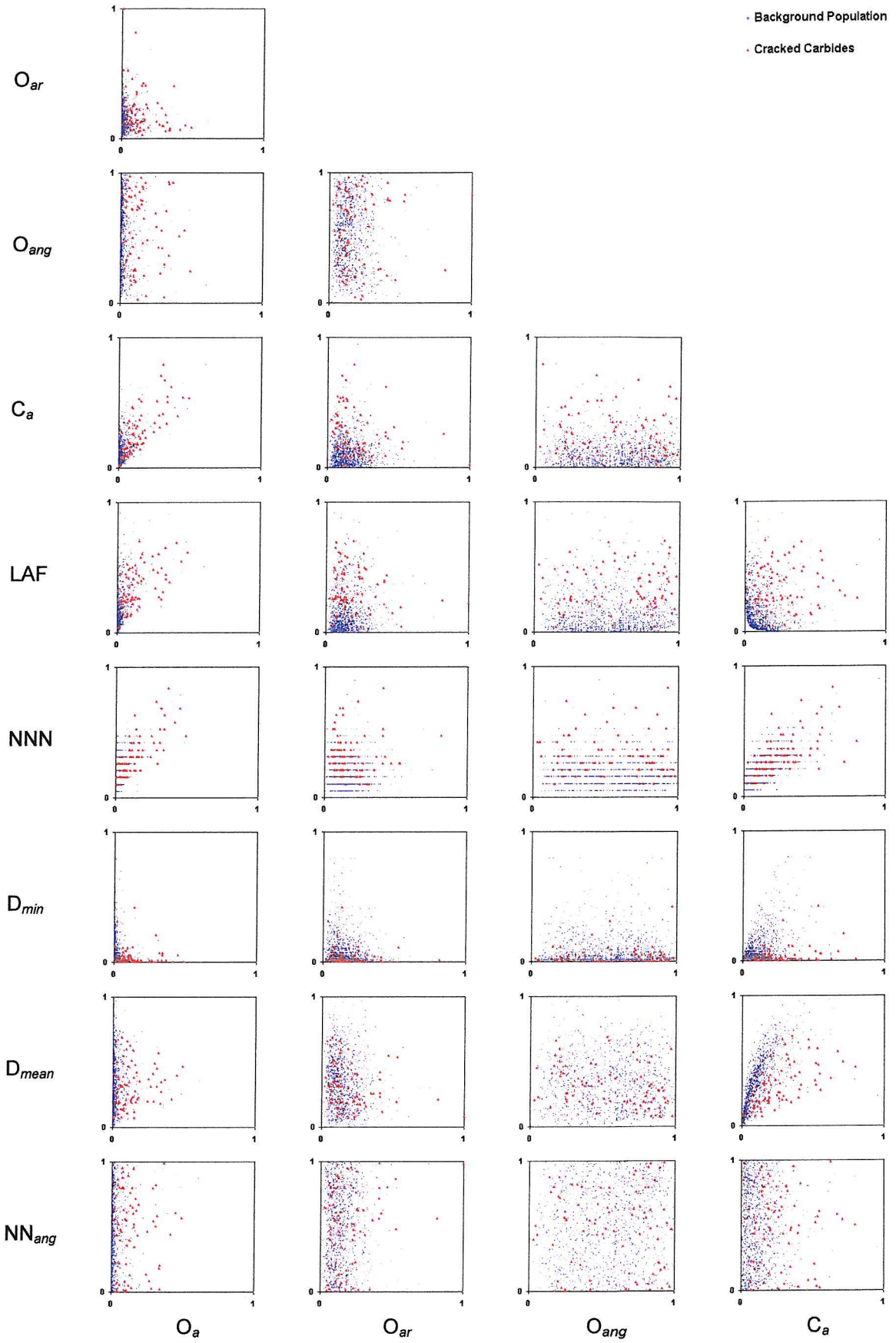

Appendix 11.5: Pair-wise scatter plots of FBT parameters in comparison of individual carbides.

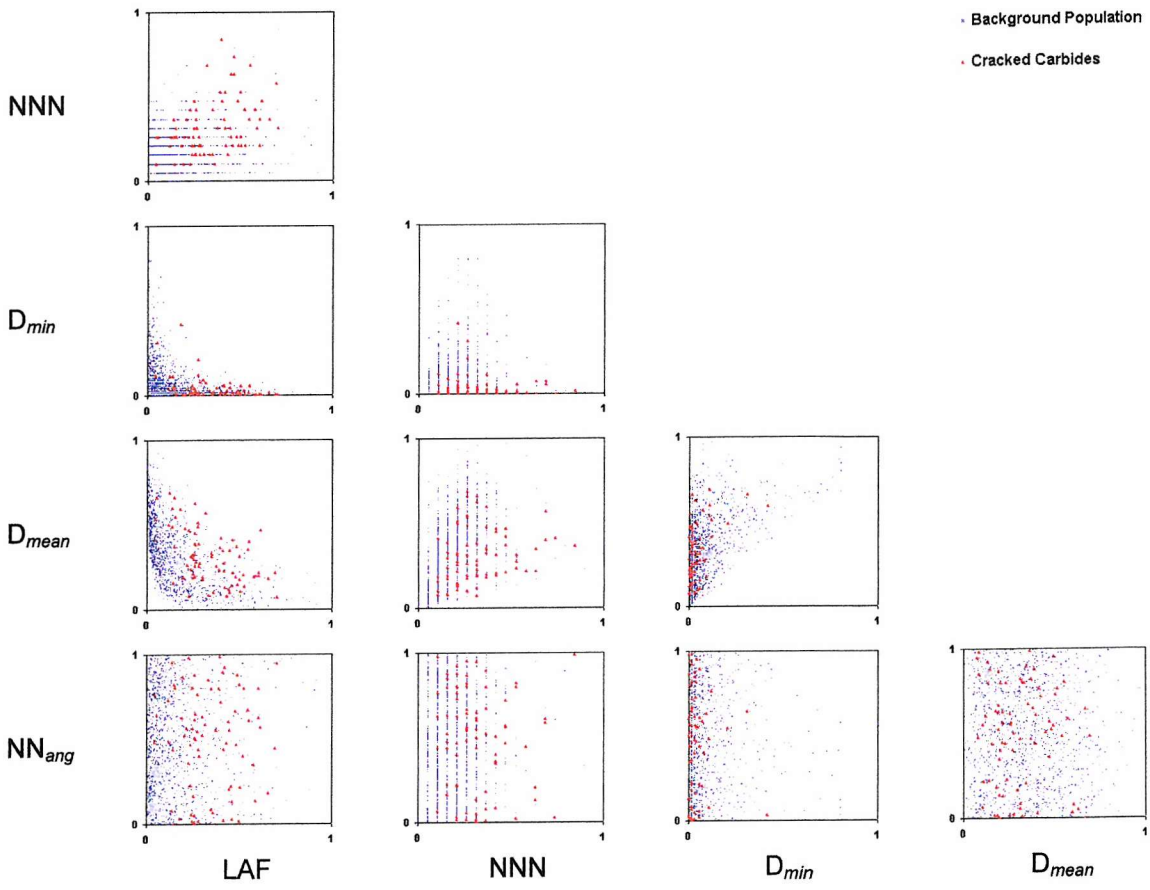

Appendix 11.6: Pair-wise scatter plots of FBT parameters in comparison of individual carbides.

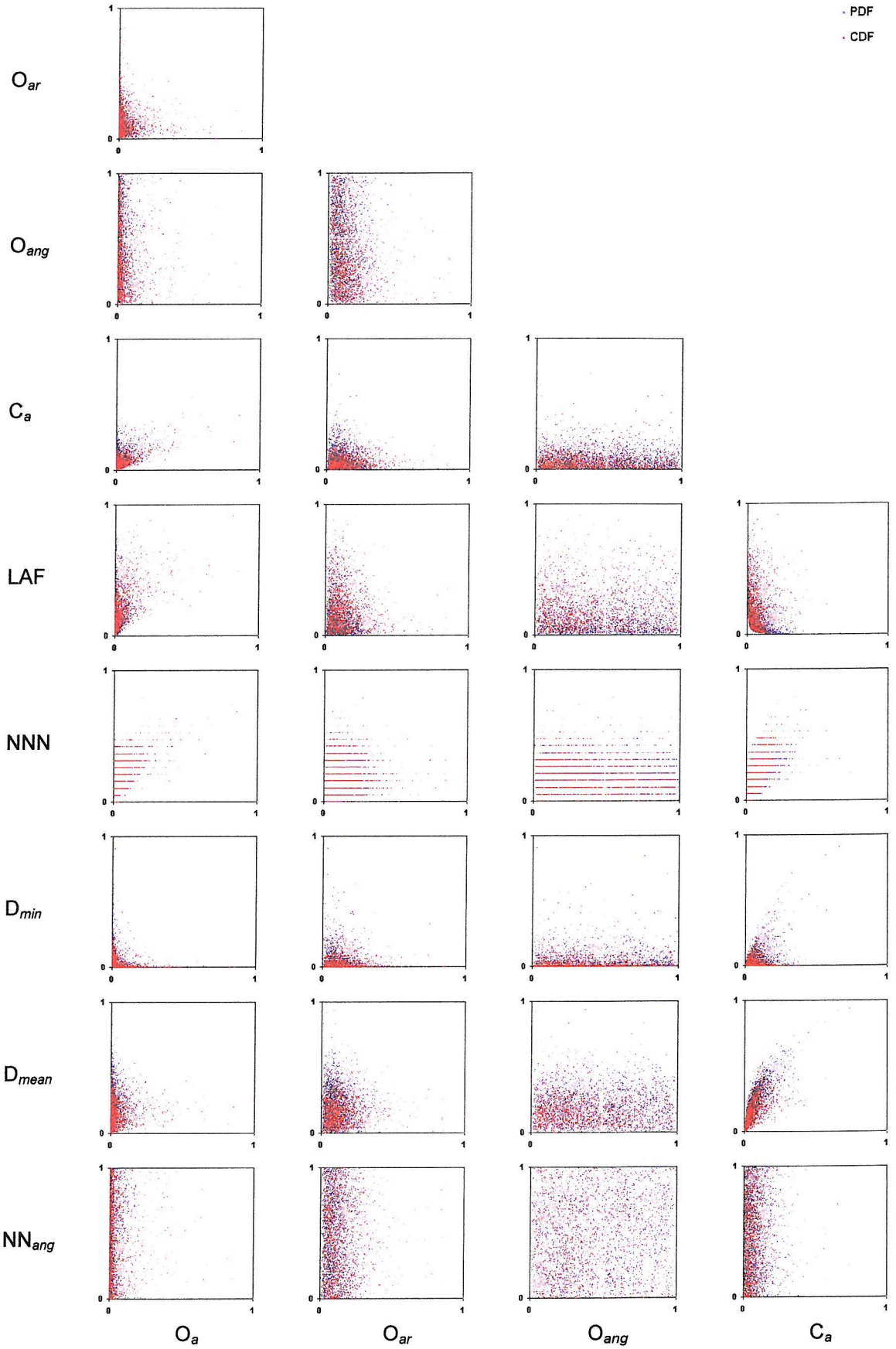

Appendix 11.7: Pair-wise scatter plots of FBT parameters in comparison of carbide populations.

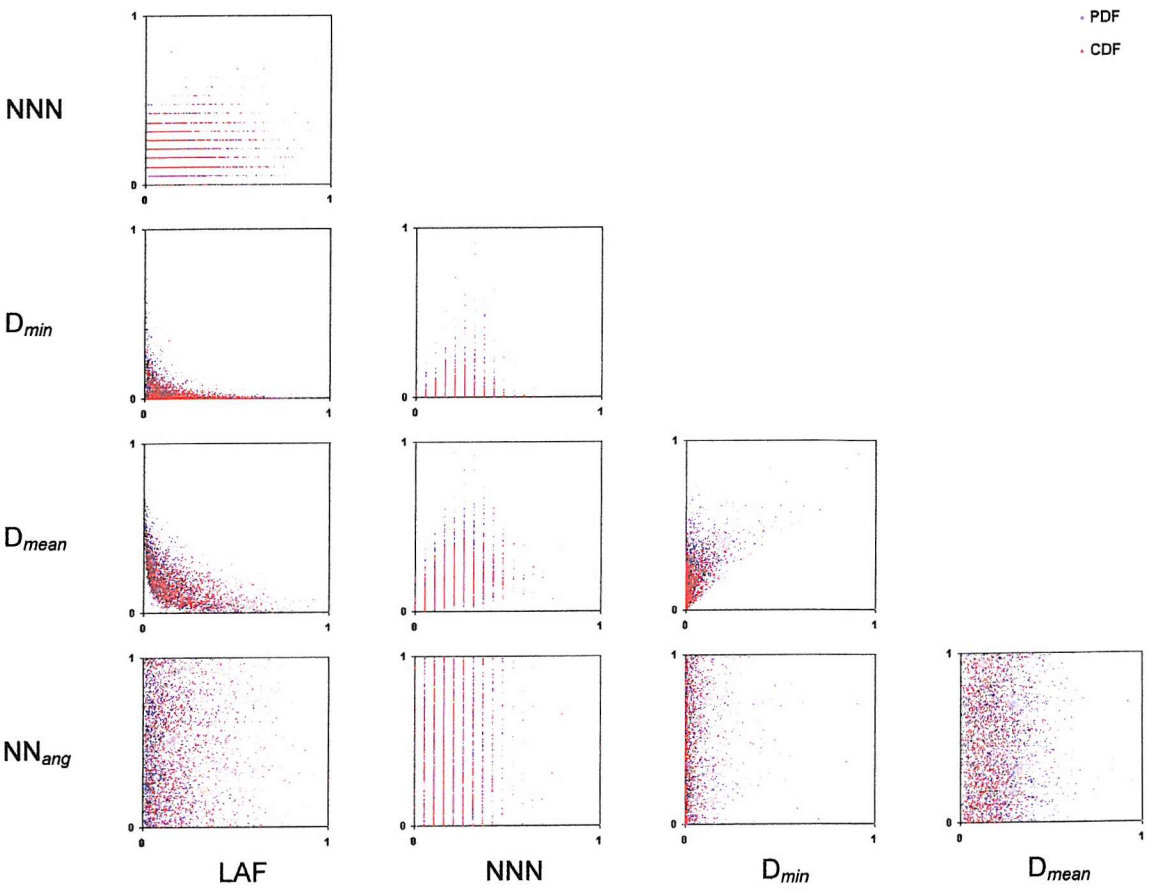

Appendix 11.8: Pair-wise scatter plots of FBT parameters in comparison of carbide populations.

12 Reference List

[1] K.G. Tembwe, *Microstructural Modelling of Cast Iron Camshafts*, University of Loughborough MSc Project, 1996

[2] Tia Francois, *Evaluation of the Fatigue Resistance of ADI Camshafts*, University of Southampton, BEng Project 1996/97

[3] PAS Reed, M. Joyce, N. Hide, J. Boselli, *Report on the Micromechanistic Fatigue Evaluation of ADI (Chilled and Unchilled Condition),* University of Southampton, Report to Federal Mogul, 1998

[4] J. Cole, *Fatigue Evaluation of ADI*, University of Southampton, BEng Project 1998/99

[5] R. P. Hockley, D. Thakar, J. Boselli, I. Sinclair, P. A. S. Reed, *Effect of Graphite Nodule Distribution on Crack Initiation and Early Growth in Austempered Ductile Iron*, Small Fatigue Cracks: Mechanisms and Applications, 1999

[6] P. A. S. Reed, R. C. Thomson, S. James, D.C. Putman, K. K. Lee, S. R. Gunn, *Modelling the Microstructural Effects in the Fatigue of Austempered Ductile Iron*, Materials Science and Engineering, Vol. A346, pp. 273-286, 2003

[7] R.C. Thomson et al, *Modelling Microstructural Evolution and Mechanical Properties of ADI*, Materials Science and Technology, 2000

[8] J.S James and R.C Thomson, Proceedings of Caston, Institute of British Foundrymen, 1998

[9] J.S James, *Microstructural Modelling of ADI Camshafts*, PhD Thesis, Loughborough University, 1999

[10] S. Suresh, *Fatigue of Materials*, Cambridge University Press

[11] K. J. Miller, K. P. Zachariah, *Cumulative Damage Laws for Fatigue Crack Initiation and Stage One Propagation*, Journal Strain Analysis Vol. 12, pp. 262, 1977

[12] K. J. Miller, *The Behaviour of Short Fatigue Cracks and Their Initiation, Part II*, Fatigue and Fracture of Engineering Material Structures, Vol. 10, pp. 95, 1987

[13] K. J. Miller, *Materials Science Perspective of Material Fatigue Resistance*, Material science and Technology Vol. 9, pp. 453, 1993

[14] A. A. Griffith, *The Phenomenon of Rupture and Flow in Solids*, Trans Roy Soc. Vol. A221, pp. 163-197, 1921

[15] E. Orowan, *Fundamentals of Brittle Behaviour of Metals*, Fatigue & Fracture of Metals, pp. 139-67, 1952

[16] Onset of Fast Crack Propagation in High Strength Steel and Aluminium Alloys, proc. 2nd Sagamore Conf. II, pp. 289-305, 1956

[17] G. R. Irwin, *Analysis of Stresses and Strain at the End of a Crack Traversing a Plate*, Journal Applied Mechanics, Vol. 24, pp. 361-4, 1957

[18] ASTM. Designation: E647-95a. Standard Test Method for Measurement of Fatigue Crack Growth Rates.

[19] T. L. Anderson, *Fracture Mechanics – Fundamentals and Applications*, CRC Press, 1994

[20] P. C. Paris, M. P. Gomez, W. P. Anderson, *A Rational Analytic Theory of Fatigue*, The Trend in Engineering 13, pp. 9-14, 1961

[21] P. C. Paris, F, Erdogan, A *Critical Analysis of Crack Propagation Laws*, Journal of Basic Engineering, Vol. 85, pp. 528-34, 1963

[22] P. J. E. Forsyth, A *two stage process of fatigue crack growth, In crack propagation*: proc. Crachfield symposium, pp. 76-94, 1962

[23] C. A. Zappfe & C. O. Worden, *Fractographic registrations of fatigue*, Trans ASM 43, pp 958-69 1951

[24] P. J. E. Forsyth & D. A. Ryder, *Fatigue Fracture*, Aircraft Engineering, Vol. 32, pp. 96-9, 1960

[25] C. Laird & G. C. Smith, *Crack Propagation in High Stress Fatigue*, Philosophical Magazine 8, pp. 847-57, 1952

[26] W. Elber, *Fatigue Crack Closure Under Cyclic Tension*, Engineering Fracture Mechanics, Vol. 2, pp. 37-45, 1970

[27] W. Elber, *The Significance of Fatigue Crack Closure In Damage Tolerant Aircraft Structure*, Special Technical Publication 486, pp. 230-42, 1971

[28] R.O. Ritchie, S. Suresh, C. M. Moss, *Near Threshold Fatigue Crack Growth in 2.25%Cr-1Mo Pressure Vessel Steel in Air and Hydrogen,* Journal Engineering Materials & Technology, Vol. 102, pp. 937-40, 1980

[29] S. Suresh, G. F. Zaminski & R. Ritchie, *Oxide Induced Crack Closure*, Metallurgical Transactions, Vol. 12A, pp. 1435-43, 1981

[30] S. Suresh & R. O. Ritchie, *A Geometric Model for Fatigue Crack Closure Induced by Fracture Surface Morphology*, Metallurgical Transactions, Vol. 13A, pp. 1627-31, 1982

[31] S. Suresh & R. O. Ritchie, *Near Threshold Fatigue Crack Propagation: A Perspective on the Role of Crack Closure*, In Fatigue Crack Growth Threshold Concepts, pp. 227-261, 1984

[32] A. G. Pineau & R. M. N. Pelloux, *Influence of Strain Induced Martensitic Transformations on Fatigue Crack Growth Rates in stainless Steels*, Metallurgical Transactions, Vol. 5A, pp. 1103-12, 1974

[33] E. Hornbogen, *Martensitic Transformation at a Propagating Crack*, Acta Metallurgica, Vol. 26, pp. 147-52, 1978

[34] J. L. Tzou, S. Suresh, R. O. Ritchie, *Fatigue Crack Propagation in Oil Environments-I. Crack Growth Behaviour in Silicon and Paraffin Oils*, Acta Metallurgica, Vol. 33, pp. 105-66, 1985

[35] S. Pearson, *Initiation of Fatigue Cracks in Commercial Aluminium Alloys and the Subsequent Propagation of Very Short Cracks*, Engineering Fracture Mechanics, Vol. 7, pp. 235-47, 1975

[36] J. Langford, *The Growth of Small Fatigue Cracks in 7075-T6 Aluminium*, Fatigue of Engineering Materials and Structures, Vol. 6, pp. 15-31

[37] K. Tanaka, M. Hojo, Y. Nakai, *Crack Initiation and Early Propagation in 3% Silicon Iron, In Fatigue Mechanisms: Advances in Quantitative Measurement of Fatigue Damage*, Special Technical Publication 811, pp. 207-32, American Society For Testing and Materials

[38] W. L. Morris, *Micro-crack Closure Phenomenon for Al 2219-T851*, Metallurgical Transactions Vol. 10A, pp. 5-11, 1979

[39] W. L. Morris, The Non-*continuum Crack Tip Deformation Behaviour of Surface Micro-crack*, Metallurgical Transactions Vol. 11A, pp. 1117-23, 1980

[40] K. Tanaka, Y. Nakai, M. Yamashita, *Fatigue Growth Threshold of Short Cracks*, International Journal of Fatigue, Vol. 17, pp. 519-33, 1981

[41] D. Taylor, *Fatigue of Short Cracks: The Limitations of Fracture Mechanics*, The Behaviour of Short Fatigue Cracks, pp. 479, 1986

[42] K. Tanaka, Y. Nakai, *Propagation and Non-Propagation Of Short Fatigue Cracks at a Sharp Notch*, Fatigue of Engineering Materials and Structures, Vol. 6, pp. 317-27, 1983

[43] N.E. Frost et al, *Metal Fatigue*, Clarendon Press, 1974

[44] L.Vincent, *Materials and Fretting Fatigue*, Fretting Fatigue ESIS 18, Mechanical Engineering Publications, 1994

[45] D.A. Hill and D. Nowell, *A Critical analysis of Fretting Fatigue Experiments*, Fretting Fatigue ESIS 18, Mechanical Engineering Publications 1994

[46] N. Darwish and R. Elliott, *Austempering of Low Manganese Ductile Irons Part 2 Influence of Austenitising Temperature*, Materials Science and Technology, Vol. 9, pp. 586-602, 1993

[47] H Bayati, R. Elliott, *Influence of Austenitising Temperature on Mechanical Properties of High Manganese Alloyed Ductile Iron*, Materials Science and Technology, Vol. 11, 1995

[48] N. Darwish and R. Elliott, *Austempering of Low Manganese Ductile Irons Part 3 Variation of Mechanical Properties with Heat Treatment Parameters*, Materials Science and Technology, Vol. 9, pp. 882-9, 1993

[49] A. S. Hamid Ali and R. Elliott, *Influence of Austenitising Temperature on Austempering of an Mn-Mo-Cu Alloyed Ductile Iron*, Materials Science and Technology, Vol. 13, pp. 24-30, 1997

[50] Aranzabal et al, *Influence of Heat Treatments on Microstructure of ADI*, Materials Science and Technology, Vol. 10, pp. 728-738, 1994

[51] P. Prasad Rao, Susil K. Putatunda, *Influence of Microstructure on Fracture Toughness of ADI*, Metallurgical and Material Transactions, Vol. 28A, pp. 1457-1470, 1997

[52] N. Darwish and R. Elliott, *Austempering of Low Manganese Ductile Irons Part 1 Processing Window*, Materials Science and Technology, Vol. 9, pp. 572-585, 1993

[53] G. I. Rees, and H. K. D. Bhadeshia, Materials Science and Technology, 8, 985, 1992

[54] N, Chester and H. K. D. Bhadeshia, Journal de Physique, Vol. C5, pp. 41, 1997

[55] J . Aranzabal et al, *Influence of the Amount and Morphology of Retained Austenite on the Mechanical Properties of an ADI*, Metallurgical and Materials Transactions, Vol. 28A, 1997

[56] R.C. Thomson, S. James, D.C. Putman, *Modelling Microstructural Evolution and Mechanical Properties of Austempered Ductile Iron*, Materials Science and Technology, Vol. 10, pp. 1412-1419, 2000

[57] P. Prasad Rao and Susil K. Putatunda: *Comparative Study of Fracture Toughness of ADI With Upper and Lower Bainitic Ferrite Structures*, Materials Science and Technology, Vol. 14, pp. 1257-65, 1998

[58] D. J. Moore, T. N. Rouns, K. B. Rundman, ASF Transactions, Vol. 95, pp. 765-74, 1987

[59] C. –K. Lin, P. –K. Lia, T. –S. Shih, *Influence of Microstructure on the Fatigue Properties of ADI – I. High-Cycle Fatigue*, International Journal of Fatigue, Vol. 18, pp. 297-307, 1996

[60] P. Prasad Rao, Susil K. Putatunda, *Influence of Microstructure on Fracture Toughness of ADI*, Metallurgical and Material Transactions, Vol. 28A, pp. 1457-1469, 1997

[61] K. H. Zum Gahr and L. Wagner: Arch. Eisenhuttenwes, Vol.50, pp. 269-74., 1979

[62] J. L. Doong, F. C. Ju, H. S. Chen, L. W. Chen: Journal of Material Science, Vol. 5, pp. 555-8, 1986

[63] J. L. Doong, C. S. Chen, Fatigue and Fracture Engineering Material Structures, Vol. 12, pp. 155-65, 1989

[64] P. Prasad Rao and Susil K. Putatunda: *Dependence of Fracture Toughness of ADI on Austempering Temperature,* Metallurgical and Material Transactions, Vol. 29A, pp. 3005-3015, 1998

[65] L. Bartosiewicz et al, *Influence of Microstructure on High Cycle Fatigue Behaviour of ADI*, Materials Characterisation, Vol. 30, 1993

[66] C. –K. Lin, T. –P. Hung, *Influence of Microstructure on the Fatigue Properties of ADI – II. Low-Cycle Fatigue*, International Journal of Fatigue 18, 309-320, 1996

[67] C. –K. Lin, Y. –L. Pai, *Low Cycle Fatigue of ADI at Various Strain Ratios*, International Journal of Fatigue 21, 45-54, 1999

[68] P. Shanmugan, R. P. Prasad, U. K. Rajendra, *Effect of Microstructure on the Fatigue Strength of an Austempered Ductile Iron,* Journal of Material Science Vol. 29, pp.4933-4940, 1994

[69] M. Bahmani et al, *The Relationship Between Fatigue Strength and Microstructure in an Austempered Cu-Ni-Mn-Mo Alloyed Ductile Iron*, Journal of Material Science, pp. 5383-5388, 1997

[70] D Putman, Email Conversation, 03/04/2003

[71] T. J. Marrow, H. Cetinel, *Short Fatigue Cracks in ADI*, Fatigue and Fracture of Engineering Materials and Structures, Vol. 23, pp. 425-34, 2000

[72] G. L. Greno, J. L. Otegui, R. E. Boeri, *Mechanisms of Fatigue Crack Growth in ADI*, International Journal of Fatigue 21, pp. 35-43, 1999

[73] T.Palin-Luc, S. Lasserre, J. Y. Berard, *Experimental Investigation of the Conventional Endurance Limit of a Spheroidal Graphite Cast Iron*, Fatigue and Fracture, Vol. 21, pp. 191-200, 1998

[74] J. Ortiz, A. P. Cisilino, J. L. Otegui, *Effect of Microcracking on the Micromechanics of Fatigue Crack growth in Austempered Ductile Iron,* Fatigue and Fracture of Engineering Materials and Structures, Vol. 24, pp. 591-605, 2001

[75] J. R. Hwang and P. J. Chung, *The Growth of Short Fatigue Cracks in Nodular Irons with Various Austempering Treatments,* Japanese Society of Mechanical Engineering Vol. 13, 1992

[76] T. J. Marrow, H. Cetinel, M. Al-Zalmah, S. MacDonald, P. J. Withers, J. Walton, *Fatigue Crack Nuclei in Austempered Ductile Iron*, Submitted to Fatigue and Fracture of Engineering Materials, 2002

[77] R. C. Dommarco, P. C. Bastias, H. A. Dall'O, G. T. Hahn, C. A. Rubin, *Rolling Contact Fatigue (RCF) Resistance of Austempered Ductile Iron (ADI)*, Wear, Vol. 221, pp. 67-74, 1998

[78] N. Rebasa, R. C. Dommarco, J. Sikora, *Wear Resistance of High Nodule Count Ductile Iron,* Wear, Vol. 253, pp. 855-863, 2002

[79] R. C. Dommarco, J. D. Salvande, *Contact Fatigue Resistance of Austempered and Partially Chilled Ductile Irons*, Wear, Vol. 254, pp. 230-236, 2003

[80] Cast Irons – ASM Specialty Handbook, The Materials Information Society, 1996

[81] J. Boselli, I. Sinclair, P.J. Gregson, P.D. Pitcher, *Quantitative Assessment of Particle Distribution Effects on Short Crack Growth in SIC_p Reinforced Al-Alloys*, Scripta Materialia, Vol. 38, pp839-844, 1997

[82] P. M. Scott and T. W. Thorpe, *A Critical Review of Crack Tip Stress Intensity Factors for Semi-elliptical Cracks*, Fatigue of Engineering Materials and Structures, Vol. 4, pp. 4, 1981

[83] W. A. Spitzig, J. F. Kelly, O. Richmond, *Metallography*, Vol. 18, pp. 235-261, 1985

[84] P.A.S. Reed, J.S. James, D.C. Putman, R.C. Thomson, K.K. Lee, S.R. Gunn, *Microstructural Effects in the Fatigue of ADI*, Paper submitted to Mat. Sci. Eng., 2001

[85] N. Yang, J. Boselli, P. J. Gregson, I. Sinclair, *Simulation and Quantitative Assessment of Finite-size Particle Distributions in Metal Matrix Composites,* Materials Science and Technology, Vol. 16, pp. 797-805, 2000

[86] N. Yang, J. Boselli, I. Sinclair, *Simulation and Quantitative Assessment of Homogeneous and Inhomogeneous Particle Distributions in Metal Matrix Composites,* Journal of Microscopy, Vol. 201, pp. 189-200, 2000

[87] H.E. Henderson, *Compliance with Specifications for Ductile Iron Castings Assures Quality*, Met. Prog., Vol 99, May 1966, pp. 82-86

[88] R.C. Thomson, J.S. James and D.C. Putman, *Modelling Microstructural Evolution and Mechanical Properties of Austempered Ductile Iron,* Materials Science and Engineering A, Vol. 346, pp. 273-286, 2003

[89] M.C. Mwanza, M.R. Joyce, K.K. Lee, S.Syngellakis, P.A.S. Reed, *Microstructural Classification of Fatigue Crack Initiation in Al based Plain Bearing Alloys*, Fatigue Damage of Structural Materials IV.

[90] S. R. Gunn, M.Brown, In Proc: IEEE *International Workshop on Neural Networks for Signal Processing,* Madison, Wisconsin, 1999

[91] K.K. Lee, C.J. Harris, S. R. Gunn, P.A.S. Reed, Proc: IJCNN, Washington DC, USA, 2001, pp. 2410-2415

[92] T. W. Clyne, P. J. Withers, *An Introduction to Metal Matrix Composites*

[93] P. J. Withers, W. M. Stobbs, O. B. Pedersen, *The Application of the Eshelby Method of Internal Stress Determination to Short Fibre Metal Matrix Composites,* Acta Metallurgica, Vol. 37, pp. 3061-3084, 1989

[94] H. Mizubayashi, J. J. Li, H. Yumoto, M. Shimotomai, *Young's Modulus of Single Phase Cementite,* Scripta Materialia, Vol. 40, pp. 773-777, 1999

[95] M, Umenoto, Z. G. Liu, K. Masuyama, K. Tsuchiya, *Influence of Alloy Additions on Production and Properties of Bulk Cementite*, Scripta Materialia, Vol. 45, pp. 391-397, 2001

[96] W. H. Hunt, J. R. Brockenbrough, P. E. Magnusen, *An Al-Si-Mg Composite Model System: Microstructural Effects on Deformation and Damage Evolution,* Scripta Metallurgica, Vol. 25, pp. 15-20, 1991

[97] J. Llorca, A. Martin, J. Ruiz, M. Elices, *Particulate fracture during deformation of a spray formed metal-matrix composite,* Metallurgical Transactions, Vol. 24, pp. 1575-1588, 1993

[98] D. J. Lloyd, *Aspects of Fracture in Particulate Reinforced Metal Matrix Composites*, Acta Metallurgica, Vol. 39, pp. 59-71, 1991

[99] T. Mochida, M. Taya, D. J. Lloyd, *Fracture of Particles in a Particle/Metal Matrix Composite Under Plastic Straining and its Effect on the Young's Modulus of the Composite*, Materials Transactions, Vol. 32, pp. 931-42, 1991

[100] Y. Brechet, *Damage Initiation in Metal Matrix Composites*, Acta Metallurgica, Vol. 39, pp. 1781-1786, 1991

[101] P. M. Singh, J. J. Lewandowski, *Effects of Heat Treatment and Reinforcement Size on Reinforcement Fracture During Tension Testing of a SiCp Discontinuously Reinforced Aluminum alloy*, Metallurgical Transactions, Vol. 24, pp. 2531-2543, 1993

[102] C. H. Caceres and J. R. Griffiths, *Damage by the Cracking of Silicon Particles in an Al-7Si-0.4Mg Alloy*, Acta Materialia, Vol. 44, pp 25-33, 1996

[103] N. M. Mawsouf, *A Micromechanical Mechanism of Fracture Initiation in Discontinuously Reinforce Metal-Matrix Composite*, Materials Characterisation, Vol. 44, pp. 321-327, 2000

[104] C. A. Lewis, P. J. Withers, *Weibull Modelling of Particle Cracking in Metal Matrix Composites*, Acta Metallurgica, Vol. 43, pp. 3685-3699, 1995

[105] C. W. Nan, D. R. Clarke, *The Influence of Particle Size and Particle Fracture on the Elastic/Plastic Deformation of Metal Matrix Composites*, Acta Materialia, Vol. 44 pp. 3801-3811, 1996.

[106] D. L. Davidson, *The Effect of Particulate SiC on Fatigue Crack Growth in a Cast-Extruded Aluminum Alloy Composite*, Metallurgical Transactions, Vol. 22, pp. 97-112, 1991

[107] J. J. Lewandowski, C. Liu, W. H. Hunt, *Effects of Matrix Microstructure and Particle Distribution on Fracture of an Aluminum Metal Matrix Composite*, Materials Science & Engineering, Vol. A 107, pp. 241-55, 1989

[108] M. Manoharan, J. J. Lewandowski, *Effect of Reinforcement Size and Matrix Microstructure on the Fracture Properties of an Aluminum Metal Matrix Composite*, Materials Science & Engineering, Vol. A150, pp. 179-86, 1992

[109] D. S. Wilkinson, E. Maire, R. Fougeres, *A Model for Damage in a Clustered Particulate Composite, Materials Science and Engineering*, Vol. A262, pp. 264-270, 1999

[110] T. Christman, A. Needleman, S. Suresh, *An Experimental and Numerical Study of Deformation in Metal Matrix Composites,* Acta Metallurgica, Vol. 37, pp. 3029-50, 1989

[111] S. Ghosh, S, Moorthy, *Particle Fracture Simulation in Non-uniform Microstructures of Metal Matrix Composites,* Acta Materialia, Vol. 46 pp. 965-982, 1998.

[112] N. Kamaya, N. Totsuka, *Influence of Interaction Between Multiple Cracks on Stress Corrosion Crack Propagation,* Corrosion Science, Vol. 44, pp. 2333-2352, 2002

[113] W. O. Soboyejo, J. F. Knott, *The Propagation of Non-Coplanar Semi-elliptical Fatigue Cracks*, Fatigue and Fracture of Engineering Materials, Vol. 14, pp. 37-49, 1991

[114] W. O. Soboyejo, K. Kishimoto, R. A. Smith, J. F. Knott, *A Study of the Interaction and Coalescence of Two Coplanar Fatigue Cracks in Bending*, Fatigue and Fracture of Engineering Materials, Vol. 12, pp. 167-174, 1989

[115] J. W. Twaddle, B. R. Hancock, *The Development of Cracks by Defeat Coalescence*, Engineering Materials Advice Service, September, pp. 185-198, 1998

[116] C. J. Bayley, R. Bell, *Experimental and Numerical Investigation of Coplanar Fatigue Crack Coalescence*, International Journal of Pressure Vessel and Piping, Vol.74 pp. 33-37, 1998

[117] C. Bayley, G. Glinka, J. Porter, *Fatigue Crack Initiation and Growth in A517 Submerged Arc Welds Under Variable Amplitude Loading*, International Journal of Fatigue, Vol. 22, pp. 799-808, 2000

[118] J. Stolarz, *Multicracking in Low Cycle Fatigue – A Surface Phenomenon?* Materials Science and Engineering, A234-236, pp. 861-864, 1997